Application of Mach-Zehnder interferometer for co-phasing extremely large telescopes

Luzma Montoya-Martinez

▶ To cite this version:

Luzma Montoya-Martinez. Application of Mach-Zehnder interferometer for co-phasing extremely large telescopes. Astrophysics [astro-ph]. Université de Provence - Aix-Marseille I, 2004. English. NNT : . tel-00010384

UNIVERSITÉ DE PROVENCE-AIX-MARSEILLE I
LABORATOIRE D'ASTROPHYSIQE DE MARSEILLE

ÉCOLE DOCTORALE « Physique et sciences de la matière »

Application de l'interféromètre de Mach-Zehnder au co-phasage des grands télescopes segmentés

THÈSE

pour obtenir le grade de *Docteur de l'Université de Provence*
Discipline: rayonnement et plasmas-optique
Présentée et soutenue publiquement le 20 septembre 2004 par

LUZ MARÍA MONTOYA-MARTÍNEZ

Directeurs de thèse : GÉRARD LEMAITRE et KJETIL DOHLEN

JURY

M. Claude Aime	président
M. Salvador Cuevas Cardona	rapporteur
M. Nicholas Devaney	rapporteur
M. Gérard Rousset	examinateur
M. Kjetil Dohlen	co-directeur de thèse
M. Gérard Lemaitre	directeur de thèse

A mis padres,

a Cris y Marian,

a Jorge.

Remerciements

I would like first to thank the RTN Program, "Adaptive Optics for ELts", the financial support of this work and for the opportunity of meeting other members of the Network.

Je veux remercier mon directeur de thèse, Gérard Lemaitre, pour son accueil et son soutien tout au long de la thèse.

A Kjetil je lui dois plus qu'un remerciement. Sans lui je ne serais jamais arrivée jusqu'au bout. Lui, il m'a appris à réfléchir et à ressortir l'esprit critique, très important pour la recherche. Même s'il avait toujours plein de choses à faire, il trouvait le temps pour se consacrer à moi. Merci aussi pour la patiente qu'il a montrée même dans les moments ou je sortais les plus grandes bêtises. Je ne peux dire que ¡BRAVO!.

A tout le personnel du Labo. A Marc pour le soutien moral qui a été très important pour moi. A Fred pour sa disponibilité inconditionnelle. A Patrick parce que sans lui le chapitre 4 n'existerai pas. Il m'a montré comme il faut travailler au banc optique sans désespérer. A Silvio et Valerie pour l'aide informatique. A Arnaud pour être mon Born & Wolf et pour son aide précieuse avec la présentation oral de cette thèse. A Léo María parce qu'il m'a beaucoup aidée avec le super résumé en français. Au début il a été mon IDL guideline mais finalement il est devenu un très bon ami. A Christine pour son soutien quotidien. A Olivia et sa famille pour les soirées à La Ciotat et sa joie.

I would like to thanks all the RTN members. Specially Marcel for his support with CAOS, Rodolph for this useful experience with turbulence, Natalia for her *warm help* in Fourier Optics, Markus for the great support in IDL, Nicholas and GTC staff for the nice welcome at La Laguna and all I learnt with them, Dolo because she is an excellent reference for my work, Achim because it is a pleasure to work with him and he is always available to resolve my questions.

Pero si en una tesis el trabajo intelectual es importante, desde luego el moral no es menos. En este sentido doy las gracias a todos los que me han apoyado y han soportado mis quejas desde lejos.

Así que gracias a Cami, Inés, Lauri, La Rubia, Nuria, Maribel y Gaspi porque nunca dudaron que yo lo conseguiría y me han mimado y animado siempre que estaba triste. Porque me ha hecho reir y ha sido mi fiel compañera de "perjudicamiento", le doy las gracias a Elena. Menos mal que Lorenzo y Maria del Mar estaban en Barcelona para hacer el retorno de vacaciones a Marsella mucho mas llevadero.

Un agradecimiento muy cariñoso para Ángeles, Ruth, Carlos, Jesús, Luis y todos los demás que hicieron mi estancia en Canarias tan agradable.

No me olvido de las chelas y las "soires en l'Intermédiaire" con los *pinches* mejicanos, Jorge y Leo y el canijo de Marc. A pesar de que se fueron muy lejos, Iqui y Marcela se quedaron muy cerca y forman parte de los momentos mas intensos vividos en Marsella. Y que decir de Juanjo "el gato", el primer español que conocí en Marsella y que me cuido como un padre hasta que llego Jorge.

A mis compis del Calar Alto, Jesus, Santos, Manolo, Felipe, Ulli y Alberto les doy las gracias porque a pesar de estos cuatro años fuera siguen queriendo que vuelva... bueno unos mas que otros.

A Begoña, porque aunque nunca vino a verme siempre estuvo conmigo.

A los "cousins", Jeremy, Ricki, Ludo, Leo et Julie porque mereció la pena venir a Marsella solo por conocerles.

A los Strehle por las comidas tan ricas que nos hicieron con la famosa "canicule" y porque junto con Christian y Barbara lo pasamos muy bien de fiesta en fiesta. Y por supuesto

Résume

La segmentation des miroirs semble être l'unique solution envisageable pour les très grands télescopes. Pour obtenir la qualité d'image nécessaire aux programmes scientifiques astronomiques, les erreurs d'alignement des segments doivent être réduites à la dizaine de nanomètres.

Cette thèse présente une nouvelle technique pour le co-phasage des miroirs segmentés basée sur un interféromètre de Mach-Zehnder comportant un filtre spatial dans un des bras. Les perturbations atmosphériques sont éliminées si la taille de filtre est de l'ordre de la tache de seeing. L'étude a été divisée en trois niveaux: étude analytique, simulation numérique et approche expérimentale. La performance de cette technique a été étudiée pour des cas réalistes en considérant les effets de bords, le bruit de photon et les caractéristiques du détecteur.

Une comparaison de trois nouvelles techniques de co-phasage est aussi présentée. Cette technique semble être un des candidats les plus prometteurs pour des grands télescopes segmentes.

Abstract

Segmentation seems to be the unique solution for Extremely Large Telescopes (ELTs). In order to achieve the high performance required for the astronomical science programs, the errors due to segment misalignment must be reduced to tens of nm. Therefore the development of new co-phasing techniques in highly segmented mirror is of critical importance.

In this thesis we developed a new technique for co-phasing segmented mirrors based on a Mach-Zehnder interferometer with spatial filter in one arm. Atmospheric turbulence is tolerated in this setup if the spatial filter has similar size to that of the seeing disk. The study has been split in three levels, analytical, simulation and experimental. The performance of this technique has been analysed for realistic cases including the edge defects, gaps, photon noise and detection parameters.

A comparison of three co-phasing techniques is also presented. This technique seems to be one of the strongest candidates for co-phasing of ELTs.

Contents

List of Acronyms

AO	Adaptive Optics
APE	Active Phase Experiment
CIR	Central Intensity Ratio
CMBR	Cosmic Microwave Background Radiation
CMOS	Complementary Metal Oxide Semiconductor
DFS	Dispersed Fringe Sensor
ELT	Extremely Large Telescope
ESO	European Southern Observatory
FFT	Fast Fourier Transform
FOV	Field of View
FWHM	Full Width Half Maximum
GF	Grid Function
INAF	Instituto Nazionale di Astrofisica
LAM	Laboratoire d'Astrophysique de Marseille
MCAO	Multi Conjugated Adaptive Optics
MZ	Mach-Zehnder
OPD	Optical Path Difference
OPTICON	Optical Infrared Coordination Network
OTF	Optical Transfer Function
PSF	Point Spread Function
PtV	Peak to Valley
RMS	Root Mean Square
SNR	Signal to Noise Ratio
SVD	Single Value Decomposition

-4-

List of Telescope Abbreviations

CELT	California Extremely Large Telescope
CFGT	Chinese Future Giant Telescope
GTC	Gran Telescopio de Canarias
GMT	Giant Magellan Telescope
GSMT	Giant Segmented Mirror Telescope
HDRT	High Dynamic Range Telescope
HET	Hobby-Eberly Telescope
JWST	James Webb Space Telescope
LAMOST	Large Aperture Multi-Object Spectroscopic Telescope
LBT	Large Binocular Telescope
LPT	Large Petal Telescope
SALT	Southern African Large Telescope
TIM	Mexican Infrared-Optical Telescope
TMT	Thirty Meter Telescope
VLT	Very Large Telescope
VLOT	Very Large Optical Telescope
OWL	Overwhelmingly Large Telescope

Chapitre 1-Resumé

Les télescopes de prochaine génération repousseront les frontières des connaissances astrophysiques et seront la clef pour répondre à de nombreuses questions astrophysiques non résolues. Par exemple, la combinaison de la sensibilité et du champ fournis par les futurs ELTs permettra d'étudier l'évolution des grandes structures de l'univers, tandis que la combinaison de la haute résolution angulaire et de la très grande qualité optique devrait permettre de trouver des exoplanètes du type tellurique.

Bien que de grands miroirs monolithiques puissent être construits, la complexité de fabrication et le coût augmentent avec la taille. L'approche la plus réaliste pour les ELTs semble donc être l'utilisation de la segmentation.

Au cours des vingt dernières années, de gros efforts ont été faits dans le but d'améliorer la qualité des images des télescopes. Ces efforts se sont focalisés sur la correction des erreurs de front d'onde par l'amélioration de la qualité optique des télescopes ainsi que par l'introduction de l'optique adaptative corrigeant les perturbations atmosphériques. La qualité de l'image sera également affectée par la segmentation. L'espace entre les segments, les aberrations intrinsèques des segments, les erreurs de bords rabattus et les erreurs de piston et basculement (tip-tilt) provoquent de nouveaux effets de diffraction qui sont qualitativement et quantitativement différents selon la taille et le nombre de segments.

Nous décrivons brièvement les effets des erreurs de front d'onde sur la qualité des images, en portant une attention particulière à ceux causés par le mauvais alignement des segments.

Chapter 1

ELTs: Motivation and Description

In the next decades, astronomy will profit from a diverse set of observing capabilities, covering a broad range of wavelengths, on the ground and in the space. Two main reasons make the development of large ground based telescopes critical to expand astrophysical knowledge. First, the possibility of observing in a range covering from the optical to the infrared. Second, ground based facilities can deploy much more complex instrumentation than spaced-based missions.

Three broad topics are proposed by the Astrophysical Community: Cosmology, Galaxies, and Planetary Systems and Stars. Scientific cases will benefit from the wide capabilities of large telescopes, including sensitivity, wavelength coverage, field of view (FOV), spectral resolution, photometric and astrometric accuracy, high image quality and stability. We briefly describe some scientific cases including the required capabilities and instrumentation to carry out those programs.

A number of *Extremely Large Telescopes* (ELT) projects are currently in phase of design study. They differ mainly in the primary mirror selection, although segmentation is the common solution adopted in every case. We describe the different approaches proposed by the most important ELT projects.

The image quality is affected by segmentation. This chapter includes a brief description of the effects induced by wavefront errors on the image quality, with special attention to the effect of segmentation misalignment.

1.1. The role of ELTs in Astronomy

The enormous capabilities of the next generation of telescopes will expand the frontiers of astrophysical knowledge and will be the key to answer many unresolved questions. As a consequence, a large number of scientific cases have been proposed for ELTs, covering different astrophysical contexts ranging from our own Solar System to the very early epochs of the Universe. The European Astrophysical community, under the auspices of the OPTICON (Optical Infrared Coordination Network), has classified these different scientific cases into three main categories: *Cosmology*, *Stars and Galaxies*, and *Planetary Systems and Stars*. We briefly present some of these science highlights that motivate and encourage the development of ELTs.

In the coming decades, one of the most important challenges of observational cosmology will be to measure the evolution of the spatial distribution and properties of the baryonic content of the Universe in its different phases: galaxies and intergalactic gas. Establishing the statistical evolution of galaxies from their epoch of formation (more than 13 Giga-light-years away) to the present day, requires taking hundreds of high-resolution spectra (R>5000) of very faint objects (typically >25 AB mag) over a wide area (FOV ~ 5').

At the same time, mapping the 3-dimensional distribution of the cosmic gas in the Universe requires the acquisition of high quality spectra of faint objects in the distant universe, numerous enough to finely sample the large observed areas (FOV ~ 5'). These observations are necessary to discriminate among the competing theories at stake today. Their requirements call for ELTs, which have high enough sensitivity and FOVs. The Figure 1.1.1 shows an example of simulated distribution of cosmic gas at z=2.

Stars are one of the main components of galaxies, therefore it is of critical importance to understand how they form and evolve. With ELTs, stars of mass comparable to the Sun may be resolved in the outskirts of galaxies as far as the Virgo cluster (the closest cluster to the Milky Way). Reaching the Virgo cluster is important since it hosts a significant population of elliptical galaxies at the same distance and spanning a large range of magnitudes. With a very high spatial resolution (~10mas), required to diminish the effect of crowding, and a collecting power capable to reach typical magnitudes of ~35 in the optical band, we will be able to define the turn-off point of the color-magnitude diagrams of the studied stellar populations.

Figure 1.1.2 shows three color-magnitude diagrams for M32. As can be seen, the increases of the telescope aperture will result in better quality results for this kind of studies.
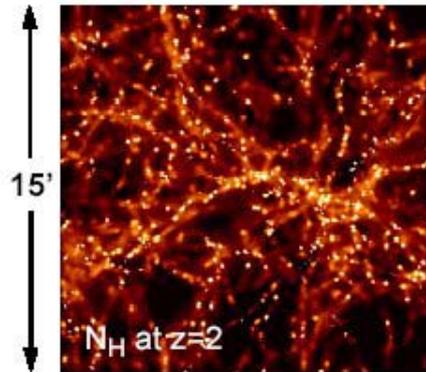
Figure 1.1.1 Projected neutral hydrogen in a simulation for z=2, from Katz et al (1996). The simulation box is 22.22 co-moving Mpc across, which corresponds to 7.4 physical Mpc at this redshift. For the CDM cosmology used, this translates into 15.1 arcmin.
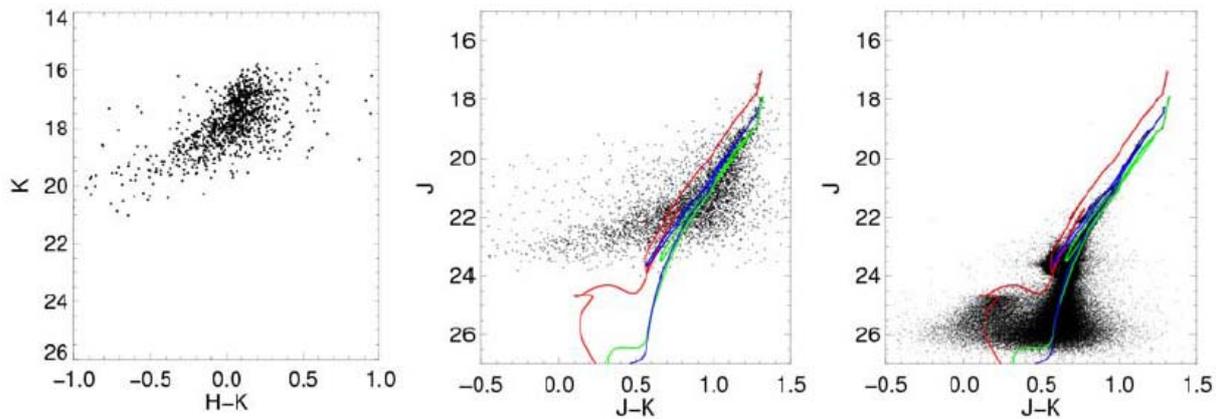
Figure 1.1.2 Stellar populations at the center of M32. Left: Color-magnitude diagram of the central 30" of M32, as observed with Gemini+Hokupa'a (Davidge et al. 2000). Middle: JWST color-magnitude diagram from a simulation assuming physical conditions similar to those of the center of M32. Right: GMST simulated color-magnitude diagram of the center of M32.

The discovery of extra-solar planets has placed our solar system in a new context and has revived the theoretical investigations of the formation and evolution of planetary system. These theories can be tested directly by measuring the gas phase dynamics and the chemical structure of protoplanetary disks. For this program high spatial (<80mas) and spectral (R~10^5) resolutions at thermal infrared wavelengths are required.

According to the scientific programs, the required capabilities can be gathered in four different operation modes:

i) Wide Field Mode: In this mode the angular resolution is limited by atmospheric conditions. It provides high sensitivity over a large FOV (~5'-10').

ii) Classical Adaptive Optics Mode: This mode will provide diffraction-limited FOV around 10" in the infrared.

iii) Multi Conjugate Adaptive Optics (MCAO) Mode: MCAO (Beckers 1988) permits the extension of the diffraction-limited FOV beyond the limits of the isoplanatic patch. Moderate image quality can be reached over FOV of 30" in the visible and 2' in the infrared.

iv) Extreme Adaptive Optic Mode: This mode provides diffraction limited images with very high quality but in small FOV (~1"-10"). The high spatial resolution and IR sensitivity of an ELT enables one of the most attractive and high priority targets of ELTs: to find the Earth like extra-solar planets around nearby bright stars.

1.2. ELT Projects

The technology developed for 10-m class telescopes serves as starting point for the design study of ELTs. In the current generation of large telescopes, two concepts primary mirrors have been pursued: monolithic mirrors and segmented mirrors.

Two technologies have been developed for current monolithic mirrors. The first one is the construction of a single large mirror made from borosilicate glass, but having large hollowed out regions to keep the weight down. This *borosilicate honeycomb* design has been pioneered by Angel & Hill (1982) and it has been successfully cast in the two 8.4-m primary mirrors of the Large Binocular Telescope (Hill & Salinari 2003). The second design is the *thin mirror* approach, primarily built by two companies, Corning (USA) and Schott (Germany). They used materials with good thermal properties, ULE (Corning) and Zerodur (Schott). Thin mirrors are being used for the four 8-m Very Large Telescope (VLT White Book, 1998). Although somewhat larger monolithic mirrors could be made, manufacturing complexity and relative cost increase with size. Therefore, the most realistic approach that can be extended to the ELTs involves the use of segmentation.

The feasibility of making segmented mirrors was first demonstrated by the Multiple Mirror Telescope (MMT) (Beckers et al, 1981) and TEMOS (Lemaître&Wang, 1993). The MMT was composed of six identical 1.8-meter telescopes in a single altitude-azimut mount. By contrast the TEMOS concept uses a primary mirror composed of large circular segments and a monolithic active secondary (Baranne&Lemaitre, 1987).

Three large segmented-mirror telescopes already exist: Keck I, Keck II (Nelson et al 1985)— which are two 10-m class telescopes composed by 36 hexagonal segments of 0.9m side— and the Hobby-Eberly Telescope (HET, Krabbendam et al 1998)- which is a 9-m telescope composed of 91 segments, each of 0.6 m side. Several others are being developed or have been proposed, including: Gran Telescopio de Canarias (GTC, Castro et al 2000) which has a similar configuration to Keck and the Southern African Large Telescope (SALT, Meiring et al 2003), whose design is based on HET. The Mexican Infrared-Optical Telescope (TIM, Cruz-Gonzalez, 2003), is a 8-m segmented telescope with 19 hexagonal segments with a maximum diameter of 1.8m. A very interesting project is the Large Aperture Multi-Object Spectroscopic Telescope (LAMOST, Wang et al 1996), which is a Schmidt telescope with a 5 degree FOV and active optics. The 6-m spherical primary mirror consists of 37 hexagonal

spherical mirrors, each of them having a diagonal of 1.1m and a thickness of 75mm. The reflecting corrector of 4.5-m is located at the center of curvature of the primary mirror, it consists of 24 hexagonal plane submirrors, each of them having a diagonal of 1.1m and a thickness of 25mm. The available large focal plane of 1.75 meters in diameter may accommodate up to 4000 fibers, by which the collected light of distant and faint celestial objects down to 20.5 magnitude is fed into the spectrographs, which promises a very high spectrum acquiring rate of several ten-thousands of spectra per night.

ELT projects are currently in the concept study stage. The main discussions concerning the optical design turn on the choice of the primary mirror, which concerns the shape of the pupil, the size and shape of the segments and the density of the pupil, taken as the percentage of pupil filled with reflective surface.

The great advantage of spherical mirrors is their segment fabrication as all segments are identical. This option has been adopted for the 100-m project Overwhelmingly Large Telescope (OWL) due to the large number of segments to be fabricated, ~3000, with the consequent disadvantage of considerably increasing the complexity of the optical design in order to correct spherical aberrations.

Although the development of segmented mirrors dates from the last decade, there is still no agreement on the choice of the segment parameters. The Thirty Meter Telescope (TMT) proposed by an American-Canadian consortium opts for hexagonal segments of 0.5 to 1m side following the example of Keck. The uses of small segments reduce cost factors related to the fabrication equipment, transportation and coating chambers. It simplifies the support mechanism and it allows higher optical quality of the individual segment. On the other hand, the choice of large segments reduces the number of actuators and edge sensors required to control the shape of the mirror. At the same time it simplifies the telescope structure and reduces the edge sensor noise propagation. This alternative has been adopted for the 25-m Giant Magellan Telescope (GMT) and the 20-m Large Petal Telescope (LPT). The GMT used 6 circular segments while LPT employs 8 irregular hexagonal segments to fill a circular shape with a minimum of edges. The shape and size of the segments plays an important role on the diffraction effects observed in the focal plane. This aspect is of relevant importance since the diffraction effects can lead to confusion in the study of faint pointlike sources.

Table 1.2.1 Optical design for ELT projects.

Projects		Optical Design	M1 Diameter	Number/size of segments	F primary	M2 Diameter
LPT (Burgarella et al 2002)		Ritchey-Chrètien /TMA[1]	20m	8 Petals 8m long	F/1	5m
HDRT (Kuhn et al 2001)		Gregorian-TMA	22m	6 Circles 6.5m Diameter	F/1	6m
GMT (Angel et al 2004)		Gregorian	25.3m	6 Circles 8.4m Diameter	F/0.7	3.5m
CFGT (Su et al 2004)		Ritchey-Chrètien	30m	1122 Partial annular 0.8 m side	F/1.2	2.1m
TMT	**VLOT** (Roberts et al 2003)	Ritchey-Chrètien	20m	150 Hexagons 0.9m side	F/1	2.4m
	CELT (Nelson 2000)	Ritchey-Chrétien	30m	1080 Hexagons 0.5m side	F/1.5	3.96m
	GSMT (Strom et al 2003)	Cassegrian	30m	618 Hexagons 0.67m side	F/1	2m
Euro50 (Ardeberg et al 2000)		Gregorian	50m	618 Hexagons 1.15m side	F/0.85	4m
OWL (Dierickx & Gilmozzi 2000)		M1 Spherical M2 Flat	100m	3048 Hexagons 0.9m side	F/1.25	34m

---

[1] TMA : Three-Mirror Anastigmat

Another parameter to be considered is the pupil density. The High Dynamic Range Telescope (HDRT) is a 22-m telescope formed by 6 off-axis, 6.5 m diameter, with a pupil density of 60%. By contrast, the Euro 50 —the 50-m telescope proposed by a consortium of European institutes— is a highly density pupil as the pupil is filled except for the obscuration due to the secondary.

In Table 1.2.1 we resume the main characteristics of the proposed ELTs. In most cases the secondary is monolithic except for OWL, where the huge size of the secondary implies its segmentation.

We remark the fast focal ratio of the primary to allow a compact telescope structure. This will make mirror manufacture harder.

The primary mirror choice will play a fundamental role in the performance of diffraction images of point sources. Several simulation studies have been carried out in order to analyse the effect of segment size and shape on the image quality (Kuhn et al 2001, Marchis & Cuevas 1999). Zamkotsian et al (2003-2004) performed the comparison of the point-spread-function (PSF) for three different mirror approaches, as seen in Figure 1.2.1. They found particularly interesting the case of polygonal petals, because the number of diffraction spikes in the PSF is minimised leading to large areas of low levels of scattered light close to the core. This is important for high dynamic range imaging.
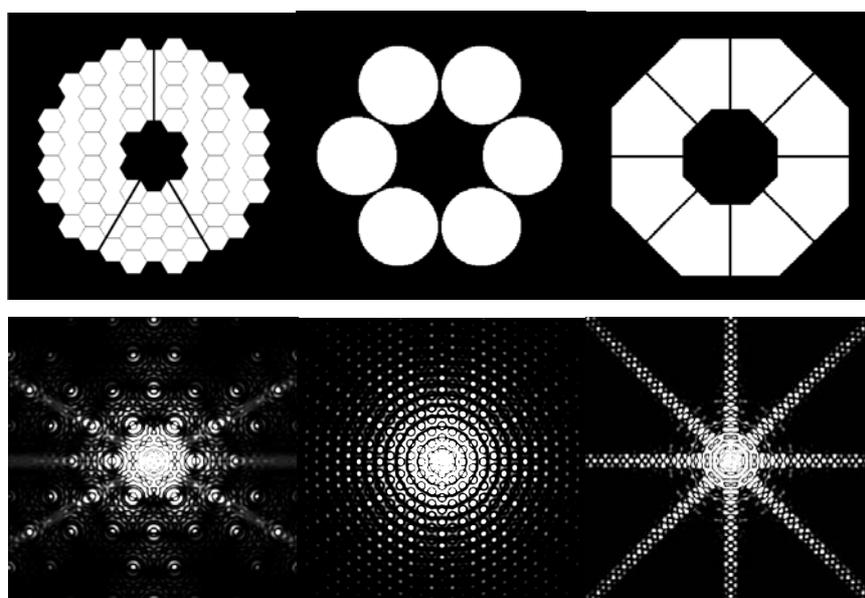
Figure 1.2.1 Three different segmentation concepts with hexagonal, circular and polygonal segments (upper row) and their corresponding PSFs (lower row), from Zamkotsian et al (2003-2004).

For certain scientific cases diffraction effects due to segment misalignment are not negligible. Diffraction effects from highly segmented mirrors have been studied in detail elsewhere (Zeider & Montgomery 1998, Troy & Chanan 2003, Yaitskova et al 2003, Bello et al, 2000), and we will briefly present them here.

1.3. Image quality of a highly segmented mirror

In the last twenty years hard efforts have been concentrated in order to improve the image quality of telescopes. Those efforts are focused in the correction of wavefront errors introduced by the atmosphere, by the use of Adaptive Optic (AO) Systems, as well as the reduction of wavefront errors related to the telescope optic quality, by the use of Active Optic Systems. Image quality will also be affected by segmentation. Gaps, individual segment aberrations, edge miss-figure errors and piston and tip-tilt misalignments result in new diffraction effects which are qualitative and quantitatively different according to the size and segment number.

In this section we briefly describe the effect of segmentation on the image quality paying special attention to the effect of segmentation misalignments. We also describe the most important properties of atmosphere turbulence and its influence on the image quality.

1.3.1. Effect of segmentation on the image quality

Generally segments have six degrees of freedom: translation along two axes in the plane of the segment, rotation about a vertical axis, rotation about two horizontal axes (tip and tilt), and translation along the vertical axis (piston). Misalignments of the three first degrees of freedom are not critical for the image quality (Mast 1982). However, movement of pistons or tip-tilts produce wavefront discontinuities which damage the image quality.

In order to quantify the quality of the image, several criteria are used. Yaitskova et al (2003), employ peak intensity and mean halo intensity of the PSF. Diericks (1992) proposed the Central Intensity Ratio (CIR), defined as the ratio between the central intensity given by the telescope divided by the central intensity given by an equivalent perfect telescope without aberrations but under the same seeing conditions. We limit this discussion to the Strehl ratio, a criteria frequently employed in astronomy. It is equal to the ratio between the central intensity of the aberrated PSF and the central intensity of the diffraction-limited PSF.

The PSF of a segmented telescope can be represented by (Yaitskova et al 2003),

$$\text{PSF}(\mathbf{w}) = \left(\frac{AN}{\lambda z} \right)^2 \text{GF}(\mathbf{w}) \text{PSF}_s(\mathbf{w}) \tag{1.1}$$

where A is the segment area, N is the number of segments, λ is the wavelength and z is the focal distance. $\text{GF}(\mathbf{w})$ and $\text{PSF}_s(\mathbf{w})$ are two functions which depend on the geometry of the

telescope segments. The function GF(**w**) is the Fourier Transform of the segmentation grid, usually a periodic array of peaks of width inversely proportional to the diameter of the full aperture. The PSF$_s$(**w**) is the PSF of an individual segment, whose width is inversely proportional to the segment size. In Figure 1.3.1 we have plotted the PSF of a 50m telescope with 714 segments, supposing that the telescope is completely phased with perfect segments and no gaps between them. In this case, zeros of the segment PSF coincide with the peaks of the GF term, so that only the central peak is observed. The six diffraction arms are the result of the hexagonal shape of the telescope pupil.
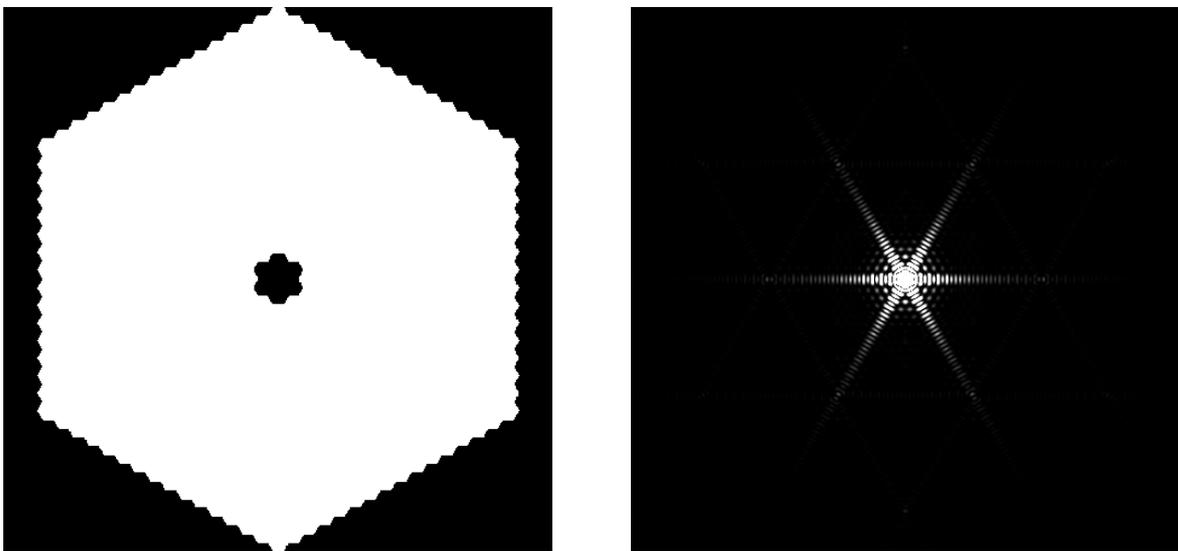
Figure 1.3.1 Pupil of a 50m class segmented telescope with 714 segments without any error (left) and its corresponding PSF(right).

The presence of piston will not influence the segment PSF. However, it will modify the grid term introducing a noisy speckle background. In Figure 1.3.2, we represent a segmented pupil with piston RMS error equal to 120nm and its corresponding PSF over a field of 0.5". The size of the speckle field is equal to the size of the segment PSF, and does not depend on the value of the piston error.

Assuming piston errors with Gaussian distribution and zero mean, the Strehl ratio of the PSF is given by;

$$S = \frac{1}{N}\left[1+(N-1)e^{-\sigma^2}\right] \qquad (1.2)$$

where N is the number of segments and σ is the standard deviation of the phase error. For highly segmented mirrors and small errors, this result is consistent with the Marechal approximation; $S \sim 1 - \sigma^2$. For a 100m class telescope with around 3000 segments, the global piston RMS error at the wavefront should be less than $\lambda/20$ (25nm@500nm) in order to get a Strehl ratio of 90%. This implies that the co-phasing technique should be able to measure discontinuities of the order of $\lambda/40$ (12nm@500nm) in the mirror surface.

For high contrast imaging, it is very important to quantify the intensity lost from the central peak. This is mainly transmitted into a diffuse halo of speckles of width λ/d and can be expressed as,

$$I = \left(\frac{d}{D}\right)^2 \left(\frac{2\pi\sigma}{\lambda}\right)^2 \qquad (1.3)$$

For a 100-m telescope, using a wavelength of 500nm, the RMS error should be less than 1nm in order to reduce the halo intensity to 10^{-10}. This implies an extreme co-phasing precision for high contrast imaging applications.
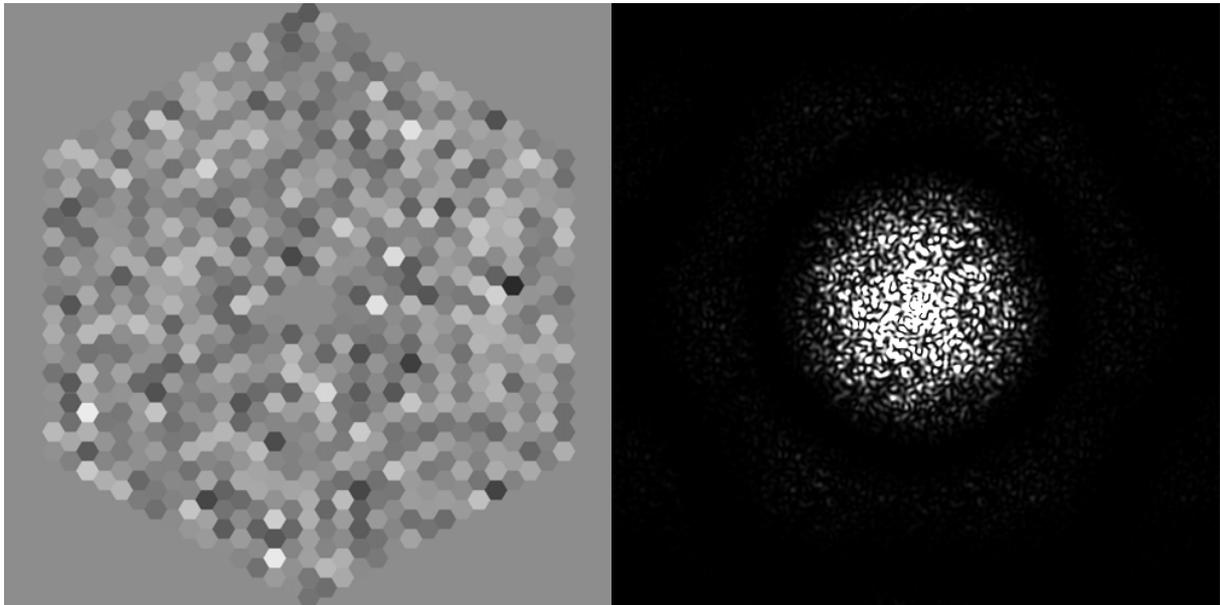

Figure 1.3.2 Segmented pupil with RMS piston error of 120nm (left) and its corresponding PSF (right).

The effect of tip-tilt errors will modify the PSF_s term of (1.1). For a small number of segments and large tip-tilt errors the PSF is the composition of the shifted individual PSFs of segments. If tip-tilt error decreases; the peaks overlap each other forming an interference

pattern, which, in the limit of zero tip-tilt error, is the PSF of the whole mirror. By increasing the number of segments, the PSF is composed by a regular grid of spots of the same size of the telescope Airy disk, in addition to the appearance of a speckle background (see Figure 1.3.3). This regular structure coincides with the interference pattern from a random blazed two-dimensional (2-D) grating (Yaitskova & Dohlen 2002). The period of the regular grid of spots is inversely proportional to the separation between segments. The Strehl ratio for small tip-tilt error can be expressed as,

$$S \approx 1 - \sigma^2 + \frac{\sigma^4}{4}\left(2.34 + \frac{2}{N}\right) \qquad (1.4)$$

Unlike the piston case, this expression is not strongly dependent on the number of segments. Once more, for a large number of segment and small errors the Marechal approximation is valid. To achieve a Strehl ratio of 90%, the global tip-tilt error in the wavefront should be less than $\lambda/20$ (25nm@500nm).
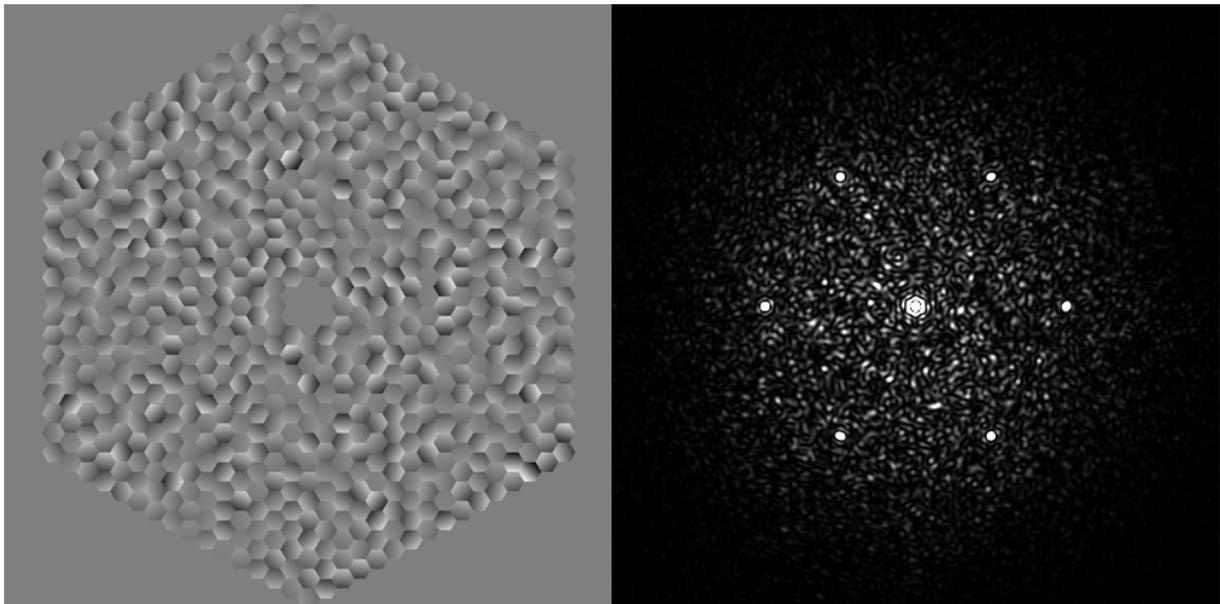

Figure 1.3.3 Segmented pupil with RMS tip-tilt error of 100nm (left) and its corresponding PSF (right).

Other error sources related to the quality of the individual segment will have similar effects on the PSF as tip-tilt errors. For example, edge defects lead to the appearance of secondary peaks and a background speckle field. Image quality performance in terms of Strehl ratio is

not significantly reduced, 0.95 Strehl ratio is achieved for typical values of edge miss-figure of the order of 5 to 10 mm width and 200nm amplitude.

1.3.2. Influence of atmospheric turbulence on the image quality

Atmospheric turbulence is caused by spatially and temporally random fluctuation of the refraction index. Fluctuations in the refraction index, mainly on account of temperature variations, result in random spatial and temporal variations of the optical path length.

Kolmogorov (1961) developed a model in which the kinetic energy was transmitted successively from the largest scale motions to the smallest ones. He assumed that the motion of the small turbulent scale is homogeneous and isotropic, i.e. the statistical characteristic of the turbulent flow depends only on the distance between any two points on the structure. The statistical distribution and number of turbulent eddies with uniform diffraction index is characterized by the power spectrum of the refractive index fluctuation, $\Phi_n(k)$, being k the spatial wavenumber related to the isotropic scale size l, as $k=2\pi/l$. Three different regimes are considered. The outer scale regime, when $k< 2\pi/L_0$, being L_0 the largest scale for the turbulent motions of the order of tens of meters, in which $\Phi_n(k)$ depends on geographical and meteorological conditions. The inner scale regime when $k>2\pi/l_0$, being l_0 the smallest size of turbulent eddies of the order of millimetres.

The Kolmogorov spectrum in the regime between the outer and inner scale, can be expressed mathematically as (Noll 1976),

$$\Phi^k(k) = 0.023\, r_0^{-5/3} |k|^{-11/3} \tag{1.5}$$

where r_0 is the Fried (Fried 1966) parameter given by,

$$r_0 = 0.185 \left[\frac{\lambda^2 \cos\gamma}{\int_0^L C_n^2(z)\mathrm{d}z} \right]^{3/5} \tag{1.6}$$

where γ is the angle of observation and $C_n^2(z)$ is the structure constant of the index of refraction fluctuation which is a function of altitude, z. Experimental measurements have demonstrated that the structure function varies from site to site and also with time. The Fried parameter r_0, it is the aperture over which there is approximately one radian RMS phase

aberration, and hence it is the maximum aperture bellow which diffraction limited resolution is possible. For example, a 10m telescope observing under turbulence conditions with r_0=10cm in the visible, will not obtain a better resolution than a 10cm telescope.

The Full Width Half Maximum (FWHM) of the atmospheric PSF is called *Seeing (β)*. It is the parameter most commonly used in astronomy to characterise atmospheric conditions and it is given by,

$$\beta = 0.98 \frac{\lambda}{r_0} \qquad (1.7)$$

To avoid the singularity of the Kolmogorov model for wavenumber close to zero an alternative model is proposed. It is known as von Karman model (Roggeman 1996), and the spectrum of the index fluctuation is given by,

$$\Phi_n^V(k) = \frac{0.0229 r_0^{-5/3}}{(k^2 + k_0^2)^{11/6}} \exp\left\{\frac{k^2}{k_m^2}\right\} \qquad (1.8)$$

where $k_0=2\pi/L_0$ and $k_m=5.92/l_0$. Both models are coincident in the regime between outer and inner scale.

Locally fluctuations of the refraction index cause phase variations on the wavefront, and propagation of a plane wave trough the turbulence introduces phase and amplitude variations.

The temporal behaviour of the atmosphere is characterized by a correlation time, τ_0,

$$\tau_0 = 0.31 \frac{r_0}{\overline{V}} \qquad (1.9)$$

where $\overline{V}$ is the mean wind speed.

Short exposure imaging refers to the situation in which exposure time is less than correlation time, τ_0. This exposure time is short enough to freeze the speckle effects of atmosphere, see Figure 1.3.4.

When the exposure time is much longer than the correlation time of atmosphere, the image is called long exposure image. In this case, atmosphere is averaged over a large number of independent realizations, given a broader and smoother PSF.

The optical transfer function (OTF) for long exposure images can be expressed as (Roggeman & Welsh 1996),

$$H_{LE}(\mathbf{f}) = T(\mathbf{f}) \exp\left\{-3.44\left(\frac{\lambda|\bar{\mathbf{f}}|}{r_0}\right)^{5/3}\right\} \tag{1.10}$$

where $T(\mathbf{f})$ is the OTF of the telescope. The simulated PSF for long exposures can be obtained from the Fourier transform of (1.10).
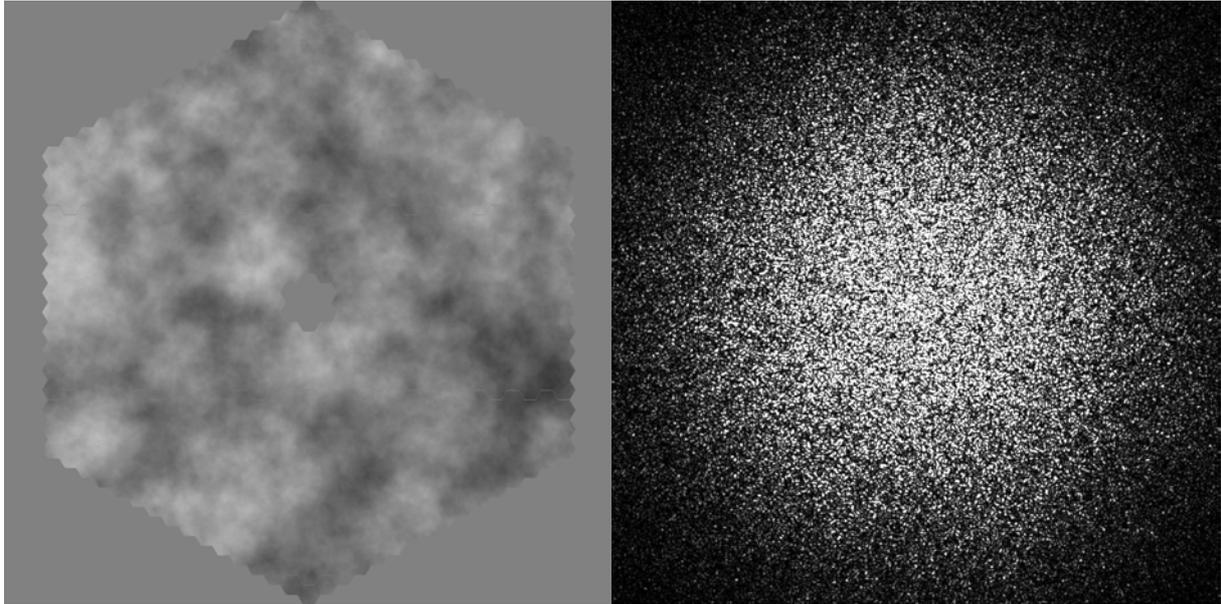
Figure 1.3.4 Simulated phase screen for 50m telescope, with r0=15cm (left), and its corresponding short exposure PSF.

AO is able to compensate in real time wavefront errors introduced by atmosphere, thus restoring image quality.

As described in section 1.1, ELTs will operate in different modes depending on the scientific target. Therefore, image quality and the degree of correction will vary according to the scientific case.

Image quality will be improved in different stages. The first stage involves correcting misalignment errors between segments to obtain the desired shape of the primary mirror. The *co-phasing* procedure should be able to detect piston errors of the order of tens of nm. This is the aim of developing new co-phasing techniques described in the next section. This procedure must be carried out before scientific observations are made and, in principle, one iteration per night should be sufficient. Other scientific programs require higher image quality. AO systems enable wavefront corrections in real time with Strehl ratios of the order

of 50%. Up to now AO systems have been applied to correct high order aberrations. In the case of ELTs, discussions focus on the development of combined systems that will correct the whole range of frequency at the same time. One of the main difficulties of AO systems for ELTs is in its manufacturing. For example, the internal pupil diameter cannot be reduced below 1m for a 100m primary considering a 10 arcmin FOV (total FOV of OWL) and a maximal beam angle of 10° on the Deformable Mirror.

If the image quality has to be improved up to Strehl ratios higher than 90% with very high contrast —which will be the case of detection of extra-solar planets— Extreme AO corrections are required. Simulation results (Riccardi et al 2003) show that the co-phasing procedure precision should be above 1 nm in order to reduce the halo due to piston. This implies real time correction of segment misalignments. To this regard, Brusa et al (1999) proposed an adaptive primary mirror able to correct the ground layer and segment misalignments simultaneously. However, this question remains unresolved in obtaining the perfect telescope performance.

Chapitre 2-Resumé

Les grands télescopes sont équipés d'optique active dans le but de maintenir automatiquement la forme et la position requise du miroir. En effet, les effets gravitationnels et thermiques génèrent des variations de grandes amplitudes dans les systèmes optiques. D'autre part, ces variations étant quasi statiques (moins d'un Herz), une opération en boucle fermée est moins contraignante que dans le cas de l'optique adaptative.

La boucle de contrôle du co-phasage est schématiquement formée de trois éléments. Les capteurs de position situés derrière ou sur le côté de chaque segment fournissent en permanence les positions relatives entre 2 segments adjacents avec une précision de quelques nanomètres. Les actionneurs situés en dessous de chaque segment compensent les déplacements entre segments. Et finalement le capteur de co-phasage fournit les informations pour la calibration périodique du capteur de position, afin de permettre la mesure absolue du piston de chaque segment.

Nous présentons ici un état de l'art des différentes techniques de co-phasage. Nous incluons la plus connue des techniques, celle proposée par Chanan et al (1998) et déjà implémentée au télescope Keck. Nous décrivons également d'autres analyseurs de co-phasage basés sur la méthode de courbure, le principe à pyramide et l'interféromètre de Mach-Zehnder (MZ), qui sera le sujet de ce travail.

Chapter 2

Review of co-phasing Techniques

Large telescopes are equipped with active optics in order to automatically maintain the required shape and position of the mirror. Most errors in the optical setup are associated to gravity and temperature variations. Given that those variations are quasi static —less than 1 Hertz— the conditions for the close loop operation are relatively relaxed compared with those required for Adaptive Optic.

The co-phasing control loop is formed basically by three elements. The position sensors located at the back or at the edge of each segment permanently provide relative positions of two adjacent segments with a few nanometres accuracy. The actuators situated underneath each segment compensate displacements between segments. Finally, the phasing sensor provides information for periodical calibration of the position sensor to enable measuring absolute piston differences between segments.

Various co-phasing sensors are based on existing wavefront sensors usually employed in AO applications, for example Curvature, Shack-Hartman or Pyramid. Although the wavefront sensor setup does not suffer major changes, the wavefront sensor in the AO application detects continuous variations in the wavefront, either curvatures in the case of Curvature sensor or slopes in the case of Pyramid and Shack-Hartman sensors. However, for co-phasing applications the interest lies on measuring discontinuities on the wavefront. In this case, the recorder signal is the result of the diffraction effect propagation due to segmentation.

In order to achieve the best performance, the co-phasing technique must deal with additional wavefront errors, i.e. segment and edge miss-figure, atmospheric turbulence, gaps, cross-talk between contiguous edge, photon noise, propagation errors, etc. Some of the methods presented here are not suitable for ground based telescopes since they do not include atmospheric errors. This is the case, for example, of the co-phasing technique described for James Webb Space Telescope, JWST (Seery 2003).

2.1. Diffraction co-phasing techniques

Diffractive techniques are based on the analysis of images produced by a lenslet array situated in the conjugate plane of the telescope pupil.

The Phasing Camera System described by Chanan et al (1998), currently operating at the Keck telescope, is a diffractive wavefront sensor in which the lenslet array is preceded by a mask at the position of the exit pupil. The mask defines a small circular subaperture of 12cm in diameter (referred to the primary) at the center of each intersegment edge. The size of the subapertures is small in comparison with the Fried parameter —of the order of 20cm— so as to ensure low dependence on atmospheric turbulence. Piston information is contained in the diffraction pattern of each subaperture. Piston is obtained from the correlation of the measured image with a simulated set of templates. In the Narrow–Band regime (Chanan et al 2000) images are cross-correlated with a set of 11 templates in the range of half a wave. The capture range of this technique can be increased by using multiple wavelengths.

In the Broadband regime (Chanan et al 1998), a set of 11 templates are simulated in the range of the coherence length of light. The step is obtained from the "coherence parameter", defined as the difference between maximum and minimum correlation coefficient.

Korhonen & Haarala (1998) proposed a procedure which is similar to Chanan with three subapertures at the corner of the segment mask as shown in Figure 2.1.1.
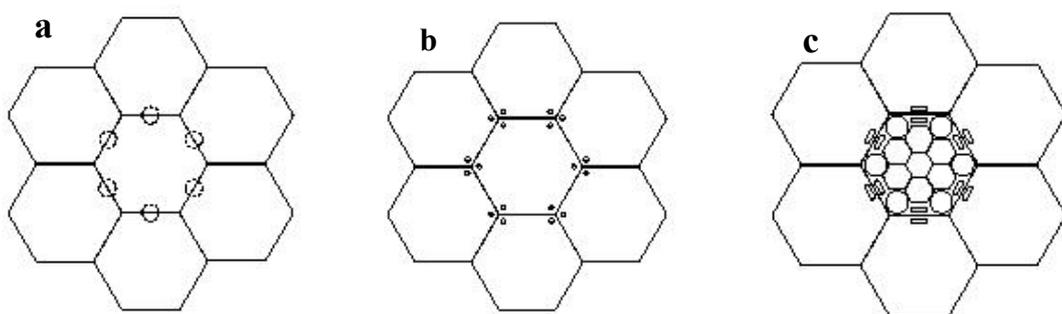

Figure 2.1.1 Masks for the Shack Hartman sensor proposed by; a: Chanan et al (1998); b: Korhonen & Haraala (1998), and c: Bello-Figueroa (2001).

Bello-Figueroa (2001) proposed a modification of the Chanan technique for the GTC telescope. The geometry of the mask, proposed for the GTC acquisition camera, allows one to

measure segment discontinuities as well as segment figure errors. They replaced the circular aperture used for Keck with a double slit. This way the effect of edge miss-figure can be avoided, as seen in Figure 2.1.1. The algorithm used to retrieve step errors is based on the properties of the diffracted image. Figure 2.1.2 shows a set of diffraction images and the vertical profile for different piston errors. A calibration curve is obtained from the difference between the two main peaks of the diffraction pattern. For a given diffracted image, the peak ratio is calculated and processed by the calibration data in order to obtain the required piston step.

Schumacher et al (2002) improved and completed the GTC study for the case of ELTs. Firstly, they fitted the diffraction images using a double Gaussian model which allows them to get a more accurate measurement of the peak difference, even under turbulence conditions. Secondly, they used weightings on individual measurement errors when the piston values of all segments were calculated by Single Value Decomposition (SVD), a standard method to find the least-squares solution to an over determined set of linear equations (Press et al 1992).
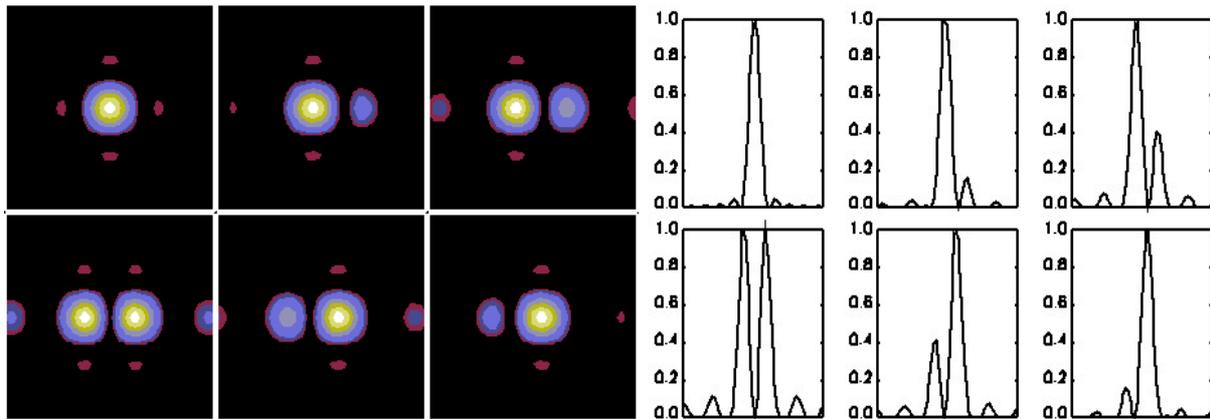

Figure 2.1.2 Simulated 2-D diffraction pattern (left) and the x-projection (right) of a double slit for 0, upper left to 5π/6 lower right piston error.

2.2. Co-phasing techniques based on Curvature sensors

The Curvature sensor introduced by Roddier & Roddier (1993) for AO is presented in Figure 2.2.1. Two detectors placed at equal distance, *l*, in front and behind the focal plane measure the intensity distribution in both planes. There is a local excess of illumination in one plane and a lack of illumination in the other as a result of the local curvature in the wavefront.
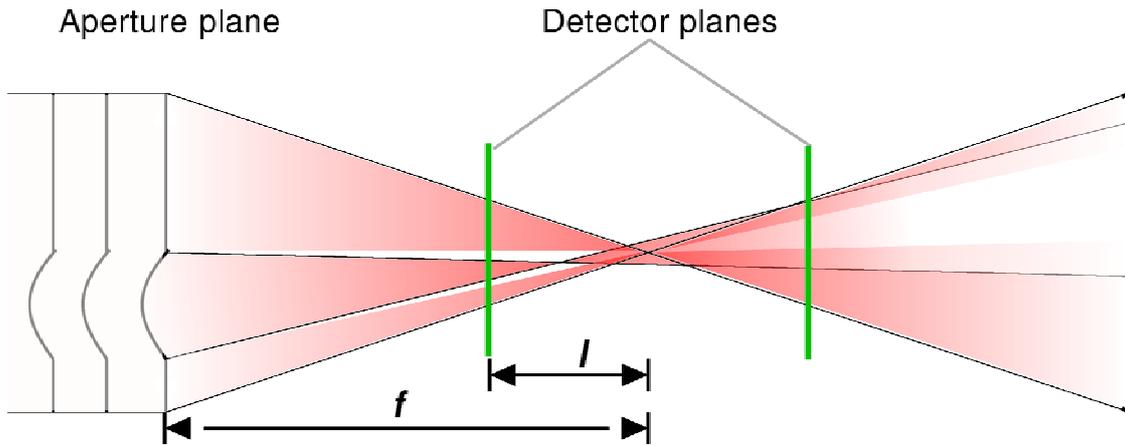

Figure 2.2.1 Principle of Curvature wavefront sensor (from Schumacher & Devaney,2004).

Roddier & Roddier define a quantity denominated Curvature Signal, which in the near–field approximation, is equal to,

$$CS = \frac{I_e - I_i}{I_e + I_i} = \Delta z \left(\frac{\partial W}{\partial \mathbf{n}} \delta_c - P \nabla^2 W \right) \tag{2.1}$$

where I_e and I_i are the extra and intra focal intensity distribution at the image plane, Δz is the defocused term which depends on the focal length *f* and on the defocused distance *l* with respect to the focal plane as $\pm f(f-l)/l$; *W* is the wavefront; *P* is a function equal to 1 inside the pupil and 0 outside; **n** is an unitary vector pointing outside the pupil and δ_c is a linear Dirac distribution around the pupil edge.

The first term in parentheses is proportional to the variation of the wavefront at the pupil edge and the second term is the wavefront Laplacian across the beam, which is proportional to the curvature of the wavefront.

Roddier assumed continuity of wavefront phase function in his mathematical description of this method. This can not be assumed in a segmented telescope, thus the term "Curvature

sensor" is not strictly appropriated to appoint a group of co-phasing techniques. Nevertheless, it is useful as a reference to a well known instrumental technique.

In the presence of phase discontinuities, the signal can be simulated using Fresnel diffraction theory. The complex amplitude in the output pupil is given by,

$$u_{zF}(\mathbf{x}) = \frac{e^{jk\Delta z}}{jk\Delta z} \int \int_{-\infty}^{\infty} U(\mathbf{x'}) \exp\left[j\frac{k}{2\Delta z}(\mathbf{x}-\mathbf{x'})^2 \right] d\mathbf{x'} \tag{2.2}$$

where, $U(\mathbf{x'})$ is the complex input amplitude, k is the wave number $2\pi/\lambda$ and Δz is the defocus term. The Fresnel approximation is valid when the defocus term Δz is much larger than the segment size.

The Fresnel integral can be considered as the convolution of the complex input amplitude with a function containing the defocused term. Since the convolution is a multiplication in the frequency domain, the complex output amplitude is simulated with FFT algorithms as;

$$u_{z,F}(\mathbf{x}) = FFT^{-1}\left\{ \frac{\exp(ik\Delta z)}{ik\Delta z} FFT\left(U(\mathbf{x'})\right) FFT\left[\exp\left(\frac{ik}{2\Delta z}\mathbf{x}^{'2} \right) \right] \right\} \tag{2.3}$$

Figure 2.2.2 shows an intra focal image and the Curvature signal for a 50 m segmented telescope with random piston error of 100nm. Piston errors appear as a modulation of intensity at the edge of the segments.
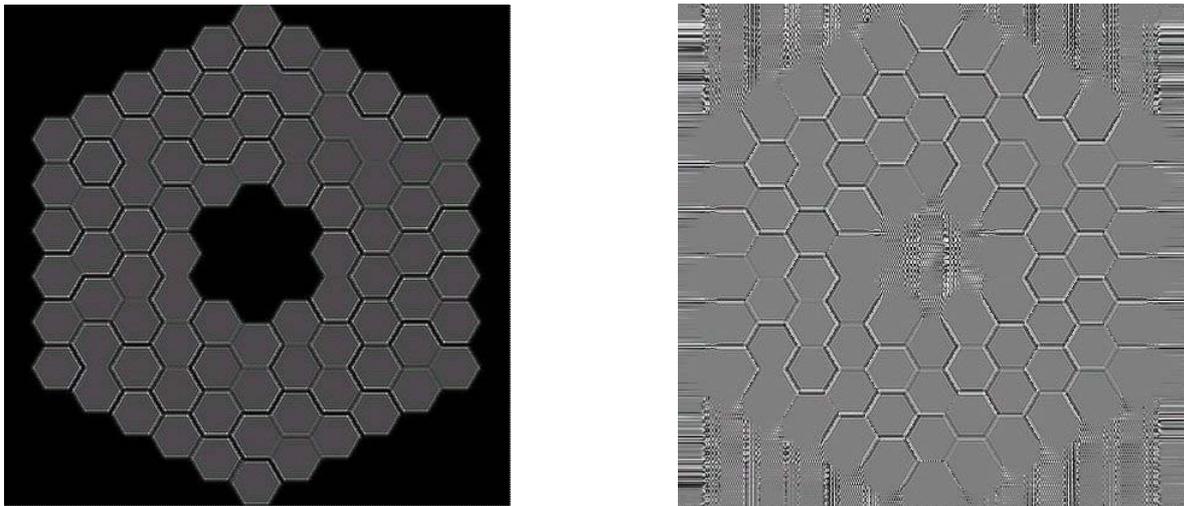

Figure 2.2.2 Intra focal image (left) and curvature signal (right) of a 30m telescope, with a defocused distance of 6m.

The signal changes in the direction perpendicular to the border while it remains constant along the edge direction. The signal width depends on the pupil defocused distance; Δz, small pupil defocused distance —thus large l— leads to narrower signal.

Rodriguez-Ramos & Fuensalida (1997) first proposed to use the Curvature sensor to measure piston errors. They proposed an iterative technique which compared the measured curvature with the simulated curvature signal of an array of segments with known piston errors. This technique fails when seeing is included. They also proposed a hybrid sensor, which includes a Shack-Hartman sensor to correct turbulence errors.

Chanan et al (1999) proposed a method which is similar to the previous one. In this method defocused pairs of images of each segment were simulated, and experimental images were correlated with the simulated templates. Measurements were done for $\lambda=3.3\mu m$ for two main reasons, i) it decreases influence of atmosphere, and ii) it keeps defocus distance in the Fresnel approximation. For perfect segment shape they achieved a precision of 5nm and a repeatability of 40nm.

Cuevas et al (2000) proposed a generalisation of the Roddier equation including discontinuity errors, based on the distribution theory. They argued that piston step is proportional to the amplitude of the first derivative of the linear Dirac delta distribution, and tip-tilt is proportional to the amplitude of the Dirac delta distribution. This generalisation is only valid if the signal width is close to zero, which is the case of weak defocused pupils.

Rodríguez-González & Fuensalida (2003) developed an analytical model based on the diffraction phenomenon of propagation. This model describes curvature signal including wavefront discontinuities. From Fresnel propagation theory they deduced the expressions of the curvature signal for a square aperture with segmentation discontinuities. The signal was characterised as a function of sensor parameters, i.e. focal length, defocus distance, wavelength, etc. They developed a model in order to retrieve piston errors by defining an integrated curvature signal for each segment. This way, it was possible to reduce the number of measurements to the number of segments, and therefore they managed to decrease time consuming and computer memory requirements. From simulations, they obtained a precision of 69nm for $\lambda=600nm$, 48nm for $\lambda=1.2\mu m$ and 13nm for $\lambda=2.4\mu m$. However, the algorithm needs to be completed with the inclusion of atmospheric errors.

2.3. Other alternatives for co-phasing

Another set of techniques is based in the phase diversity principle proposed by Gonsalves & Chidlaw (1979). The pupil aberrations are calculated from the simultaneous measurements of a focused and a slightly defocused image. Lofdahl et al (1998) performed an experiment at Keck II telescope which involved measuring a large number of pairs of images. The average of the individual result gave the misalignment measurement. However, the results obtained in this experiment were not satisfactory, probably due to the poor seeing conditions in which this experiment was carried out.

Phase diversity has been also proposed by Baron et al (2003) for co-phasing of multi-aperture arrays using extended sources. The performance of the phase diversity algorithm is severally affected by the redundancy and dilution of the sub-apertures. Sorrente et al (2004) experimentally tested the validity of this technique obtaining consistent results with numerical simulations.

Labeyrie et al (2002) proposed an alternative method for co-phasing multi-aperture arrays —particularly applicable to hypertelescopes with a densified pupil (Labeyrie 1996) — based on the dispersed-speckle methods. This technique exploits the chromatic dependence of speckled images. It was demonstrated that the wavelength-dependent three-dimensional (3-D) complex input amplitude is the 3-D Fourier Transform of the cube data formed of speckled images at different wavelengths. The piston step map was reconstructed by a 3-D Fineup algorithm.

The JWST would require a co-phasing procedure with the advantage of avoiding atmospheric effects, unlike ground based telescopes. The phasing protocol combines two co-sensing techniques: i) The Dispersed Fringe Sensor (DFS) provides a robust phasing signal over about 1 μm of piston error. It uses a transmissive grism which spreads the light according to its wavelength, forming a spectrum on the camera. Piston differences are measured from the intensity modulations on the spectrum (Shi et al 2003); ii) White Light Interferometry (WLI) provides more than tens of nanometres of precision. Each segment is pistoned over a range which depends on the filter width. The broadband PSF corresponding to each piston position is recorded. The relation of the intensity of the central pixel of the PSF versus the piston position is the WLI signal for that segment (Shi et al 2003).

2.4. Pyramid sensor for measuring dephased errors

The concept of the Pyramid wavefront sensor is based on the principle of the knife edge test (Foucault 1859) introduced by Ragazzoni (1996) for AO, see Figure 2.4.1. A glass pyramid is placed in the focal plane of the telescope, so that each side of the pyramid acts as a spatial filter, producing four different images of the pupil in the observation plane. The combination of the intensity distribution over the four quadrants is proportional to the local slopes of the wavefront, assuming geometrical approximation. By introducing a modulation on the wavefront tilt, the sensitivity and dynamic range of the sensor can be tuned. Small modulation amplitude provides better sensitivity in order to measure small wavefront aberration, while large modulation leads to larger dynamic range with less precision when measuring large aberrations.
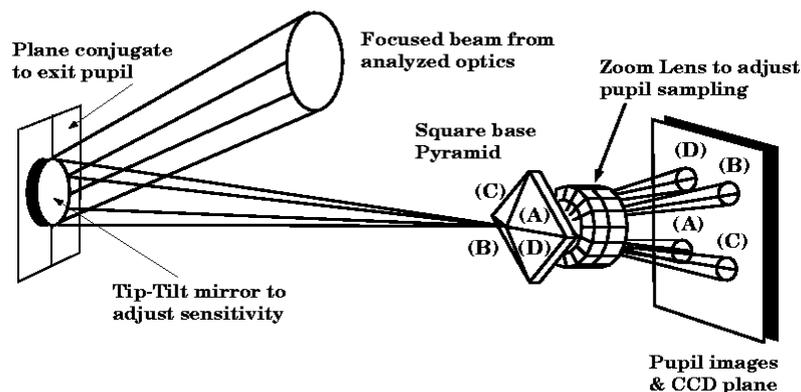

Figure 2.4.1 Scheme of a Pyramid wavefront sensor. Figure taken from Esposito (2000).

Modulation can be introduced either i) dynamically, by moving the pyramid or placing an oscillating tip-tilt mirror in the exit pupil conjugate plate, or ii) statically, by placing a diffusing element in an intermediate image of the pupil (Ragazzoni et al 2002).

Esposito & Devaney (2002) proposed a method for co-phasing segmented mirrors using a Pyramid wavefront sensor. Although in the geometric optics regime the Pyramid Sensor detects local wavefront tilts, diffraction of wavefront discontinuities give rise to a signal in the Pyramid sensor which can be used to measure piston. The optical configuration is the same but the tip-tilt modulation is no longer required. The amplitude of the signal is a sinusoidal function of the piston step. The sensor has the ability to measure misalignment of the segments and wavefront aberrations simultaneously.

2.5. Interferometric techniques for co-phasing segmented mirrors

Interferometric techniques measure piston errors by analysing the interference pattern produced either in a plane conjugated to the primary mirror or locally, at the intersegment zone. There are many ways of implementing interfometic techniques for co-phasing applications. The interferometric techniques presented here can be classified according to the type of source employed, either artificial or natural. They differ firstly in the interferometric technique they adopt, which can be mainly Michelson, Shearing or Mach-Zehnder (MZ) interferometers, and secondly in the optical configuration in relation to the interferometer location, sometimes in the centre of curvature others in the focal plane. We next expose some examples.
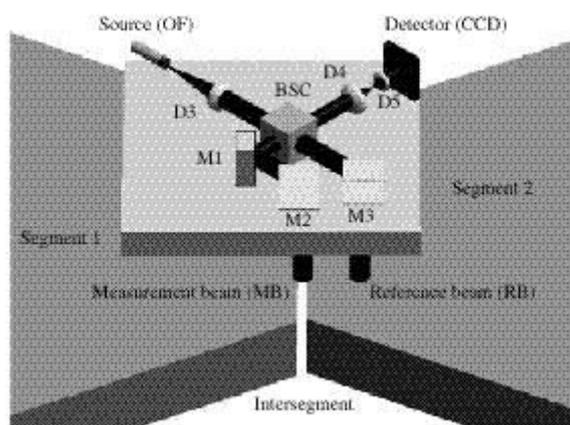

Figure 2.5.1 3-D layout interferometer proposed by Pizarro. Figure taken from Pizarro et al. (2002).

Pizarro et al (2002) proposed to measure piston errors using a Michelson interferometer mounted on a robotic arm which position the interferometer in front of the segment edges, as shown in Figure 2.5.1. There is an internal light source which illuminates the segments, the reference beam reflected from one segment interferes with the beam reflected from intersegment region. Piston errors cause mismatching of the fringes from each side of the edge segment. Relative segment tilt causes the fringe period to change and relative segment tip causes the fringes to deviate from the vertical. The position of zero piston error can be determined by aligning the white light fringe, while increased accuracy is obtained using

narrowband light to give several fringes. The main advantage of this method is that the co-phasing is done during day time. Experimental measurements (Pinto et al 2004) show that a precision of 5nm with a range of 30μm is achieved.

Kishner (1991) proposed measuring absolute distances with an interferometer placed in the centre of curvature of the primary mirror, as seen in Figure 2.5.2. Reflectors components were positioned on the segment surface. Interferences formed between the reference beam and the beam coming from the reflecting points. This method allows them to measure both, misalignment errors and aberrations of the segment surface depending on the number of reflectors placed onto the segment. This method is very sensitive to the fluctuation on the refractive index thus to the atmospheric turbulence.
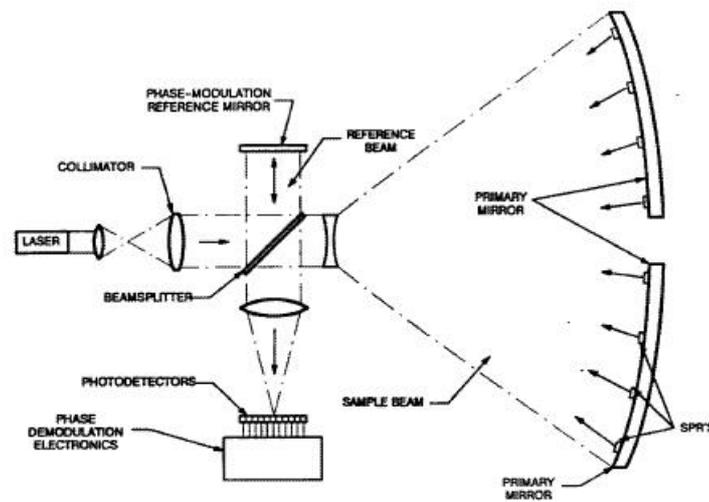

Figure 2.5.2 Sample point interferometer proposed by Kishner. Figure taken from Kishner (1991).

Voitsekovich et al (2002) proposed an approach based in a shearing interferometer with a simple setup composed of two lenses and a filter between them, which provides not only relative piston information but also information on relative tilt and defocus. Intensity distribution on the image plane is formed by a central interference pattern produced by to adjacent segments, enclosed by the direct field and shifted field of the surroundings segments. They provide a description of the filter design and manufacturing. The reconstruction of the piston map error requires to measure two interferograms using two different filter orientations. This method has a maximum precision of λ/45 at the wavefront, when a significant noise level is considered. When atmospheric errors are considered, the distance

between the interference points (~1m) is much bigger than r_0 (~0.25m), therefore the phase fluctuations are de-correlated and the interferogram is blurred by atmosphere.

Horton et al (1990) used a radial shearing interferometer as shown in Figure 2.5.3. Two images of the segment pupil with different magnification will interfere producing a fringe pattern in the exit pupil. A rotating tilted transparent plate situated in the focal plane modulates the tilt fringes used for sampling the segment misalignment.
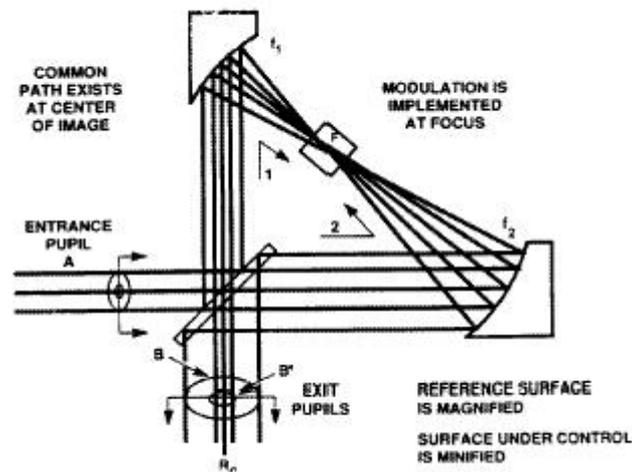

Figure 2.5.3 Shearing interferometer proposed by Horton et al. Figure taken from Horton et al (1990).

Dohlen & Fresneau (2000) proposed a dual wavelength random phase shift interferometer for phasing segmented mirrors using an artificial source located at the centre of curvature of the primary. They suggested the implementation of this technique for stellar sensors using a MZ interferometer, as proposed by Angel (1994) for high precision AO.

This principle was later elaborated by Montoya et al (2002) and its description is the subject of this work.

Chapitre 3-Resumé

Une nouvelle technique de co-phasage des miroirs segmentés, basée sur l'interféromètre de MZ, est présentée dans ce chapitre. Dans un interféromètre de MZ, une lame séparatrice divise le faisceau provenant du télescope en deux bras. Un trou placé au plan focal d'un des bras agit comme filtre spatial, fournissant une onde de référence cohérente avec l'onde entrante. Si la taille du trou est plus grande que la tache d'Airy, l'onde de référence contient les composantes basse fréquence de l'onde objet. Après réflexion sur les miroirs plans, les faisceaux filtrés et non filtrés sont recombinés par une lame séparatrice, formant deux interférogrammes complémentaires. Ces interférogrammes contiennent seulement les hautes fréquences du front d'onde entrant, éliminant ainsi les perturbations atmosphériques et ne laissant que les erreurs de segmentation.

Nous avons réalisé une étude analytique des interférogrammes de MZ pour le cas mono-dimensionnel avec des erreurs de piston. Des analyses complémentaires de ces interférogrammes utilisant des simulations numériques montrent un bon accord avec les résultats analytiques.

Nous avons décrit plusieurs algorithmes pour retrouver les erreurs de front d'onde causées par la segmentation, et nous avons étudié leurs précisions lorsqu'on inclut non seulement les erreurs de discontinuité mais également la turbulence atmosphérique et les erreurs causées par les bords rabattus. En changeant la taille du trou, les performances en tenant compte des erreurs atmosphériques peuvent être optimisées. Plus critiques sont les effets de bords rabattus produits durant la procédure de polissage. Cependant, une précision de 10nm peut être atteinte dans tous les cas.

La technique du MZ employant la lumière d'une étoile naturelle, il est important de déterminer l'influence du bruit de photon sur les performances de cette méthode. Les conditions requises concernant la magnitude limite de l'étoile ne sont pas très drastiques puisqu'une étoile plus brillante que la magnitude 14 en bande V suffira pour assurer une précision de 10nm.

Chapter 3

Mach-Zehnder co-phasing technique

In this chapter we introduce a novel technique for co-phasing of segmented mirrors based on a MZ interferometer. We present a general description of this method, in which we justify the use of a MZ interferometer for measuring wavefront discontinuities.

We have performed an analytical study of the MZ interferograms for the one-dimensional (1-D) case for pure piston error. Further analysis of the MZ interferograms using numerical simulations shows a good agreement between the results of both, analytical and numerical approaches. We also present a coronograph approach as an alternative instrument based in the same principle as the MZ technique.

Finally, different algorithms to retrieve wavefront errors are described. We report on the precision obtained when including not only discontinuity errors but also atmospheric turbulence and edge defects. The detection parameters and photon noise have been also implemented in the simulation. Our analysis resulted in an optimal configuration achieving the highest performance of the instrument.

3.1. General Description

The purpose of a MZ wavefront sensor is to measure phase properties of the incoming wavefront by applying the appropriate spatial filtering in one of the interferometer arms. The idea of using this kind of interferometer to measure atmospheric wavefront errors was first introduced by Angel (1994). A scheme of the MZ interferometer is shown in Figure 3.1.1.
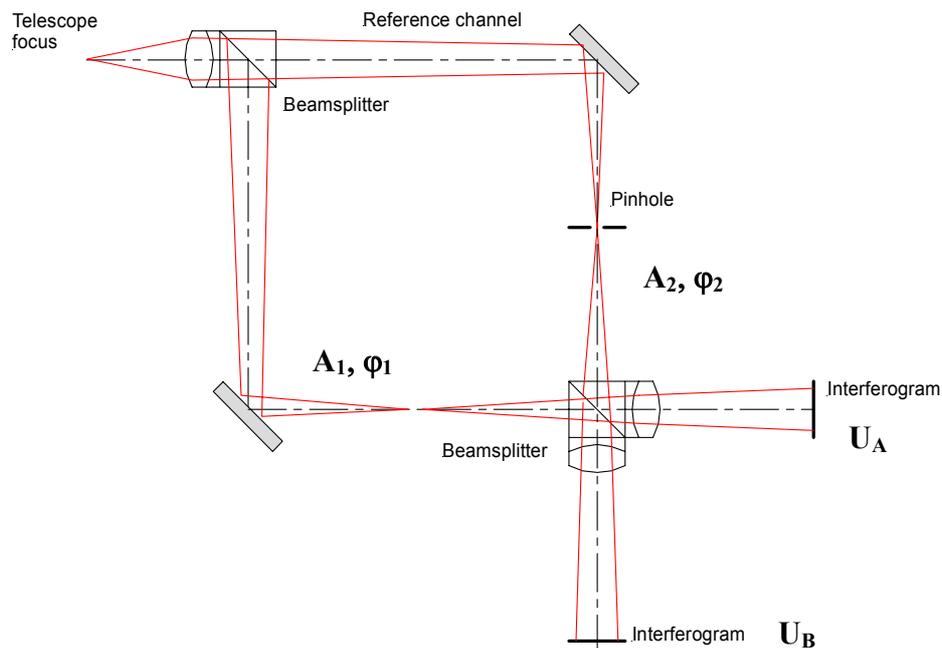
Figure 3.1.1 Scheme of a MZ interferometer.

In MZ interferometer, a beam splitter divides the incoming beam from the telescope focus. A pinhole placed in the focal plane of one arm acts as a spatial filter, providing the reference wave coherent to the incoming wave. After reflection at plane mirrors, the two beams are recombined by a second beam splitter, forming two complementary interference patterns. If the pinhole size is smaller than the Airy disk, the reference beam is a spherical wave. In this case the difference of intensity between two interferograms directly provides the local phase. On the contrary, if the pinhole size is larger than the Airy disk, the reference wave contains the low frequency components of the object wave. At recombination, as result of the subtraction of the two wavefront arms, the interferograms contain only the high frequencies of the incoming wave.

This principle is the basis of this interferometric assembly for measuring wavefront discontinuities caused, for example, by segmentation of the telescope surface. Piston and tip-tilt errors on segments produce jumps on the wavefront. As it is known from the Fourier analysis, a step function is mostly manifested in the high-frequency region of the spectrum. Therefore, it is possible to separate the segmentation component from other components with fainter high-frequencies, by choosing a sufficiently large pinhole size.
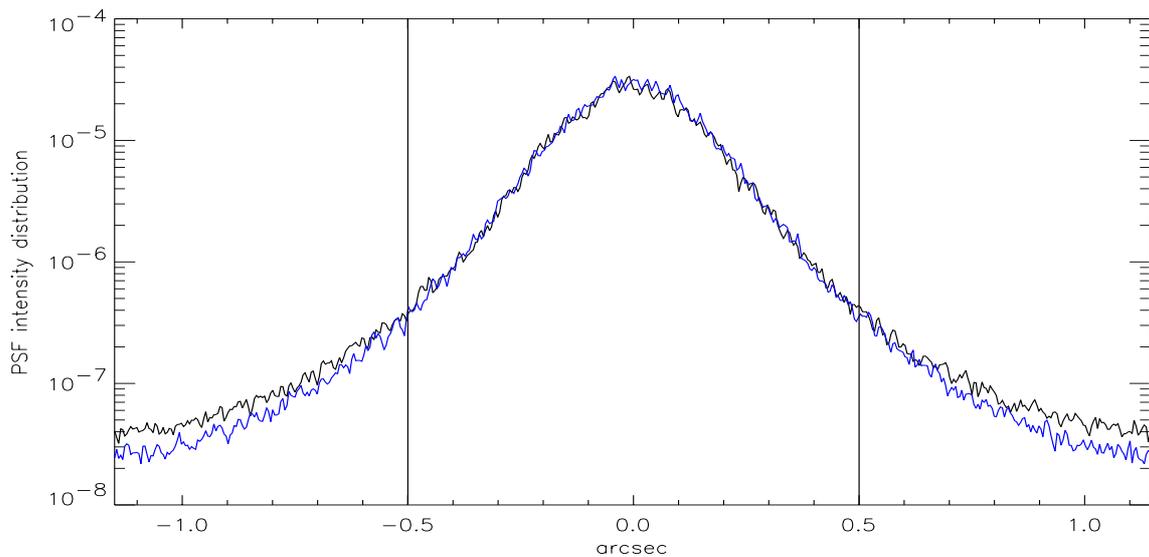

Figure 3.1.2 Intensity distribution of a PSF for an input wavefront with piston error of 45nm in the mirror surface (black) and no piston error (blue) in presence of atmosphere with r_0=25cm.

This property is well illustrated in Figure 3.1.2, where we have plotted the cross section of the PSF of a step function compared with the cross section of the PSF of an atmospheric phase function. We observe that for low spatial frequencies the atmospheric PSF dominates, while for frequencies higher than ~0.5″ the wings of the step PSF lie above. Choosing the proper pinhole size allows us to cancel out phase errors due to the atmosphere.

The advantage of this technique is that the same instrument is suitable for AO or co-phasing applications. The AO applications have been deeply studied by Langlois (2001) and the aim of this work is the study of this technique for co-phasing applications.

3.2. Analytical study of a Mach-Zehnder Interferometer

One of the advantages of the MZ interferometer is the fact that wavefront errors are measured directly from the interference pattern registered on the detectors. The intensity levels of the interferograms are proportional to the phase difference between the two arms. By conservation of energy, these two patterns are complementary when the beam-splitter is non-absorbent: maxima in one pattern correspond to minima in the other.

The two complex amplitudes at the two output pupil planes of a MZ interferometer are the following:

$$U_{A,B}(x,y) = \frac{-1}{\sqrt{2}}\left(A_1(x,y)e^{i\varphi_1(x,y)} \pm A_2(x,y)e^{i\varphi_2(x,y)} \right) \qquad (3.1)$$

where, and A_1, φ_1 are the amplitude and phase of the reference wavefront, and A_2, φ_2 are the amplitude and phase of the filtered wavefront.

Intensities of the two output interferograms are calculated as $I=UU^*$ where U^* denotes U complex conjugated,

$$I_{A,B}(x,y) = \left(\frac{I_1(x,y)+I_2(x,y)}{2} \right)\left[1 \pm V\cos\left(\varphi_2(x,y)-\varphi_1(x,y) \right) \right] \qquad (3.2)$$

where I_1 is the intensity of the filtered arm, I_2 is the intensity of the reference arm before recombination, and V is the visibility of the fringes in the output pupil plane, and is expressed by,

$$V = \frac{I_{max}-I_{min}}{I_{max}+I_{min}} = 2\frac{\sqrt{I_1(x,y)I_2(x,y)}}{I_1(x,y)+I_2(x,y)} \qquad (3.3)$$

As expected, the intensity values of the interferograms are proportional to the phase difference.

From these interferograms we can not retrieve the sign of the phase due to the symmetry of the cosine function, cos(φ₁-φ₂)=cos(φ₂-φ₁). This problem can be solved by introducing a constant optical path difference (OPD) in one of the arms. Later on, we will study the effects caused by the OPD on the MZ interferograms.

Let us now derive the analytical equation which gives the intensity of the interferograms.

3.2.1. Analytical expression of 1-D interferograms: the piston error case

The aim of developing this theoretical analysis, is the better understanding of the resulting signal of the MZ interferometer.
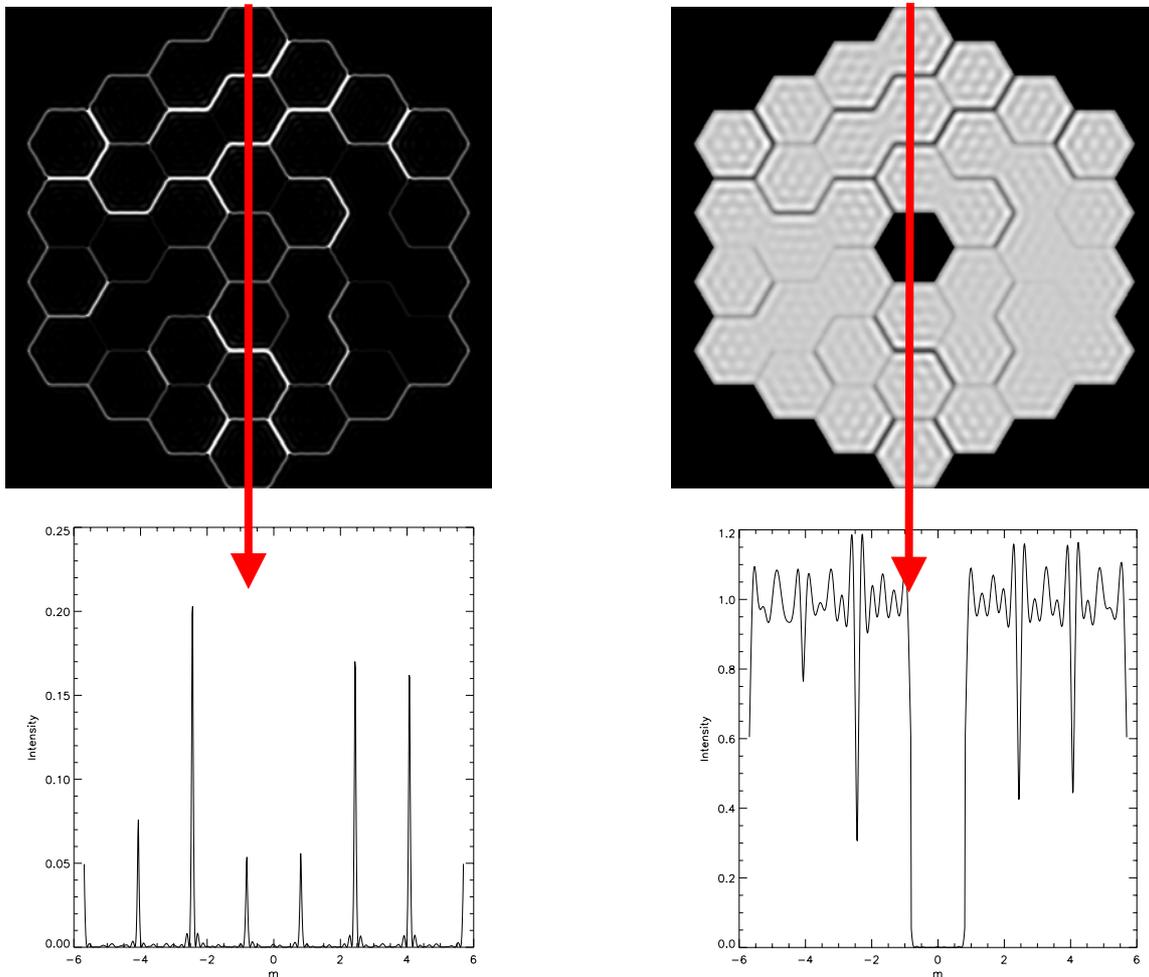

Figure 3.2.1 Interferograms at the two output of MZ interferometer (upper row). Transversal cut along the main y-axis of the interferograms (lower row).

In Figure 3.2.1, we show the two output interferograms for a 10-m GTC type. It can be noticed that peak signals appear at the edge between segments. Our analysis will describe these signals and their behaviour for several interesting cases.

In order to derive the expression of the intensity distribution of the interferograms we will use the Fraunhoffer approximation of the Diffraction theory. For this purpose we will assume the case of monochromatic light.

Let $U_1(p,q)$ be the pupil telescope function. The complex amplitude in the focal plane is given by the Fourier integral,

$$u_1(\xi,\eta) = \frac{1}{\lambda} \int_{\Re^2} U_1(p,q) e^{i\frac{2\pi}{\lambda}(p\xi+q\eta)} \, \mathrm{d}p \mathrm{d}q \qquad (3.4)$$

where λ is the wavelength.

To easily follow the mathematical description, we will represent the coordinates related to the focal plane with Greek characters and coordinates related to pupil plane with Latin characters.

The complex amplitude in the focal plane behind the mask will be the product $u_1(\xi,\eta)\,m(\xi,\eta)$, where $m(\xi,\eta)$ is the mask function. In order to obtain the output complex amplitude, we compute the Fourier transform of this product as follows,

$$U_2(x,y) = \frac{1}{\lambda} \int_{\Re^2} u_1(\xi,\eta) m(\xi,\eta) e^{-i\frac{2\pi}{\lambda}(x\xi+y\eta)} \, \mathrm{d}\xi \mathrm{d}\eta \qquad (3.5)$$

which can be interpreted as the convolution between the pupil telescope function, $U_1(x,y)$ and the Fourier transform of the mask,

$$M(x,y) = \int_{\Re^2} m(\xi,\eta) e^{-i\frac{2\pi}{\lambda}(x\xi+y\eta)} \, \mathrm{d}\xi \mathrm{d}\eta \qquad (3.6)$$

thus equation (3.5)) can be expressed as,

$$U_2(x,y) = \frac{1}{\lambda^2}\left[U_1(x,y) \otimes M(x,y)\right] = \frac{1}{\lambda^2} \int_{\Re^2} U_1(x-u,y-v) M(u,v) \mathrm{d}u \mathrm{d}v \qquad (3.7)$$

where $\otimes$ denotes convolution.

As we show below, the insertion of an OPD in one arm will provide some advantages. In this case, the complex amplitudes of the two output wavefronts will be,

$$U_{A,B}(x,y) = \frac{1}{2}\left[U_2(x,y) \pm U_1(x,y) e^{i\theta}\right] \qquad (3.8)$$

where the $\pm$ sign corresponds to each output of the interferometer and θ, is the OPD between the two arms. The intensity is related to the complex amplitude as $I=UU^*$, so the intensities measured at the outputs of the interferometer will be,

$$I_{A,B}(x,y) = \frac{1}{4}\left\{\left|U_1(x,y)\right|^2 + \left|U_2(x,y)\right|^2 \pm 2\,\mathrm{Re}\left(U_1^*(x,y) U_2(x,y) e^{i\theta}\right)\right\} \qquad (3.9)$$

To simplify the mathematical treatment and due to the fact that the interesting part of our analysis is the signal located between segments, we will consider instead of the whole pupil the case of two adjacent segments as shown in Figure 3.2.2. We will see that this approximation is valid if the localisation condition is fulfilled. This condition ensures that the signals produced at different edges of the same segment do not interfere.
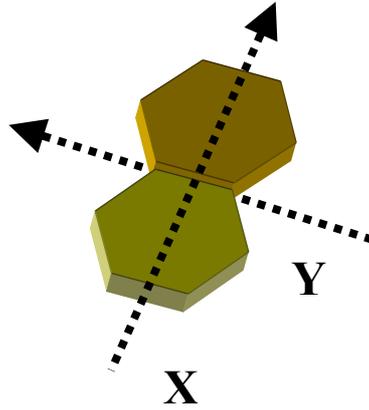

Figure 3.2.2 Coordinate system for two adjacent segments case.

We will study the simplest case, assuming that there is no gap between segments. For convenience we set the amplitude of each segment to one, so that the complex amplitude can be expressed as follows,

$$U_1(x,y) = \begin{cases} e^{i\varphi_1(x,y)}, & x < 0 \\ e^{i\varphi_2(x,y)}, & x > 0 \end{cases} \qquad (3.10)$$

where $\varphi_i(x,y)$ is the phase of segment i.

The contribution of each error source can be studied separately. As a first approach we have included only piston error, ignoring the contribution of edge and segment miss-figure, tip-tilt between segments and atmospheric turbulence. In this case, $U_1(x,y)$ is constant along the y-direction and will depend only on x-coordinate. The equation can be expressed as,

$$U_1(x,y) = U_1(x) = \frac{\mathrm{sign}(x)+1}{2} e^{i\varphi_2} + \frac{-\mathrm{sign}(x)+1}{2} e^{i\varphi_2} \qquad (3.11)$$

Two different mask shapes have been considered. We define the circular pinhole as a mask, as shown in Figure 3.2.3, with constant transmittance inside a circle of diameter *a* and

null outside, and the Gaussian pinhole, whose transmission function is a Gaussian with FWHM equal to 1.18*a*.
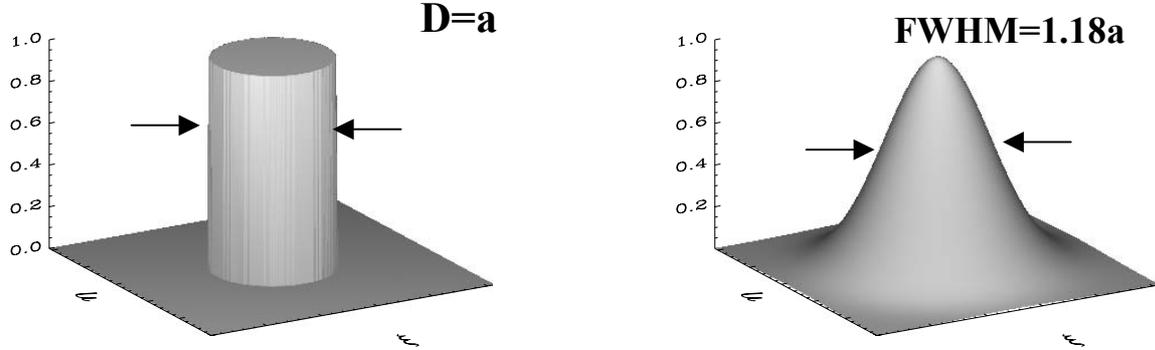

Figure 3.2.3 Mask Transmission Functions for circular pinhole (left) and Gaussian Pinhole (right).

The Fourier transform of the circular mask (in polar coordinates) will be the well known Airy pattern (Goodman 1996),

$$M(\rho) = \frac{2\pi a^2 J_1(ka\rho)}{ka\rho} \tag{3.12}$$

and the Fourier transform of the Gaussian mask will be,

$$M(\mathbf{t}) = \frac{\pi a^2}{2} \exp\left[-\left(\frac{\pi a}{\sqrt{2}\lambda}\mathbf{t}\right)^2\right] \tag{3.13}$$

where **t** is the position vector in Cartesians coordinates.

The next step is to solve integral (3.7) introducing (3.11) and the Fourier transform of the mask. We obtain a general expression for the two outputs of the interferometer,

$$I_{A,B}(x,y) = \frac{1}{4}\left\{ \frac{1}{2}\cos(\Delta\varphi)\left[1 - F^2\left(c|x|\right)\right] + \frac{1}{2}\left[3 + F^3\left(c|x|\right)\right] \right.$$
$$\left. \pm \cos(\theta)\left[1 + F\left(c|x|\right)\right] \pm \cos\left(\theta - \text{sign}(x)\Delta\varphi\right)\left[1 - F\left(c|x|\right)\right] \right\} \tag{3.14}$$

where $\Delta\varphi = \varphi_2 - \varphi_1$ is the phase step between segments, θ is the OPD between two arms of the interferometer and F($c|x|$) is a function characteristic of the mask, which for the circular pinhole is expressed as,

$$F\left(c|x|\right) = \text{Si}\left(c|x|\right) = \frac{2}{\pi}\int_0^{c|x|}\frac{\sin(t)}{t}dt \qquad c = \frac{\pi a}{\lambda} \tag{3.15}$$

and for the Gaussian pinhole is expressed as,

$$\mathrm{F}(c|x|) = \mathrm{ercf}(c|x|) = \frac{2c}{\sqrt{\pi}} \int_0^{|x|} e^{-(ct)^2} \, dt \qquad c = \frac{\pi a}{\lambda\sqrt{2}} \tag{3.16}$$

where a is the diameter of a circular pinhole or 0.85FWHM of a Gaussian pinhole.

In Figure 3.2.4 we illustrate the profile of the F function for both masks. It can be observed that Si function and Error function (Erfc) have the same shape except for the presence of some oscillations close to zero in the case of the Si function, which are not apparent in the case of the Ercf function. These oscillations are the result of the diffraction effect of the edge of the pinhole.
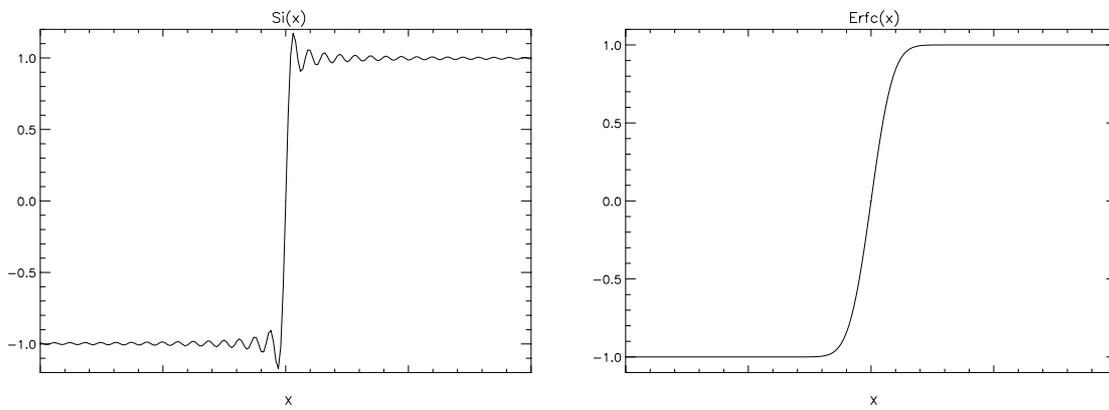

Figure 3.2.4 Representation of Si function (left) and Erfc function (right).

In Figure 3.2.5 we have plotted the resulting intensity profiles for both outputs and both masks. We have considered a wavefront piston error of 125nm, for λ=500nm, a pinhole size of 1.5" and null OPD. Profiles are similar in the area between segments. However, while the profile of the Gaussian mask is constant far from the edge, the circular mask profile presents oscillations whose amplitude decreases as the distance to the intersegment point increases.

One way of reducing the signal background and increasing the signal amplitude consist of considering the difference between two outputs. This value will be referred to as the **Mach-Zehnder signal** and it can be expressed as follows,

$$S(x) = \frac{1}{2}\left\{ \cos(\theta)\left[1 + F\left(c|x|\right)\right] + \cos\left(\theta - \mathrm{sign}(x)\Delta\varphi\right)\left[1 - F\left(c|x|\right)\right]\right\} \tag{3.17}$$
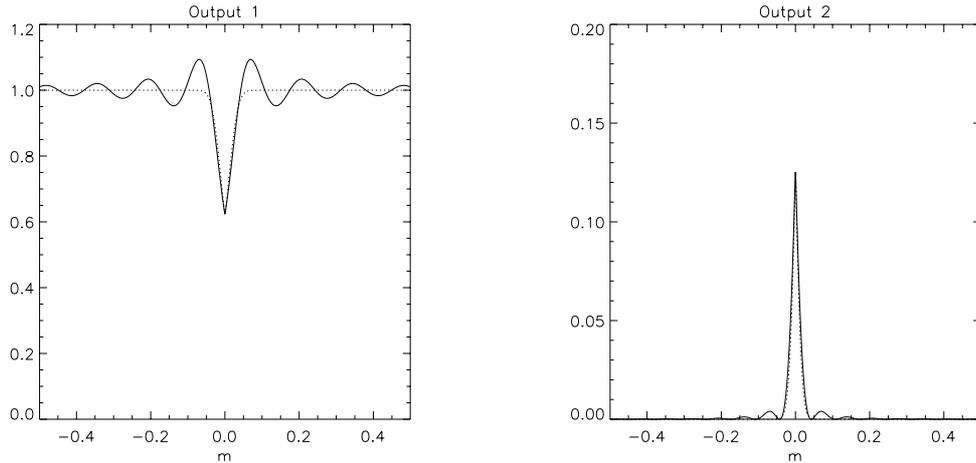
Figure 3.2.5 Profiles of the output signals of the MZ for circular pinhole (solid) and Gaussian pinhole (dotted).

Once we have obtained the analytical expression for the interferogram profiles it is time to study the effect which causes the variation of the parameters involved in this expression, i.e, the introduction of an OPD (θ), the size of the pinhole (*c*) and the shape of the pinhole (F). Our goal is to optimise the performance of the MZ interferometer by taking into account these parameters.

3.2.2. Behaviour of the MZ signal when introducing an OPD

The introduction of an OPD in one of the arms allows retrieving the sign of the piston step, and for certain cases it provides a linear response. In Figure 3.2.6 the MZ signals for null OPD and different piston step are plotted.
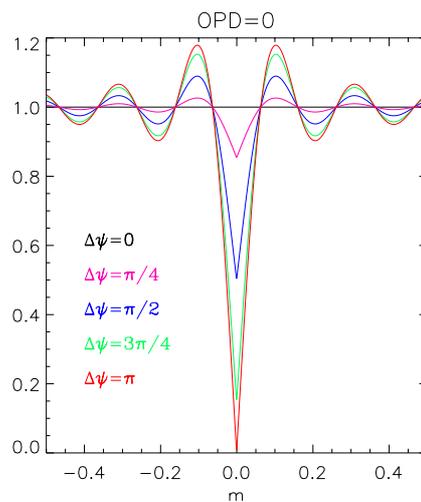

Figure 3.2.6 MZ signals profile for different piston step, for OPD=0 and λ=500nm, pinhole size of 1.5".

The piston information is contained within a distinct peak which appears at the segment boundary, as expected from (3.16), if the OPD is equal to zero, the signal is proportional to the cosine of the phase difference, and therefore the sign of the phase is lost. Introducing an OPD, the argument of the cosine function will change the signal shape. In Figure 3.2.7 we represent the profiles of the two outputs of the interferometer (blue and green lines) and the MZ signal (black line) for a wavefront piston error of $\lambda/4$ (at λ=500nm) for different values of OPD. We observe that the two outputs become complementary when the OPD approach to $\lambda/4$. This means that both signals are identical but with opposite sign. In the case of OPD equal to $\lambda/4$ this complementary property has two advantages, firstly the two outputs have the same background level, so that when we subtract them the background is eliminated, and second the amplitude of the signal, i.e the difference between the maxima and minima, is doubled when two outputs are subtracted.
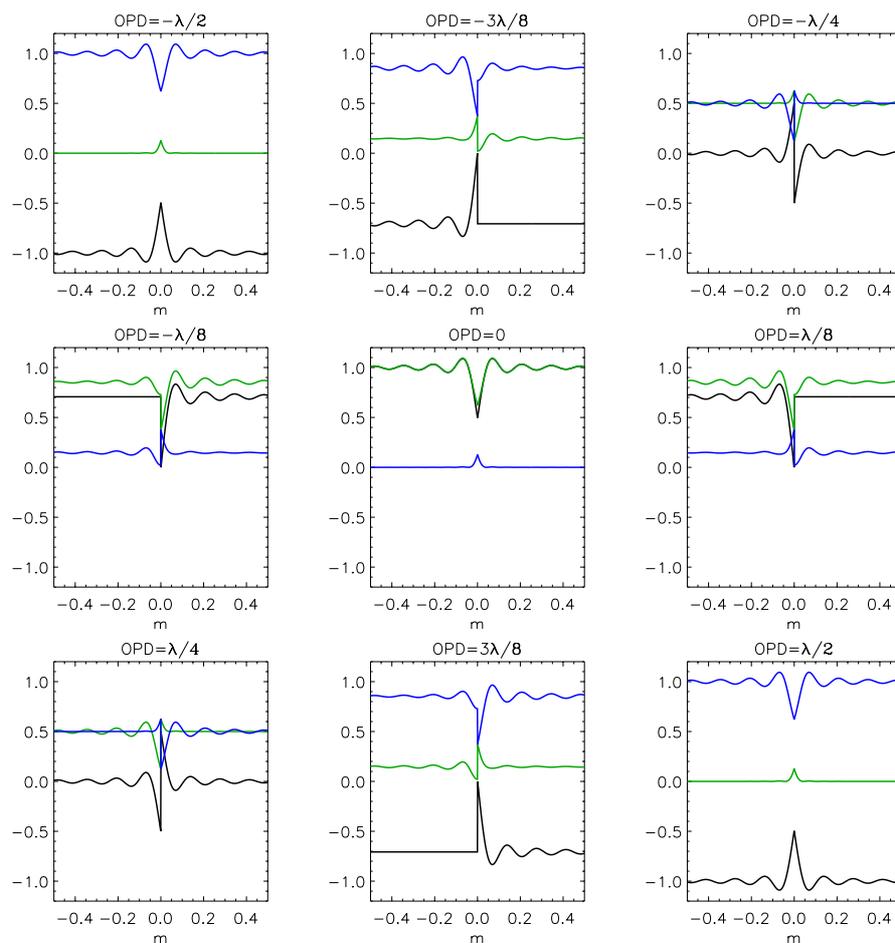

Figure 3.2.7 MZ signal (black), output 1 (blue), output 2 (green) for different OPDs, for piston step of $\lambda/4$ in the wavefront, and pinhole size of 1.5".

We also notice, that for OPD=λ/4, the signal given by (3.17) is a sinusoidal function of the piston step, and thus the signal will have a linear behaviour in the range of piston [-λ/4,λ/4], allowing the sign distinction.

According to the previously mentioned arguments we will set the OPD to λ/4 in the subsequent analysis.

3.2.3. Behaviour of the MZ signal with pinhole size

The pinhole size will play an essential role in the MZ setup, since, as already said, the pinhole is the spatial frequency filter which remove the perturbation introduced by the atmospheric turbulence.

In Figure 3.2.8 the MZ signals for different pinhole sizes are plotted for a piston step of 125nm on the wavefront. The amplitude of the signal does not change but the width of the signal decreases as the pinhole size increases.
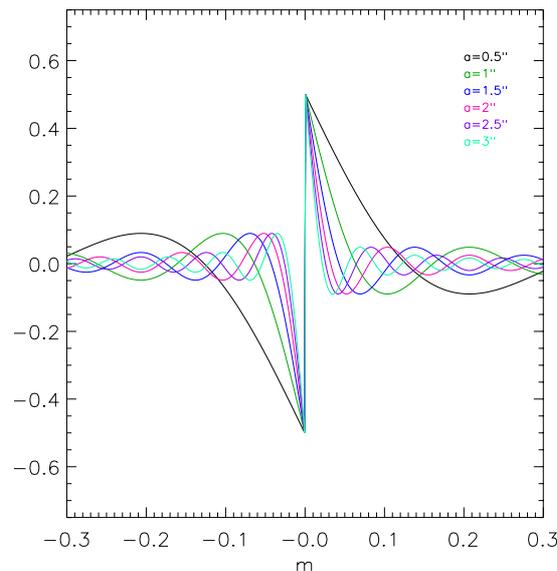

Figure 3.2.8 MZ signal for different size of circular pinhole for a piston step of λ/4.

There exists a linear relationship between the size of the pinhole and the width of the profile. For convenience, we will consider the width of the signal as the distance between the first points where the MZ signal is equal to zero at each side of the segment. After imposing this condition in (3.15) and (3.16) the width for the circular pinhole is given by,

$$w = \frac{4\lambda}{\pi a}$$ (3.18)

and for a Gaussian pinhole is,

$$w = \frac{4\sqrt{2}\lambda}{\pi a}$$ (3.19)

We notice that if the width of the signal is very large, there is a risk of overlapping between signals from different edges of the same segment. The condition of signal localisation is given by the characteristic spatial size $1/c$ obtained in (3.15), which should be much shorter than the size of the segment d. Taking λ=500nm and d=1.5m the localisation condition gives $a \gg 0.03$". If localisation is fulfilled, the signals from different borders do not overlap and we can consider each intersegment border separately.

The choice of the pinhole will not only depend on the atmospheric error, instead the gaps and edge defects will have influence on the signal width. Therefore they have to be considered when choosing the optimal pinhole size.

3.3. Coronograph: a simplified approach to the Mach-Zehnder interferometer

The Mach- Zehnder interferometer proposed in this work uses a pinhole in the focal plane to filter the input wavefront. A coronograph with a phase mask in the focal plane also acts as a frequency filter. By choosing the appropriated phase mask, the two outputs of the MZ interferometer can be obtained from two independent coronograph configurations. The main advantage of the coronograph is the simplicity in the opto-mechanical design compared to a MZ interferometer, however the access to a single output is less convenient than a double output system.

In order to compare the phase mask coronograph with the MZ interferometer we have found the analytical expression for the intensity of the output wavefronts with the same reasoning used for the MZ case. In the present analysis we also supposed a two adjacent segment configuration with a step between them as showed in Figure 3.2.2.
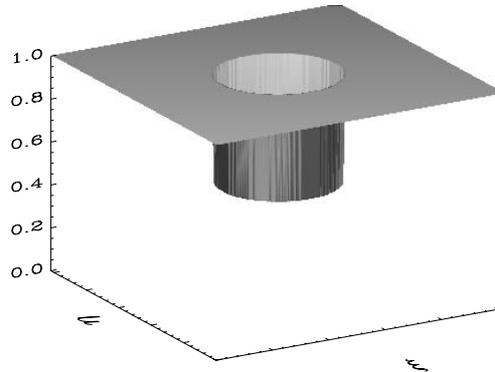

Figure 3.3.1 Example of the transmission function of a phase mask for the coronograph.

A phase mask is represented in Figure 3.3.1 and it is defined by,

$$m(\rho, a) = \begin{cases} Ae^{i\phi_0} & \text{if } \rho \leq a \\ 1 & \text{if } \rho > a \end{cases} \tag{3.20}$$

where A and ϕ_0 are the amplitude and phase of the mask respectively. To simplify the calculations the phase mask can be seen as the combination of two masks, one mask

transmitting in the whole space and a pinhole with amplitude equal to $1-Ae^{i\varphi_0}$. In this case, the phase mask is expressed as,

$$m(\rho,a)=1-\left(1-Ae^{i\phi_0}\right)circ\left(\rho,a\right)$$ (3.21)

where circ(ρ,a) is a function with value 1 inside a circle of radius a and 0 outside. The expression of the Fourier Transform of the phase mask is given by;

$$M(x,y)=\delta(x,y)-\left(1-Ae^{i\phi_0}\right)\frac{2\pi a^2 J_1\left(ka\rho\right)}{ka\rho}$$ (3.22)

where $\delta(x,y)$ is the Dirac delta, k is the wave number and J_1 is the Bessel function of first order. Substituting (3.22) in (3.7) after some calculations we arrive to the expression of the intensity given by

$$I(x)=\Bigg\{\ \left(\text{Si}(ka|x|)-\text{Si}^2(ka|x|)\right)A\cos(\phi_0)$$
$$+\frac{1}{2}\left[A^2\left(1-\text{Si}^2(ka|x|)\right)-\left(\text{Si}(ka|x|)-1\right)^2\right]\cos(\Delta\varphi)$$
$$+\frac{1}{2}\left(\text{Si}(ka|x|)-1\right)^2+\frac{A^2}{2}\left(\text{Si}^2(ka|x|)+1\right)$$
$$+\frac{1}{2}\left(\text{Si}(ka|x|)-1\right)^2 A\cos\left(\phi_0-\text{sign}(x)\Delta\varphi\right)+\frac{1}{2}\left(\text{Si}^2(ka|x|)-1\right)A\cos\left(\phi_0+\text{sign}(x)\Delta\varphi\right)\Bigg\}$$

where Si is a function given by (3.15), and $\Delta\varphi$ is the step between the adjacent segments. Comparing this expression with those obtained for the MZ case (3.14), we find that two outputs of the MZ interferogram can be reproduced with a coronographic version using a phase mask with amplitude A and phase ϕ_0, given by,

$$A=\sqrt{2\pm 2\cos(\theta)}\qquad \phi_0=\arctan\left(\frac{\pm\sin(\theta)}{1\pm\cos(\theta)}\right)$$ (3.23)

where θ is the OPD between the MZ arms, and the symbol $\pm$ represents each output of the MZ interferometer. The transmission A and phase ϕ_0 for this case are simply related by;

$$A=2\cos\left(\phi_0\right)$$ (3.24)

In the MZ configuration proposed here, the OPD between the two arms of the interferometers is set to $\pi/2$. Substituting this value in (3.23), the equivalent phase masks for each output in the coronographic version have an amplitude, A of 1.41 and a phase, ϕ_0 of $\pm$ $\pi/4$. In theory a transmission greater than 1 is not possible, but in practice this ambiguity can be solved by setting the transmission inside the mask to 1 and to $1/A$ outside it.

The coronographic version offers a large number of possibilities apart from the MZ equivalence. We have studied the signal obtained for different phase and amplitude distributions. In Figure 3.3.2 we represent one of the most interesting cases. The phase mask with amplitude equal to 1 and phase equal to $\pi/4$ gives almost an optimal symmetric signal except for piston errors in the ranges $[-\pi,-3\pi/4]$ and $[3\pi/4,\pi]$, where the signal is slightly asymmetrical. The signal becomes symmetrical for piston equal to $\pm\pi$, unlike the MZ case, where the signal is zero. The periodicity of the signal in λ is very convenient because it allows us to double the capture range. In the MZ case, the periodicity of the signal is $\lambda/2$, and thus a complementary analysis is required to increase the capture range.
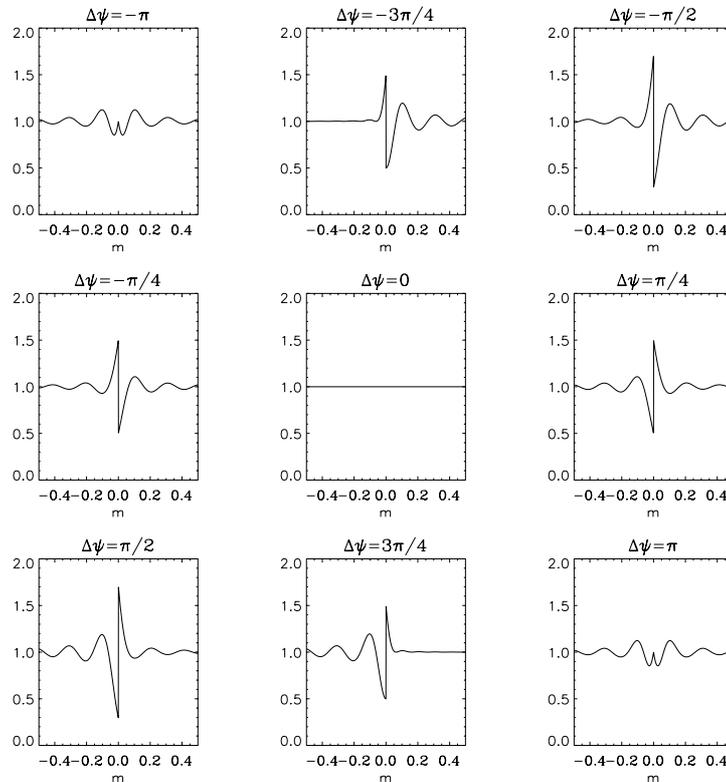

Figure 3.3.2 Signal profiles for the coronographic version with a phase mask of amplitude 1 and phase equal to $\pi/4$ in absence of atmospheric and for different piston values from $-\pi$ to π.

The coronographic version has revealed as a promising alternative to the MZ technique with the main advantage of its simplification on the optical setup. However deeper analysis including atmospheric turbulence, segment miss-figure errors as well as piston retrieval algorithms should be performed in order to ensure the validity of this approach.

3.4. Numerical Simulations

In this section we describe the simulation package that we have developed to implement the MZ co-phasing technique. This package is mainly divided into three parts:

The first part relates to the simulation of the MZ signal, including telescope segmentation parameters, wavefront errors and MZ parameters.

The second part includes detection parameters of the system, i.e. resolution of the detector, pixelisation and detection noise.

The third part comprises the analysis, in which we include the calibration criteria and the retrieval method explored to obtain phase errors.
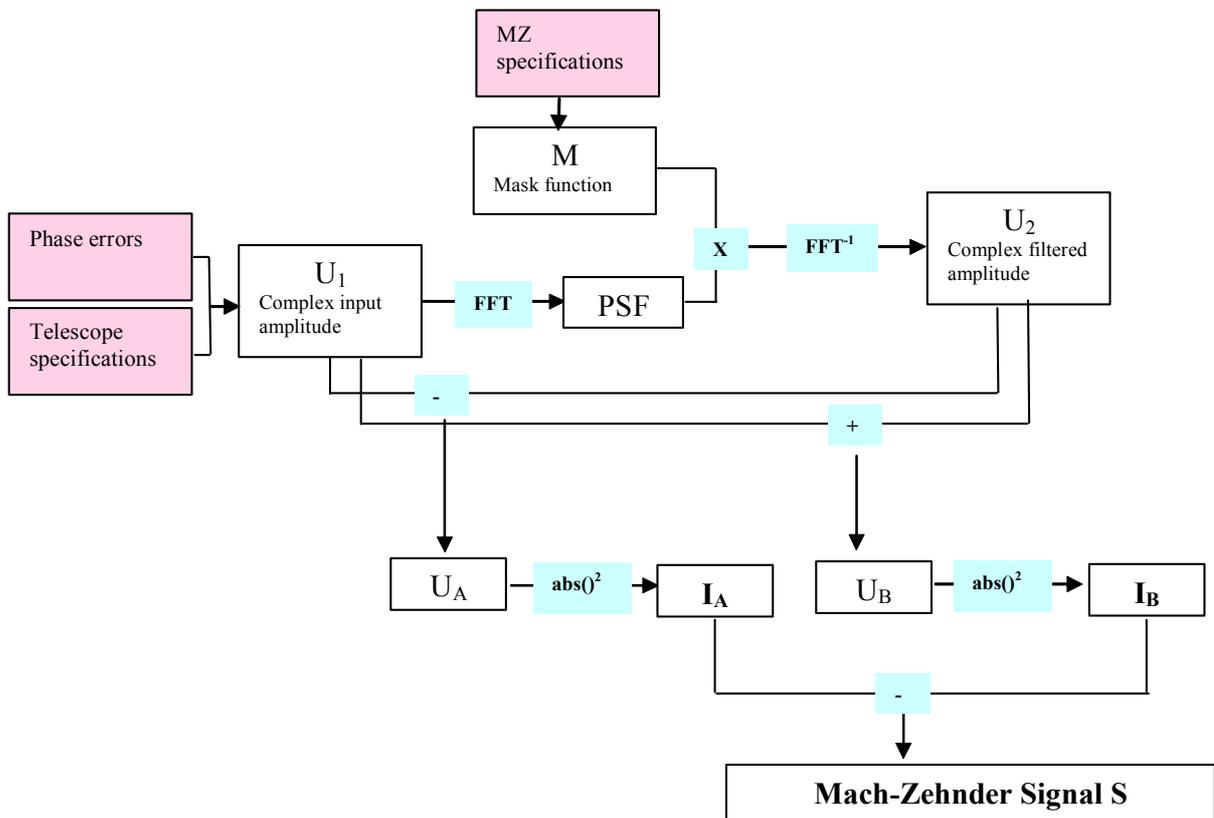

Figure 3.4.1 Flux diagram of MZ signal simulation.

Concerning to the first block of the simulation, the algorithm employed to simulate the MZ Signal is described in Figure 3.4.1. As input variables we introduce:

- *Telescope parameters*: we have assumed an hexagonal geometry, defined by the number of segments, segment size and number of points across the entrance pupil. Using these parameters, a segment index pupil can be generated as shown in Figure 3.4.2 for a 10-m class segmented telescope. Each segment is indexed with a different number and it is associated to one of the segment rings coloured in the figure. The obscured segments are not indexed. Edges are labelled with a number and its corresponding segment index as shown in Figure 3.4.2.
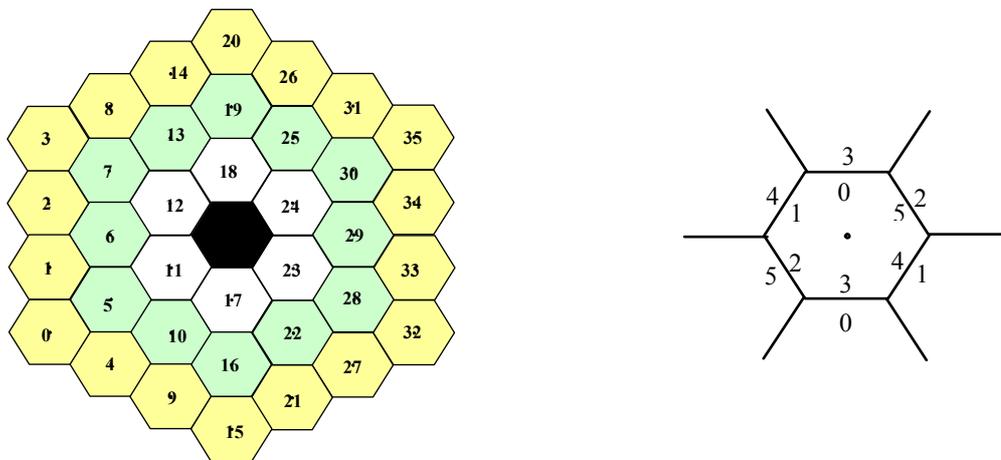

Figure 3.4.2 Segment index (left), border index (right).

- *MZ specifications*: it comprises the OPD between the arms of the interferometer and the size and shape of the pinhole. An optional input is the introduction of a second pinhole in the second arm. This option is required for the comparison with the experimental data and it will be described later.

- *Phase errors*: piston, tip-tilt or higher order wavefront errors are introduced as input RMS and they are randomly distributed for each segment. The size of gaps between segments and edge miss-figure errors produced in the polishing procedure are not implemented for the whole telescope due to the high resolution required. However they are included in the 1-D simulation to analyse its effect. The atmospheric turbulence was directly introduced as a phase term. A phase screen characterised by r_0 was generated for each single image. Long exposure images were simulated by averaging the signal for many phase screens.

Once the simulation parameters are described, the complex input amplitude is simply obtained from the product of the amplitude and the phase term. The mask function and the

complex filtered amplitude are calculated by means of Fast Fourier Transform (FFT) algorithms. As seen in section 3.2.1, the complex amplitudes at each output of the interferometer are obtained from the sum or the difference between U_1 and U_2. The intensities are calculated from the squared modulus of the amplitudes.

The main constraints of simulation are computation time and local memory requirements. As we will have a large number of segments within a large pupil, the FFT will need huge arrays that will often be out of the computer capacity. We are able to simulate pupil arrays up to 2048 pixels although for ELTs this resolution is obviously insufficient.

Nevertheless, the first step of the phasing procedure is phasing retrieval at each edge. Therefore, we will first analyse the signal profile of two adjacent segments, as it was done in the analytical study. Moreover, the 2-D signal can be seen as a recombination of 1-D profiles or even as the mean of 1-D profiles along the edge. In Figure 3.4.3 we represent the recombined 1-D profile from a 2-D image (symbols) and the 1-D simulated profile with the same parameters (solid line). The difference between them is less than 1%, so we consider the 1-D case as an appropriate approximation to study the physical behaviour of the signal.
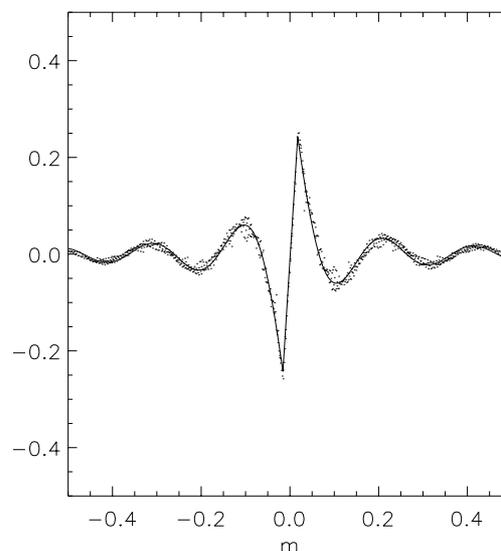

Figure 3.4.3 1-D reconstructed profile (symbols) from 2-D simulation and the 1-D simulated profile (solid line) for piston step of $\lambda/4$ and pinhole size of 1.5".

3.4.1. Simulation of 1-D MZ signal

In order to compare the results of the simulations with the analytical results, we present in this section the simulation corresponding to two adjacent segments as it is shown in Figure 3.2.2 for pure piston error.

In Figure 3.4.4 we have plotted the signal for a pinhole of 1.5" with a piston step of 125nm for λ=500nm. The analytical profile seems to greatly agree with the simulated one.
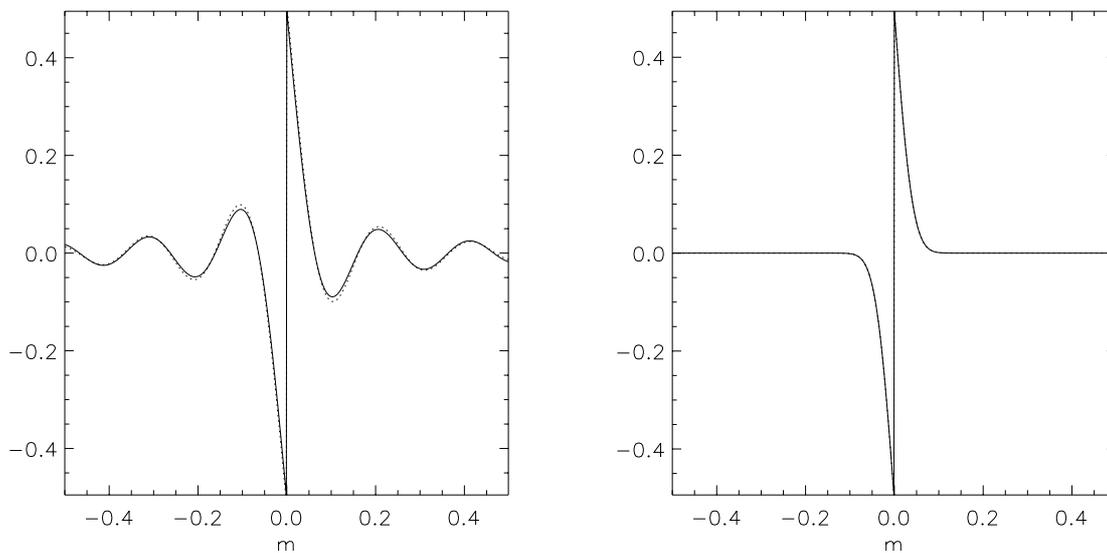
Figure 3.4.4 Analytical signal (solid line) and numerical simulated (dots) for circular pinhole (left) and Gaussian pinhole (right).

In principle, we can use both methods to reconstruct the 1-D MZ signal. But the analytical expression becomes complicated when edge defects are included. In addition, in order to have a more realistic estimation of the signal behaviour with atmospheric turbulence, we prefer to simulate long exposure images by averaging short exposure images rather than by directly introducing the atmospheric OTF in the analytical expression. For this reason we decided to use numerical simulations in the following analysis.

3.4.2. Aliasing effect

An ideal MZ signal has an infinity length. As we have seen before, its intensity is maximal at the edge and progressively decreases to zero far from the border.
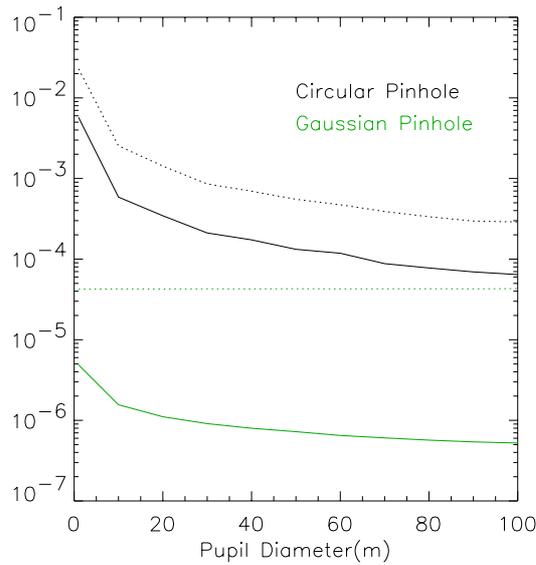
Figure 3.4.5 Standard deviation (solid) and PtV (dotted) between the analytical signal and simulated signal for circular and Gaussian pinhole.

In Figure 3.4.5 we have plotted the standard deviation (σ) and the Peak to Valley (PtV) between the analytical signal, which is supposed to be the ideal case without aliasing, and the simulated signal, for a pinhole of 1.5". We see that σ decreases when enlarging the diameter of the pupil. Hence the aliasing effect is negligible for the case of a Gaussian pinhole while for the circular pinhole and small aperture it becomes important.

The aliasing effect may be produced when the pupil array is not large enough to cover the MZ signal. The part of the signal which should be out of the array is seen by the computer as a reverberation which will be added to the MZ signal. The aliasing effect can be reduced from 1% to 0.3% using pupil diameters larger than 10m.
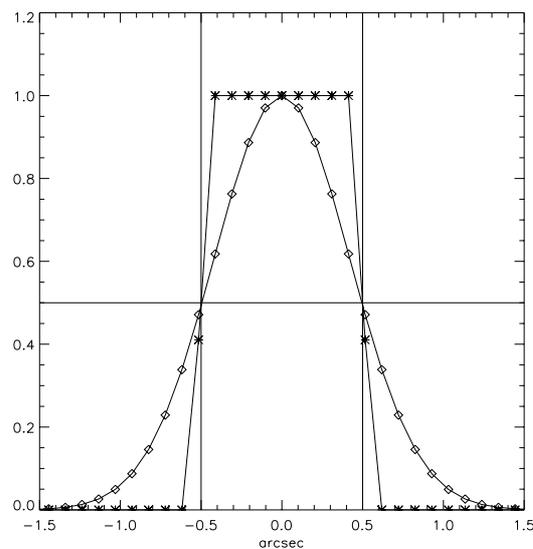
Figure 3.4.6 Profiles for circular (stars) and Gaussian (diamonds) pinhole shapes.

Another error source introduced in the simulation process comes from the sampling of the pinhole. For the Gaussian pinhole this effect is less important since the Gaussian is a continuous function as seen in Figure 3.4.6. On the contrary, the circular pinhole is represented by a discontinuous function which is 1 inside the pinhole and zero outside. The pinhole diameter does not always correspond to an integer number of pixels, so an interpolation has to be done by taking into account the discontinuities at the borders. We have interpolated in a way that the FWHM of the simulated pinhole corresponds to the given pinhole size, as shown in Figure 3.4.6. Although it is an improvement, a systematic error remains between the simulated and analytical signals due to the discontinuity in the pinhole.

3.4.3. Influence of Turbulence on the MZ signal

Any co-phasing method is sensitive to the phase aberrations caused by a turbulent atmosphere. One possible but generally inconvenient option is to perform the calibration on an adaptively compensated image. Another one is to try to reduce the effect by tuning the setup parameters of the co-phasing technique. A MZ wavefront sensor would be quite efficient in that respect, since the effect of atmospheric turbulence can be blurred out by adjusting the pinhole size which is confirmed in Figure 3.4.7. In this figure we plot the instantaneous phase of the input wavefront with r_0=25cm and a step error of 125nm. The

wavefront is filtered with a pinhole of 1.5", large enough to dump the high frequencies originated by the turbulence. In the left plot of the figure we observe that all high frequencies of the filtered phase (dotted line) are smoothed over. There is an offset of $\pi/2$ between the two phases coming from the OPD between the two arms of the interferometer. When performing the phase difference (right plot) and removing the OPD, the high frequencies show up and the step difference can be easily distinguished.
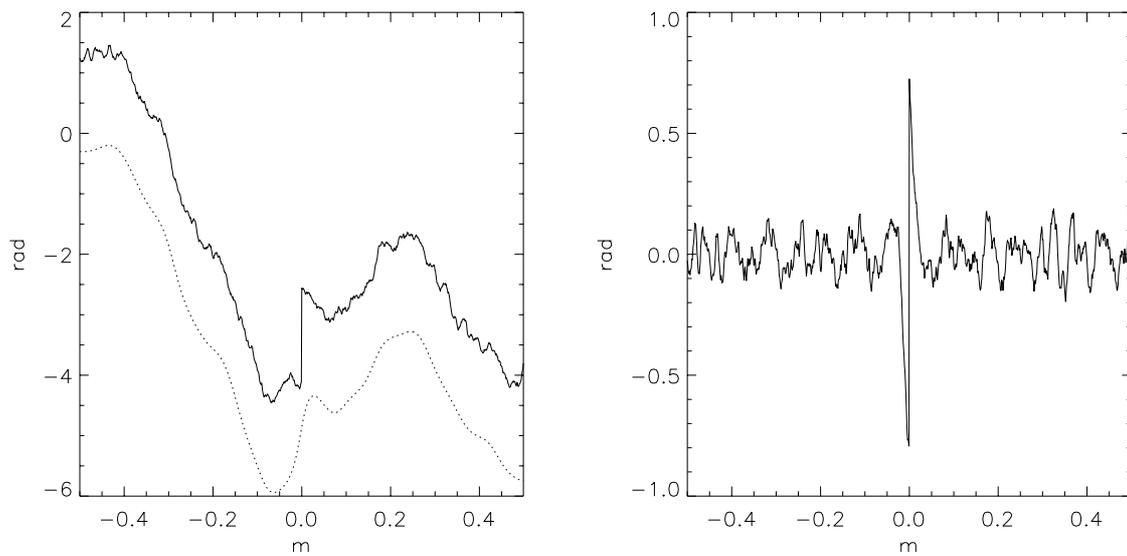

Figure 3.4.7 Left: Phase of the input wavefront (solid), phase of the wavefront after filtering (dotted). Right: Phase Difference.

We introduce atmospheric turbulence with phase screens injected directly on the phase term of the input complex amplitude. They are generated by FFT methods assuming a Von Karman spectrum given by (1.8) (Roddier 1981).

The generated phase screen is calculated from the inverse FFT of $\overline{\varphi}(\xi,\eta)$ whose modulus is obtained from expression (1.8) and whose phase is random uniformly distributed.

The correlation of the turbulence with time is given by the atmospheric time constant τ_0, as described in section 1.3.2. Two turbulent regimes are defined depending on the atmospheric time constant. i) The short exposure regime, when the exposure time is shorter than τ_0, corresponds to the frozen atmospheric aberrations. ii) The long exposure regime, when the aberrations are averaged and thus the exposure time is much longer than τ_0.

In our simulation we have considered three different turbulence conditions with r_0 equal to 25cm, 15cm and 10cm which for λ=500nm corresponds to seeing conditions of 0.41", 0.64" and 1.04" respectively. From (1.9), considering a wind speed of 10m/s we obtain that the atmospheric coherence times are 8ms, 5ms and 3ms, respectively.

We have first simulated the case of short exposure images with an exposure time of 3ms. In Figure 3.4.8 we have plotted a short exposure profile for piston step of 125nm (λ=500nm) on the wavefront using a pinhole of 1.5". Although the atmosphere components are strong the main peaks can be distinguished, but the error measurement depends on the atmospheric temporal variations. For this reason long exposure images are required in order to ensure low measurement error.
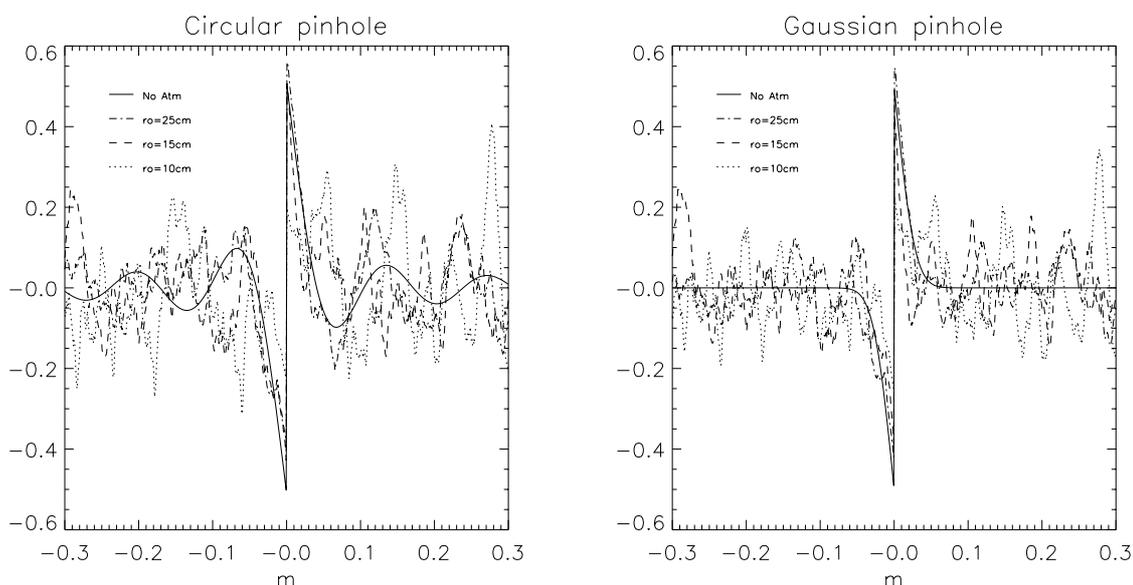

Figure 3.4.8 Signal profiles for different atmospheric conditions for a pinhole of 1.5" and piton step of λ/4 for Gasussian and circular pinholes.

Since the atmospheric coherence time is of the order of 1ms, we have chosen an exposure time 1000 longer than τ_0, which is 1second. We have generated 1000 phase screens for each seeing condition. A profile for each phase screen has been simulated and the average of the 1000 profiles is the long exposure profile plotted in Figure 3.4.9.
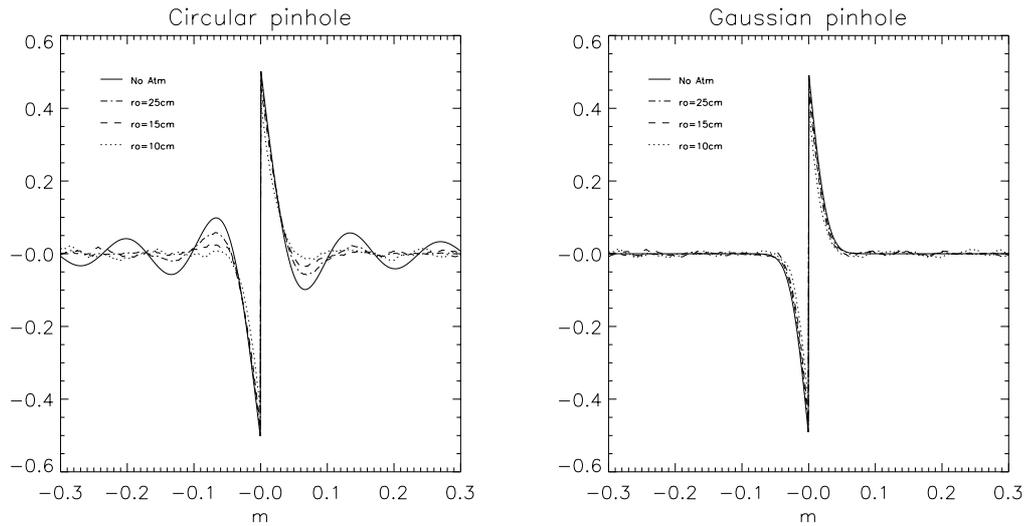
Figure 3.4.9 Signal profiles for long exposures for different atmospheric conditions, for a pinhole of 1.5" and piston step of λ/4 for circular and Gaussian pinholes.

For long exposure images the effect of atmosphere is blurred out. In the circular pinhole case the secondary peaks observed in the ideal signal are attenuated by the atmosphere. However this fact is not critical since we will measure the intensity of the signal at the main peaks.

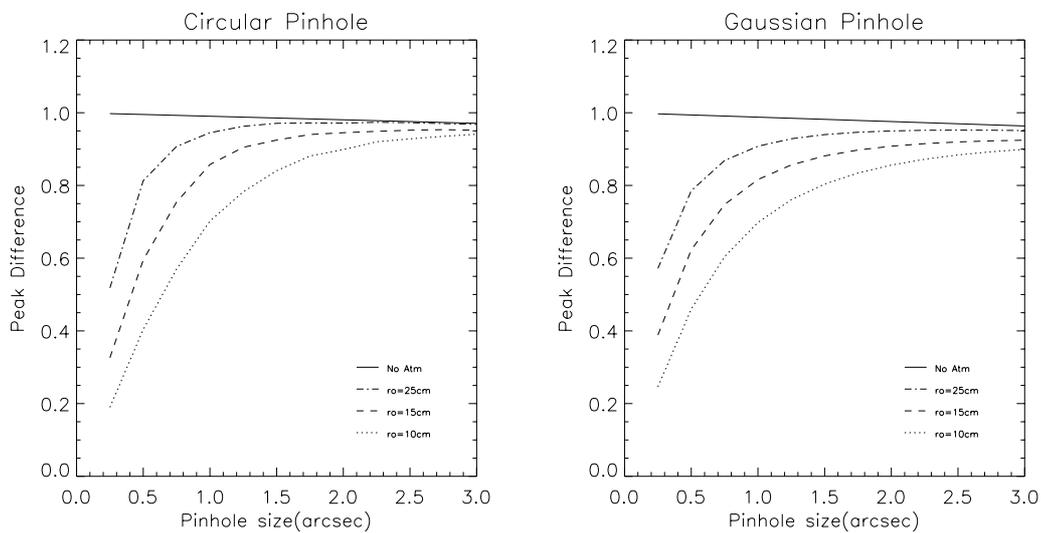**Figure 3.4.10** Amplitude of the signal as a function of pinhole size for long exposures for different atmospheres and piston step of λ/4 for circular and Gaussian pinhole.

In Figure 3.4.10 we have plotted the PtV of the profile for different pinhole sizes and different atmospheric conditions. If the pinhole size is small compared to λ/r_0, the atmosphere

is not well filtered and the PtV fall down with respect to the ideal case. In all of the three cases exposed here the pinhole should be greater than 1.5" to achieve 80% of the ideal PtV of the signal.

For the long exposure regime the accuracy of the piston measurement will be determined by the size of the pinhole. We can conclude that the atmospheric errors do not hamper the retrieval of piston information if the pinhole size is conveniently chosen.

3.4.4. Influence of Gaps on the MZ signal

In this section we intend to analyse the effect of the gap between segments on the signal. As described in chapter 2, a segmented pupil is forced to have a space between segments. In Figure 3.4.11 we have plotted the MZ signal profiles for 10mm gap (g), using a pinhole of 1.5" and a piston step of $\lambda/4$. The gap not only decreases the width of the signal but also its amplitude due to the lost of energy in the gap region.
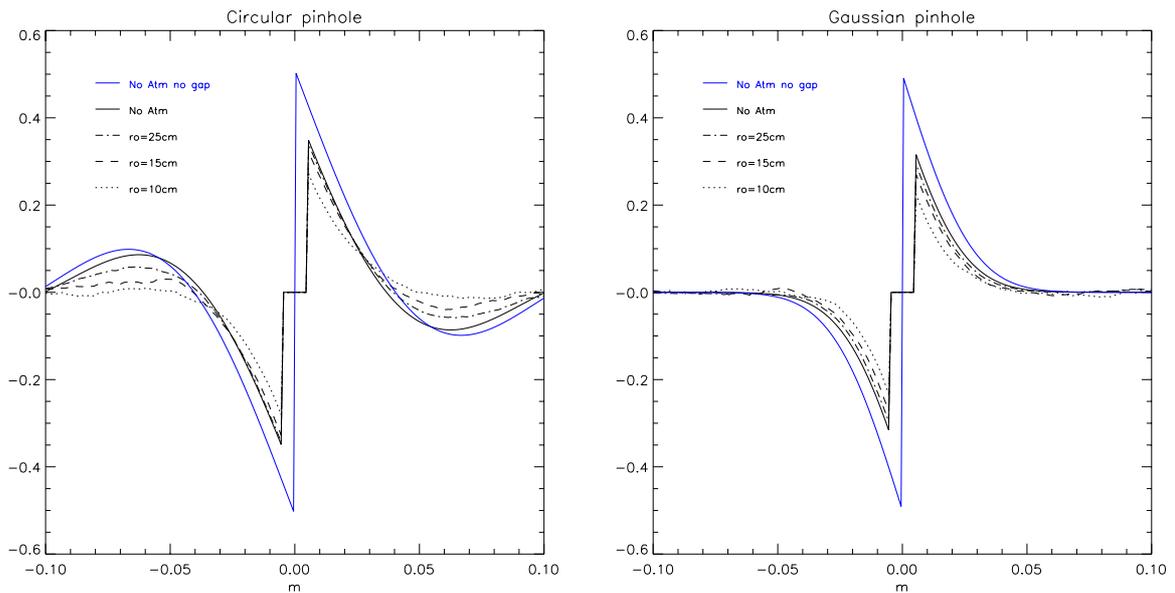

Figure 3.4.11 MZ signal profile with gap of 10mm using a pinhole of 1.5" and piston error of $\lambda/4$ for different seeing conditions and circular and Gaussian pinholes.

An expression similar to (3.17) can be obtained if gaps are included,

$$S(x) = \frac{1}{2}\left\{\cos(\theta)\left[1 + F\left(c\left(|x| + g/2\right)\right)\right] + \cos\left(\theta - \text{sign}(x)\Delta\varphi\right)\left[1 - F\left(c\left(|x| + g/2\right)\right)\right]\right\} \quad (3.25)$$

where, F is the function given by (3.15) and (3.16), g is the gap width, θ is the OPD and $\Delta\varphi$ is the step difference.

From this expression the width of the signal, defined as the distance between the first zeros at each side of the edge is expressed as,

$$w_g = w - g = \frac{4\lambda}{\pi a} - g \qquad\qquad \text{for Circular}$$

$$(3.26)$$

$$w_g = w - g = \frac{4\sqrt{2}\lambda}{\pi a} - g \qquad\qquad \text{for Gaussian}$$

where w is the width for the case without gaps, and a is the pinhole size.

3.4.5. Influence of the edge defects on the MZ signal

Edge defects may be the most important effects to keep in mind, since they could be an obstacle when measuring step errors.

The edge miss-figure may have different profiles which can be described with exponential, quadratic or more complicated functions. We have focused our study on the case of turned down edge. They are defined with a quadratic function of widths, w_1, w_2 and amplitudes a_1, a_2. A schematic view is shown in Figure 3.4.12.

Figure 3.4.12 Parameters of turned down edge.
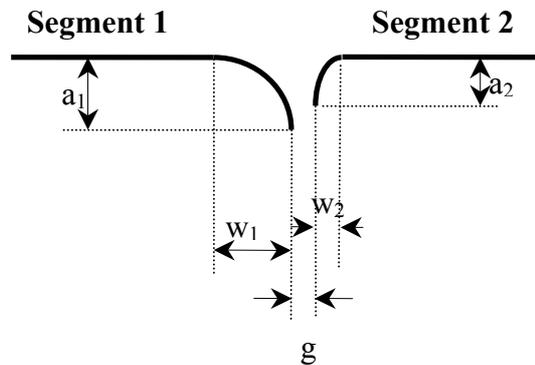
The declination of the signal from the one with perfect segments is mostly essential around the edge within the area $w_1 + w_2$. The width, depth and symmetry of edge have different effects on the MZ signal. In Figure 3.4.13, several profiles for different edge width and same depth are represented. The effect of edge defects is revealed by the presence of peaks in the central

part of the interferogram that will shadow the step components. We appreciate a loss of symmetry coming from the non-symmetrical turned down edges. The width of the edge increases the width of the peaks and decreases the signal amplitude.
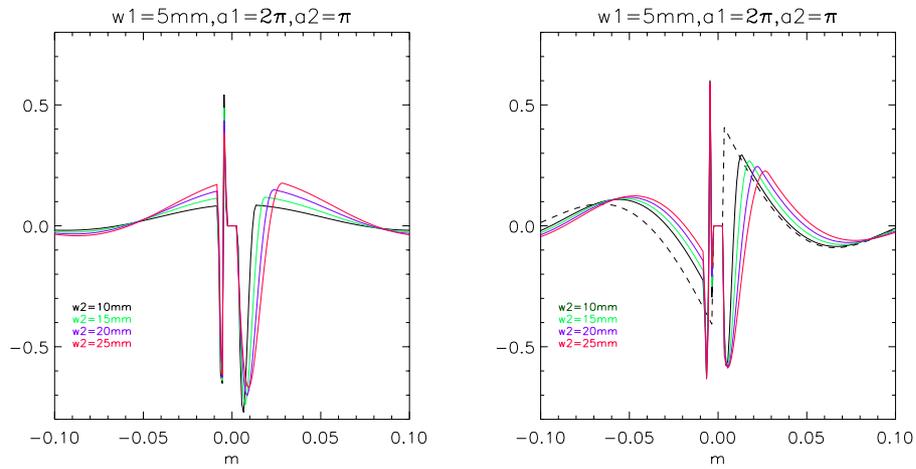

Figure 3.4.13 MZ signal profiles for different edge defects, with constant amplitudes a1=2π and a2=π and variable widths, gap=5mm, 1.5" pinhole size for piston error equal 0 (left) and λ/4 (right). Dashed line is the MZ signal profile for gap=5mm.

In Figure 3.4.14 the profiles for fixed edge width but different edge depth are plotted. A new secondary peak appears every time the depth is a multiple of π.

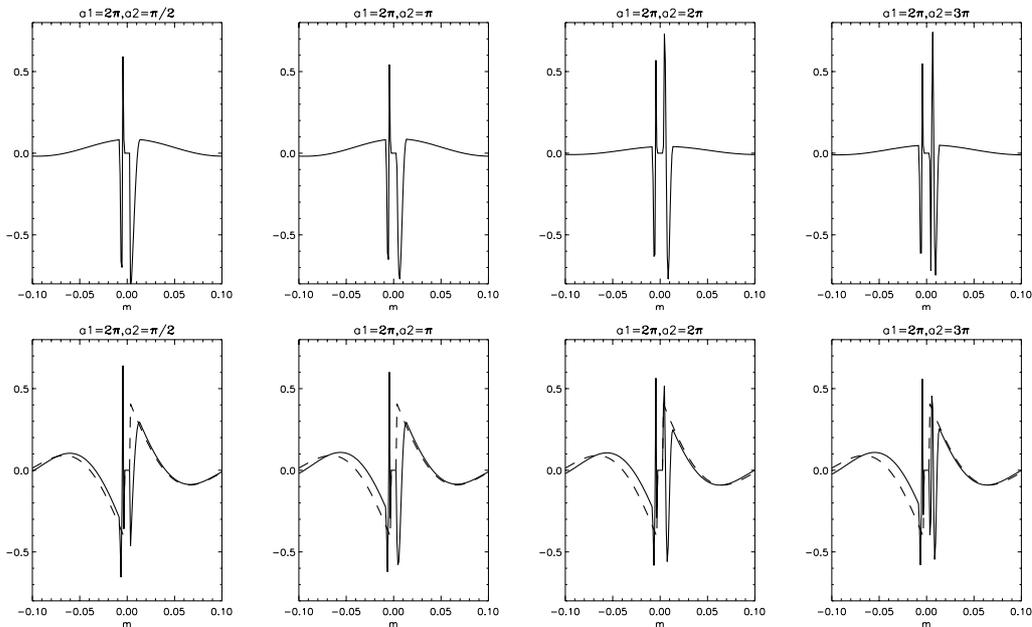

Figure 3.4.14 MZ signal profiles for edge defects with w1=5mm and w2=10mm and variable amplitudes, gap=5mm, 1.5" pinhole size for piston error equal 0 (upper row) and λ/4 (lower row).Dashed line is the MZ signal profile for gap=5mm.

The most important effect to retain from Figure 3.4.13 and Figure 3.4.14 is that edge miss-figure gives non zero signal for zero piston error, and this offset depends on the difference between edge parameters of two adjacent segments.

In order to quantify the offset introduced by the edge defect we have measured the piston given by the non-zero signal as a function of depth and width asymmetry between segment edges (Figure 3.4.15). For identical edges the offset is zero. For edges with identical amplitudes and different widths the offset follows a linear law with the width difference. On the other hand for constant width difference, the offset has a sinusoidal behaviour with the amplitude difference. Maximal offsets occur for larger width combinations. In same cases the edge defects in both size of the border are compensated.

All this analysis would help to investigate new trails in order to discern piston error from edge defects.
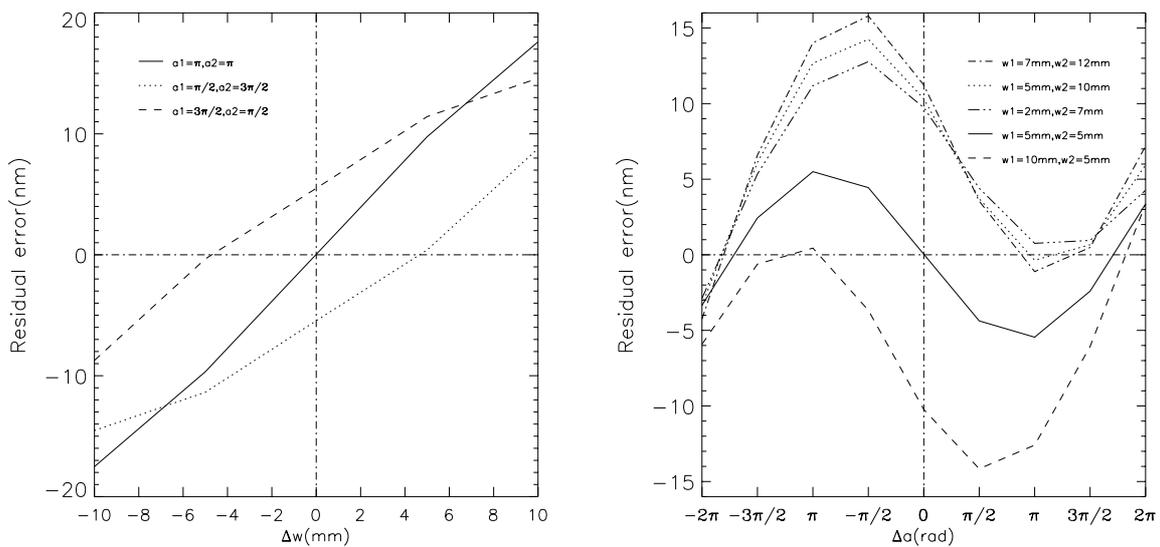
Figure 3.4.15 Residual error due to edge defect as a function of asymmetry of the edge width (right) and edge amplitude (left) for a circular pinhole equal to 1".

3.4.6. Pixelisation and Sampling

Until now we have simulated MZ signals with very high resolution, in order to understand their physical behaviour. Our aim is to obtain a reliable piston value from the MZ signal including as many parameters as possible, therefore the analysis is completed by including the detection parameters. It is found convenient to consider detection items of two different

processes refereed to as *pixelisation* and *sampling*. The pixelisation, considers that the signal is filtered because of the extended surface of the pixel and the sampling of the signal, is the process of converting continuous signals into discreet ones.

The pixelisation process is expressed by,

$$f_p(x) = f(x) \otimes \mathrm{Rect}(\mathrm{x}, \mathrm{X}_{\mathrm{pixel}}) \qquad (3.27)$$

where *f(x)* is the continuous MZ signal, and

$$\mathrm{Rect}(x, X) = \begin{cases} 1, & -X/2 < x < X/2 \\ 0, & \text{otherwise} \end{cases} \qquad (3.28)$$

is the top-hat function, representing the pixel.

In what follows we denote functions in the spatial domain with small letters and those in the frequency domain with capital letters. The band limited spectrum of the signal is given by,

$$F_p(\nu) = \mathrm{FT}\big(f(x)\big) \times \mathrm{Sinc}\left(\frac{\nu}{\mathrm{X}_{\mathrm{pixel}}}\right) \qquad (3.29)$$

where FT represents the Fourier transform. The pixelisation process determines the resolution of the signal in the spatial domain and the band limiting spectrum in the frequency domain. The smaller the pixels, the larger the spectrum bandwidth and thus the more signal details are appreciated.

The sampling of the signal is obtained by multiplying the signal by a sampling grid, which is expressed as a periodical space delta function,

$$f_{pc}(x) = f_p(x) \times \sum_{n=-\infty}^{+\infty} \delta(x - n\Delta X) \qquad (3.30)$$

where *ΔX* is the sampling period. The signal sampled with period *ΔX* yields the original spectrum replicated in the frequency domain with period *1/ΔX,*

$$F_{pc}(\nu) = F_p(\nu) \otimes \sum_{n=-\infty}^{+\infty} \delta(\nu - n/\Delta X) \qquad (3.31)$$

The sampling frequency *1/ΔX* must be larger than twice the maximum frequency (ν_{max}) present in the signal, to avoid aliasing artefacts. This minimum frequency is known as Nyquist frequency. Figure 3.4.16 shows this aliasing effect.
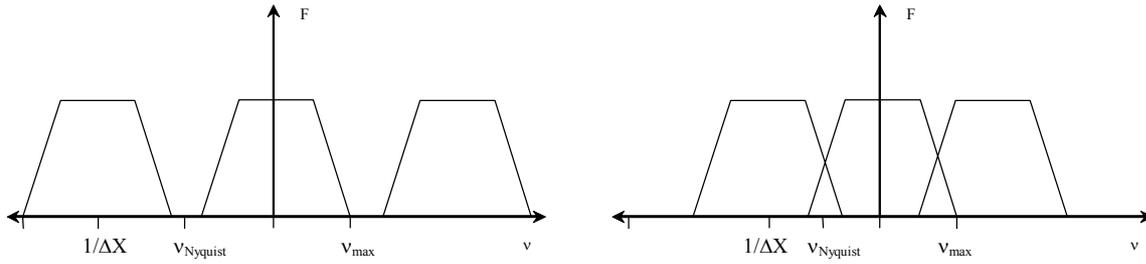
Figure 3.4.16 Left: Spectrum of the signal with a sampling frequency larger than the Nyquist frequency. Right: Aliasing effect due to the fact that the sampling frequency is smaller than the Nyquist frequency.

We have obtained a band limited spectrum and a sampled signal. Since the signal must be also limited in the space domain, we multiply it by a top-hat function (Rect) of width X_0,

$$f_{pcb}(x) = f_{pc}(x) \times \text{Rect}(x, X_0) \qquad (3.32)$$

This way the spectrum will be smoothed and signal features with frequencies less than $1/X_0$ will not be resolved:

$$F_{pcb}(\nu) = F_{pc}(\nu) \otimes \text{Sinc}\left(\frac{\nu}{X_0}\right) \qquad (3.33)$$

Indeed X_0 represents the size of the detector array. The bigger the detector size the better the spectrum is reconstructed.

Finally, the spectrum must also be sampled with a grid sampled function of period $1/X_0$. The sampling in the frequency domain corresponds to the signal replicated in the spatial domain with period X_0. The final signal is expressed as:

$$\overline{f}(x) = \left\{ \left[f(x) \otimes \text{Rect}(x, X_{pixel}) \right] \times \sum_{n=-\infty}^{+\infty} \delta(x - n\Delta X) \times \text{Rect}(x, X_0) \right\} \otimes \sum_{n=-\infty}^{+\infty} \delta(x - nX_0) \quad (3.34)$$

and the spectrum of the signal is given by,

$$\overline{F}(\nu) = \left\{ \left[F(\nu) \times \text{Sinc}\left(\frac{\nu}{X_{pixel}}\right) \right] \otimes \sum_{n=-\infty}^{+\infty} \delta(\nu - n/\Delta X) \otimes \text{Sinc}\left(\frac{\nu}{X_0}\right) \right\} \times \sum_{n=-\infty}^{+\infty} \delta(\nu - n/X_0) \quad (3.35)$$

The numerical implementation of the detector parameters can be done in two different ways. The first method consists on simulating a high resolution 2-D MZ signal and rebinning it to the desired detector size. The rebinning comprises pixilation and sampling processes. The second option reconstructs a 2-D image from the 1-D profile. A 1-D profile with very high resolution is simulated, next it is convolved with a rectangular function whose width equals

the pixel size. The 2-D image results from the combination of the sampled convolved 1-D profiles. The advantage of the second method is the reduction of allocated computer memory.

In a real detector the edge of the segment is not always placed between two consecutive pixels, therefore the signal is not well sampled between two segments. The spatial resolution can be artificially increased if the pupil is slightly rotated with respect to the detector. This way the edge crosses the pixels at different positions. Each pixel of the detector belongs to the i-column and j-row. By scanning the signal along the edge, the position of the center of each pixel in meters with respect to the edge is given by,

$$P_{i,j} = \left(\frac{d}{2} - (i+0.5)s \right) \tan(\alpha) + (j+0.5)s - \frac{d}{2} \tag{3.36}$$

where, d is the segment size, s is the pixel scale in m/pixel, α is the angle of rotation. This way a 1-D MZ signal can be reconstructed with a higher resolution than that of the detector one as shown in Figure 3.4.17.
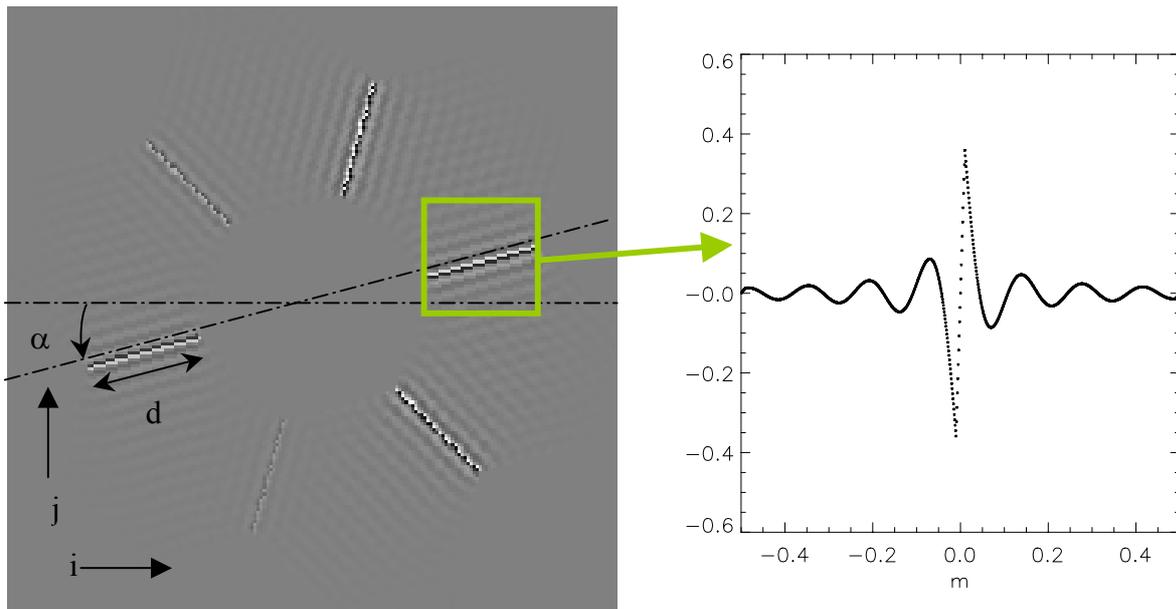

Figure 3.4.17 Reconstructed 1-D profile from a rotated 2-D interferogram. This way the resolution is increased.

This result confirms that using 1-D profiles instead of 2-D images in our simulations with the purpose of reducing the computer time and allocated memory, is valid.

In Figure 3.4.18 we compare the MZ signal with very high resolution with the signal convolved with a rectangular function of size equal to 25mm for pure piston equal to $\lambda/6$ and a pinhole size of 1.5", assuming no atmospheric errors. We have plotted six different cases for different values of the gap and edge sizes. As a consequence of the pixelisation process described above, the amplitude of the signal decreases and when edge errors are present (panels b, c, e and f), the high frequencies around the border between segments disappear. The gap and edge defects are not resolved because the pixel size is bigger than the characteristic size of the edge defects.
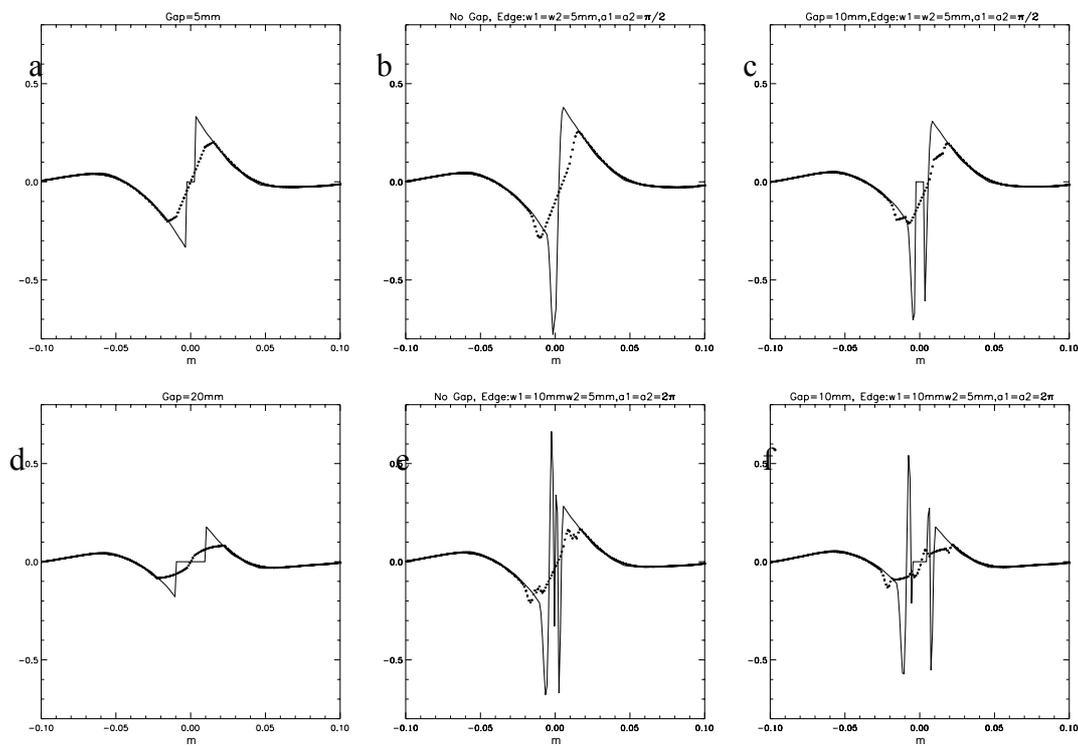

Figure 3.4.18 Signal profile with very high resolution (solid) and pixelised signal profile using a 25mm pixel width (dotted), for a 1.5'' circular pinhole and atmosphere r0=15cm and piston step of $\lambda/6$, a: with no edge errors and no gap; b: no gap and edge of a1=a2=$\pi/2$, w1=w2=5mm; c: gap=10mm and edge of w1=w2=5mm, a1=a2=$\pi/2$; d: gap=20mm, no edge errors; e: No gap and edge w1=w2=10mm,a1=a2=2π; f: gap=10mm and edge w1=w2=10mm, a1=a2=2π.

The effect of the detection parameters will depend on the profile of the signal with a very high resolution.

In Figure 3.4.19 we show a set of plots with the same edge parameters used in panel f of Figure 3.4.18 —amplitudes equal to 2π and edge widths equal to 10mm and 5mm — but different gap sizes. In none of these four cases, the gap and edge widths are not resolved because of the pixel size used. Gaps result in a reduction of the signal amplitude, as already discussed in section 3.4.4. In addition to this effect, the lower resolution decreases also the signal amplitude. For gap widths larger than 15mm the two main peaks of the signal profile disappear, and therefore the piston step information is more difficult to retrieve.

Figure 3.4.19 Signals with piston error of $\lambda/6$ (solid-line) and 0(dashed-line) and the difference between them (dotted-line) for r_0=15cm, pinhole size of 1.5'', edges with amplitudes equal to π and widths equal to 10mm and 5mm and gap sizes of : a, 5mm; b, 10mm; c ,15mm, d; 20mm.

The effect of the detection parameters when edge defects are present is more complicated to describe because of the irregular shape of the signal profile. In Figure 3.4.20 we plot a set of signals with gap size equal to 10mm and four different symmetrical edge defects. We observe that the signal becomes more irregular when the width of the edge increases because the total width is closer to the pixel size. For small edge widths the depth of the edge has less influence than for large edge widths. As the total size of the edge increases, the signal with (solid line) and without (dashed line) piston error becomes closer, therefore the piston information is masked by the edge effects.
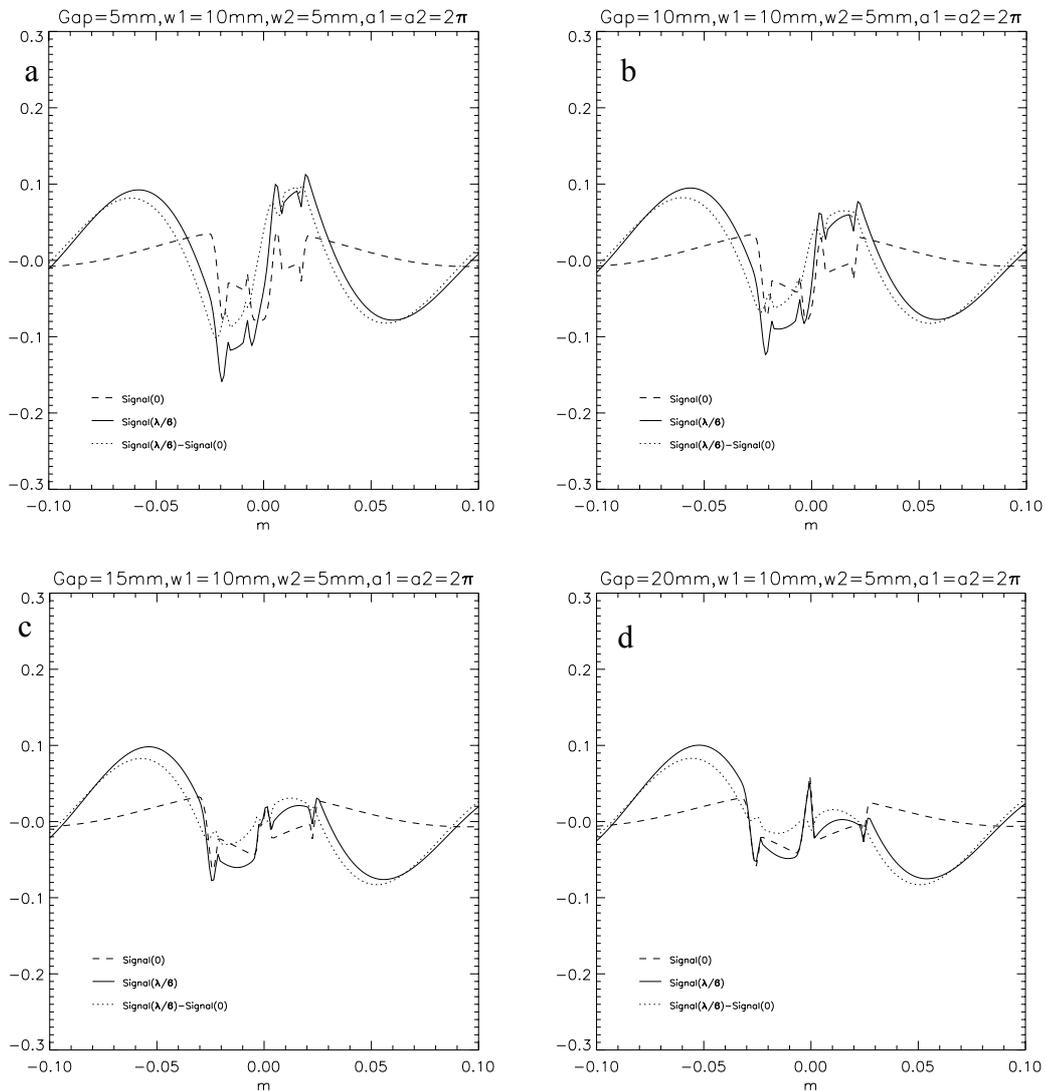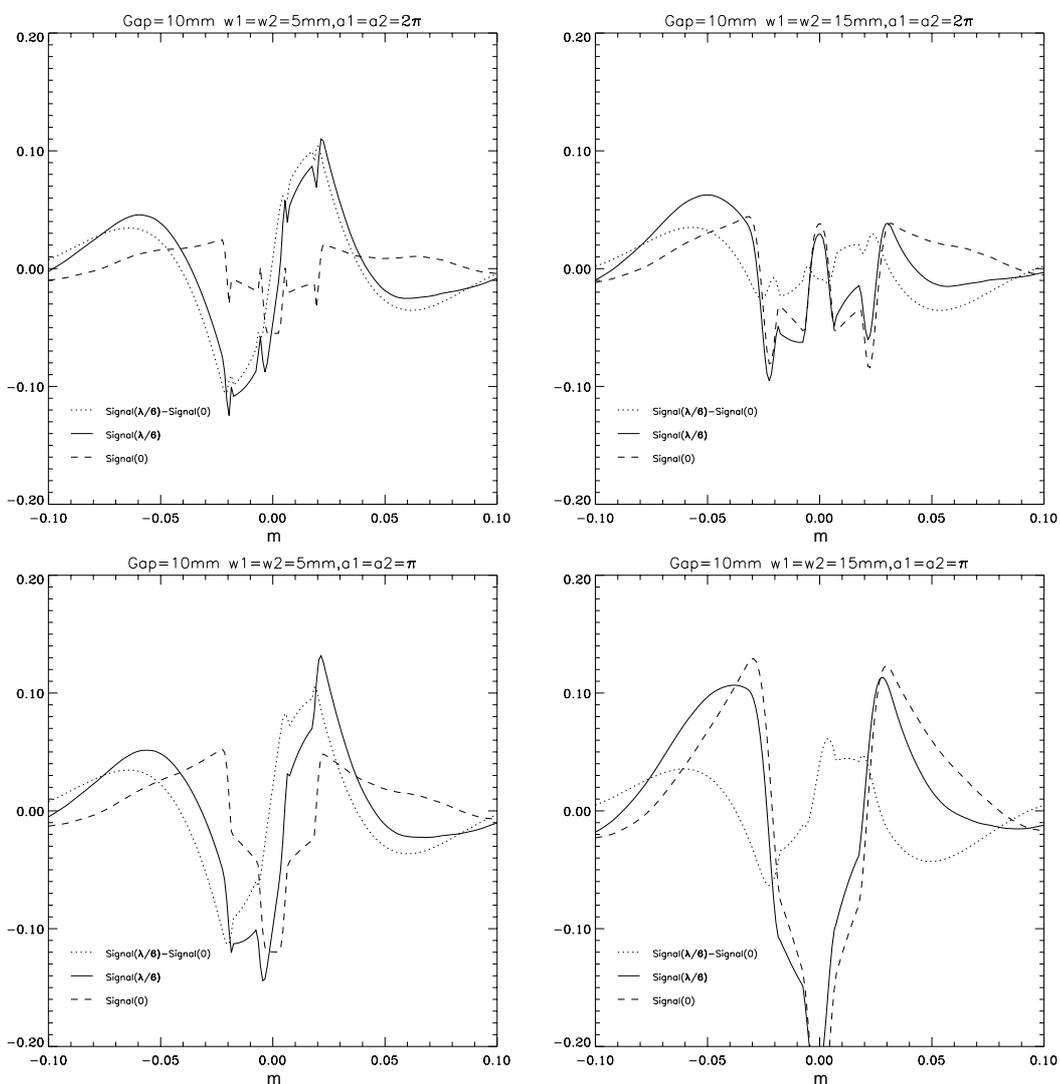

Figure 3.4.20 Signals with piston error of $\lambda/6$ (solid line) and 0 (dashed line) and the difference between them (dotted line) for r0=15cm, pinhole size of 1.5'' and different edge defects.

In Figure 3.4.21 we plot the difference between the signals with piston $\lambda/6$ and piston 0 for different atmospheric conditions and pinhole sizes. For a small pinhole the variation of the signal amplitude is large from one atmosphere to the other, while for large pinhole size we have no signal anymore. For a pinhole size around 1.5" we get a signal with same amplitude for all values of r_0. This is in agreement with our previous results, because the pixel size is large enough to resolve r_0.
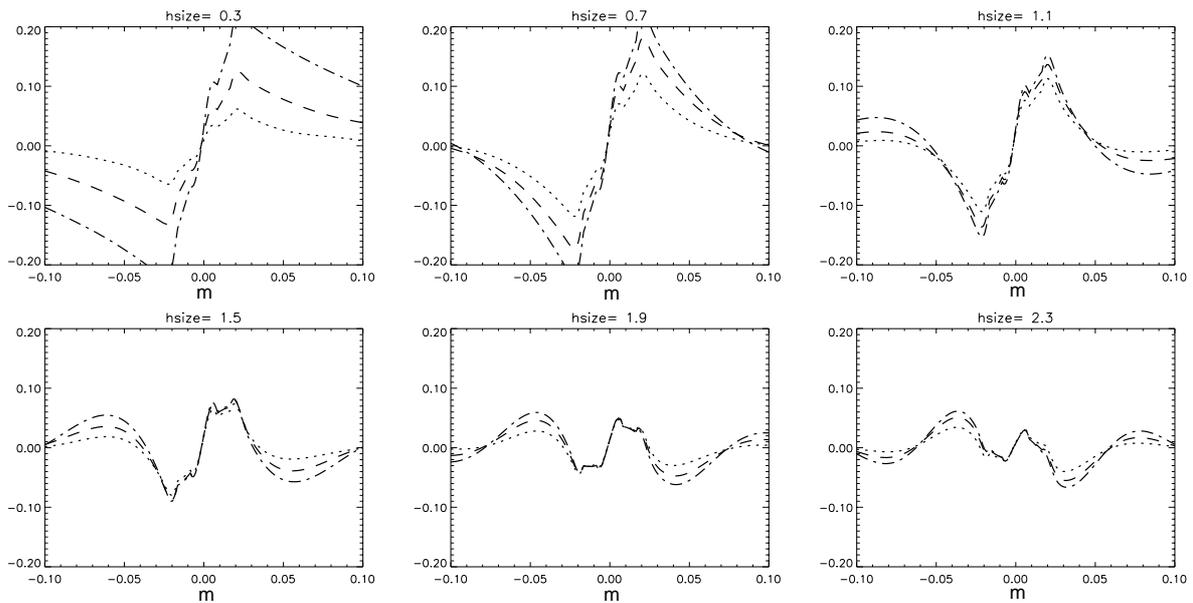

Figure 3.4.21 Difference of the signals for piston 0 and $\lambda/6$ for r_0=10cm (dot),15cm (dash) and 25cm (dot-dash) and different pinhole sizes, gap=10mm, w1=10mm,w2=15mm,a1=a2=π.

The main conclusion of this analysis is that piston error is not easily distinguishable from other error sources. There is an unknown offset due to the non-zero signal introduced by edge defects that will reduce the performance. However as we will discuss later, for standard edge values the precision on the piston measurements still fit within the co-phasing specifications. New trails should be followed to be able to know this offset and therefore improve the performance on the piston measurement.

3.4.7. **Multi-wavelength measurement**

All the interferometric methods are valid within a useful range which depends on the wavelength used. The maximum unambiguous measured piston step is $\pm\lambda/2$ at the wavefront,

i.e $\pm\lambda/4$ at the mirror surface. It means that for the case of λ=650nm, the interferometric tool is not able to retrieve a piston step larger than 162nm.

One powerful solution for extending the range and therefore solve 2π ambiguity is the use measurements at different wavelengths. Several methods intended to solve this problem can be found in the literature.

Löfdahl et al (2001) perform the measurement at different wavelengths and compare them in order to determine the true piston step. All the possible solutions for the piston step at a given wavelength are,

$$PS[k] = \varphi \pm \Delta\varphi + k\lambda \tag{3.37}$$

where φ is the measurement result within the range of one wavelength, $\Delta\varphi$ is the measurement error and k is an integer number. The true solution is found resolving,

$$PS = \varphi_1 \pm \Delta\varphi_1 + k\lambda_1 = \varphi_2 \pm \Delta\varphi_2 + j\lambda_2 \tag{3.38}$$

The constraints for j and k that ensure an unambiguous result are

$$\begin{aligned}|\varphi_1 + k\lambda_1| + \Delta\varphi_1 < \lambda_{max} \\ |\varphi_2 + j\lambda_2| + \Delta\varphi_2 < \lambda_{max}\end{aligned} \tag{3.39}$$

where $2\lambda_{max}=|k|\lambda_1=|j|\lambda_2$. Löfdahl et al (2001) fixed a maximum error on the piston measurement to resolve (3.38). Shumacher et al (2000) explored all the possible solutions that fulfil the conditions (3.39) considering the error of each piston measurement. In their simulations they obtained an optimal range of 4500nm using two wavelengths when the error of the piston measurement does not exceed 50nm.

Cheng & Wyant (1984) present a method based on the measurement of an equivalent phase from the phase obtained with two individual wavelengths.

The phase ϕ_t, of each wavelength is calculated as,

$$\phi_1 = \frac{2\pi\varphi}{\lambda_1} \quad , \quad \phi_2 = \frac{2\pi\varphi}{\lambda_2} \tag{3.40}$$

where φ is the piston step. The difference between the phases obtained for each wavelength yields the equivalent phase expressed as,

$$\phi_{eq} = \frac{2\pi\varphi}{\lambda_{eq}} \tag{3.41}$$

where $\lambda_{eq} = \dfrac{\lambda_1 \lambda_2}{|\lambda_1 - \lambda_2|}$ is the equivalent wavelength which defines the capture range. To ensure a good performance of this method, the precision of the measurement of the phase should be better than $\lambda/10$ and the two wavelengths should be carefully chosen; good results are found for $\lambda_{eq} \sim 4\lambda_1$.

The implementation of multi-wavelength in the MZ co-phasing technique presents one difficulty due to the fact that the OPD changes with the wavelength. This problem can be avoided by using an achromatic plate. Other solution consists on correcting the calibration data to the shifting on the OPD. We are currently investigating this possibility.

3.4.8. Tip-Tilt considerations

Segment misalignment includes not only piston errors but also tip-tilt aberrations. The present work is based on pure piston errors, however an overview of the effect of tip-tilt error on the MZ signal is presented in this section.
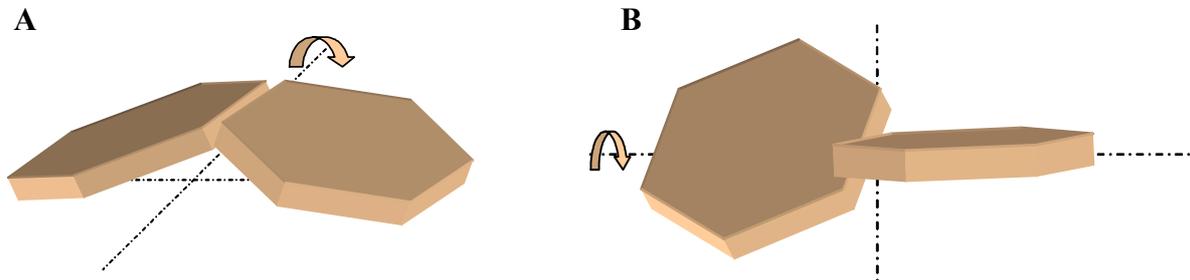

Figure 3.4.22 Tip tilt components in two adjacent configuration.

The tip-tilt errors have two components represented in Figure 3.4.22. The rotation of the segment respect to the axis along the segment edge (panel A), that can be described as

$$\varphi_x(x, y) = \frac{2\pi}{\lambda}(2x \pm d)\alpha_x \qquad (3.42)$$

where α_x is the bend angle with respect to the segment plane, and the rotation of the segment with respect to the horizontal axis perpendicular to the segment edge (panel B)

$$\varphi_y(y) = \frac{2\pi}{\lambda}\left[2y\alpha_y\right] \qquad (3.43)$$

where α_y is the rotation angle and d is the distance between the segment centers.

Yaistskova et al (2004) found an analytical expression for MZ signal following a similar reasoning as for pure piston error. In Figure 3.4.23 we have plotted the simulated surfaces of the MZ signal for different tilt errors using a circular pinhole of 1". Unlike the case of a pure piston error, the signal including tilt errors is not anymore constant along axis y. As already seen, piston errors, x-tilt and y-tilt have different influence on symmetric and anti-symmetric properties of the signal. Yaitskova et al (2004) proposed a method based on these symmetry properties to retrieve the discontinuity errors. However a global analysis of the effect of tilts on the MZ signal remains to be studied.
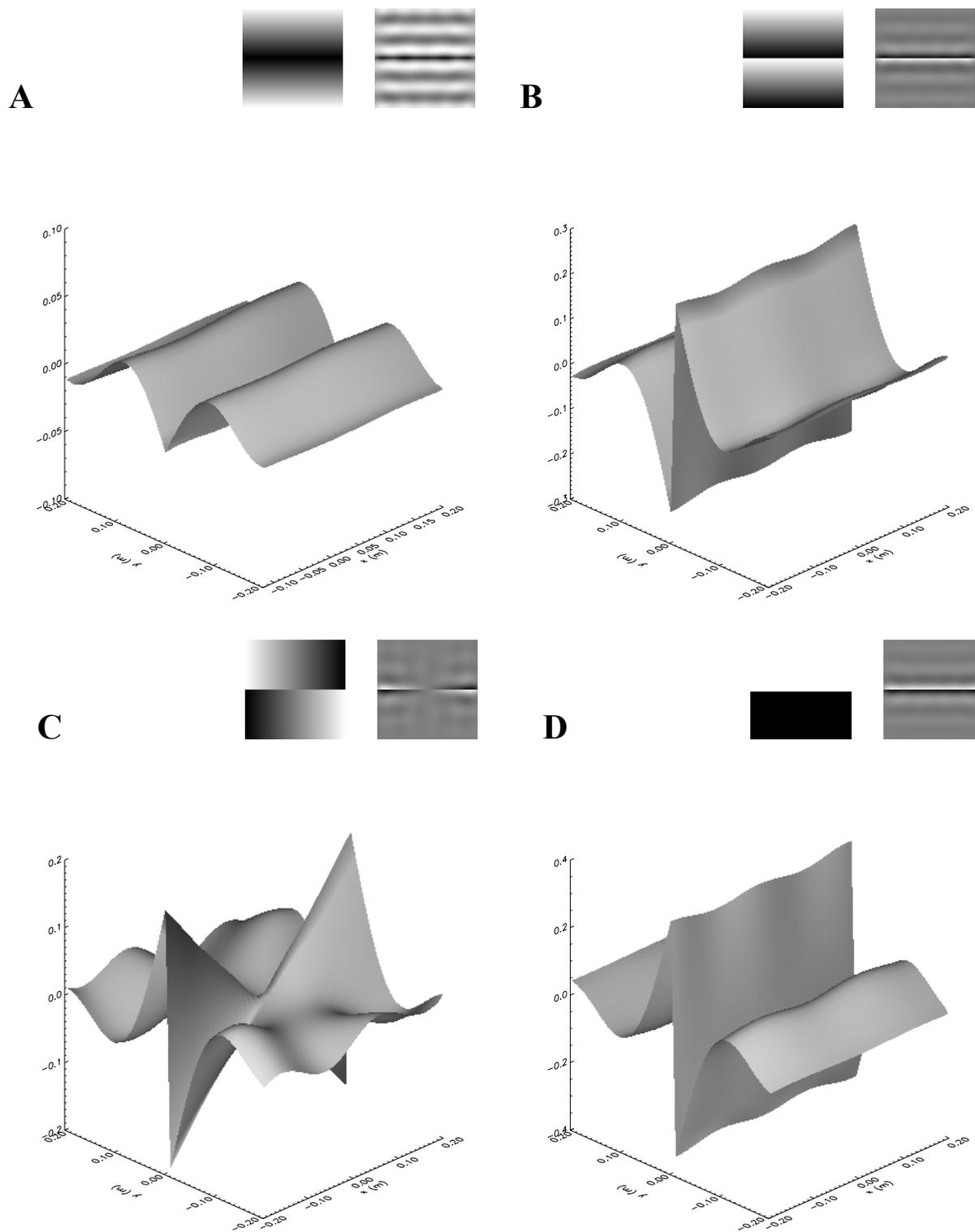
Figure 3.4.23 MZ signal surfaces for: A, equal x-tilts of λ/4, B, opposite x-tilts of λ/4, C, opposite y-tilts of λ/4 and D pure piston of λ/4.

3.5. Performance of a Mach-Zehnder co-phasing sensor

In the previous sections we performed a deep analysis on the physical behaviour of the MZ signal as a function of different parameters. This analysis has revealed that discontinuity errors are present in the MZ signal even in presence of atmospheric turbulence. However, the MZ signal contains gap and edge defect information which is difficult to discern from segment discontinuities. In this section we will test the performance of an algorithm intended to retrieve the piston error from the MZ signal. We will state the range of validity of the proposed algorithm as a function of different error sources.

Chanan et al (2000) proposed an algorithm based on correlation coefficients. The image of the unknown piston step is compared to a set of simulated images for different piston errors. The piston error is given by the degree of similarity with respect to the set of images. A resolution a better resolution than the piston-step difference between two templates is achieved by quadratic interpolation of the correlation coefficients. Another algorithm proposed by Bello-Figueroa (2001), consists on calibrating an intrinsic attribute of the signal related to the piston error. We will employ this approach since it turned out to be the best after the comparison, carried out by Schumacher et al (2002), of both algorithms.

We have tested two criteria in the implementation of the calibration algorithm. Given that, as mentioned in the previous section, the amplitude of the MZ signal is proportional to the piston step, we will adopt the PtV of the signal as our first criterion. The difficulty lies in the determination of maximum and minimum of the signal because they are localized in few pixels close to the edge. The second alternative, referred as integral criterion, computes the difference between the integrals of the signal from the edge to a certain distance in both senses of the segment edge. The integration area is a free parameter to be optimised. We must prevent crosslink between edges of the same segments and we must keep a good signal to noise ratio (SNR). In the ideal case, i.e. excluding edge defects and gaps, the optimal integration area corresponds to the width between the first zeros of the signal at both side of the edge, and they are given by equations (3.18) for circular pinhole and (3.19) for Gaussian pinhole.

The calibration curve will be performed from a set of MZ simulated signals for different piston errors. In the ideal case, we obtain that this calibration curve is perfectly fitted by the function:

$$M(\Delta\varphi) = A\sin(\Delta\varphi) \qquad (3.44)$$

where $M(\Delta\varphi)$ is the integral or peak difference of the signal, $\Delta\varphi$ is the unknown piston step and A is the calibration coefficient, whose value is equal to the PtV or integral of the signal for piston step of $\pi/2$.

In Figure 3.5.1 we have plotted a set of calibration curves for different pinhole sizes, using both criteria. The calibration coefficient A for the integral criterion decreases with increasing pinhole, because the collecting area is bigger for smaller pinholes.
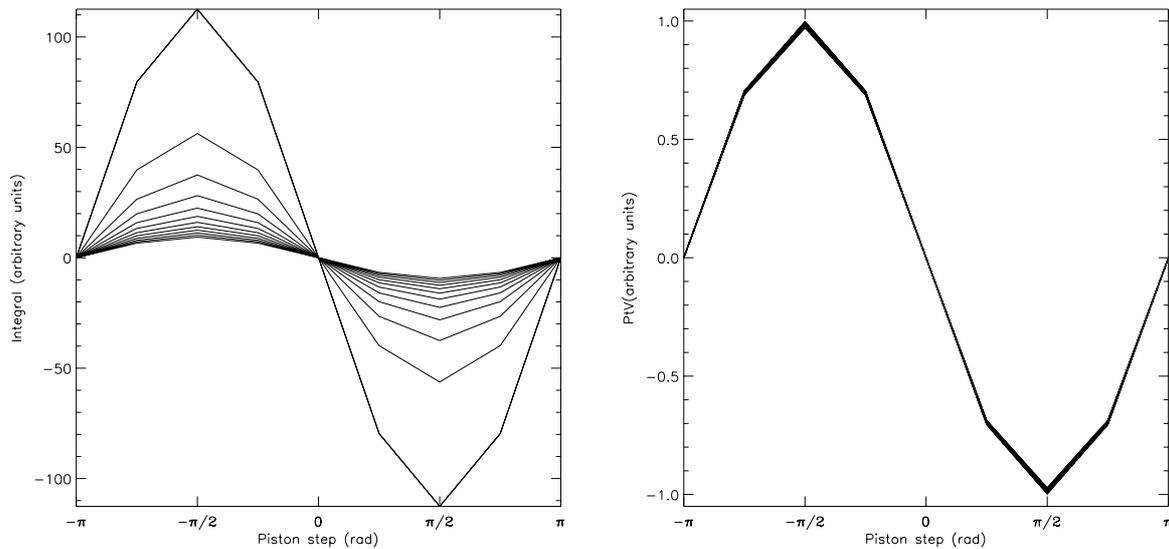

Figure 3.5.1 Calibration curves using integral criterion (left) and peak difference criterion (right) for different size of circular pinhole (0.25" to 3").

Since the calibration curves are periodical functions of piston step, the capture range is limited to $-\lambda/4$ to $\lambda/4$. Further measurements at different wavelengths should be taken to resolve the π ambiguity.

We will study the sensitivity of these algorithms to retrieve piston errors within this capture range. Our goal is to optimise the algorithm in order to minimise the effect of other error sources as edge defects, gaps and atmospheric wavefront errors. For this purpose we define the *piston measurement error* as the difference between the real piston step value and the value calculated from the calibration curve.

In the simulation presented here the segment size is set to 1m and the wavelength to 500nm. We have also included the detection parameters considering a projected pixel scale of 25mm.

3.5.1. MZ co-phasing sensor performance as a function of atmospheric turbulence

We have simulated long exposure images for different piston errors and different pinhole size. We have computed the integral and the PtV of the signal. We already studied in section 3.4.3 the dependence of the PtV with pinhole size. In Figure 3.5.2 we have plotted the dependence of the integral of the signal with pinhole size under different seeing conditions and both pinholes. We appreciate the same tendency as for the PtV. The integral value holds over the ideal case for small pinhole sizes and it approaches to the ideal value for pinholes larger than a certain value depending on the atmospheric conditions.
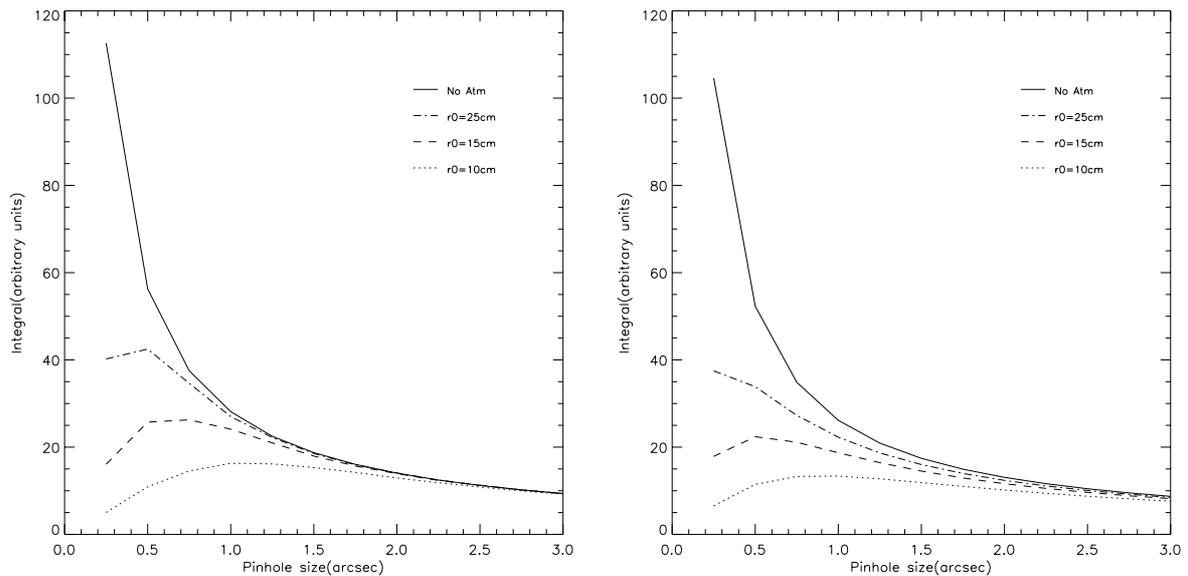
Figure 3.5.2 Integral of signal as a function of pinhole size for different seeing conditions for circular pinhole (left) and Gaussian pinhole (right).

In order to quantify the errors introduced by the atmosphere we have calculated the piston measurement error (in the wavefront) in the linear range from $-\lambda/4$ to $\lambda/4$. In Figure 3.5.3 we compare the measurements obtained for a circular and Gaussian pinhole of 1.5" under different seeing conditions using both criteria. For the circular pinhole the performance of the

integral criterion is better for good seeing conditions, while for bad seeing the secondary peaks of the MZ signal profile are attenuated and the PtV criterion gives better results. This is always the case for the Gaussian pinhole. In principle a better performance with the integral criterion should be expected in any case, because of the higher SNR. This is not the case, because the noise of the atmosphere is stronger far from the border than in the main peaks.

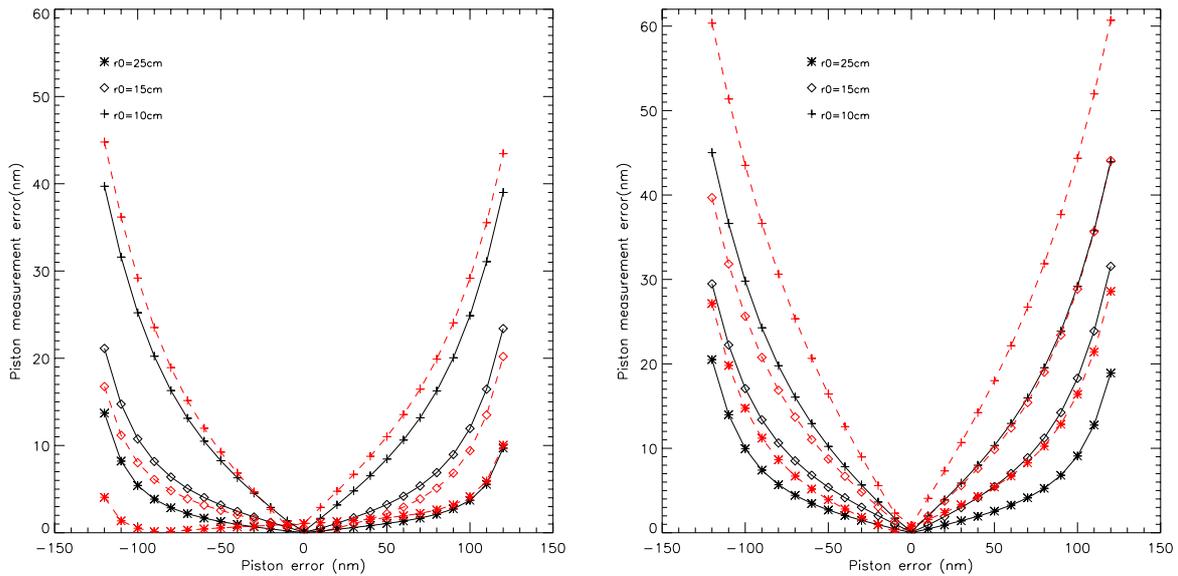**Figure 3.5.3** Piston measurement error, under various seeing conditions, for circular pinhole (left) and Gaussian pinhole (right) of 1.5" size as a function of initial piston step. The black-solid lines correspond to PtV criterion and red-dashed line to integral criterion.

We also appreciate that the curves are not symmetric with respect to zero piston. This asymmetry comes from a global tilt of the simulated phase screens. In a first iteration under good seeing conditions a precision of $\lambda/25$ (20nm@ 500nm) can be reached.

It is also interesting to study the precision of the technique as a function of pinhole. This analysis allows us to adjust more accurately the optimal pinhole size under atmospheric conditions. In Figure 3.5.4 we have plotted the measurement error as a function of pinhole size for different seeing conditions for a piston step of $\lambda/8$ (62nm@500nm) on the wavefront. As expected the precision decreases with decreasing the pinhole size. We also appreciate that the integral criterion for circular pinhole size gives better results for a seeing of 15cm than for a seeing of 25cm, this is due to the aliasing effect described in section 3.4.2, which is more relevant when the secondary peaks are not attenuated. However, even for the worse seeing

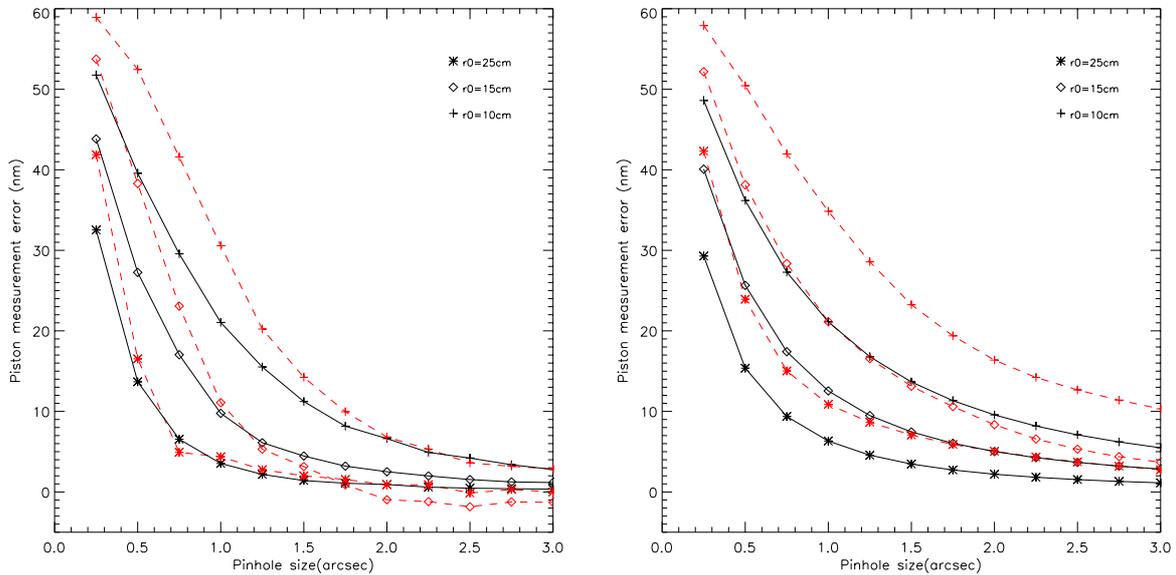conditions a precision of $\lambda/25$ (20nm @500nm) can be achieved for pinhole size larger than 1.5".

Figure 3.5.4 Piston measurement error under different seeing conditions as a function of circular (right) and Gaussian (left) pinhole size for a piston error of $\lambda/8$(62nm@500nm). Black-solid lines correspond to PtV criterion and red-dashed lines to integral criterion.

The performance of this algorithm can be considerably improved by an iterative process. In Figure 3.5.5 we represent the precision on the measure of the piston error for a pinhole of 1.5" and three different atmospheres. As can be seen, the convergence of the measured piston error is fast because the measured piston approaches the linear range of the calibration curve. A precision better than $\lambda/100$ (5nm@500nm) on the wavefront can be achieved after 3 iterations even for the worse atmospheric conditions.

Since the performance for both pinholes stay in the same range of error, hereafter we will refer all the results to the circular pinhole.
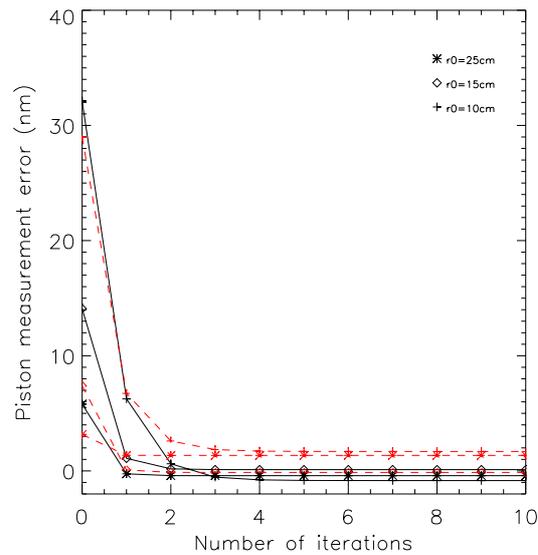
Figure 3.5.5 Piston measurement error as a function of number of iterations (initial piston error of 62nm), for three different atmospheric conditions and circular pinhole of 1.5", red-dashed corresponds to integral criterion and black-solid corresponds to PtV criterion.

3.5.2. MZ co-phasing sensor performance as a function of gaps

In this section we quantify the error on the piston measurement introduced by the combination of the atmosphere and gaps. The same procedure as in the previous section is followed. In Figure 3.5.6-A, we have potted the piston measurement error for a pinhole of 1.5", a gap size equal to 5mm, under different seeing conditions as a function of piston step. We observe that the performance is considerably reduced. This is due to the reduction of the width of the MZ signal in presence of gaps, as mentioned in section 3.4.4. This performance degradation can be avoided if gaps are included in the calibration data, as shown in Figure 3.5.6-B. This assumption is consistent in a real case provided that the size of gaps is accurately known.
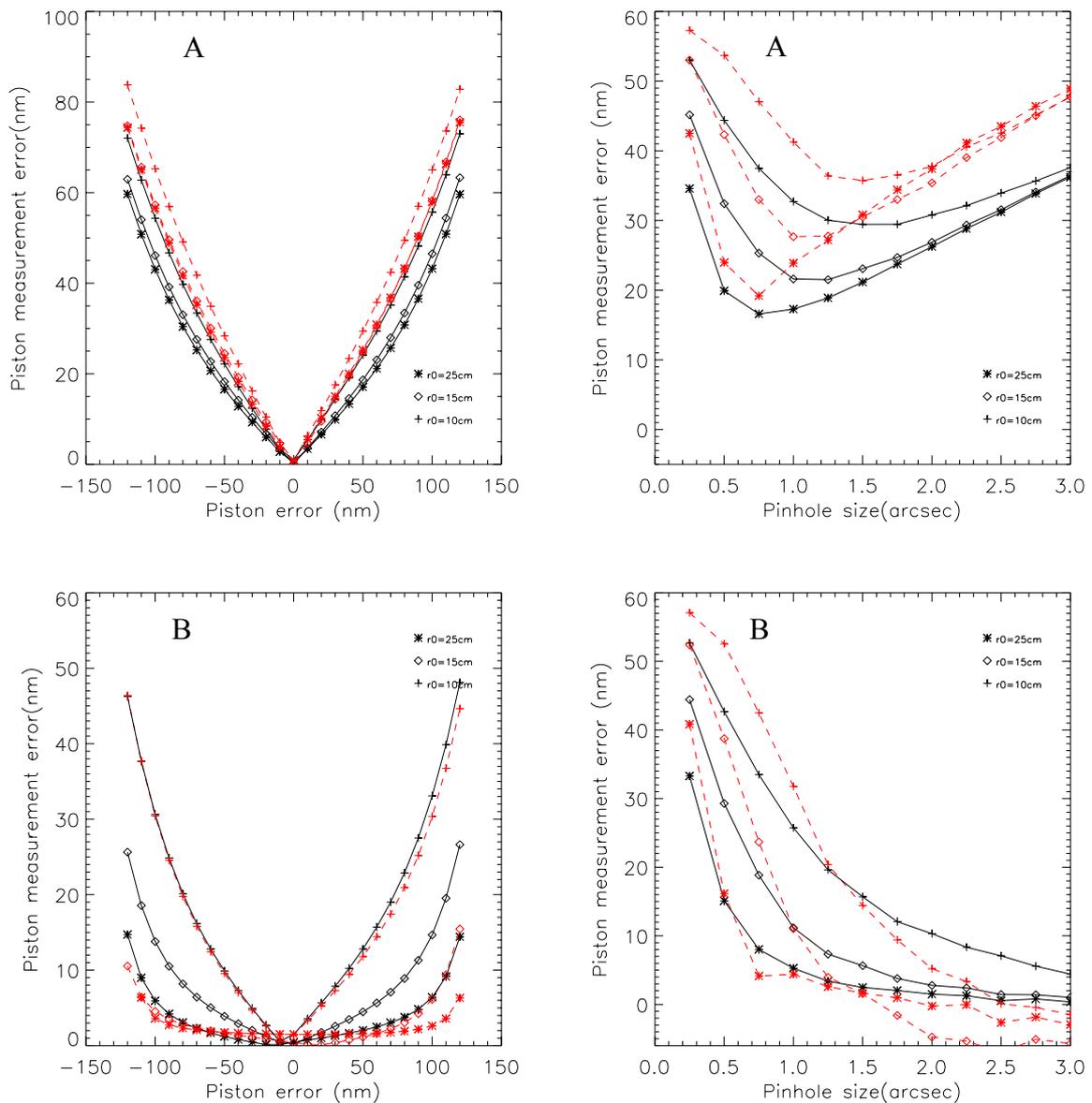
Figure 3.5.6 Piston measurement error under different seeing conditions, with gap of 5mm as a function of initial piston step with pinhole size of 1.5" (left) and pinhole size for a piston step of $\lambda/8$(62nm@500nm) (right). Black-solid lines correspond to PtV criterion and red-dashed lines to integral criterion. A: calibration without gaps. B: calibration including gaps.

Although the performance obtained with both criteria is similar, hereafter we will employ only the integral criterion, because of the difficulty to define the maximum and minima of the MZ signal, as we have seen in section 3.5.3, when edge defect are included.

In Figure 3.5.7 we have plotted the piston measurement error for different gap widths and seeing conditions as a function of pinhole size. It can be observed that the performance for

pinholes smaller than 1.5" is limited by the seeing conditions while for larger pinholes is limited by the gap size. So that, if we set the optimal pinhole to 1.5", after some iterations the performance is similar to the case without gap, i.e $\lambda/100$ (5nm @500nm), as can be seen in Figure 3.5.7.
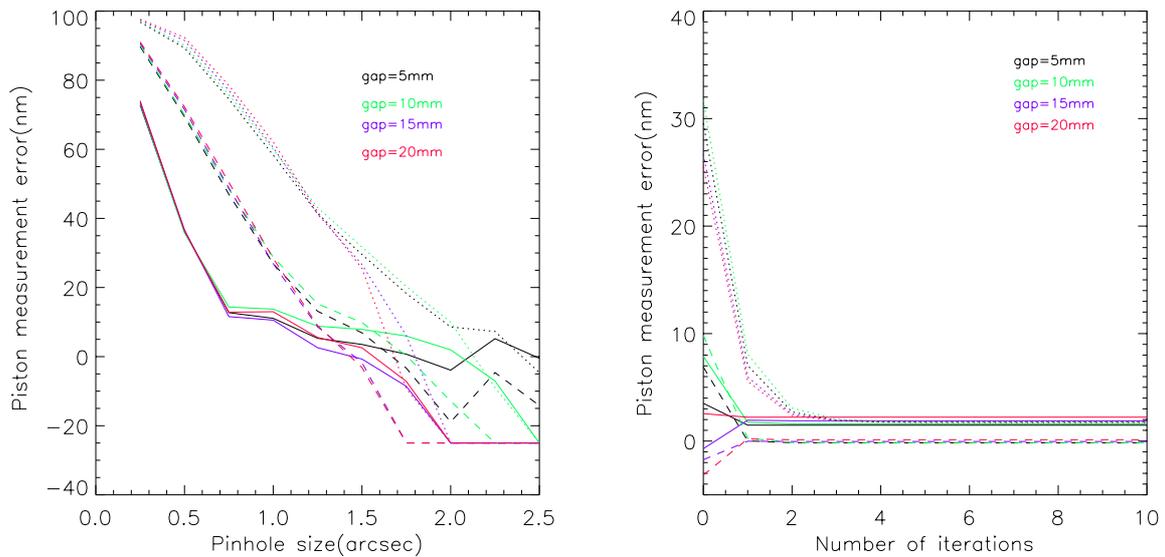

Figure 3.5.7 Piston measurement error: As a function of pinhole size for different gaps and atmospheric conditions for a initial piston step of $\lambda/5$ (100nm@500nm) (left), as a function of number of iterations for different gaps and atmospheric conditions (25cm solid lines, 15cm dashed lines and 10cm dotted lines) and pinhole size of 1.5" (right).

3.5.3. MZ co-phasing sensor performance as a function of edge defects

As described in section 1.3.1, while segment edge defects do not have a big influence in the quality of the PSF of the telescope, they are clearly present in the MZ signal and they represent an obstacle when retrieving the piston information revealed in the MZ interferogram. As seen in section 3.4.5, there is a residual signal for piston step equal zero which depends on the characteristics of the edge. A priori this zero offset can be estimated if the edge parameters of each segment are included in the calibration data. These parameters can be directly measured at the segment edge or extracted from the MZ signal. Our detailed study of this last possibility lead to the conclusion that the width of the edge can be estimated from a careful analysis of the two outputs. Nevertheless the amplitude is not discerned from piston step nor from the shape of the edge. Since the requirements for an extremely accurate

co-phasing, demand the elimination of all the contaminating effects, the knowledge of edge defects is mandatory, therefore we continue working on this problem.

If edge defects are not known, the goal is to minimise the offset due to the presence of edge. We have studied several approaches based on different choices of the calibration data. The best performance is obtained when including the knowledge of the gaps in the calibration data.
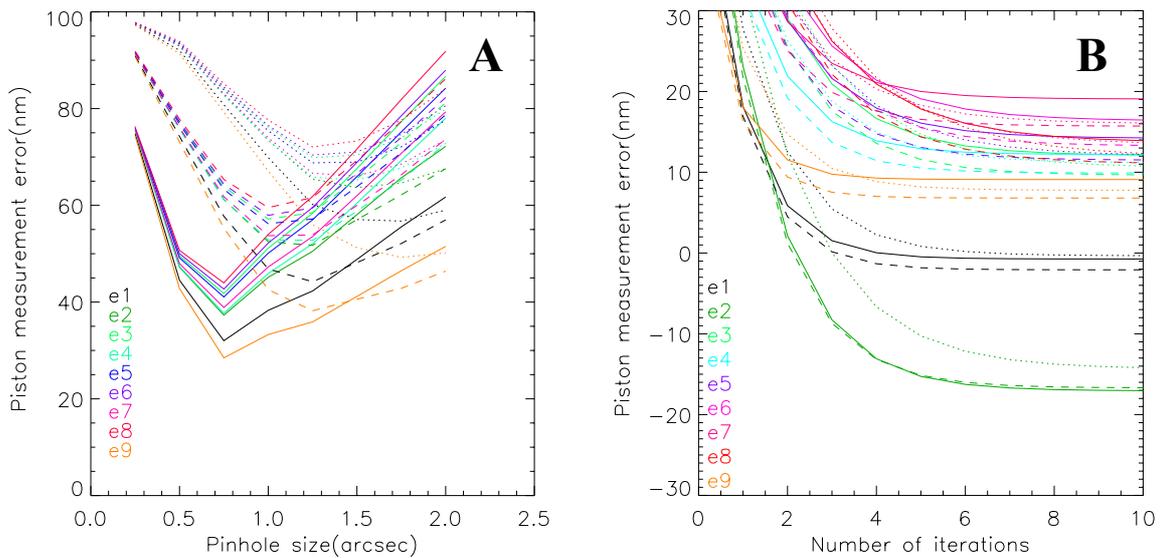

Figure 3.5.8 Piston measurement error (A) as a function of pinhole size, (B) as a function of number of iterations for pinhole of 1.5", for different edge defects and seeing of 10cm (dotted), 15cm (dashed) and 25cm (solid), for initial piston step of $\lambda/5$(100nm@500nm).

Table 3.5.1 Edge dimensions corresponding to Figure 3.5.8.

Edge	e1	e2	e3	e4	e5	e6	e7	e8	e9
w_1(mm)	5	10	5	5	5	5	5	5	5
w_2(mm)	5	5	10	10	10	10	10	10	10
a_1(rad)	π	π	π	$\pi/2$	2π	3π	π	π	π
a_2(rad)	2π	2π	2π	2π	2π	2π	π	3π	$\pi/2$

In Figure 3.5.8-A, we represent the piston measurement error for an initial piston step of $\lambda/5$ (100nm@500nm) for different atmospheric conditions and different edge defects as a function of pinhole size. The performance improves when the pinhole size decreases. The piston measurement error presents a minimum when the pinhole size is twice the size of the seeing disk and contrary to the case without edge defect, the performance becomes worse for

larger pinholes. We appreciate that for small pinhole sizes the performance is dominated by the effect of the atmosphere while for large pinhole sizes the accuracy of the measurements are determined by the edge defects. Nevertheless the performance can be gratefully improved after some iterations, as seen in Figure 3.5.8-B. We appreciate that the worse performance is given by the best atmosphere of 25cm. Therefore the pinhole size should be readjusted. In Figure 3.5.9 we represent the piston measurement error after 10 iterations as a function of pinhole size. Reducing the pinhole size to 1", the best performance is obtained with the best seeing conditions, and in any case an error below λ/50 (10nm@500nm) can be achieved depending on the edge miss-figure. This result is satisfactory to ensure the required quality of the segmented surface.

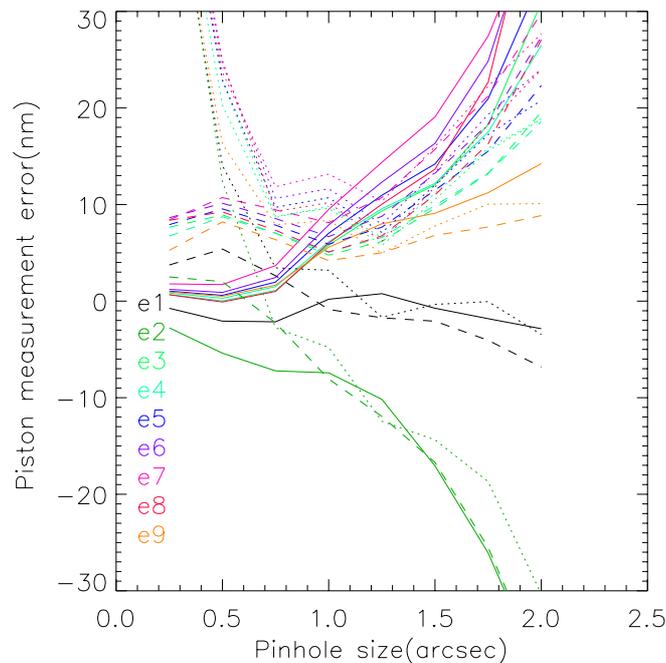**Figure 3.5.9** Piston measurement error as a function of pinhole size after 10 iterations for an initial piston step of λ/5 (100nm@50nm) and three seeing conditions, 25cm (solid),15cm (dashed), 10cm (dotted).

If the edge defects are known a priori and we include this information in the calibration data, the precision can be improved up to λ/100 (5nm@500nm) as for the case including only atmosphere.

As a conclusion we notice that in order to maintain the best performance, the optimal pinhole size which was set to 1.5" by the atmospheric conditions, should be reduced to 1" in order to minimise the edge miss-figure effects.

3.5.4. MZ co-phasing sensor performance as a function of photon noise

In this section we calculate the limiting stellar magnitude required to phase the mirror by using a MZ wavefront sensor. The limiting stellar magnitude will depend on the SNR.

For the ideal case of a detector with gain equal 1 and avoiding detector noise, the SNR is given by,

$$SNR = \frac{S}{N} = \sqrt{S} \tag{3.45}$$

where S is the number of detected photons and $N = \sqrt{S}$ is the photon noise.

As described in section 3.5, by using the integral criterion the signal is equal to:

$$S = S_1 - S_3 - \left(S_2 - S_4\right) \tag{3.46}$$

where S_1, S_2, are the numbers of photons arriving to regions 1 and 2 of one detector and S_3, S_4 are the number of photons arriving to the regions 3 and 4 in the second detector as represented in Figure 3.5.10.
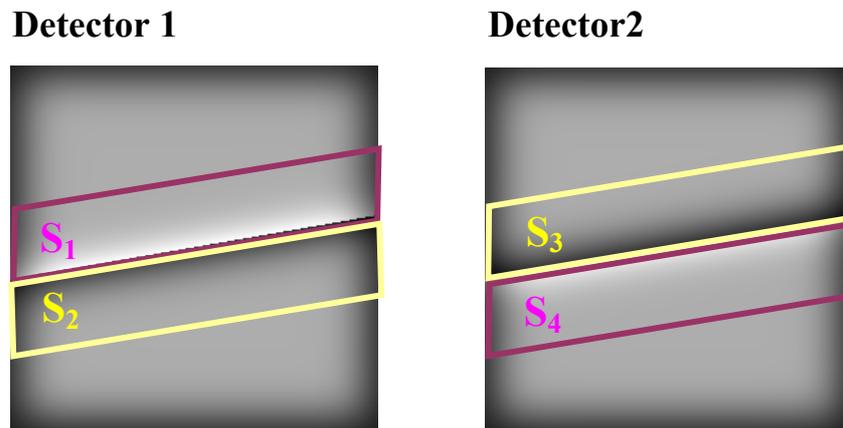

Detector 1   **Detector2**

Figure 3.5.10 Detector areas included in the calculation of the integral criteria of the MZ signal.

To simplify the calculations we assume that the total number of photons arrived to each detector are the same, that is,

$$S_T = S_1 + S_2 \approx S_3 + S_4$$

We also make use of the symmetrical properties of the interferograms,

$$S_1 \approx S_4 \quad \text{and} \quad S_2 \approx S_3$$

therefore the signal can be expressed as,

$$S = 2\left(S_1 - S_2\right) \tag{3.47}$$

Since we consider only photonic noise which is assumed to follow Poissonian statistics, the standard deviation is given by,

$$\sigma_S = \sqrt{2\left(S_1 + S_2\right)} = \sqrt{2S_T} \tag{3.48}$$

The piston step is retrieved from the sinusoidal relation,

$$\Delta\varphi = \sin^{-1}\left(\frac{S}{A}\right) \approx \frac{S}{A} \tag{3.49}$$

where, A is the calibration coefficient obtained from simulation and $\Delta\varphi$ is the measured piston error. Since we are interested in the final precision, i.e small piston values, the signal has a value close to zero and we can apply the approximation $\sin(x) \sim x$

The error in the measured piston is given by,

$$\sigma_{\Delta\varphi} = \frac{\partial \Delta\varphi}{\partial S}\sigma_S \approx \frac{\sigma_S}{A} = \frac{\sqrt{2S_T}}{A} \tag{3.50}$$

In consequence the SNR of the piston measurement is equal to;

$$SNR \approx \frac{\Delta\varphi A}{\sqrt{2S_T}} \approx \Delta\varphi \overline{A}\sqrt{S_p n_{pixel}} \tag{3.51}$$

where S_p is the average number of photons on one pixel of one detector, n_{pixel} is the number of pixels in the integration area and $\overline{A}$ is the normalised calibration coefficient equal to $\dfrac{A}{S_T}$.

As seen in the previous section the error budget including atmosphere, gaps and edge defects is of the order of 10nm, in the worse case. In Figure 3.5.11 we plot the number of photons per pixel for different pinhole sizes to achieve a precision on the piston measurement of 5nm, 10nm and 15nm. Since the signal gets tighter when the pinhole size increases, i.e the integration area is smaller, the number of photons per pixel required to achieve a certain precision increases.
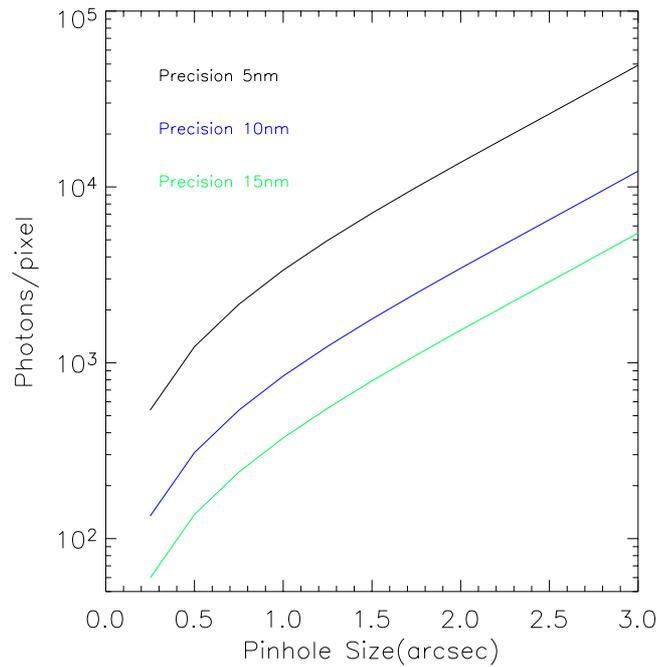
Figure 3.5.11 Number of photons per pixel required to achieve precision of 5nm, 10nm or 15nm as a function of pinhole size.

The magnitude of a star is related to the number of photons arriving to the detector as follows,

$$S_p = 1.51 \cdot 10^7 F_0 t \Sigma \varepsilon \frac{\Delta \lambda}{\lambda} 10^{-\frac{M}{2.5}} \tag{3.52}$$

where S_p is the average number of photons per pixel arriving to one detector, F_0 is the spectral flux density from a zero magnitude star at the top of the atmosphere, t is the exposure time, Σ is the pixel surface projected onto the pupil, ε is the system efficiency which is the product of the transmission from the top of the atmosphere to the detector and the detector quantum efficiency, $\Delta \lambda$ is the bandwidth, λ is the central wavelength and M is the magnitude of the star. In Figure 3.5.12 we have represented the limiting stellar magnitude for two exposure times, and the spectral band to achieve the required precision. We have assumed a system efficiency of 0.5, a linear pixel size of 25mm, a pinhole with diameter equal to 1", the spectral flux of zero magnitude equal to 3640Jy[2] for V band, 3080Jy for R band and 2550Jy for I band. The central wavelength and bandwidth are: 550nm and 88nm for V band, 640nm

---

[2] 1 Jy(Jansky)=10^{-23}erg s^{-1}cm^{-2} Hz^{-1}

and 147nm for R band, and 790nm and 150nm for I band. In the worse case a star brighter than 8 magnitude in V is necessary to phased segmented telescopes.
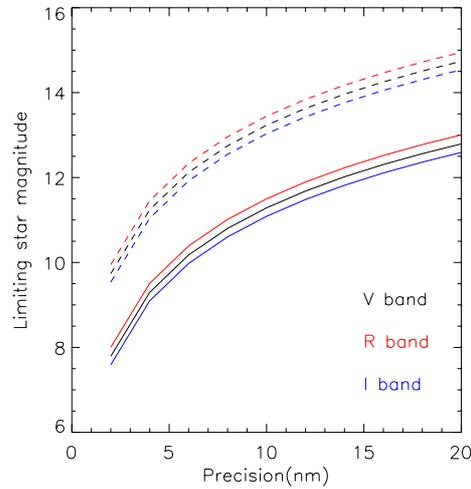

Figure 3.5.12 Limiting star magnitude as a function of the precision for three bands, exposure time of 10seconds (solid line) and 60seconds (dashed line) using a pinhole of 1".

The required FOV can be obtained from the probability of finding at least one star within a region of radius *r* on the sky. Since the distribution of stars within a given region of the sky follows Poisson statistics, the probability P is given by,

$$P = 1 - e^{-r^2 \nu \pi} \tag{3.53}$$

where ν is the density of stars brighter than magnitude M per deg² in the considered region.

The star density can be obtained from models of galaxies or from measurements by use of catalogues. We have calculated the star density on the North and South of the Galactic Poles (NGP, SGP) and in the Galactic Center (GC) from the Guide Star Catalogue[3].

From Table 3.5.2 it can be seen that a minimum FOV of 32 arcmin is necessary to ensure accurate piston measurements at all times in order to run the co-phasing measurement in close

---

[3] The Guide Star Catalogue was produced at the Space Telescope Science Institute under U.S. Government grant. These data are based on photographic data obtained using the Oshin Schmidt Telescope on Palomar Mountain and the UK Schmidt Telescope. The Oschin Schmidt Telescope is operated by the California Institute of Technology and Palomar Observatory. The UK Schmidt Telescope was operated by the Royal Observatory Edinburgh, with funding from the UK Science and Engineering Research Council (later the UK Particle and Astronomy Research Council), until 1988 June, and thereafter by the Anglo-Australian Observatory. The blue plates of the southern Sky Atlas and its Equatorial Extension (together known as the SERC-J), as well as the Equatorial Red (ER) were all taken with the UK Schmidt.

loop. The technical FOV proposed for OWL would be of the order of 6 arcmin which implies stars brighter than 15.3 for the close loop co-phasing procedure. This means that the integration time should be increased up to 26 minutes for a precision of 5nm and 6 minutes for a precision of 10nm.

Table 3.5.2 Limiting Stellar Magnitude and the corresponding required accessible FOV to find such a star with a probability of 90% at the NGP, SGP and GC.

Precision(nm)	Magnitude (R)	$FOV_{NGP,SGP}$(arcmin)	FOV_{GC}(arcmin)
5	11.4	~32	~14
10	13.4	~11	~5

From the results of the simulations presented in this work, the MZ co-phasing technique emerges as a strong candidate for co-phasing ELTs. However experimental results should be carried out in order to confirm the validity of this technique.

3.6. Summary

We have proposed a new technique based on a MZ interferometer with a pinhole acting as spatial filter for measuring discontinuity errors. The principle of this technique has been deeply discussed. We have developed an analytical approach which describes the 1-D signal profile for pure piston error and two different pinhole shapes. The OPD of $\pi/2$ introduced in one arm, allow us to retrieve the sign of the piston error.

We have developed a code which can simulate the MZ interferometers for a segmented mirror. The effects of atmosphere, gap, and miss-figure errors have been studied. The most important observed effect is the presence of non zero signal for zero piston error that decreases the precision of the method.

The performance of the MZ co-phasing technique has been studied. We have calculated the piston measurement error under different conditions. The size of the pinhole should be enlarged to minimise the atmospheric effects while it should be reduced to minimise the miss-figure edge effects. Taking into account these considerations, the optimal pinhole size is 1". A precision of 10nm can be achieved even in the worse case.

The influence of photon noise has also been studied. Stellar magnitudes brighter than 13 in the visible band suffice to ensure a precision better than 10nm.

Chapitre 4-Resumé

Nous avons réalisé une expérience en laboratoire pour valider la technique de co-phasage de Mach Zehnder. Cette expérience est composée de trois éléments : le simulateur de turbulence, le simulateur de segment et l'interféromètre de MZ, comme montré sur la Figure 4.1.1.

Deux approches ont été testées pour le simulateur de segment. La première consiste en cinq segments individuels hexagonaux déposés sur une plaque circulaire en zerodur. La seconde approche est une copie du télescope GTC, avec 37 segments et 4 hauteurs différentes de pistons.

Le simulateur de turbulence est le masque réflectif à phase tournante développé au GEPI (Observatoire de Paris-Meudon) pour les tests de performance de l'instrument VLT-NAOS (Nasmyth Adaptative Optics System). Le paramètre de Fried a été estimé à partir de la largeur à mi-hauteur des gaussiennes ajustées sur les PSF, mesurées à partir de 22 images de courte pose. Nous avons obtenu une valeur moyenne du paramètre de Fried r_0 égale à 64cm, avec des pics atteignant 2m.

L'implémentation expérimentale du MZ est légèrement différente de celle proposée dans la partie simulation. Une caméra est située à chaque sortie de l'interféromètre, mais des raisons techniques ne nous ont pas permis de prendre des images simultanées aux deux sorties, comme initialement prévu. Nous avons cependant été forcés d'étudier l'utilisation d'une seule sortie, en utilisant des images supplémentaires obtenues en bloquant chacun des deux bras pour normaliser les interférogrammes.

Les résultats expérimentaux sans atmosphère sont en accord avec ceux des simulations, bien que le décalage entre les fronts d'onde, la mise au point des pupilles et les effets résiduels de vignettage induisent de grosses dispersions dans les mesures des pistons les plus élevés. Les résultats avec atmosphère sont moins satisfaisants à cause des erreurs atmosphériques de « tip-tilt » et à cause d'un désalignement variable au cours du temps entre le trou et le disque du *seeing*. Cependant ces problèmes sont en cours d'étude pour améliorer l'installation du MZ pour sa future implémentation dans le démonstrateur APE (Active Phase Experiment).

Chapter 4

Laboratory test of the Mach-Zehnder co-phasing technique

We have performed a laboratory experiment to validate the MZ co-phasing technique. This experiment consists of three main elements: the turbulence simulator, the segment simulator and the MZ interferometer. A detailed description of each component is presented in this chapter.

The experimental setup is slightly different to the one proposed in chapter 3. However, the simulation code permits to implement those modifications. We show a comparison between simulated and experimental results for the cases with and without atmosphere and using the PtV criterion.

This experiment will serve as starting point for one of the module of the Active Phase Experiment (APE). This experiment is a verification bench of four new co-phasing techniques that will be directly tested on the sky (Gonte et al 2004).

4.1. Optical design for testing the MZ co-phasing technique

The experimental setup designed to verify the validity of the MZ co-phasing technique is shown in Figure 4.1.1. It is composed by three main elements: the source simulator consisting of a fiber-fed super-luminescent diode (S), a turbulence simulator (A) and a segment simulator (B), the MZ interferometer (MZ) and two detectors (D1, D2).
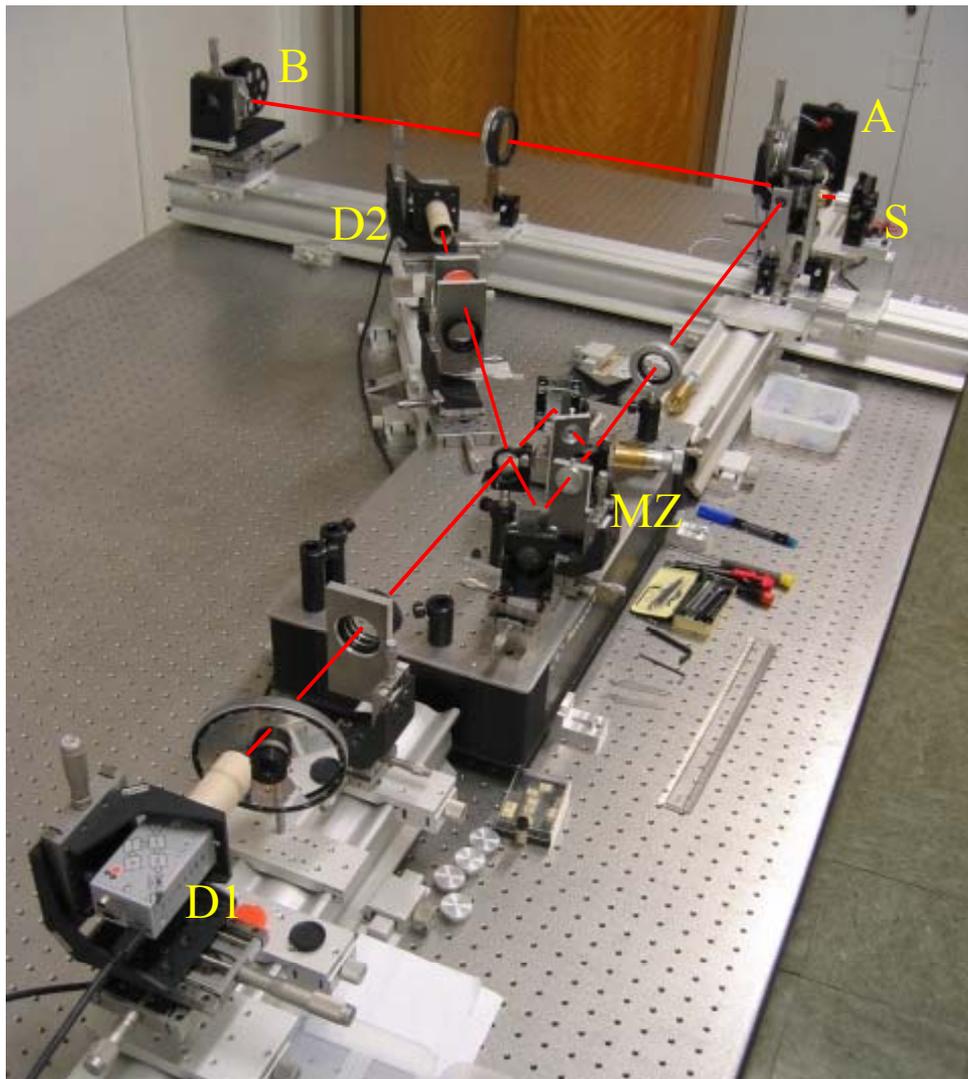

Figure 4.1.1 Photograph of the MZ co-phasing experiment.

A super luminescent diode with central wavelength of 675nm and spectral width of 10nm is used as point source. In Figure 4.1.2 we show a detailed scheme of the source device. A 3mm Lyot-stop situated in the collimated beam sets the position of the output pupil plane.

Figure 4.1.2 Scheme of the source.

The output beam coming from the source is collimated by L1 as seen in Figure 4.1.3. A pupil image of 50mm is formed on the segment simulator plane. The L1 lens has been shifted laterally so that the reflected beam coming from the segment simulator goes to the beam splitter B1. The lens L2 collimates the beam and a pupil image of 5mm is formed in the turbulence simulator. The out-coming beam is then collimated by L3 into the MZ interferometer. Lens L4 forms an image of the source in the focal plane where the pinhole is placed. The recombination of the filtered beam A, and the non-filtered beam B forms the interference pattern that would be measured with the camera.

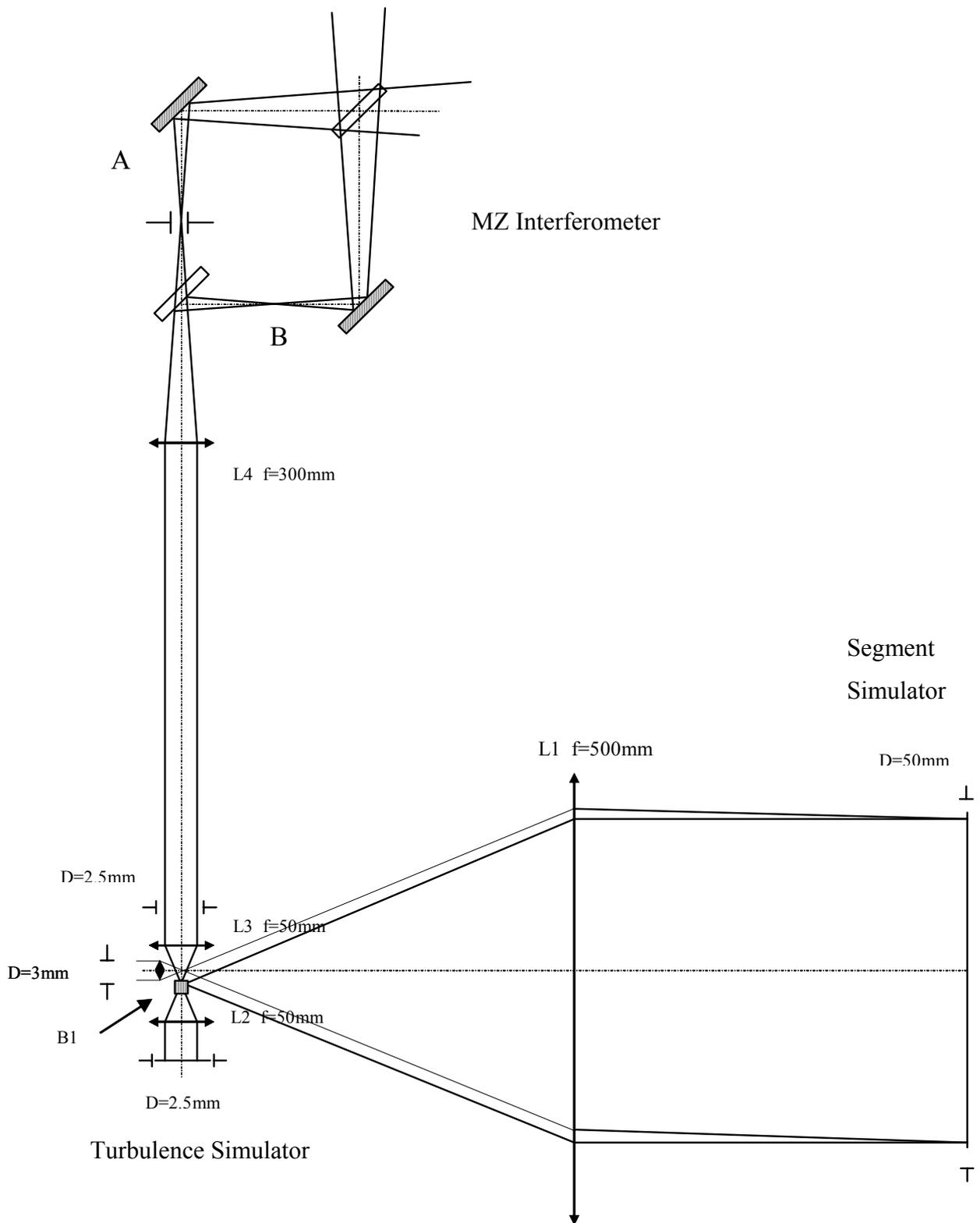Now, a brief description of each element is given next.

A

MZ Interferometer

B

L4 f=300mm

Segment

Simulator

L1 f=500mm

D=50mm

⊥

D=2.5mm

L3 f=50mm

⊥

D=3mm

⊤

B1

L2 f=50mm

D=2.5mm

⊤

Turbulence Simulator

Figure 4.1.3 Scheme of MZ experiment.

4.1.1. Segment Simulator

Our aim is to reproduce a real segmented pupil with phase step errors between segments. For this purpose the segment plates must fulfil the requirements resumed in Table 4.1.1.

Table 4.1.1 Specifications for piston plate.

Accuracy of piston step	±1.3nm
Optical quality of piston step	PtV ≤13nm
Pattern tolerance	±1μm respect to nominal position
Transition width	95% within 1μm
Surface Roughness	≤2nm
Reflectance	≤80%
Accuracy of pattern position/substrate	Centred with tolerance of 100μm
Substrate flatness	P-V ~λ/4, λ=600nm
Substrate surface roughness	≤2nm

The greatest difficulty lies on the quality specifications of the substrate due to the dimensions of the plates. We have studied two different approaches which we describe below.

GTC plate

A reproduction of the 10m class GTC telescope has been built by the Institute of Electronic Materials Technology in Poland. This simulator contains 37 segments with four different fixed heights as shown in Figure 4.1.4. The plate was manufactured using ion beam machining of Silicon wafer.
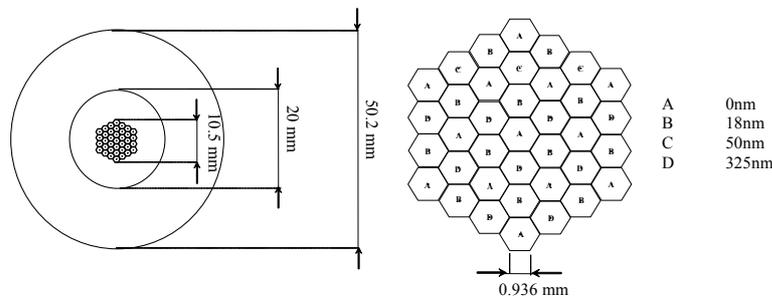

Figure 4.1.4 GTC plate dimensions.

In Figure 4.1.5 we show the interferogram of the GTC plate measured by two wavelength phase-shifting interferometry on a Michelson interferometer designed by Liotard & Zamkotsian (2004). The GTC plate fulfilled the requirements specified in Table 4.1.1.
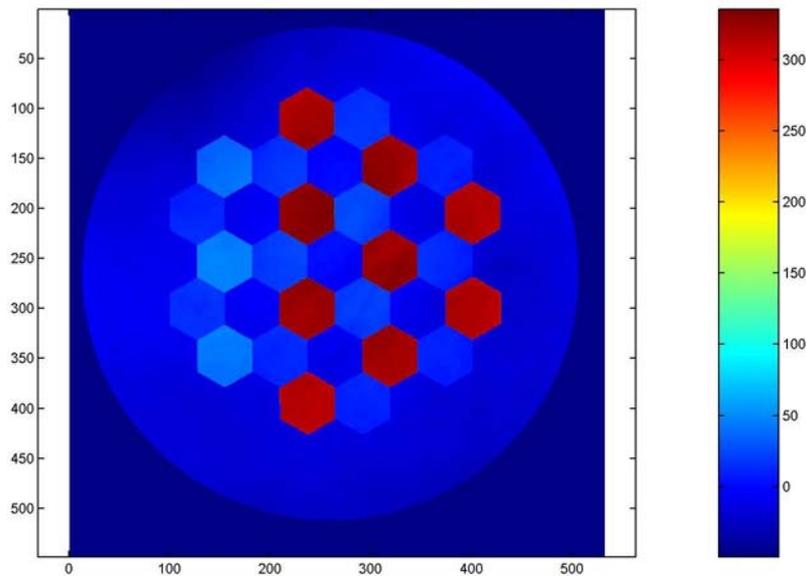

Figure 4.1.5 Interferogram of the GTC plate measured with two wavelengths.

Isolated piston plates

The second alternative explored was a mechanism of six isolated plates with fixed piston steps. For this purpose we employed zerodur substrate of 25mm diameter and 10mm thickness with a surface quality better than15 nm RMS error and 70nm PtV manufactured by Cybernetix.

The treatment of the piston steps was performed in the Department of "Galaxies, Etoiles, Physique et Instrumentation (GEPI)" at Observatoire de Paris. An hexagonal patch of certain height is deposed over each plate using microlitography methods. The flat-to-flat segment dimension is 10mm. The patch thickness of each plate are: 30nm, 75nm, 150nm, 230nm, -30nm. All plates are mounted in a wheel as shown in Figure 4.1.6 (a) that easily permits to change from one to another.

The interferometric analysis of one of the plates is shown in Figure 4.1.6 (b). The measured step corresponds to the specified piston step with a precision lower than 5nm. The observed low-order phase variations are mainly due to setup misalignment.
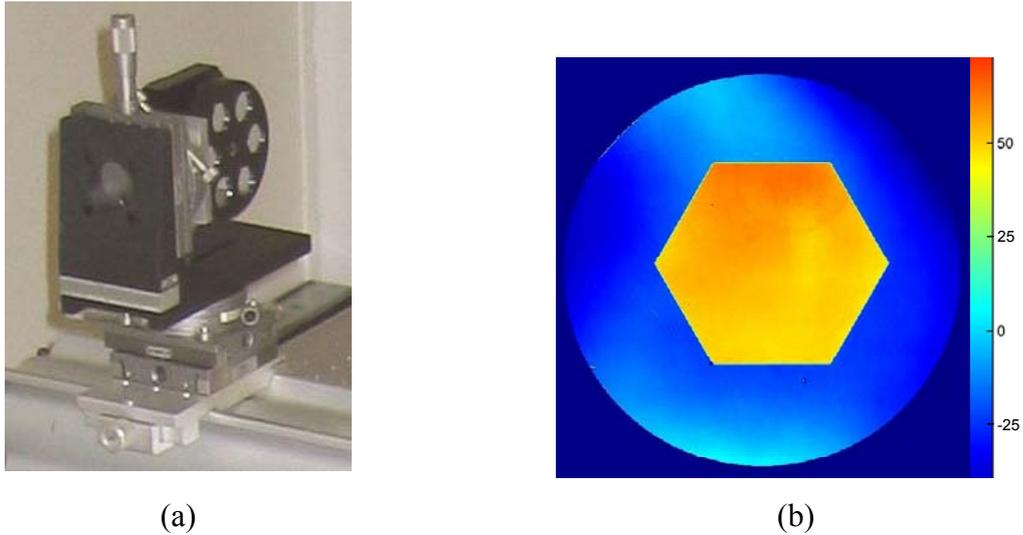
(a)	(b)

Figure 4.1.6 Segment simulator assembly (a) and the result of interferometric analysis of the 75nm segment plates (b).

4.1.2. Turbulence Simulator

The turbulence simulator shown in Figure 4.1.7 is a duplicate of the reflective rotating phase mask developed by the GEPI department for performance tests of the VLT-NAOS (Nasmyth Adaptive Optics System) instrument (Rousset et al 2003). They were produced by depositing and optically matching a resin layer on a 50 mm diameter circular BK7 substrate. The resin surface was then coated with an aluminium reflective coating. An image of the phase difference was computer simulated and imprinted on the resin (Arsenault et al 1998).
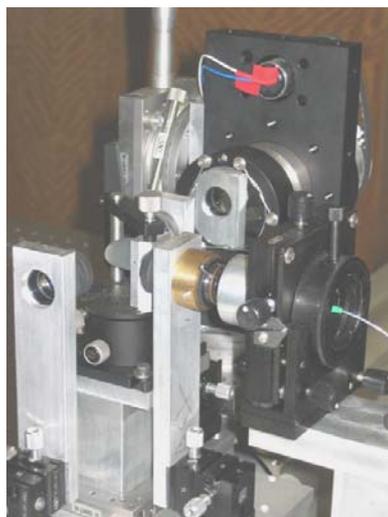

Figure 4.1.7 Turbulence Simulator.

-105-

The phase screen was designed for the VLT telescope with 8m aperture projected on 5.5 mm on the screen. In our case the isolated piston plates have 2.5 mm diameter which corresponds to an aperture of 4m instead of 8m. The characteristics of the phase screen given by the provider are quoted in Table 4.1.2.

Table 4.1.2 Phase screen specifications.

Seeing	λ	r_0	r_0 (Phase screen)	Thickness (Phase screen)
0.45"	675 nm	25.8 cm	177 μm	~700nm

The phase screen is mounted on a wheel whose speed is regulated by the voltage. The scaling of the screen is such that a typical rotational rate of 20 RPM simulates a wind speed of 64m/s. The rotating turbulence simulator allows realistic performance testing of the method. However, it was soon noticed that the simulated turbulence varied strongly as a function of angular position. This variation was quantified by calculating the Fried parameter (r_0), estimated from the FWHM of Gaussian fits to the measured PSFs, from 22 short-exposure images. Figure 4.1.8 (a) shows a histogram of the obtained values of r_0, which indicates that, instead of a typical value of 25cm the mean seeing is equal to 64cm with peaks reaching 2m.

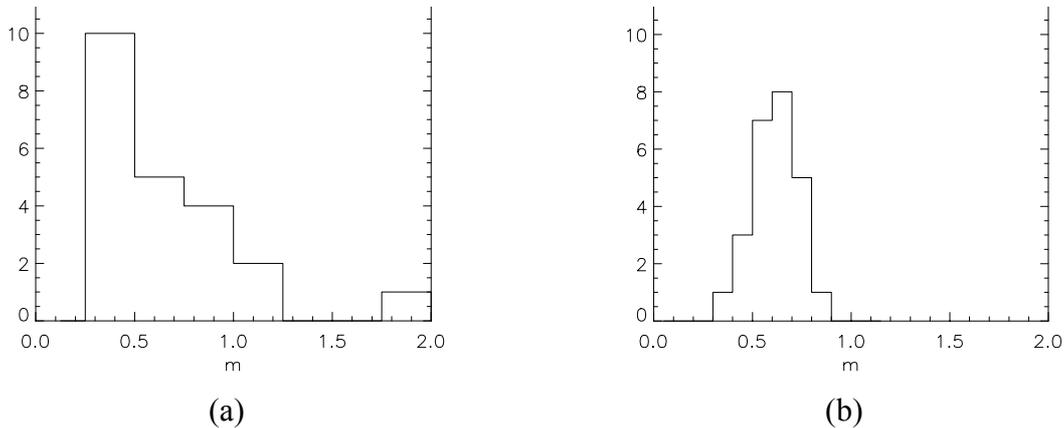(a)   (b)

Figure 4.1.8 Seeing statistics of our atmospheric turbulence generator in the case of short exposures (a) and long exposures (b).

The mean seeing level is not a serious problem, since it is just a matter of scaling between segment size and turbulence screen. However, as we will see, the strong variability of the instantaneous seeing appears to increase difficulty to the comparison between observations

and simulations. For long (1s) exposure images, representing approximately 1/3 of a screen rotation, the mean seeing was estimated to 61 cm with a standard deviation of 11cm, see Figure 4.1.8 (b).

4.1.3. Mach-Zehnder interferometer layout

The MZ interferometer layout is represented in Figure 4.1.9. It is composed by two flat mirrors M1 and M2, two beam splitters, BS1 and BS2 and two pinholes placed in the focal plane of lens L3 lens in both arms of the MZ interferometer. A camera is placed at each output of the interferometer.

The alignment procedure of the MZ interferometer is particularly tedious in this case because of romboidal dispositions of its components. Each beam splitter has two degrees of freedom, corresponding to the tip-tilt. Each mirror has three degrees of freedom: the tip-tilt and the translation along the optical axis. This total of degrees of freedom makes difficult an accurate alignment.
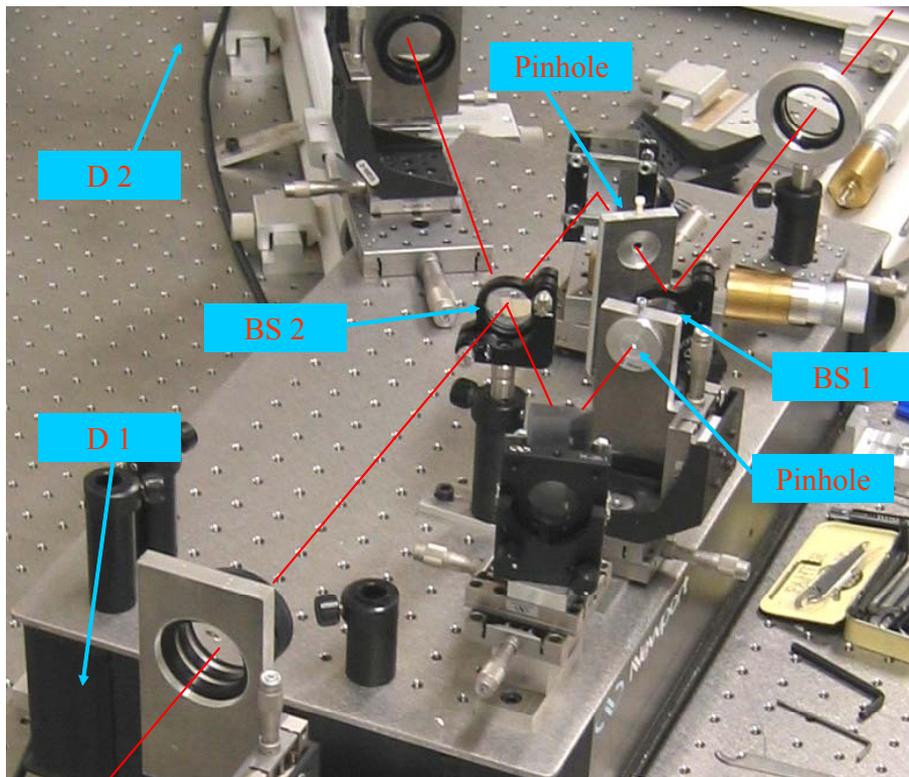

Figure 4.1.9 MZ interferometer layout.

Several pinhole sizes have been tested in order to compare experiment and theory. The size of one of the pinholes has been chosen so that the high frequencies of atmosphere turbulence are filtered. The aperture beam was chosen with a high F number to ensure a feasible pinhole size. The main inconvenient of such low beams is the vignetting of the optical elements. Figure 4.1.10 shows an image of a highly saturated at the output of the interferometer. The diffraction arms due to the hexagonal patch are clearly seen, stretching out in six directions as expected. The two arms stretching out to the right are vignetted. Although this effect has been reduced to some extent, some residual vignetting is still present. In order to limit this asymmetry of the pupil image, a second, much larger pinhole is introduced in the second arm. This way we obtain circularly symmetrical vignetting (indicated in yellow in the Figure 4.1.10). While this has the additional effect of avoiding the sharp features of the MZ signal at the segment edge, it also reduces the peak signal values, and the effect must be included in the simulations in order to produce comparable results.
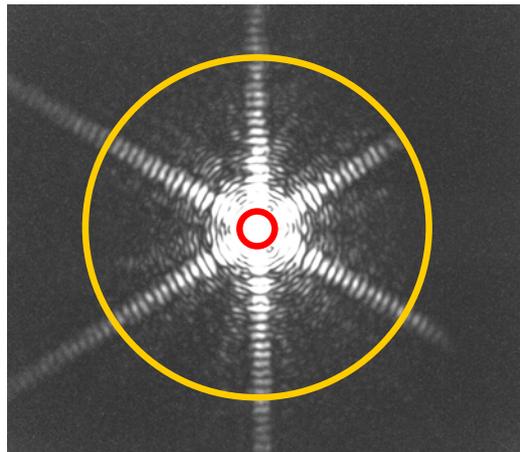

Figure 4.1.10 PSF at the focal plane formed by a segment plate.

Two 1kx1k CMOSs (PixeLINK PL-741 model) are placed at both outputs of the interferometer. The particular design of this interferometer allows us to measure in the detectors either the interferograms or the PSF.

4.2. Analysis of the experimental results

The implementation of this MZ is slightly different to the one proposed in chapter 3. A camera is located at each output of the interferometer. Technical restrictions do not allowed to take simultaneous images at the two outputs, as it was planned. We were therefore forced to investigate the use of a single output (I), using supplementary images (I_1 and I_2) obtained by blocking in turn each of the two arms in order to normalise the interferograms. The normalised signal, $\overline{S}$, is directly deduced from (3.2), and it is given by

$$\overline{S} = \frac{I_A - (I_1 + I_2)}{\sqrt{I_1 I_2}} \tag{4.1}$$

where I_A is the intensity of the output interferogram, I_1 and I_2 are the intensities of the each blocked arm. This procedure, as illustrated in Figure 4.2.1, works very well, and although it is less efficient in terms of throughput, in practice, its implementation may turn out to be easier than that of the dual-output version.
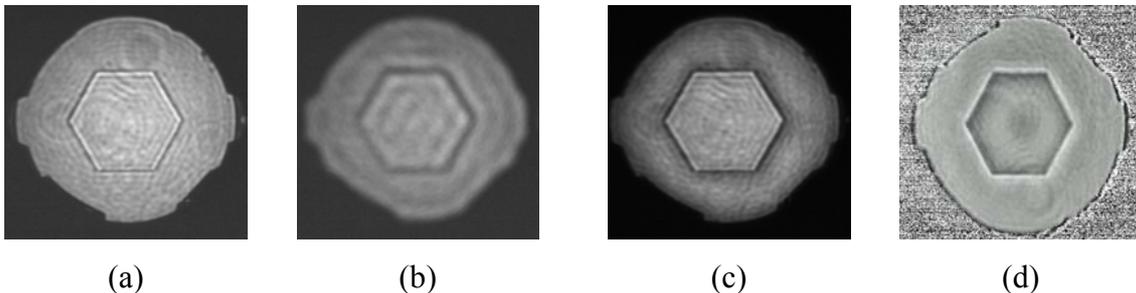

(a)   (b)   (c)   (d)

Figure 4.2.1 Measured Intensity distribution of a: arm 1 I_1; b: arm 2 I_2, c: output interferogram I_A, d: normalised interfrogram $\overline{S}$.

The mono-dimensional profile is obtained from the mean of normalised signal profiles perpendicular to horizontal edges.

Apart from the proper difficulties of aligning the MZ interferometer (tilts and shear) and the location of the zero optical path difference (OPD), the most delicate operation is the fine OPD adjustment. In order to recover the sign of piston steps, the phase difference between the two interfering wavefronts must be equal to $\pi/2$, corresponding to a mirror displacement of 80nm at 630nm. To achieve such extremely fine adjustments, one of the mirrors of the interferometer is mounted on a stage equipped with a differential micrometer screw whose

axis is nearly parallel to the mirror surface. This provides a 150-times reduction in the axial mirror movement, corresponding to a displacement of 6.5nm per 1μm micrometer graduation. Thermal stability and air movements also become important in this context, and although ad-hoc measures were taken to limit air fluctuations within the interferometer, this demonstration experiment does not provide the nanometric stability required for an operational instrument.
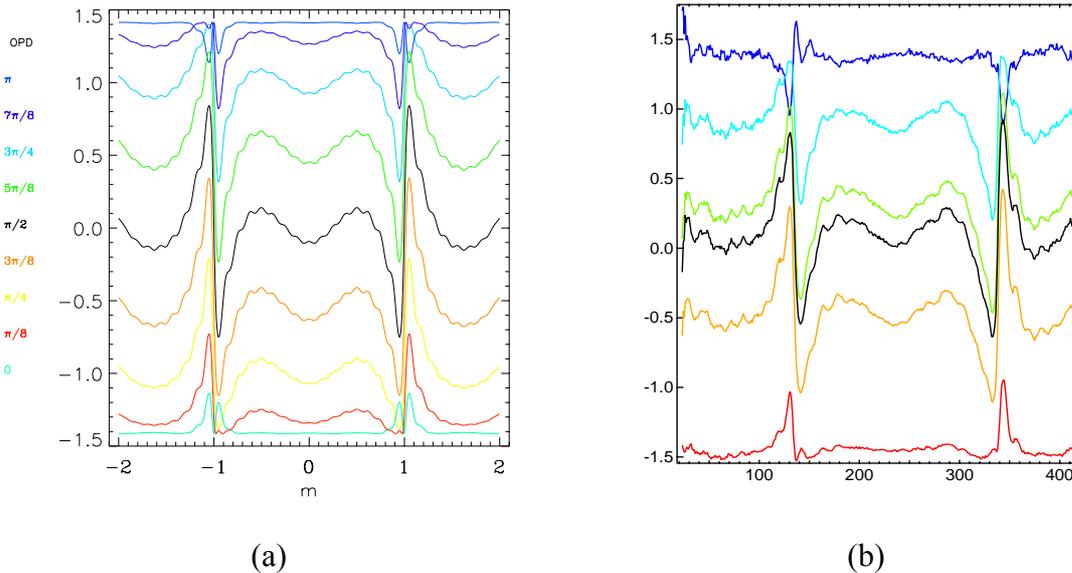

(a)   (b)

Figure 4.2.2 Simulated (a) and Experimental (b) normalised profiles for different OPD adjustments using a piston step of 75nm.

In Figure 4.2.2 we have plotted the simulated normalised profiles obtained for different OPD values (a), compared with the experimental ones (b), for the a piston step plate of 75nm with a pinhole of 1mm (0.85" projected into the sky). Plotting the PtV of the signal against OPD (see Figure 4.2.3, solid line) shows that its variation is slow close to $\pi/2$; the error is less than 10% for OPD values within $\pm\pi/8$. Besides, deviations from the optimal OPD are nearly proportional to the mean signal level (Figure 4.2.3, dashed line), allowing corrections of the signal amplitude within a wide range of OPDs. A procedure for OPD adjustment based on real-time display of the average image intensity has been devised and proven to give good results.
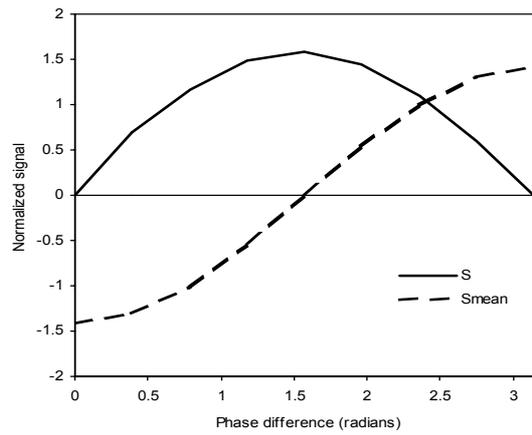
Figure 4.2.3 Plot of PtV signal (solid line) and mean signal level (dashed line) against OPD.

We have studied the behaviour of the normalised signal with different pinhole sizes. As expected, the signal becomes narrower when the pinhole size increases, but opposite to the case of one pinhole configuration, the PtV of the signal decreases with the pinhole size. This is due to the effect of the large pinhole placed in the other arm of the interferometer.
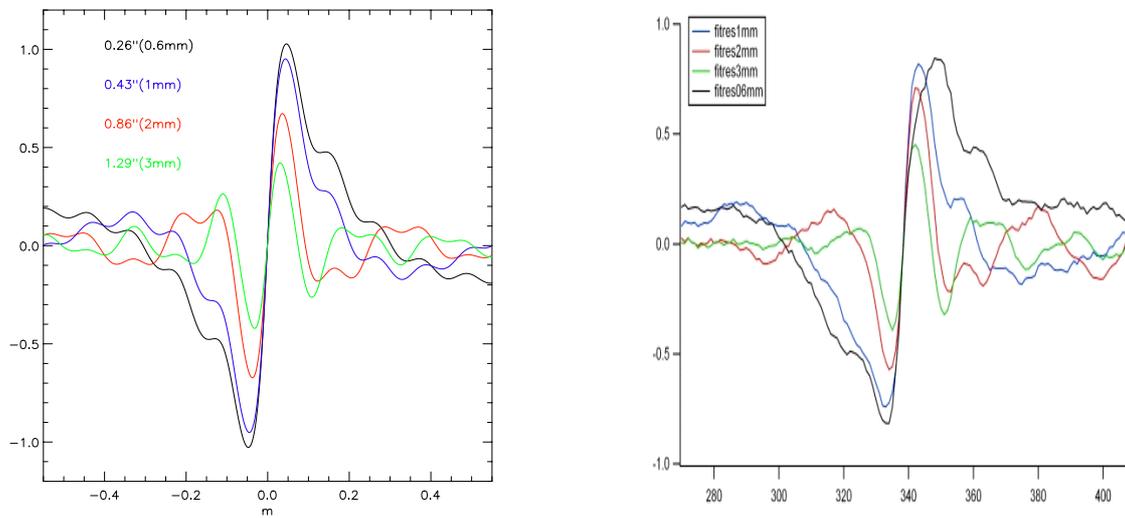

Figure 4.2.4 Normalised signal for different pinhole size for piston 75nm without atmospheric turbulence.

The results presented in Figure 4.2.4. have been obtained with a large pinhole of 6mm which is equivalent to 5.2" projected into the sky. If the size of the small pinhole approaches to the size of the large one, both arms are equally filtered and thus the amplitude decreases reaching the zero value when both pinholes are identical.

When atmospheric errors are included, we observe the same tendency as in the case of one pinhole configuration. The PtV of the signal for small pinholes is much smaller when atmosphere is considered than in the ideal case. This is due to the fact that the pinhole is not large enough to filter atmosphere. However, for larger pinholes the PtV is quasi identical to the ideal case.

We obtained from simulations that the optimal pinhole is twice the size of the seeing disk. This conclusion is in agreement with the results obtained in the experiment, since the best pinhole is the 1mm one, which is twice the seeing disk (0.529mm).

4.2.1. Performance without atmosphere

We have measured the five segments without atmosphere and we have compared the results with the simulated data. The measurements have been taken for the upper and lower borders of the segment for two OPDs of $\pm\lambda/4$.
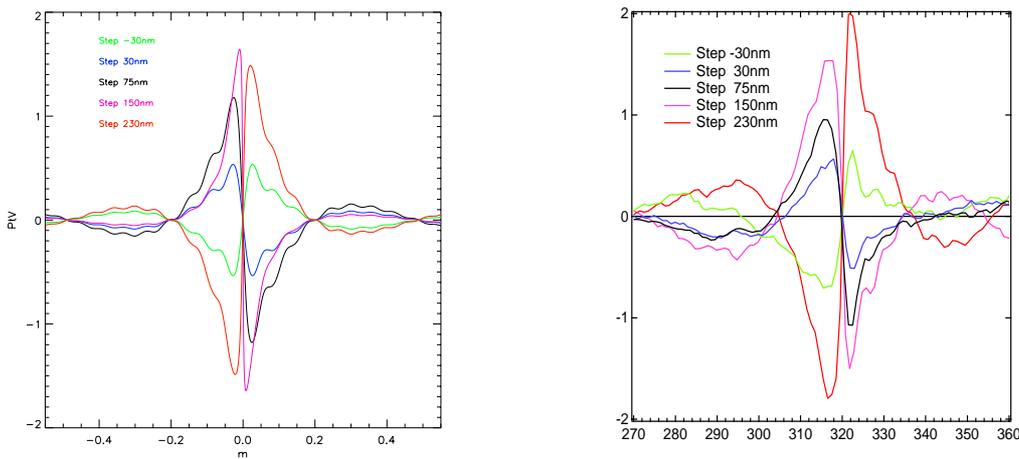

Figure 4.2.5 Simulated (left) and experimental (right) signal profiles for one border of each segment without atmosphere.

In Figure 4.2.5 simulated (left) and measured (right) signal profiles near a segment border are compared in the absence of atmospheric turbulence for each of the five piston plates. Experimentally, this configuration is obtained by replacing the turbulence simulator by a flat mirror. We confirm a good agreement between simulated and experimental results. We appreciate a singularity for the simulated case when the wavefront piston step is close to $\lambda/2$ (that is, 150nm in the surface). This is obtained from dividing the difference between the two

outputs by the sum of them. In the experimental data this sharp profile is smoothed because the signal is sampled and the pixels have a certain size as explained before. The modulation of the signal wings is due to an aliasing effect.

While the correspondence is good for small piston values, the signals of the two larger steps are somewhat different. Figure 4.2.6 gives a more quantitative analysis of these results, representing the average PtV values for each piston step (symbols) and comparing them with the theoretical expectation (solid line).

Two series of 10 images are taken, and a vertical profile containing two steps (Edge 1 and Edge 2) is extracted from each image. From the vertical profile, PtV values are measured and then averaged. Vertical error bars indicate standard deviations. The first serie is taken with an OPD adjusted to $+\pi/2$, for the second serie the OPD is adjusted to $-\pi/2$. Good correspondence for the three smallest piston values is confirmed, as well as the curious behaviour for larger piston steps. Changing the OPD hardly influences on the results. This indicates that the reproducibility of the OPD adjustment procedure is sufficient, although the difference between the two segment edges is large.
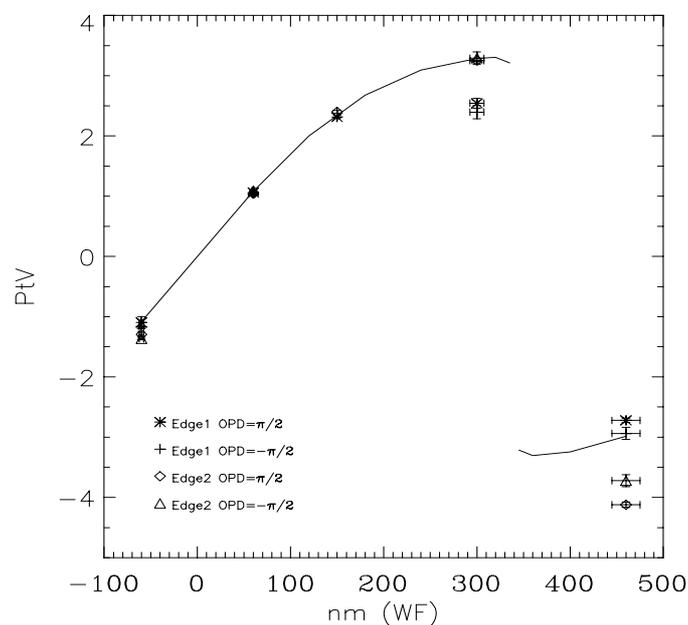

Figure 4.2.6 Comparison of the amplitude of the signal between experimental data (points) and simulated data (solid line).

This effect has not yet been understood, but the contributing factors are thought to include, shearing, pupil focus, and residual vignetting effects. A shearing between the two arms of the

interferometers is represented in Figure 4.2.7. The contour of the image of the filter arm with the smaller pinhole is superposed to the image of the filtered arm with the larger hole. It can be noticed that the contour is not well aligned to the image. This results in an asymmetry on the normalised signal profile with respect to the edge of the segment as can be appreciated in the plot of the profile.
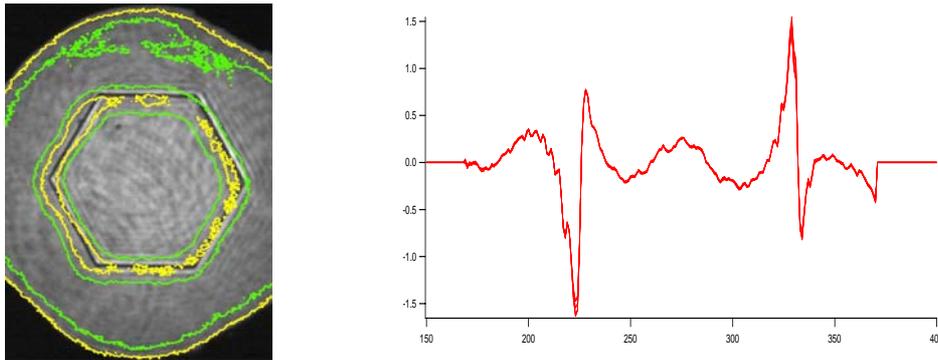

Figure 4.2.7 Shearing between the two arms of the interferometer and the resulting profile of the normalized signal.

Misalignments in the optical bench, either because the PSF is not well centered on the pinholes, or because of vignetting, produce asymmetries in the intensity distribution of the whole interferogram. In Figure 4.2.8 we show the interferogram and the normalised profile along the vertical axis. The borders are not equally illuminated, this asymmetry leads to a difference of amplitude on the normalised profile between both edges.
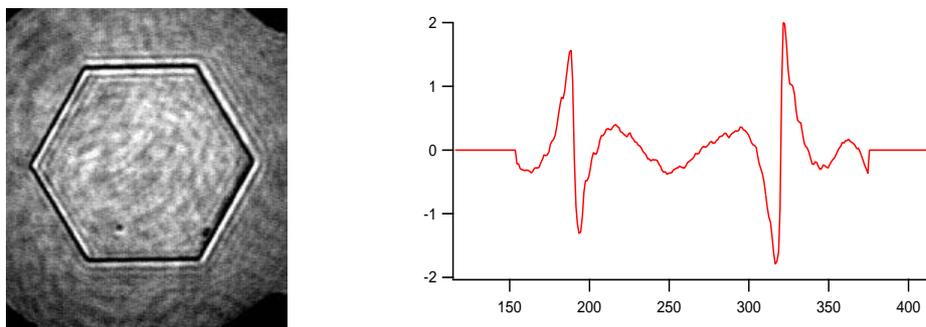

Figure 4.2.8 MZ interferogram if residual vignetting are presents and the resulting normalised profile.

We have also performed the measurement for the standard MZ signal as defined in section 3.2.1, which are:

$$S = \frac{I_A - I_B}{I_A + I_B} \qquad (4.2)$$

where I_A and I_B are the interferograms at both outputs of the interometer. It should be noticed that the signal is normalized with the sum of both interfergrams. The signal S has been obtained from one output using two complementary OPDs.

In Figure 4.2.9 we compare the PtV of the experimental and simulated signal profiles. The precision on the OPD setting is not accurate, thus both outputs are not exactly recorded with complementary OPDs. This fact leads to a new measurement error apart from the error sources already mentioned.
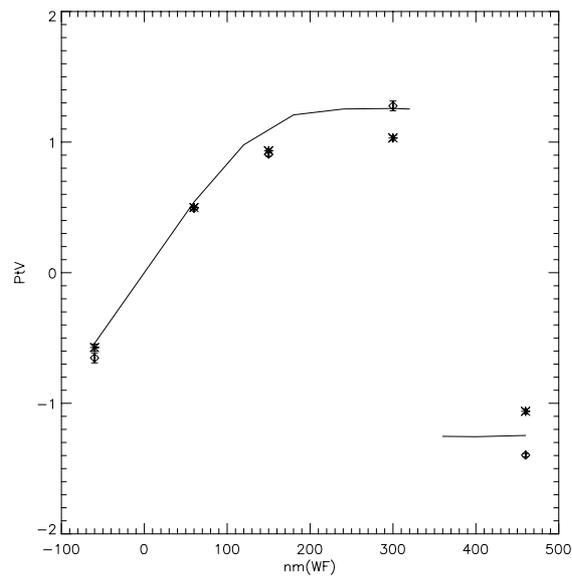

Figure 4.2.9 Comparison of the amplitude of the standard MZ signal between experimental data (points) and simulated data (line).

4.2.2. Performance with atmosphere

Figure 4.2.10 compares simulations obtained using r_0=61cm with 1-second exposure images. A qualitative comparison indicates a very good correspondence between both. A more quantitative analysis, representing the same experimental cases as in Figure 4.2.10 and simulated performance for four different seeing conditions, gives a more complex picture (Figure 4.2.11). Compared with the measurements without seeing, results for small piston

values have much larger variability and are generally below the expected values. A better fit is obtained for the two largest piston steps, but only at the cost of even larger variability.

(a)   (b)
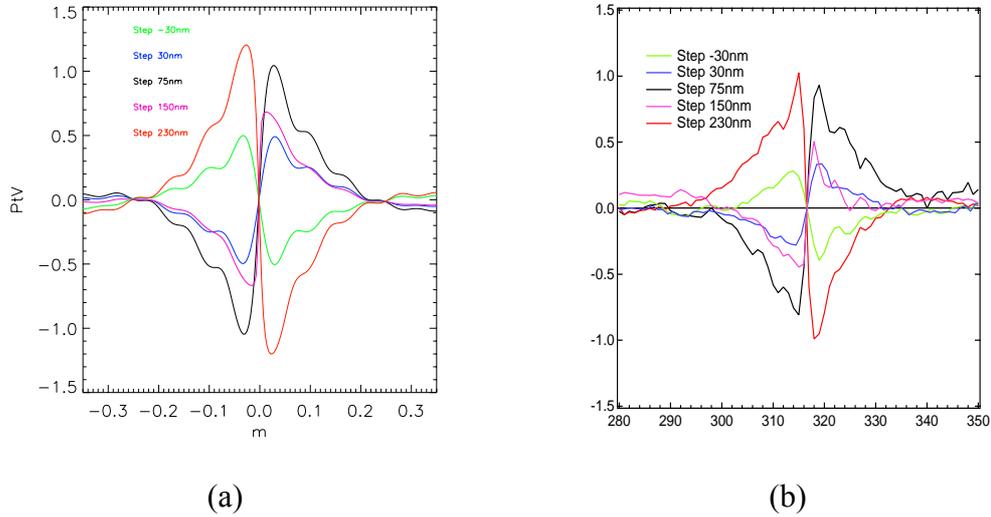
Figure 4.2.10 Simulated (a) and experimental (b) signal profiles for one border of each segment with atmosphere.
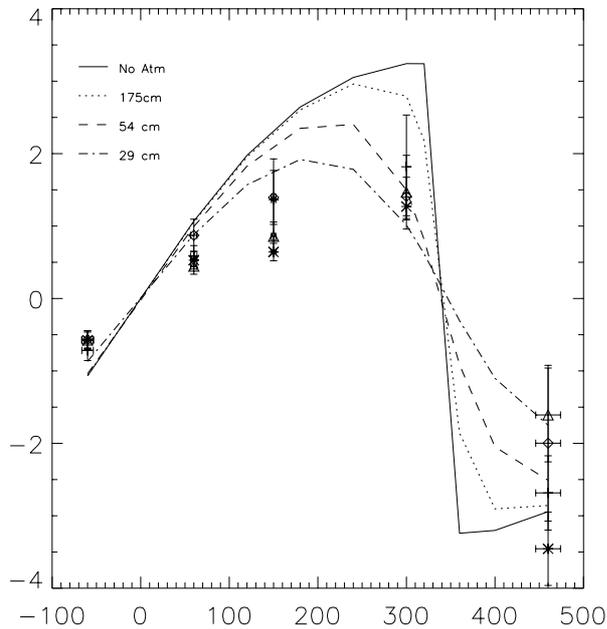

Figure 4.2.11 Comparison of the averaged experimental PtV signal amplitude (symbols) with simulated data (lines) for different atmospheric conditions (c).

In addition to the problems mentioned above for the case without turbulence, it seems that the problems encountered here may be due to the large variability of instantaneous seeing conditions. While simulations are made using a sequence of 1000 independent phase screens, each of them created using identical turbulence statistics, 1-second exposures with our turbulence simulator corresponds to some 120 independent phase screens with largely different statistics (Figure 4.1.8-(a)). As observed from the simulated curves in Figure 4.2.11, the turbulence statistics has great influence on the signal PtV, especially for large piston steps.

Another error source is related to the atmospheric tip-tilt error, causing time-variable misalignment between the pinhole and the seeing disk. Problematic in itself, this effect is aggravated by the fact that the three images used to construct the MZ signal are not taken simultaneously. Although the effect should be reduced by increasing the exposure time, it may be interesting to consider the use of a real-time tip tilt corrector in a practical implementation of this concept.

4.3. Summary

In this chapter we have presented the description of the MZ setup developed in our Laboratory. Two segment simulators have been proposed. The first approach is a set of five single hexagonal segments, and the second approach is a copy of the GTC telescope with 5 piston steps distributed in the 37 segments.

The first results have been obtained using a single output instead of the difference between the two outputs of the interferometer. Good agreement is obtained between simulated and experimental data for the case without atmosphere. However, vignettting, pupil defocus, shearing and misalignment of the systems leads to asymmetries and diminish the signal amplitude, thus provoking measurement errors. In the case with atmosphere, there is a great standard deviation This is due to misalignments between the pinhole and the seeing disk caused by the variability of atmosphere.

The work presented here is just a preliminary approach. The GTC plate should be tested. The resulting performance by using both outputs simultaneously, as well as the verification of the integral criterion compared to the PtV one, have to be studied in order to retrieve the step errors.

Chapitre 5-Resumé

Dans le cadre du réseau de recherche et de formation « Optique Adaptative pour les très grands télescopes », l'évaluation des performances de quatre techniques de co-phasage a été réalisée. Quatre instituts ont contribué au développement de ce travail. Cette étude a non seulement compris l'évaluation des performances des techniques pour un télescope de la classe des 100m mais également la description et la mise au point expérimentale de chacune des techniques.

Les techniques comprises dans ce projet sont :

1. La technique de Chanan, travail réalisé en collaboration entre le GTC (Espagne) et le LAM(France).
2. La technique de courbure, travail entrepris également par le GTC et LAM.
3. La technique de Mach-Zehnder, travail réalisé par l'ESO (Allemagne) et le LAM.
4. La technique en pyramide, travail réalisé par le GTC et l'INAF (Italie).

Dans la comparaison des quatre techniques, nous avons considéré les performances en termes de précision et de domaine de validité, la sensibilité aux différentes sources d'erreurs ainsi que la complexité de fabrication. Le traitement du signal pour récupérer les erreurs de piston est essentiellement le même pour les quatre techniques. Cependant, la réponse en fonction du niveau du piston est différente ; la méthode de Chanan a une réponse linéaire alors que les autres techniques ont une réponse sinusoïdale réduisant le domaine de validité en lumière monochromatique. Dans tous les cas, les effets de l'atmosphère et des erreurs de bords rabattus peuvent être réduits en optimisant les paramètres expérimentaux. La précision finale atteinte dans tous les cas est de l'ordre de 10 nm. Nous montrons également que ces techniques ne sont pas limitées par le bruit de photons.

Il n'y a pas de contrainte majeure pour la réalisation à l'exception de la méthode de Chanan pour laquelle la fabrication et l'alignement du réseau de lentilles pour un ELT pourrait présenter certaines difficultés. Une autre limitation de cette technique est l'impossibilité de découpler les signaux quand plus d'un miroir de télescope est segmenté, comme ce sera le cas pour OWL.

Chapter 5

Comparison of co-phasing techniques

Within the frame of the Research and Training Network "Adaptive Optics for Extremely Large Telescopes", four co-phasing techniques have been compared. Four institutes have contributed to the development of this work. The studies have involved the performance of each technique for a 100-m class telescope as well as the description and experimental demonstration of each technique.

These four techniques are;

1. Chanan technique, work carried out in collaboration between Gran Telescopio Canarias (Spain GTC), and Laboratoire d'Astrophysique de Marseille (France LAM).

2. Curvature technique, work carried out by GTC and LAM.

3. MZ technique, work performed by the European South Observatory, (Germany ESO) and LAM.

4. Pyramid technique, work carried out by GTC and Instituto Nazionale di Astrofisica, (Italy INAF).

This chapter intends to present the main results of simulations for the Chanan, Curvature and MZ techniques. We describe their advantages and drawbacks with respect to several aspects of the co-phasing process: signal characterisation, piston retrieval, practical and manufacturing issue and the technique applied to the case of multiple segmented mirror telescopes, such OWL, which is designed with the primary and secondary segmented mirrors.

5.1. Signal Characterisation

In chapter 2, we have reviewed the basic principles of the co-phasing techniques. The simulation of the signal for the Chanan technique is essentially different than for the others. In the Chanan technique, the subaperture and lenslet combination (one or more per segment boundary) are physically independent. It is thus possible to individually simulate the Chanan signal for each subaperture, allowing the simulation of segmented mirrors with a virtually unlimited number of segments. In the case of the other techniques under consideration, the complete pupil has to be processed at once.

Two main reasons led us to use 1-D simulations across the single segment border. First, because the 1-D simulations can be performed with a higher resolution, thus a better understanding of the signal behaviour is possible. Second, because the available memory of the computer system will limit the size of the 2-D mirror that can be simulated.

The profile of the signal perpendicular to the edge of the segment for each method is represented in Figure 5.1.1. We appreciate a similitude between the signals obtained from Curvature and MZ. They all have an anti-symmetrical profile with respect to the segment edge.
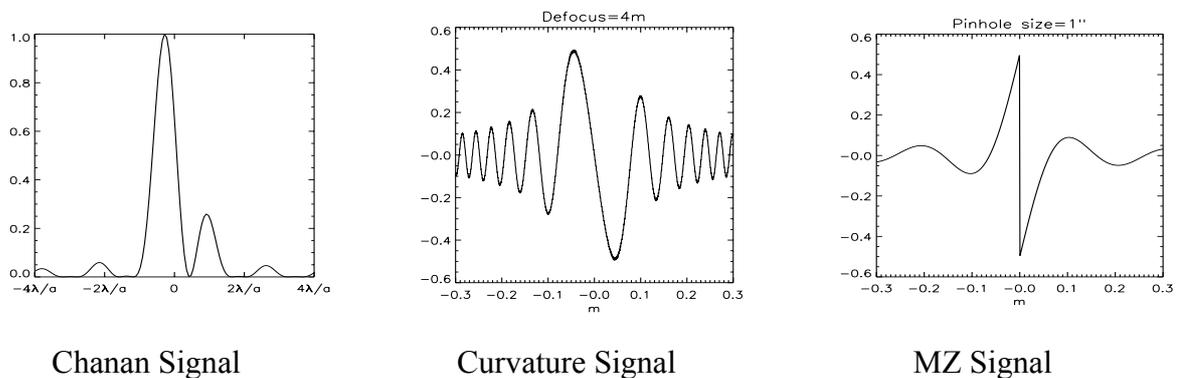

| Chanan Signal | Curvature Signal | MZ Signal |

Figure 5.1.1 Signals obtained with different techniques, when only piston error of $\lambda/4$ on the wavefront (λ=500nm) is included.

The width and amplitude of the signal vary as a function of a setup parameter characteristic of each technique. For the Chanan technique, this parameter is the size of the subaperture, for the Curvature sensor it is the defocus distance and for the MZ it is the pinhole size.

As a basic requirement, the signal width for the case of Curvature and MZ should fulfil the localisation condition in order to avoid overlapping of signals from opposite segment borders. The localisation condition is fulfilled if the signal width is much less than the segment size. For the Curvature technique the signal width is defined as the FWHM of one main peak of the signal. It can be expressed (Rodriguez-Gonzalez & Fuensalida 2003) as,

$$\rho = \sqrt{\frac{\lambda \Delta z}{2}} \tag{5.1}$$

where Δz is the defocus pupil distance. For the MZ case, the width of the signal is given by expressions (3.18) and (3.19). In both cases the width of the signal is a function of the wavelength and setup parameter.

The optimum of this parameter depends on the atmospheric conditions, segment errors and segment size.

5.1.1. Sensibility to atmosphere, gaps and edge defects

One of the most important characteristics of any co-phasing technique is the ability to minimise errors introduced by turbulence or segment edge miss-figures.

To this respect the Chanan technique is the most efficient. An aperture with size smaller than the Fried parameter avoids atmospheric effects and —masking the segment edges— eliminates the effects of miss-figure errors.

In the case of the Curvature method the effect of atmosphere could be controlled by the defocused distance. The sensitivity to seeing is larger for small wavelengths and large widths, ρ. Therefore the signal width should be smaller than r_0 to guarantee a good performance. Schumacher & Devaney (2004) found that to minimise the edge miss-figure effect the width ρ should be larger than 18 times the edge width. This means that under seeing conditions of r_0=10cm, total edge width larger than 10 mm will start to degrade the performance of this method.

For the MZ case, the pinhole size should be at least of the size of the seeing disk. After the analysis presented in chapter 3, the atmospheric errors are minimised by increasing the pinhole size, while effects of gaps and edge defects are minimised by decreasing the pinhole size. It has been found that an optimal pinhole diameter of twice the size of the seeing disk ensures good performance for edge widths smaller than 10mm.

It is interesting to notice the similitude between Curvature and MZ techniques. In both cases the effect of the atmosphere is minimised by decreasing the signal width and the effect of edge are minimised by increasing the signal width.

5.2. Piston Retrieval

The algorithms employed to retrieve the piston error between adjacent segments is based on the relation between a characteristic value of the signal and the piston error. This characteristic value can be either the peak difference or the difference of the integrals of the signal between the edge and the first zero at both sides of the edge.

For Curvature and MZ techniques the piston error is a periodical function of the characteristic value with a periodicity of λ. In the case of the Chanan technique the characteristic value is a polynomial of third degree.

Sinusoidal calibration curves have two disadvantages. Firstly, the sinusoidal calibration curves are steep close to 0 and $\lambda/2$, but flat close to $\pm\lambda/4$. Therefore measurement errors will have a small effect on the steep region, but significantly higher effects on the flat region. For this reason an iterative process ensures the required end-precision. The second disadvantage is that the range is limited to $[-\lambda/4, +\lambda/4]$ which is half the range for linear calibration curves. For the case of Curvature this ambiguity is solved by analysing the intra and extra focus image independently. In the MZ case, this information can be obtained by analysing the two outputs separately or by shifting the pinhole (Yaitskova 2003). The range can also be increased by redefining the MZ signal as it has been pointed in chapter 4.

5.2.1. Precision, Capture Range and limiting magnitude

A co-phasing technique should be able to reach an end-precision of the order of few tens of nm. On the other hand the required capture range is of the order of tens of microns. As already discussed in section 3.4.7, the capture range is limited by the wavelength. It can be increased by making use of multi-wavelength algorithms, in which measurements taken at different wavelengths are used to solve the λ ambiguity. We have discussed in 3.4.7 that to guarantee an unambiguous solution, the sum of the measurement error at both wavelengths should be less than the difference of the measured piston steps at each wavelength. Multi-wavelength algorithms work better for linear calibration curves because measurement errors do not depend on the piston step, while for sinusoidal calibration functions the piston error is not fixed, with a maximum close to $\lambda/4$ and minima in the linear region. In this case, the π-ambiguity inherent to sinusoidal calibration curves should be resolved before applying the multi-wavelength algorithm. Even if the π-ambiguity is resolved, the multi-wavelength

algorithm gives a higher range in the case of linear calibration curves compared with sinusoidal ones, since the disturbances close to $\lambda/4$ result in high measurement errors. It should be noticed that these errors cannot be reduced iteratively, because the multi-wavelength algorithm is part of each iteration step. To obtain the same capture range as in a linear case, measurements at more than two wavelengths should be performed.

In Table 5.2.1 we resume the precision of these measurements within the range limited by the wavelength, the end precision after the iteration process and the capture range obtained from simulations for each technique. The simulations were performed including atmospheric errors, but rejecting effects due to edge and gaps. The effect of edge has been deeply studied in this work for the case of MZ, and elsewhere for the case of Curvature (Schumacher & Devaney 2004) and Chanan (Bello-Figueroa 2001). The simulations were run using the optimal setup parameters discussed in the previous section.

Table 5.2.1 Precision and capture range simulated for different techniques, with atmospheric errors, without gaps and edge defects.

	Chanan	*Curvature*	*MZ*
First iteration single wavelength precision	5nm	150nm	60nm
Close loop single wavelength precision	4nm	~8nm	~5nm
Capture Range	±2μm(2-λ) ±200μm(3-λ)	±10μm(3-λ)	±10μm(3-λ)

From the results presented in Table 5.2.1 we conclude that the required precision to co-phase two adjacent segments, is achieved with all techniques. The Chanan technique has two advantages wit regard to the other methods: larger capture range — although ten micron should be enough to co-phase segmented mirrors— and achievement of the required precision in absence of an iteration process.

The precision of these co-phasing techniques will also be limited by photon noise. These co-phasing techniques will use natural sources. The limiting stellar magnitude required to ensure a certain precision is calculated following the reasoning presented in 3.5.4. The same result is found for all the techniques, because the collecting area is similar for every case. To ensure a precision of 10 nm with 1minute exposure time, stars brighter than 13 magnitude in the visible are required. In section 3.5.4 we have calculated the FOV required for ensuring

90% sky coverage for this limiting star magnitude. This FOV of 10 arcmin is comparable with the technical FOV of ELTs, thus none of these co-phasing techniques is limited by the photon noise.

5.2.2. APE the Active Phase Experiment

The essential purpose of the APE (Gonte et al 2004) experiment is to explore, integrate and validate non-adaptive wavefront control schemes and technologies for an ELT. This includes: i) Evaluating and comparing the performance of phasing wavefront sensors, in the laboratory and on-sky; ii) Integrating segmented aperture control into an active system, and driving both the active system and the segments control system from the output of the system.

To this end, APE is conceived as a technical instrument to be eventually installed and tested on-sky at a Nasmyth focus of a VLT unit telescope, the telescope providing all active functions and the APE instrument emulating the optical effect of segmentation.

In practice, (Figure 5.2.1), this will be realized by re-imaging the telescope pupil onto a small segmented mirror, and by directing the output beam(s) of the instrument towards a metrology module. This metrology module will include the three phasing wavefront sensors, i.e., Curvatrure, Pyramid and MZ and optionally, a conventional Shack-Hartmann sensor.
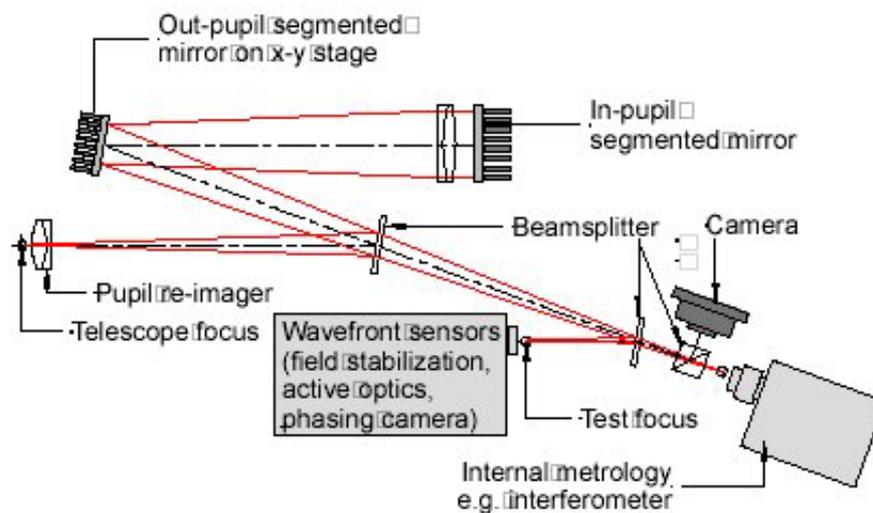

Figure 5.2.1 Schematical layout of the APE test bench (Diericks et al 2003)

5.3. Practical and Manufacturing considerations

In principle with the current technology there is no manufacture limitation for any of the co-phasing sensors considered here. However the Chanan technique has a drawback with respect to the complex manufacture of the lenslet, which increases with the number of segments. For example, in the case of OWL, there are 64 segments along the longest axis which corresponds to 126 subapertures.

Another important aspect is the alignment complexity. In the Chanan technique the alignment of the lenslet to the image of the primary mirror should be at least better than the gap between segments. An alignment accuracy of 1mm in the primary corresponds to 0.6μm in the alignment of the lenslet array.

The alignment between the defocused images in the case of Curvature —or between the interferograms in the case of MZ— requires sub-pixel precision since the signal width is very narrow. However, this alignment can be achieved by interpolation algorithms.

The MZ interferometer must be implemented as a monoblock configuration in order to avoid pinhole misalignment and to maintain the components stability. The OPD should be implemented in such a way that the MZ signal profile variation at different wavelengths remains minimal.

Another fact to be considered is the detector size. For the Chanan technique the FOV of each diffracted image must be at least five times larger than the RMS (σ) motion due to seeing to avoid overlapping. The variance of image motion in units of arcsec² (Roddier 1999) is,

$$\sigma^2 = 0.348 \left(\lambda / d \right)^{1/3} \left(\lambda / r_0 \right)^{5/3} \tag{5.2}$$

where λ/r_0 is the seeing in arcsec and d is the subaperture size. Assuming a wavelength of 650nm, a rectangular size of the subaperture equal to 12cm, 65 diffracted images in one direction, and a pixel scale of 0.2arcsec, then a 1K detector is enough if the seeing conditions are not worse than 0.9arcsec. This does not imply a manufacturing problem for the current technology.

The detector size for the Curvature method must be able to record the pupil image with enough resolution. The resolution should be better than two pixels per r_0 and at least four pixels per signal width. This means that the detector size should fulfil the following condition:

$$N > 4\frac{D}{\rho} \qquad\qquad (5.3)$$

where N is the number of pixels across the pupil, D is the pupil diameter, ρ is the Curvature signal width. For OWL, with a primary of 100m, assuming λ=500nm, f=300m and a defocus distance of 1m, at least a 4K detector is required.

For MZ technique the same reasoning as in the precedent case can be followed. The detector size should be larger than $Da\pi/\lambda$, where a is the pinhole size, D is the pupil diameter and λ is the wavelength. For a pinhole of 1" and considering the same parameters as before, a 4k detector is required to ensure enough resolution.

The ELT generation will introduce new technical challenges and will give rise to novel questions. In particular this is the case for telescope design projects with more than one segmented mirror. Until now co-phasing techniques have been applied to a single segmented mirror. If there is more than one segmented mirror, the signals of both mirrors will be present in the sensor images, as shown in Figure 5.3.1 for OWL. One possible solution, if the segmentation patterns have different sizes when projected onto the exit pupil, is to separate the signals by filtering in Fourier space. However this solution is not suitable for the Chanan technique. The efficiency of the Fourier solution has not been deeply investigated yet.

Another problem of ELTs is the shadow of the secondary mirror support. The pupil of ELTs may be divided into several parts, separated by gaps with the size of the support structure. Applying any co-phasing technique will result in mirror parts being individually co-phased, but with random phase differences between the parts. An advantage of the MZ and Curvature co-phasing techniques is their simplicity to adjust their properties by small modifications of the setup. In this context, the signal width could be enlarged to a size significantly larger than the gaps between these parts if atmospheric errors are corrected with an AO system. In the Curvature sensor this is achieved by simply reducing the defocus distance and in the MZ case by reducing the pinhole size. However, since the gap due to the support structure will not exceed the segment size, the parts can be correctly phased from the measurements of the edge which are not masked by the gap.
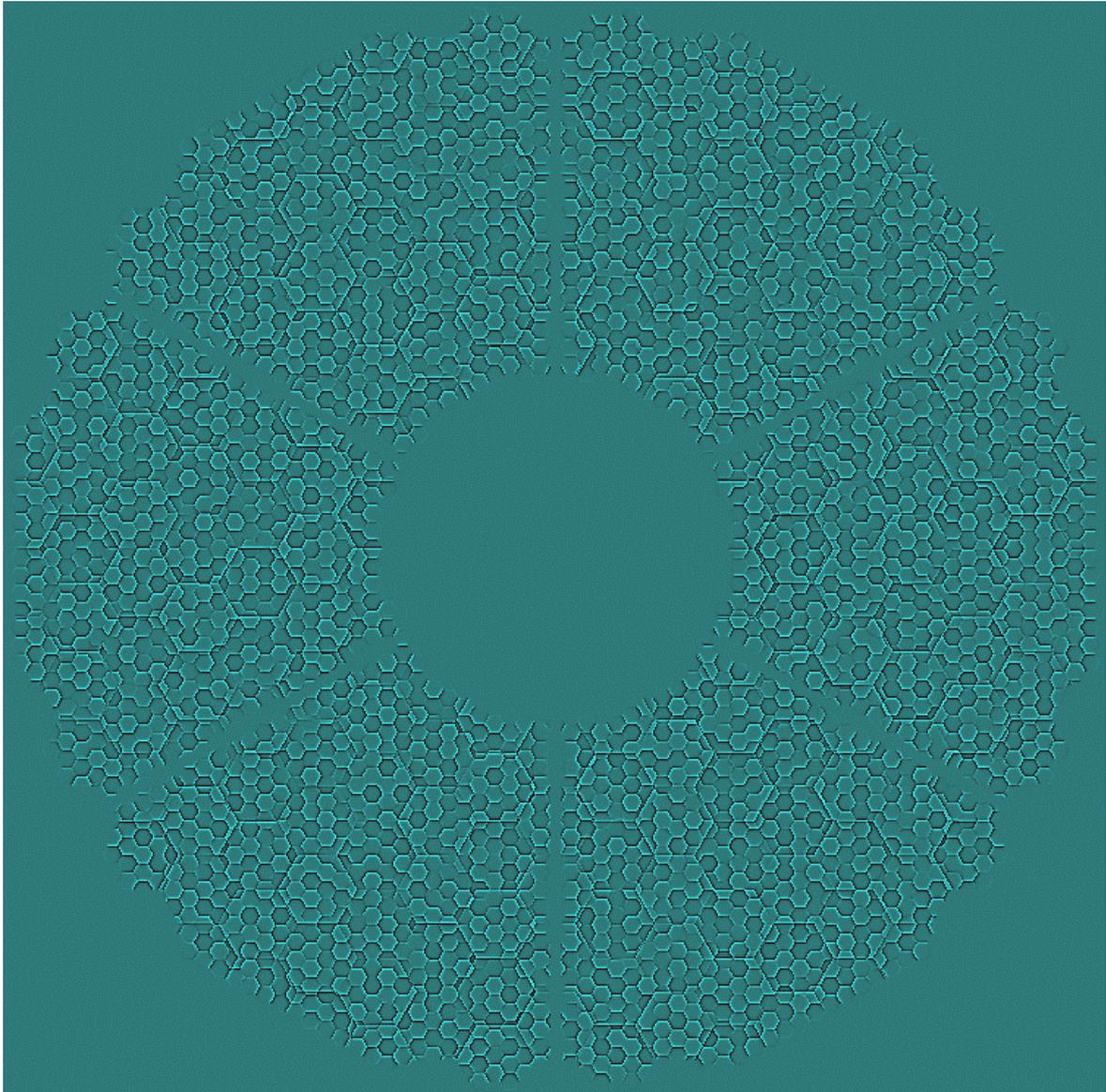
Figure 5.3.1 MZ interferogram of two mirrors for OWL (courtesy N.Yaitskova, ESO)

5.4. Summary

In this chapter we have compared four novel techniques for co-phasing segmented mirrors. The performance of these techniques can be optimised by adjusting the setup parameters: the mask for Chanan, the defocus distance for Curvature, the modulation for Pyramid and the pinhole size for MZ. A precision better than 10nm can be achieved in any case. The capture range is doubled for the case of Chanan compared to the rest of techniques. However the capture range can be increased by using two or more wavelengths.

All these techniques can employ natural sources since there is enough sky coverage for the limit stellar magnitude required.

There are no major hardness in the practical implementation of these techniques, except for the manufacturing of the lenslet array and mask for highly segmented pupil when using the Chanan technique.

A great advantage of the Curvature and MZ technique is the possibility of retrieving separately by Fourier filtering the piston step if more than one telescope mirror is segmented.

Conclusion et Perspectives

La segmentation des miroirs semble être l'unique solution envisageable pour les ELTs. Pour obtenir la qualité d'image nécessaire aux programmes scientifiques astronomiques, les erreurs dues au mauvais alignement des segments doivent être réduites à la dizaine de nanomètres. En conséquence, le développement de nouvelles techniques de co-phasage capable de mesurer des erreurs de piston avec une précision de l'ordre du nanomètre sur un télescope très segmenté est essentiel.

Une nouvelle technique pour le co-phasage des miroirs segmentés basée sur un interféromètre de MZ a été présentée dans cette thèse. L'étude a été divisée en trois niveaux : étude analytique, simulation numérique et approche expérimentale.

L'étude analytique nous a fourni une meilleure compréhension du comportement du signal obtenu avec MZ en fonction des paramètres expérimentaux. Des pics secondaires apparaissent sur le signal du MZ avec un trou circulaire alors qu'ils sont lissés avec un trou gaussien et la largeur du signal diminue avec la taille du trou. De plus, il apparaît que l'introduction d'une différence de marche non nulle entre les deux bras est nécessaire pour retrouver le signe du piston.

La simulation a permis d'analyser les performances de la technique de MZ en fonction de nouveaux paramètres tels que les perturbations atmosphériques, les effets de bords rabattus, le bruit de photon et les caractéristiques du détecteur. Pour cette étude, nous avons d'abord prouvé que l'approximation mono-dimensionnelle est valide. Les erreurs atmosphériques et l'interstice entre les segments réduisent l'amplitude et la largeur du signal. L'effet principal des bords rabattus est un signal non nul pour une erreur de piston nulle gênant ainsi la mesure du piston. Il serait intéressant d'analyser comment cette constante peut être retrouvée.

L'erreur de piston est retrouvée à partir de la calibration obtenue à partir du signal du MZ Deux critères ont été caractérisés ; il est démontré qu'un critère basé sur l'intégrale du signal donne de meilleures performances qu'un critère sur l'amplitude. Nous avons aussi vu que les erreurs atmosphériques ne dégradent pas la performance alors que les bords rabattus représentent une limitation pour les performances de la méthode. Une précision de 10 nm peut être obtenue après un processus itératif et les performances peuvent être améliorées en introduisant la taille des interstices et des bords rabattus dans les données de calibration.

Le bruit de photon ne limite pas les performances de la technique de co-phasage MZ. En effet, des étoiles de magnitudes inférieures à 13 en bande V assurent une précision meilleure que 10 nm.

Toutes les mesures optiques monochromatiques présentent un domaine de gamme de mesure limitée. Dans le cas du MZ, l'amplitude maximale est de $\lambda/2$. Des mesures polychromatiques seront donc nécessaires pour augmenter ce domaine de mesure. Cet aspect n'a pas été analysé en détail et reste un des premiers points à étudier dans un futur proche.

Le troisième niveau d'étude a été la conception d'un banc expérimental pour vérifier la validité de cette technique. L'expérience comporte un simulateur de turbulence atmosphérique, un simulateur de segment et un interféromètre de MZ. Les résultats obtenus sont en accord avec les simulations bien que des problèmes liés à la focalisation de la pupille, à la séparation des faisceaux du MZ et au vignettage restent à résoudre. Nous avons aussi trouvé une grande incertitude sur la mesure de grandes différence de marche en présence de perturbations atmosphériques. Cela doit être dû au tip-tilt introduit par l'atmosphère provoquant un désalignement du trou vis à vis de la PSF variable dans le temps. Malheureusement, les retards et les difficultés de fabrication ont rendu impossible les mesures avec le simulateur de GTC. Il est très important de terminer cette expérience pour comparer nos résultats avec ceux issus de la technique de courbure.

Une comparaison de trois techniques de co-phasage est aussi présentée : la méthode proposée par Chanan et al, celle basée sur l'analyseur de courbure et enfin celle basée sur interféromètre de MZ. Nous montrons que les performances peuvent être optimisées en ajustant les paramètres expérimentaux. La précision et le domaine de validité pour toutes ces techniques remplissent le cahier des charges d'une méthode de co-phasage. Nous avons vu qu'aucune de ces techniques ne présente de difficultés majeures de mise en œuvre. Un démonstrateur de co-phasage nommé APE sera testé sur le ciel pour vérifier les performances de chaque technique.

Au vu des résultats présentés ici, la technique de MZ semble être parmi les candidats les plus prometteurs pour le co-phasage des ELTs. Toutefois des points restent à résoudre comme les effets des erreurs de tip-tilt. D'autres études incluant les défauts des bords et d'autres sources d'erreurs doivent être menées pour trouver une solution satisfaisante au problème.

Mais le principal problème non encore résolu est comment obtenir la précision de l'ordre du nanomètre pour l'optique adaptative extrême, c'est à dire à très grand rapport de Strehl.

Aucune des techniques de co-phasage proposées jusqu'à présent n'atteint un tel niveau de précision. En conséquence, de nouvelles analyses doivent être effectuées pour éliminer complètement tous les effets indésirables.

Chapter 6

Conclusions and Perspectives

Segmentation seems to be the unique solution for ELTs. In order to achieve the high performance required for the astronomical science programs, the errors due to segment misalignment must be reduced to tens of nm. Therefore the development of new co-phasing techniques capable of measure piston error with a precision of the order of nm operating in highly segmented mirror is of critical importance.

A new technique for co-phasing segmented mirrors based on a MZ interferometer has been presented in this thesis. The study has been split in three levels, analytical, simulation and experimental.

The analytical study has yielded a better understanding of the MZ signal behaviour with the setup parameters. Secondary peaks appear on the MZ signal for circular pinhole, while they are smoothed for Gaussian pinhole. The width of the signal decreases with the pinhole size. The introduction of an OPD is necessary to enable piston sign retrieval.

The simulation study has allowed the understanding and performance of the MZ technique including atmospheric errors, miss-figure and gap at segment edge, photon noise and detector parameters. For this study we have proved that the 1-D approximation is valid. Atmospheric errors and gaps reduce the signal amplitude and width. The main effect of edge miss-figure errors is the non zero signal for zero piston error. This fact is a drawback for piston retrieval. It will be interesting to investigate how this offset could be easily derived.

The piston error is retrieved from the calibration value obtained from the MZ signal. Two criteria have been characterised here. It has been demonstrated that the integral criterion produces a better performance than the amplitude criterion. We have seen that atmospheric errors do not damage the performance while edge miss-figure represents a limitation for the performance of the method. A precision of 10nm can be achieved after an iteration process. Better performance can be achieved including the knowledge of gaps and edge defect in the calibration data.

The photon noise presents no limitation for the performance of the MZ co-phasing technique. Magnitudes brighter than 13 in V, ensure a precision better than 10nm.

There is a useful capture range for the measurements taken with optical methods in one wavelength. In the MZ case, the capture range is limited to λ/2, therefore further measurements in different wavelengths are required in order to increase the capture range. This aspect has not been investigated in detail and it remains as one of the first points to be explored in the next future.

The third level of study has been the experiment design to verify the validation of this technique. The experiment consists of a turbulence simulator, a segment simulator and a MZ interferometer. The results of simulations agree with experimental ones, although some problems related to pupil focus, shearing and vignetting remain to be resolved. We have also found a large variability on the measurement with atmosphere for big step height. This may be due to the atmospheric tip-tilt error, causing time-variable misalignment between the pinhole and the seeing disk. Unfortunately, the delays and manufacture difficulties did not make possible the test of the GTC piston plate. It is very important to finish this experiment in order to contrast our results with those carried out with the Curvature technique.

A comparison of three co-phasing techniques is also presented, Chanan, Curvature and MZ. We show that the performance can be optimised adjusting the setup parameters. The precision and capture range for all these techniques fulfil the requirements of a co-phasing technique. We saw that most of the techniques do not present major manufacturing drawbacks. A global experiment called APE will be tested on the sky to verify the performance of each technique.

The MZ technique seems to be one of the strongest candidates for co-phasing of ELTs, because of the promising results presented here. However some points still remain open like the effect of tip-tilt errors. Further studies including edge defects and other error sources have to be carried out for a proper solution to the problem.

But the main unresolved problem is how to achieve the precision of ~1nm for Extreme AO. None of the co-phasing methods proposed up to now provides this precision. Therefore new trails must be investigated to completely eliminate all the undesirable effects.

ANNEX

In order to find the analytical expression of the intensity of the outputs of a Mach-Zehnder interferometer when a pinhole with a top-hat transmission function is placed in the focal plane, we will solve the expression given by (3.8). The complex input amplitude is given by expression (3.11) and the filtered complex amplitude can be expressed as,

$$U_2(x,y) = U_2(x) = \frac{1}{\lambda^2} \left\{ \int_{-\infty}^{\infty} \int_{-\infty}^{\infty} \frac{\text{sign}(x-u)+1}{2} e^{i\varphi_2} M(u,v)\,\mathrm{d}u\,\mathrm{d}v \right.$$
$$\left. + \int_{-\infty}^{\infty} \int_{-\infty}^{\infty} \frac{-\text{sign}(x-u)+1}{2} e^{i\varphi_1} M(u,v)\,\mathrm{d}u\,\mathrm{d}v \right\}$$

(A.1)

where M(u,v) is the Fourier Transform of the mask, and φ1, φ2 is the piton of each segment.

The first step is to express this equation in polar coordinates, for this porpoise we use the variable change,

$$x\text{ - }u = x - \rho\cos\omega \qquad\qquad y\text{ - }v = y - \rho\sin\omega$$

so that $U_2(x)$ can be expressed as,

$$U_2(x) = \frac{1}{\lambda^2} \left\{ \int_0^{\infty} \rho\,\mathrm{d}\rho \int_0^{2\pi} \frac{\text{sign}(x-\rho\cos\omega)+1}{2} e^{i\varphi_2} M(\rho)\,\mathrm{d}\omega \right.$$
$$\left. + \int_0^{\infty} \rho\,\mathrm{d}\rho \int_0^{2\pi} \frac{-\text{sign}(x-\rho\cos\omega)+1}{2} e^{i\varphi_1} M(\rho)\,\mathrm{d}\omega \right\}$$

(A.2)

This integral can be split in two, depending on the absolute value of x,

$$U_2(x) = \frac{1}{\lambda^2} \left\{ \left(\int_0^{|x|} \rho\,\mathrm{d}\rho + \int_{|x|}^{\infty} \rho\,\mathrm{d}\rho \right) \int_0^{2\pi} \frac{\text{sign}(x-\rho\cos\omega)+1}{2} e^{i\varphi_2} M(\rho)\,\mathrm{d}\omega \right.$$
$$\left. + \left(\int_0^{|x|} \rho\,\mathrm{d}\rho + \int_{|x|}^{\infty} \rho\,\mathrm{d}\rho \right) \int_0^{2\pi} \frac{-\text{sign}(x-\rho\cos\omega)+1}{2} e^{i\varphi_1} M(\rho)\,\mathrm{d}\omega \right\}$$

(A.3)

Each of this four integrals depends on the value of the angle, ω. We define α_0=arcos(|x|/ρ), as the angle of the first quadrant where |x| and ρ have the same value.

Now we will evaluate the four integrals separately.

$$I_1 = \int\limits_0^{|x|} \rho\, d\rho \int\limits_0^{2\pi} \frac{\mathrm{sign}(x-\rho\cos\omega)+1}{2} e^{i\varphi_2} M(\rho)\, d\omega$$

$$= \left(\mathrm{sign}(x)+1\right)\pi e^{i\varphi_2} \int\limits_0^{|x|} \rho M(\rho)\, d\rho$$

$$I_2 = \int\limits_{|x|}^{\infty} \rho\, d\rho \int\limits_0^{2\pi} \frac{\mathrm{sign}(x-\rho\cos\omega)+1}{2} e^{i\varphi_2} M(\rho)\, d\omega$$

$$= \int\limits_{|x|}^{\infty} \rho e^{i\varphi_2} M(\rho)\, d\rho \left[\left(\mathrm{sign}(x)+1\right)\pi - 2\,\mathrm{sign}(x)\alpha_0\right]$$

(A.4)

$$I_3 = \int\limits_0^{|x|} \rho\, d\rho \int\limits_0^{2\pi} \frac{-\mathrm{sign}(x-\rho\cos\omega)+1}{2} e^{i\varphi_1} M(\rho)\, d\omega$$

$$= \left(1-\mathrm{sign}(x)\right)\pi e^{i\varphi_1} \int\limits_0^{|x|} \rho M(\rho)\, d\rho$$

$$I_4 = \int\limits_{|x|}^{\infty} \rho\, d\rho \int\limits_0^{2\pi} \frac{-\mathrm{sign}(x-\rho\cos\omega)+1}{2} e^{i\varphi_1} M(\rho)\, d\omega$$

$$= \int\limits_{|x|}^{\infty} \rho e^{i\varphi_1} M(\rho)\, d\rho \left[\left(1-\mathrm{sign}(x)\right)\pi + 2\,\mathrm{sign}(x)\alpha_0\right]$$

Simplifying,

$$I_1 + I_2 = \left(\mathrm{sign}(x)+1\right)\pi e^{i\varphi_2} \int\limits_0^{\infty} \rho M(\rho)\, d\rho - 2\,\mathrm{sign}(x)e^{i\varphi_2} \int\limits_{|x|}^{\infty} \rho M(\rho)\alpha_0\, d\rho$$

(A.5)

$$I_3 + I_4 = \left(1-\mathrm{sign}(x)\right)\pi e^{i\varphi_1} \int\limits_0^{\infty} \rho M(\rho)\, d\rho + 2\,\mathrm{sign}(x)e^{i\varphi_1} \int\limits_{|x|}^{\infty} \rho M(\rho)\alpha_0\, d\rho$$

Next step is to introduce the value of $M(\rho)$ given by (3.12). To resolve those integrals we have to calculate analytically the values of:

$$\int\limits_0^{\infty} \rho M(\rho)\, d\rho = 2\pi a^2 \int\limits_0^{\infty} \rho \frac{J_1(ka\rho)}{ka\rho}\, d\rho = \frac{\lambda^2}{2\pi}$$

(A.6)

$$\int\limits_{|x|}^{\infty} \rho M(\rho)\alpha_0\, d\rho = 2\pi a^2 \int\limits_{|x|}^{\infty} \rho \frac{J_1(ka\rho)}{ka\rho}\arccos(|x|/\rho)\, d\rho = \frac{2\pi a}{k} \int\limits_{|x|}^{\infty} J_1(ka\rho)\arccos(|x|/\rho)\, d\rho$$

where a is the pinhole diameter.

We integrate the later integral by parts with the following variable changes:

$$u = \arccos(|x| / \rho) \qquad u' = \frac{|x|}{\rho\sqrt{\rho^2 - |x|^2}}$$

$$v = -\frac{J_0(ka\rho)}{ka} \qquad v' = J_1(ka\rho) \tag{A.7}$$

Using the integrals of Prudnikov et al 1986 ("Integrals and Series", Volume 2, page 178, eq.19), we obtain:

$$\int_{|x|}^{\infty} J_1(ka\rho) \arccos(|x| / \rho)\, d\rho = \frac{1}{ka}\left[-\arccos(|x| / \rho) J_0(ka\rho) + |x|\int_{|x|}^{\infty} \frac{1}{\rho\sqrt{\rho^2 - |x|^2}} J_0(ka\rho)\, d\rho \right]$$

$$= 0 + \frac{|x|}{ka}\left(\frac{\pi}{2|x|} - \frac{\pi}{2|x|} \mathrm{Si}(ka|x|) \right) = \frac{\pi}{2ka}\left(1 - \mathrm{Si}(ka|x|)\right) \tag{A.8}$$

The function Si(ka|x|) is the integral of the Sinc function defined as,

$$\mathrm{Si}(ka|x|) = \frac{2}{\pi}\int_0^{ka|x|} \frac{\sin(t)}{t}\, dt \tag{A. 9}$$

And the integrals given by (A.5) can be expressed:

$$I_1 + I_2 = \frac{\lambda^2}{2} e^{i\varphi_2}\left(1 + \mathrm{sign}(x)\,\mathrm{Si}(ka|x|)\right)$$

$$I_3 + I_4 = \frac{\lambda^2}{2} e^{i\varphi_1}\left(1 - \mathrm{sign}(x)\,\mathrm{Si}(ka|x|)\right) \tag{A.10}$$

Finally the complex amplitude (A.3) has the form:

$$U_2(x) = \frac{e^{i\varphi_1}}{2}\left(1 - \mathrm{sign}(x)\,\mathrm{Si}(ka|x|)\right) + \frac{e^{i\varphi_2}}{2}\left(1 + \mathrm{sign}(x)\,\mathrm{Si}(ka|x|)\right)$$

$$= \frac{e^{i\varphi_1}}{2}\left(1 - \mathrm{Si}(kax)\right) + \frac{e^{i\varphi_2}}{2}\left(1 + \mathrm{Si}(kax)\right) \tag{A.11}$$

Introducing this value in (3.8), we obtain the complex amplitude at two outputs of the interferometer:

$$U_A(x) = \frac{1}{2}\left\{ e^{i\varphi_1}\left[1 - \mathrm{Si}(kax) + e^{i\theta}(1 - \mathrm{sign}(x))\right] + e^{i\varphi_2}\left[1 + \mathrm{Si}(kax) - e^{i\theta}(1 + \mathrm{sign}(x))\right] \right\}$$

$$U_B(x) = \frac{1}{2}\left\{ e^{i\varphi_1}\left[1 - \mathrm{Si}(kax) - e^{i\theta}(1 - \mathrm{sign}(x))\right] + e^{i\varphi_2}\left[1 + \mathrm{Si}(kax) + e^{i\theta}(1 + \mathrm{sign}(x))\right] \right\} \tag{A.12}$$

where θ is the OPD between both arms of the interferometer.

From (3.9) the intensities of each arm are:

$$I_{A,B}(x) = \frac{1}{4}\left\{\frac{1}{2}\cos(\Delta\varphi)\left(1 - \text{Si}^2(ka|x|)\right) + \frac{1}{2}\left(3 + \text{Si}^2(ka|x|)\right)\right.$$

$$\left. \pm \cos(\theta)\left(1 + \text{Si}(ka|x|)\right) \pm \cos(\theta - \text{sign}(x)\Delta\varphi)\left(1 - \text{Si}(ka|x|)\right)\right\}$$

(A.13)

And the MZ signal has the form:

$$S_{MZ}(x) = \frac{1}{2}\left\{\cos(\theta)\left(1 + \text{Si}(ka|x|)\right) \pm \cos(\theta - \text{sign}(x)\Delta\varphi)\left(1 - \text{Si}(ka|x|)\right)\right\}$$

(A.14)

Bibliography

Angel, J.R.P., "Ground-based imaging of extrasolar planets using adaptive optics", in *Nature*, **368**, 203-207, (1994).

Angel, R., Lawrence, J., Storey, J., "Concept for a second Giant Magellan Telescope (GMT) in Antarctica", in *2nd Bäckaskog Workshop on Extremely Large Telescopes*, Proc. SPIE, (2003).

Angel, J.R.P., Hill, J.M., "Manufacture of large glass honeycomb mirrors", Proc. SPIE **332**, 298-306, (1982).

Ardeberg, A.L., Andersen, T., Rodriguez-Espinosa, M., "Euro50 extremely large telescope" in *Future Giant Telescopes*, J.R.P. Angel and R. Gilmozzi, eds., Proc. SPIE **4840**, 214-225, (2002).

Arsenault et al, "NAOS Simulator Unit Design Report", in *Technical Report VLT-TRE-NAO-11650-400000_0001*, (1998).

Baron, F., Cassaing, F., Banc, A., Laubier, D., "Cophasing a wide field multi-aperture by phase diversity: influence of aperture redundancy and dilution", in *Interferometry in Space*, Michael Shao, ed, Proc. SPIE **4852**, 663-673, (2003).

Baranne, A., Lemaitre G., "Combinaisons optiques pour les très grands télescopes: le concept TEMOS", in *C.R.Acad.Sci.Paris*, **305**, 445-450, (1987).

Beckers, J., "Increasing the size of the isoplanatic patch with multiconjugate adaptive optics", in *ESO conference on very large telescopes and their instrumentation,* Ulrich, M., ed*.*, **2**, 693-703, (1988).

Beckers, J.M et al, " The multiple mirror telescope " in *Telescopes for the 1980s*. (A81-49821 24-89) Palo Alto, CA, Annual Reviews, 63-128, (1981).

Bello-Figueroa, C.D., Devaney, N., Castro, J., " The effect of piston errors on the image quality of ground-based segmented mirror telescopes", in *Revista Mejicana de Astronomía y Astrofísica*, **36**,57-66, (2000).

Bello-Figueroa, C.D, "Improving the image of large segmented telescopes", Ph.D. Thesis, IAC-Univ. de La Laguna, (2001).

Born, M.&Wolf, E., "Principles of Optics", Pergamon press, (1959).

Brusa, G., Riccardi, A., Accardo, M., Biliotti, V., Carbillet, M., Del Vecchio, C., Esposito, S., Femenía, B., Feeney, O., Fini,L., Gennari, S., Miglietta, L., Salinari, P.,Stefanini, P., "From adaptive secondary mirrors to extra-thin extra-large adaptive primary mirrors" in *Proceedings of the Backaskog workshop on extremely large telescopes*, Andersen, T., Ardeberg,A., and Gilmozzi R., eds., Proc.ESO **57**, 181-201,(1999).

Burgarella, D., Dohlen, K., Ferrari, M., Sayede, F., Hammer, F., Zamkotsian, F., "Next generation Canada-France-Hawaii telescope", in *Future Giant Telescopes*, J.R.P. Angel and R. Gilmozzi, eds., Proc. SPIE **4840**, 93-103, (2002).

Castro, F.J., Devaney, N., Jochum, L., Ronquillo, B., Cavaller L., "The status of the design and fabrication of the GTC mirrors", in *Optical Design, Materials, Fabrication and Maintenance*, P.Dierickx, ed., Proc. SPIE **4003**, 23-33, (2000).

Chanan, G., Troy, M., Sirko, E., "Phase discontinuity sensing: a method of phasing segmented mirrors in the infrared", in *Appl.Opt.* **38**, 704-713, (1999).

Chanan, G., Ohara, C., Troy, M, "Phasing the mirror segments of the Keck telescopes II: The Narrow-band phasing algorithm", in *Appl.Opt.* **39**, 4706-4714, (2000).

Chanan, G., Troy, M., Dekens, F., Mitchaels, S., Nelson, J., Mast, T., Kirkman, D., "Phasing the mirror segments of the Keck telescopes: the broadband phasing algorithm", in *Appl.Opt.* **37**, 140-155, (1998).

Chanan, G., Troy, M., Ohara, C., "Phasing the primary mirror segments of the Keck telescope: a comparison of different techniques", in *Optical Design, Materials, Fabrication and Maintenance*, P.Dierickx, ed., Proc. SPIE **4003**, 182-202, (2000).

Cheng,Y.Y, Wyant, J.C., "Multiple-wavelength phase-shifting interferometry", in *Appl.Opt.* **24**, 804-807, (1985).

Creath, K., "Step height measurement using two-wavelength phase-shifting interferometry", in *Appl.Opt.* **26**, 2810-2816, (1987).

Cruz-Gonzalez, I., "TIM:Mexican Optical-Infrared Telescope for the OAN/SPM", in *Large Ground-based Telescopes*. Oschmann, J. M.; Stepp, L. M., eds, Proc. SPIE **4837**, 36-50, (2003).

Cuevas, S., Orlov, V.G., Garfias, F., Voitsekhovich, V., Sanchez, L., "Curvature equation for segmented telescopes", in *Optical Design, Material, Fabrication, and Maintenance*, P.Dierickx, ed., Proc.SPIE **4003**, 291-302, (2000).

Davidge, T.J.; Rigaut, F.; Chun, M.; Brandner, W.; Potter, D.; Northcott, M.; Graves, J.E., "The Peak Brightness and Spatial Distribution of Asymptotic Giant Branch Stars Near the Nucleus of M32" in *Astrophysical Journal* **545**, 89-92,(2000).

Dierickx, P., "Optical performances of large ground-based telescopes" in *Journal of Modern Optics* **39**, 569-588, (1992).

Dierickx, P., Gilmozzi, R., "Progress of the OWL 100-m telescope conceptual design", in *Telescope Structures, Enclosures, Controls, Assembly/Integration/Validation, and Commissioning*, Sebring, T. and Andersen, T., eds, Proc.SPIE **4004**, 290-299, (2000).

Diericks, P., Beckers, J., Brunetto, R., Conana, R., Fedrigo, E., Gilmozzi, R., Hubin, N., Le Louran, M., Marchetti, E., Monnet, G., Noethe, L., Quattri, M., Sarazin, M., Spyromillo, J., Yaitskova, N., "The Eye of the beholder: designing the OWL", in *Future Giant Telescopes*, Angel, R. and Gilmolzzi, R., eds, Proc.SPIE 4840,151-170,(2003)

Dohlen, K., Fresneau, F., "Medium-scale demonstration of the dual wavelength, random phase shift interferometer for segment phasing", in *Proceedings of the Backaskog workshop on extremely large telescopes*, Andersen,T., Ardeberg,A., Gilmozzi,R., ESO proc. **57**, (2000).

Dohlen, K., Decortital, F., Fresneau, F., Lanzoni, P., "Dual-wavelength random-phase-shift interferometer for phasing large segmented primaries", in *Advanced Technology Optical/IR Telescopes VI*, Stepp, M.L., ed., Proc.SPIE **3352**, 551-559 (1998).

Esposito, S., Devaney, N., "Segmented telescopes co-phasing using pyramid sensor", in *Beyond conventional adaptive optics*, Vernet, E., Ragazzoni, R., Esposito, S., Hubin, N., Proc.ESO **58**, 161, (2002).

Fried, D.L., "Optical resolution through randomly inhomogeneous medium for very long and very short exposures", in *J.Opt.Soc.Am.* **56**, 1372-1379, (1965).

Foucault, L., "Mémoire sur la construction des télescopes en verre argentés" in *Ann.Obs.Imp.Paris,* **5**, 197, (1859).

Gonsalves, R.A., Chidlaw, R., "Wavefront sensing by phase retrieval", in *Applications of digital imaging processing III*, Proc.SPIE **207**, 32-39, (1979).

Gonte,F., Yaitskova,N., Diericks, P., Courtevilla, A., Esposito, S., Devaney, N., Dohlen, K., Ferrari,M., Montoya, L., "APE: a breadboard to evaluate new phasing technologies for a future European Giant Telescope", in *Astronomical Telescope and Instrumentation*, Proc.SPIE, (2004).

Goodman, J.W., "Introduction to Fourier optics", McGraw-Hill international editions, (1996).

Hill, J., Salinari, P., "Large Binocular Project", in *Large Ground-based Telescopes*, Oschmann, J. M.; Stepp, L. M., eds., Proc. SPIE **4837**, 140-153, (2003).

Horton, R.F., Huben, E.E., Bernotas, L.A., Yee, L.G.B., Roberts, A.V., "Absolute piston phasing of segmented-mirror optical systems using depth-modulated white light interferometry", in *Advanced technology optical telescopes IV*, Proc.SPIE **1236**, 974-984, (1990).

Katz, Neal; Weinberg, D.H.; Hernquist, L.; Miralda-Escude, J., "Damped Lyman-Alpha and Lyman Limit Absorbers in the Cold Dark Matter Model" in *Astrophysical Journal Letters* **457**, 57-60, (1996).

Kishner, S.J., "High-bandwidth alignment sensing in active optical systems", in *Analysis of Optical Structures*, D.C.O'Shea, ed., Proc.SPIE **1532**, 215-229, (1991).

Kolmogorov, A.N., "The local structure of turbulence incompressible viscous fluids for very large Reynolds", in *Turbulence, Classical Papers and Statistical Theory*, S.K. Friedlander, L. Topper, eds., 181-155, (1961).

Korhonen, T., Haarala, S., "Optical sensor for the control of segmented or active mirrors", in *Very Large Telescopes and their Iinstrumentation*, M. Ulrich, ed., Proc. ESO, (1988).

Krabbendam, V.L., Sebring, T.A., Ray, F.B, Fowler, S.R., "Development and performance of Hobby-Eberly Telescope segmented mirror", in *Advanced Technology Optical/IR Telescopes VI*, L.Stepp, ed., Proc.SPIE **3352**, 436-445, (1998).

Kuhn, J.R., Moretto, G., Racine, R., Roddier, F., Coulter, R., "Concepts for a large-aperture, high dynamic range telescope", *PASP* **113**, 1486-1510, (2001).

Labeyrie, A., "Resolved imaging of extra-solar planets with future 10-100km optical interferometrics arrays", in *A&A Supp.* **118**, 517-524, (1996)

Labeyrie, A., Borkowski, V., Martinache, F., Arnold, L., Dejonghe, J., Riaud, P., Lardiere, O., Guillet, S., "Adaptive optics for ground based hypertelescopes", *in Beyond conventional adaptive optics*, Vernet, E., Ragazzoni, R., Esposito, S., Hubin, N., ESO Conf. and Workshop Proc., p.109 (2002).

Langlois, M., "High order adaptive optics to detect faint companions around nearby stars", Ph.D. Thesis, Observatoire de Paris, (2001).

Lemaitre, G., Wang, M., " Optical results with TEMOS 4: a 1.4 meter telescope designed with a primary of spherical segments and a metal secondary mirror actively aspherized", in *Metal Mirrors*, Richard G. Bingham; David D. Walker; Eds, Proc. SPIE 1931, 43-52, (1993).

Liotard, A., Zamkotsian, F., "Static and dynamic micro deformable mirror characterisation by phase-shifting and time-averaged interferometry", in *Astronomical Telescope and Instrumentation*, Proc.SPIE, (2004).

Löfdahl, M.G., Kendrick, R.L., Harwit, A., "Phase diversity experiment to measure piston misalignment on the segmented primary mirror of the Keck II telescope", in *Space telescopes and instruments*, P.Y. Bely, J.B. Breckinrindge, eds., Proc. SPIE **3356**, p.1190, (1998).

Löfdahl, M.G., Eriksson, H., "An algorithm for resolving 2π ambiguities in interferometric measurements by use of multiple wavelengths", in *Opt.Eng.* **40**, 2019-2058, (2001).

Mast, T., Nelson, J., Welch, W., "The Effects of Primary Mirror Segmentation on the Image Quality", in *Ten Meter Telescope Report* **68,** (1982).

Marchis, F., Cuevas S., "Optical tolerances of active telescopes architectures for adaptive optics", in *Revista Mejicana de Astronomía y Astrofísica,* **35**, 31-44, (1999).

Martinache, F., "Global wavefornt sensing for interferometers and mosaic telescopes: the dispersed speckles principle", in *J.Opt.A: Pure Appl.Opt.* **6,** 216-220, (2004).

Meiring, J.G.; Buckley, D. A.H., Lomberg, M.C., Stobie, R.S "Southern African Large Telescope (SALT) project: progress and status after 2 years" in *Large Ground-based Telescopes.* Oschmann, J. M.; Stepp, L. M., eds., Proc. SPIE **483**7, 11-25, (2003).

Montoya-Martinez, L., Yaitskova, N., Diericksx, P., Dohlen, K., "Mach-Zehnder wave front sensor for phasing of segmented telescopes", in *Future Giant Telescopes,* J.R.P. Angel and R.Gilmozzi, eds., Proc.SPIE **4840**, 564-573, (2002).

Nelson, J., Mast, T., Faber, S., "The design of the Keck Observatory and telescope" Keck Observatory Report **90**, 5-1 to 5-44, (1985)

Nelson, J., "Design concepts for the California Extremely Large Telescope (CELT)", in *Telescope Structures, Enclosures, Controls, Assembly/Integration/Validation, and Commissioning,* T.Sebring and T.Andersen, eds, Proc.SPIE **4004**, 282-289, (2000).

Noll, R.J., "Zernike polynomials and atmospheric turbulence", in *J.Opt.Soc.Am.* **66**, 207-211 (1976).

Orlov, V.G., Cuevas, S., Garfias, F., Voitsekhovich, V.V, Sánchez, L.J, "Co-phasing of segmented mirror telescopes with curvature sensing", in *Telescopes Structures, Enclosures, Controls, Assembly/Integration/Validation, and Commissioning*, T.A.Sebring, T.Andersen, eds., Proc.SPIE **4004**, 540-551,(2000).

Pinto, A., Laguarta, F., Artigas, R., Cadevall, C., "Testing and applicability of the UPC-ZEBRA interferometer as a phasing system in segmented-mirror telescopes", in *Appl.Opt.* **43**, 1091-1096, (2004).

Pizarro, C., Arasa, J., Laguarta, F., Tomàs, N., Pintò, A., "Design of an interferometric system for the measurement of phasing errors in segmented mirrors", *Appl.Opt.* **41**, 4562-4570, (2002).

Press, W., Flannery, B.P., Teukolsky, S.A., Vetterling, W.T., "Numerical Recipes in C: the Art of Scientific Computing", Cambridge University, New York (1992).

Roberts, S.C., Morbey,C.L., Crabtree,D.R., Carlberg,R., Crampton, D., Davidge, T.J., Fitzsimmons,J.T., Gedig, M.H., Halliday, D.J., Hesser, J. E., et al "Canadian very large optical telescope technical studies" in *Future Giant Telescopes.* Angel, J.R.P., Gilmozzi, R. Proc. SPIE **4840**, 104-115, (2003).

Ragazzoni, R., "Pupil plane wavefront sensing with an oscillating prism", in *J.of Modern Optics* **43**, 289-293, (1996).

Ragazzoni, R., Diolaiti, E., Vernet, E., "A pyramid wavefront sensor with no dynamic modulation", in *Optics Communications* **208**, 51-60, (2002).

Riccardi, A., et al, "Primary Adaptive Mirrors for ELTs: a report on preliminary studies", in *Proceedings of the 2nd Backaskog workshop on extremely large telescopes,* Sweden (2003).

Roddier, C., Roddier, F., "Wavefront-reconstruction from defocused images and the testing of ground –based optical telescopes", in *J.Opt.Soc.Am.A.* **10,** 2277-2287, (1993).

Roddier, F., "Adaptive Optics in Astronomy", Cambridge University Press, (1999).

Rodriguez-González, J.M, Fuensalida, J.J, "Difractional treatment of curvature sensing in segmented-mirror telescopes", in *Large Ground –based Telescopes*, J.M. Oschmann, L.M. Stepp, Proc.SPIE **4837**, 726-736, (2003).

Rodriguez-González, J.M, Fuensalida, J.J, "Results of diffraction effects in segmented mirrors: co-phasing with integrated curvature signal", in *Large Ground –based Telescopes*, J.M. Oschmann, L.M. Stepp, Proc.SPIE **4837**, 737-748, (2003).

Rodriguez-Ramos, J.M., Fuensalida, J., "Piston detection of a segmented mirror telescope using a curvature sensor: preliminary results with numerical simulations", in *Optical Telescopes of Today and Tomorrow*, Arne L. Ardeberg ed.; Proc. SPIE **2871**, 613-616, (1997).

Roggeman, M.C., Welsh, B., "Imaging through turbulence", CRC Press, (1996).

Rousset, G, Lacombe, F., Puget, P., Hubin, N., Gendron, E., Fusco, T., Arsenault, R., Charton, J., Feautrier, P., Gigan, P., Kern, P., Lagrange, A., Madec, P., Mouillet, D., Rabaud, D., Rabou, P., Stadler, E., Zins, G., "NAOS, the first AO system of the VLT: on sky performance", in *Adaptive Optical System Technologies II*, Wizinowich, P., Bonaccini, D., eds., Proc. SPIE **4839**, 140-149, (2003).

Seery, B., "Next Generation Space Telescope (NGST): Hubble's scientific and technological successor", in *IR Space Telescopes and Instruments*, Mether, J.C., ed, Proc.SPIE **4850**, 170-178, (2003).

Shi, F., Redding, D.C., Lowman, A.E., Ohara, C., Burns, L.A., Petrone III, P., Bowser, W., Basinge, S.A., "Segmented mirror coarse phasing with white light interferometry: modelling and experiment of NGST's wavefront control testbed", in *IR Space Telescopes and Instruments*, J.C.Mather, ed., Proc.SPIE **4850**, 380-387, (2003).

Shi, F., Redding, D.C., Lowman, A.E., Bowser, W., Burns, L.A., Petrone III, P., Ohara, C., Basinge, S.A., "Segmented mirror coarse phasing with dispersed fringe sensor: experiment on NGST's wavefront control testbed", in *IR Space Telescopes and Instruments*, J.C.Mather, ed., Proc.SPIE **4850**, 318-328, (2003).

Schumacher, A., Devaney, N., Montoya, L., "Phasing segmented mirrors: a modification of the narrow-band technique and its application to extremely large telescopes", *Appl.Opt*. **41**, 1297-1307, (2002).

Schumacher, A., Devaney, N., "Diffraction Image Phase Step Sensing: cophasing segmented mirrors with minimal hardware requirements", to be published in *Appl. Opt*.

Sorrente, B., Cassaing, F., Baron, F., Coundrain, C., Fleury, B., Mendez, F., Mugnier, L., Bentadj-Paris, V., Michau, V., Montri, J., Rousset, G., Rousset-Rouvière, L., Velluet, M.-T., "Multiple-Aperture Optical Telescope : Cophasing Sensor testbed", in *5th International Conference on space Optics* (2004).

Strom, S.E., Stepp, L. M.; Gregory, B. "Giant segmented mirror telescope: a point design based on science drivers" in *Future Giant Telescopes*. Angel, J. R. P., Gilmozzi, R.,eds., Proc. SPIE **4840**, 116-128, (2003).

Su, D., Wang, Y., Cui, X., "A Configuration for Future Giant Telescope", in *Chin.J.Astron.Astrophys*., **28**, 356-366, (2004).

Troy, M., Chanan, G., "Diffraction effects from giant segmented-mirror telescopes", *Appl.Opt*. **42**, 3745-3753, (2003)

The VLT White Book, Garching: ESO, (1998).

Voitsekhovich, V.V, Bara, S., Orlov, V.G, "Co-Phasing of segmented telescopes: A new approach to piston measurements. I. Optical concept", in *A&A* **382**, 746-751, (2002).

Wang, S-g., Su, D-q., Chu, Y-q., Cui, X., Wang, Y-n.,"Special configuration of a very large Schmidt telescope of extensive astronomical spectroscopic observation', in *Applied Optics* **35**, 5155-5161, (1996).

Yaitskova, N., Dohlen, K., "Simulation of imaging performance for extremely large telescopes", in *Optical Design, Materials, Fabrication, and Maintenance*, P.Diericks, ed., Proc.SPIE **4003**, 279-290, (2000).

Yaitskova, N. Dohlen, K., "Tip Tilt for extremely large segmented telescopes: detailed theoretical point-spread-function analysis and numerical simulation results. Analytical Description." In *J.Opt.Soc.Am.A.* **19,** 1274-1285, (2002).

Yaitskova, N., Dohlen, K., Dierickx, P., "Analytical study of diffraction effects in extremely large segmented telescopes", in *J.Opt.Soc.Am.A.* **20**, 1563-1575, (2003).

Yaitskova, N., "Performance analysis of Mach-Zehnder interferometer for detection of wavefront discontinuities", in *Astronomical Adaptive Optics Systems and Applications*. Tyson, R. K.; Lloyd-Hart, M., eds., Proc.SPIE **5169**, 62-71, (2003).

Yaitskova, N., Montoya-Martinez, L., Dohlen, K., Dierickx, P., "A Mach-Zehnder phasing sensor for extremely large segmented telescopes: Laboratory results and closed loop algorithm", in *Astronomical Telescope and Instrumentation,* Proc.SPIE, (2004).

Zamkotsian,F., Dohlen, K., Fusco, T., "Optical performance of pupil segmentation for 20-30m class telescopes", in 2nd *Bäckaskog Workshop on Extremely Large Telescopes*, Sweden, (2003).

Zamkotsian,F., Dohlen, K., Fusco, T., "Optical Performance and phase error budgeting of future ELTs", in *Astronomical Telescope and Instrumentation*, Proc. SPIE, (2004).

Zeider, G., Montgomery, E., "Diffraction effect with segmented aperture", in *Space Telescope and Instruments V*, P.Bely and J.Breckinridge, eds., Proc SPIE **3356**, 799-809, (1998)

List of Figures

List of Tables

List of Publications

1. Yaitskova, N, **Montoya-Martinez, L.**,Dohlen, K., Diericks, P. "Mach-Zehnder phasing sensor for extremely large segmented telescopes: signal analysis and closed loop operation." in *Astronomical Telescope and Instrumentation*, Proc.SPIE, (2004).

2. Gonte, F., Yaitskova, N., Diericks, P., Courteville, A., Esposito, S., Devaney, N., Dohlen, K., Ferrari, M., **Montoya, L.** "APE: a breadboard to evaluate new phasing technologies for future European giant optical telescope" in *Astronomical Telescope and Instrumentation*, Proc.SPIE, (2004).

3. **Montoya Martinez, L.**, Yaitskova, N., Dierickx, P., Dohlen, K. "Mach Zender wavefront sensor for phasing of segmented telescopes" in *Future Giant Telescopes,* J.R.P. Angel and R.Gilmozzi, eds., Proc.SPIE **4840**, 564-573, (2002).

4. Schumacher, A., Devaney, N., **Montoya, L.,**"Phasing segmented mirror: a modification of the Keck narrow-band technique and its application to extremely large telescopes" in *Applied Optics* **41**, 1297-1307 (2002).

5. Schumacher, A., **Montoya, L.**, Devaney, N., Dohlen, K., Dierickx, P., "Phasing ELTs for Adaptive Optics: Preliminary results of a Comparison of techniques" in *Beyond conventional adaptive optic*, E.Vernet, R. Ragazzoni, S. Esposito, N. Hubin eds., ESO Proc.**58**, 143 (2001).

A Mach-Zehnder phasing sensor for extremely large segmented telescopes: Laboratory results and closed loop algorithm

Natalia Yaitskova[*a], Luzma Montoya-Martinez[b], Kjetil Dohlen[b], Philippe Dierickx[a]

[a]European Southern Observatory
[b]Laboratoire d'Astrophysique de Marseille

ABSTRACT

Phasing segmented telescopes requires accurate phase measurements at the segment borders using an optical sensor. We develop such a sensor based on the Mach-Zehnder interferometer. The operation of the concept was previously demonstrated in computer simulation and also through the detailed theoretical analysis. In this paper we show the result of the laboratory experiment, which confirm the main predictions have made. The back loop control for phasing of segmented mirrors optical, similar to the one with the use of capacitive sensors, is presented and illustrated.

Key words: telescopes, segmentation, phasing, wavefront control, diffraction.

1. INTRODUCTION

Projects for future extremely large telescopes (ELTs) rely on the giant segmented mirrors. The current design of 100m OWL project [1] assume 100m primary mirror consisting of 3048 hexagonal segments with 1.6m flat-to-flat width. The secondary mirror of OWL is flat 26m in diameter, consisting of 234 segments identical to those of the primary mirror.

One of the critical tasks associated with the giant telescope is phasing of their segmented surfaces. To achieve the resolution commensurable with the monolith telescope of the same diameter the segments must be phased with the precision better than 10nm surface rms [2,3]. Three principal hardware systems are requited for the segment active control [4]: positioning sensors provide real time information about segment relative displacements; segment actuators compensate for these displacements; a phasing camera provides the periodical calibration of sensors' readings. Three new alignment concepts as an alternative to the Keck phasing camera are being currently investigated, based on the principle of pupil plane sensing: the curvature sensor [5,6], the pyramid sensor [7], and Mach-Zehnder interferometer [8]. In all optical methods the signal is well located near the intersegment border and proportional to the local phase step.

The thorough theoretical study and direct numerical simulation were presented in our previous publications [8,9]. In this paper we present some new results. This is, first, the laboratory demonstration of the Mach – Zehnder interferometry for the phase step measurement in the condition of turbulence. In the section 4 we describe the new method for piston, tip and tilt reconstruction with the following demonstration of the simulated result for the close loop for phasing of a segmented telescope.

---

[*] nyaitsko@eso.org, Karl Schwarzschildstr. 2 D-85748 Garching bei Muenchen, Germany, phone +49 89 3200 6581

2. LABORATORY TEST OF THE MACH-ZEHNDER CO-PHASING TECHNIQUE

2.1 Exposition

The principal scheme of Mach-Zehnder interferometer is shown in Figure 1. The incoming from the telescope focus beam is split in two arms of the interferometer. A pinhole placed in the focal plane of the one arm acts as a spatial filter providing the reference wave coherent to the incoming wave. The two beams are recombined and form two complementary interference patterns recorded by two imaging detectors. The difference between the interferograms, to which we refer as to signal, contains the information about a local piston error. The constant optical path difference (OPD) between the arms equal to the quota of the wavelength is requite to distinguish the sigh of the piston. The sufficiently large pinhole diameter, ~1arcsec for the wavelength 0.5μm, helps to filter out all low order wavefront aberration, including the atmospheric, and leave only the very high frequencies produced by a piston step. Te more detailed description of the principal and study of the different errors may be found elsewhere [8].
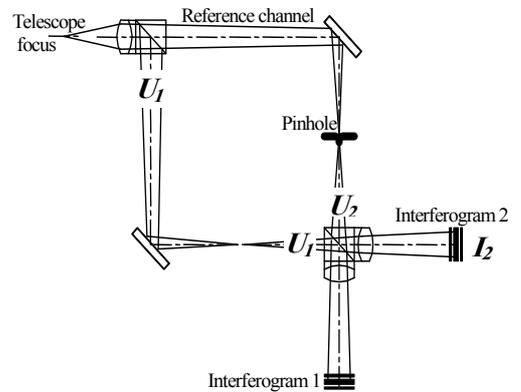
Figure 1. Schematic representation of the Mach-Zehnder interferometer

Figure 2 shows the experimental setup. A source simulator consists of a fiber-fed super-luminescent diode (S), turbulence simulator (A) and segment simulator (B). The setup includes the MZ interferometer (MZ) and two detectors (D1, D2). The turbulence simulator is a duplicate of the reflective rotating phase mask developed at GEPI (Observatoire de Paris) for performance tests of the VLT-NAOS instrument [10]. The scaling of the screen is such that a typical rotational rate of 20 RPM simulates a wind speed of 64m/s. The segment simulator, also developed by GEPI, consists of 25-mm diameter mirrors onto which are deposed a hexagonal patch of a certain thickness, representing a dephased segment. Six different such mirrors are mounted in a wheel, with patch thickness -30nm, 0nm, 30nm, 75nm, 150nm, and 230nm. Flat-to-flat segment dimension is 10mm. The interferometric analysis of one of the plates is shown in Figure 3. The low-order phase variations observed are mainly due to the measurement setup.
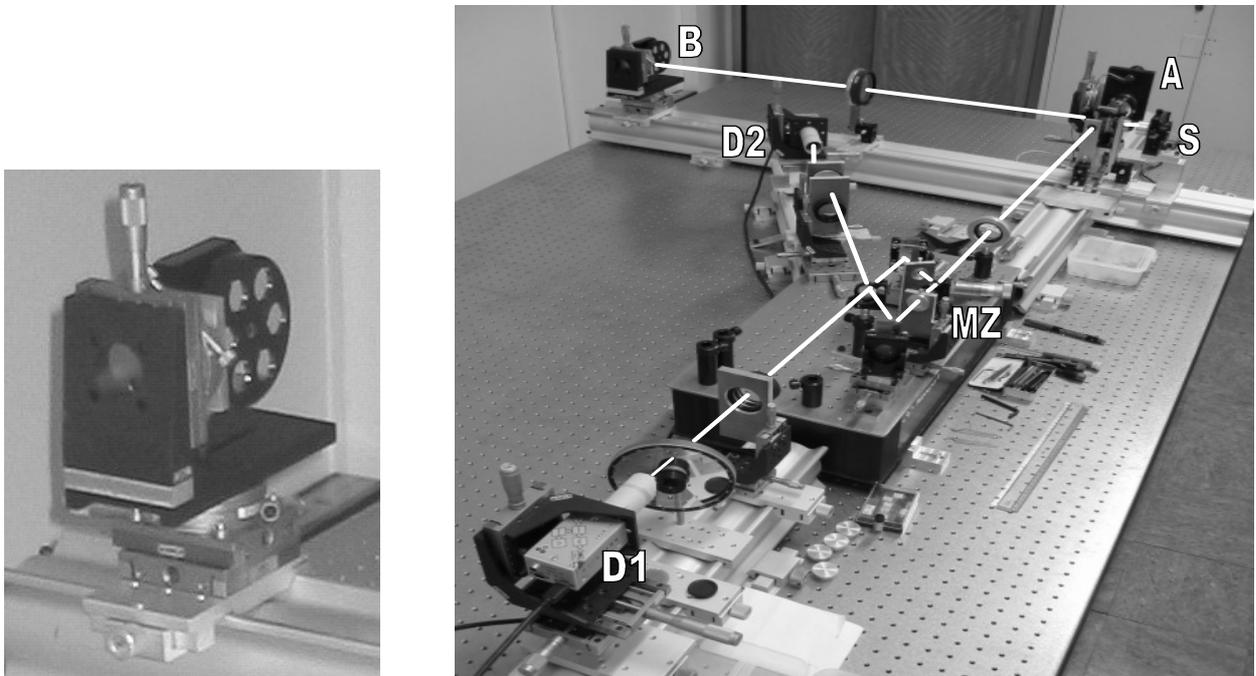
Figure 2. Photograph of the experimental setup (right) and detail of a segment simulator assembly (left).
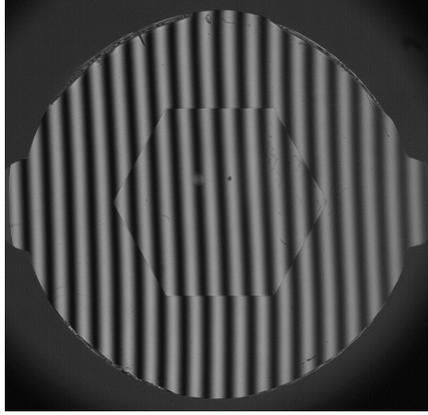
Figure 3. Result of interferometric analysis of the 75nm segment plate
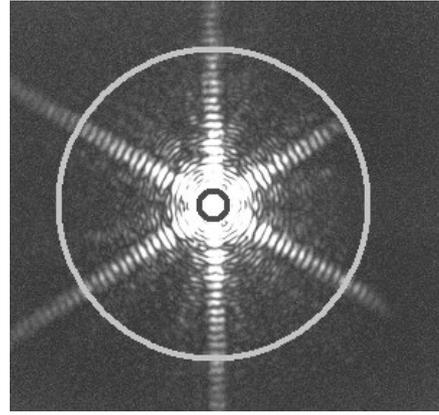
Figure 4. Point spread function formed by a segment plate.

Figure 4 shows a highly saturated star image formed by a mirror with a phase patch. The six diffraction lines due to the hexagonal patch are clearly seen. However, the two arms stretching out to the right are vignetted, and although this vignetting has been reduced to some extent, some will always occur. To avoid the image skewness caursed by this vignetting, a much larger pinhole is introduced in the second arm (indicated in a big circle in the Figure 4). While this has an additional effect of avoiding the sharp features of the Mach-Zehnder signal at the segment edge, it also reduces the peak signal values, and the effect must be included in simulations in order to produce the comparable results.

A camera is located at each output of the interferometer, but technical restrictions have not allowed us to take simultaneous images at the two outputs as was planned. We have therefore been forced to investigate the use of a single-output (I), using supplementary images (I_1 and I_2) obtained by blocking in turn each of the two arms to normalize the interferograms:

$$S = \frac{I - (I_1 + I_2)}{\sqrt{I_1 I_2}} \tag{1}$$

This signal, obtained in this procedure, is identical to the one obtained as a difference between two outputs. Although it is less efficient in terms of throughput, it may turn out to be easier to implement practically than the dual-output version. Three images (I, I_1 and I_2) and the processed image are shown in Figure 5.

(a)   (b)   (c)   (d)

Figure 5. Measured intensity distribution of arm 1 (a), arm 2 (b), the interferogram (c), and of the normalized signal.

2.2 Experimental results

Apart from the difficulties involved with the aligning of the Mach-Zehnder interferometer (tilts and shear) and location of the zero optical path difference (OPD), the most delicate operation is the fine OPD adjustment. In order to recover the sign of the piston steps, the phase difference between the two interfering wave fronts must be equal to $\pi/2$, corresponding to a mirro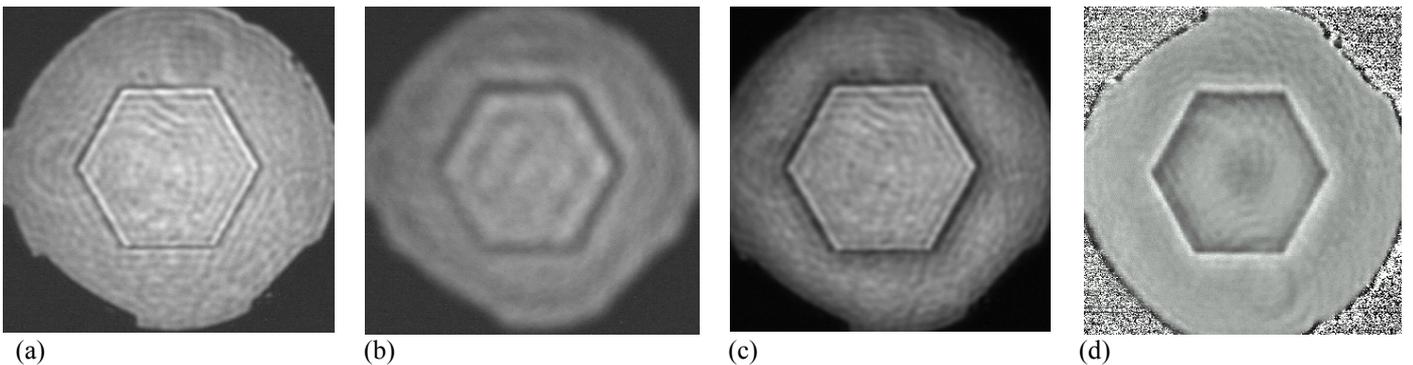r displacement of 80nm at 630nm. To achieve such extremely fine adjustments, one of the mirrors within the interferometer is mounted on a stage equipped with a differential micrometer screw whose axis is nearly parallel with the mirror surface. This provides a 150-times reduction in the axial mirror movement, corresponding to a displacement of 6.5nm per 1µm micrometer graduation. Thermal stability and air movements also become important in this context, and although ad-hoc measures were taken to limit air fluctuations within the interferometer, this demonstration experiment does not provide the nanometric stability that would be required of an operational instrument.

In Figure 6 (a, b) we plot the normalized profiles (intensity of the signal *S* across the border) obtained by simulation for the different OPD values (a), compared with the experimentally obtained profiles (b). Note that for the OPD equal to $\pi/2$ the amplitude of the signal and the antisymmetry of the signal with respect to the segment boundary achieve the maximum. Plotting the peak-to-valley (PTV) of the signal amplitude against the OPD (Figure 6 c, solid line) shows that its variation is slow close to $\pi/2$; the error is less than 10% for OPD within $\pm\pi/8$. Also, deviations from the optimal OPD are nearly proportional to the mean signal level (Fig. 6 c, dash line), allowing the potentially correcting the signal amplitude within a wide range of OPDs. A procedure for OPD adjustment based on real-time display of the average image intensity has been devised and proven to give good results.

(a)
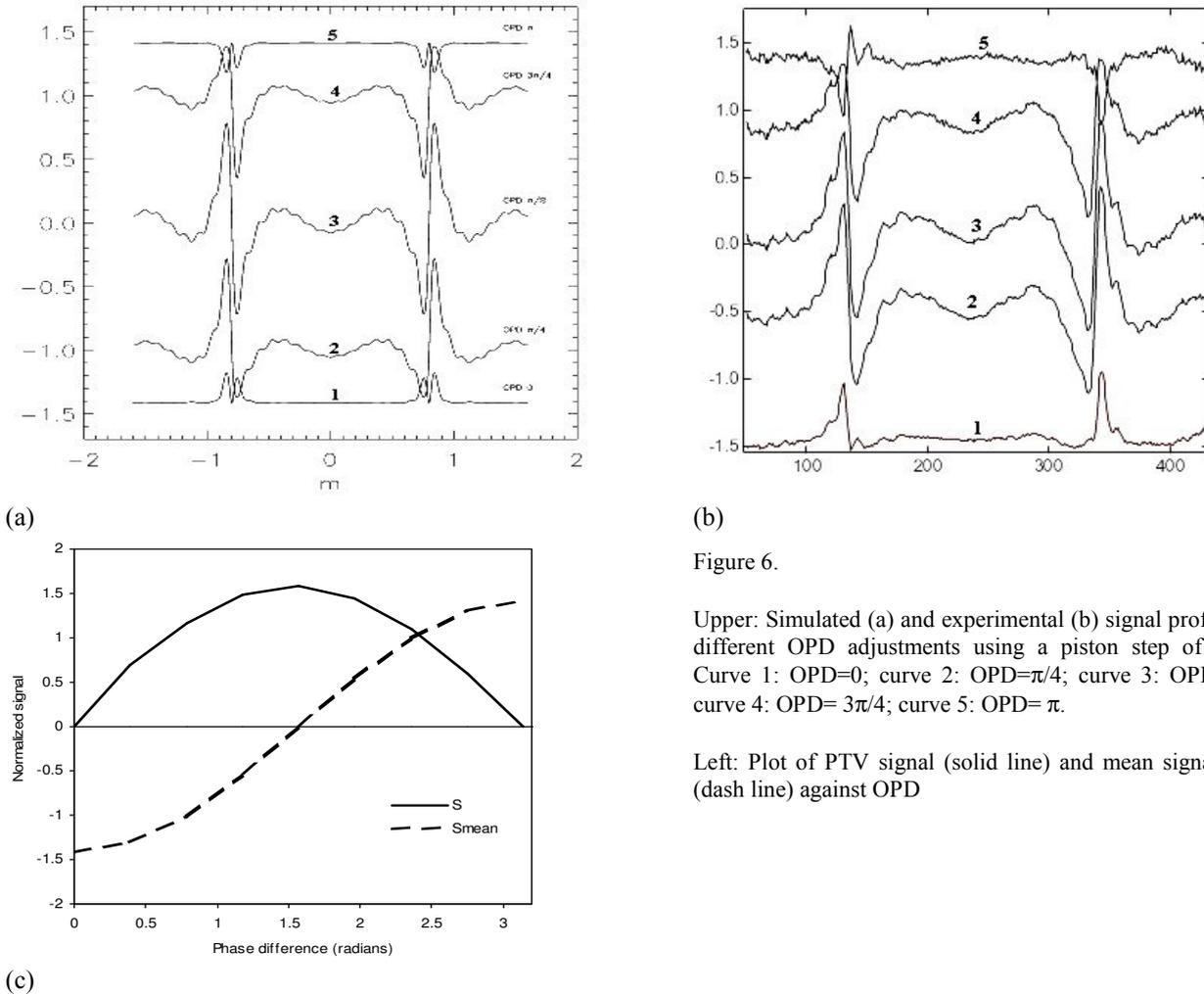
(b)

Figure 6.

Upper: Simulated (a) and experimental (b) signal profiles for different OPD adjustments using a piston step of 75nm. Curve 1: OPD=0; curve 2: OPD=$\pi/4$; curve 3: OPD= $\pi/2$; curve 4: OPD= $3\pi/4$; curve 5: OPD= π.

Left: Plot of PTV signal (solid line) and mean signal level (dash line) against OPD

(c)

2.3 Performance without atmosphere

Figure 7 (a and b) compares the simulated and the measured signal profiles in the absence of the atmospheric turbulence for each of the five piston plates. Experimentally, this configuration is obtained by replacing the turbulence simulator with a flat mirror. While the correspondence is good for the small piston values, the signal for the two larger steps are somewhat different. Figure 7c gives a more quantitative analysis of these results, representing the average PTV values for each piston step (symbols) compared with theoretical expectation (full line). Two series of 10 images is taken, and a vertical profile containing two steps (edge 1 and 2) is extracted from each image from which PTV values are measured and then averaged; vertical error bars indicate standard deviations. The first series is taken with an OPD adjusted to +π/2, for the second series the OPD is adjusted to -π/2. The good correspondence for the three smallest piston values is confirmed, as is the curious behavior for larger piston steps. While changing the OPD is of little influence on the results, indicating that the reproducibility of the OPD adjustment procedure is sufficient, the difference between the two segment edges is large. This effect is not yet understood, but the contributing factors are thought to include shearing, pupil focus, and residual vignetting effects.
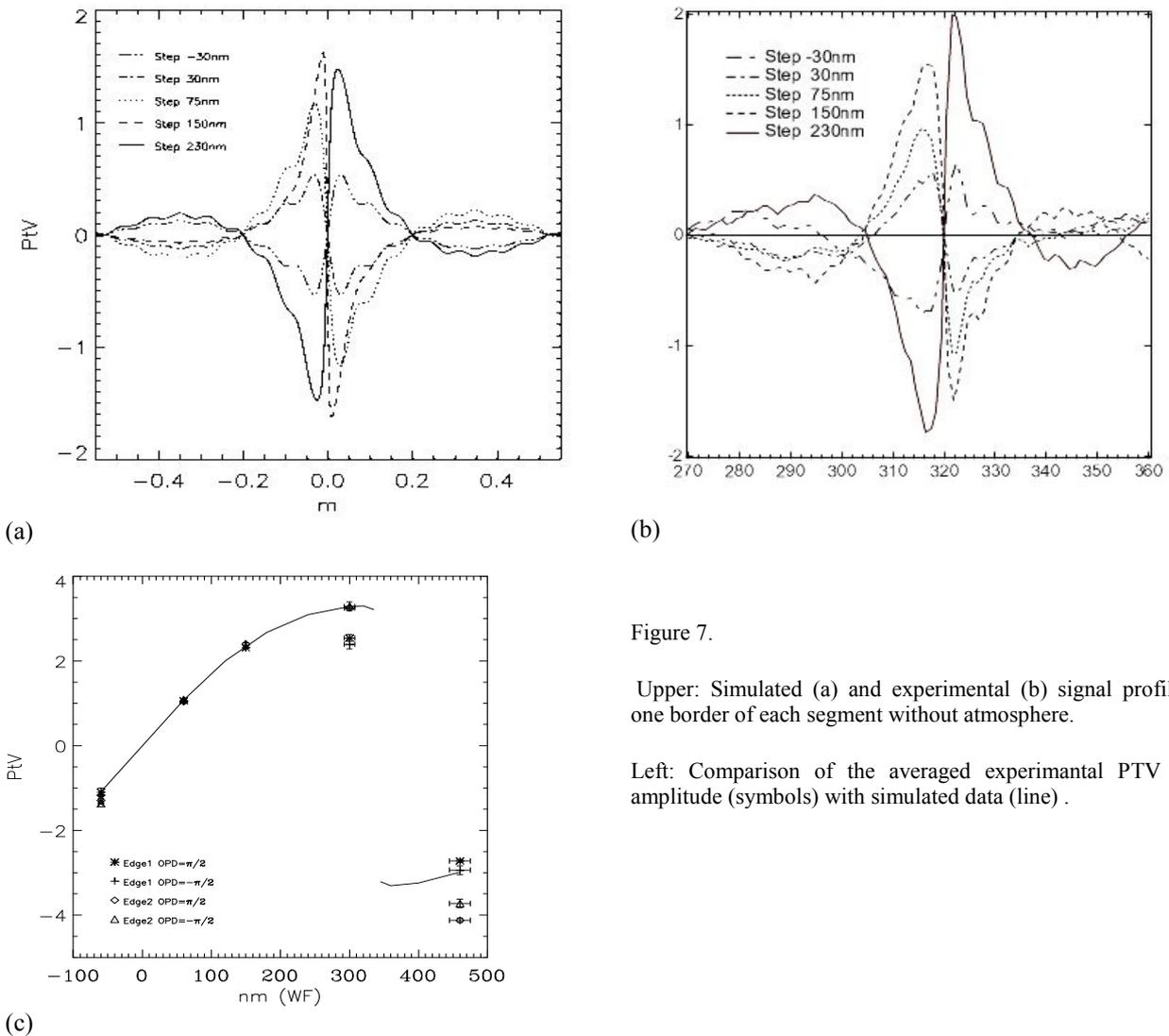

(a)

(b)

(c)

Figure 7.

 Upper: Simulated (a) and experimental (b) signal profiles for one border of each segment without atmosphere.

Left: Comparison of the averaged experimantal PTV signal amplitude (symbols) with simulated data (line) .

2.4 Performance with atmosphere

Installing in the rotating turbulence simulator allows the realistic performance testing of the method. However, it was soon noticed that the simulated turbulence varied strongly as a function of angular position. The variation was quantified by calculating the Fried parameter (r_0), estimated from the FWHM of Gaussian fits to the measured PSFs, from 22 short-exposure images. Figure 8 shows a histogram of the r_0 values obtained, indicating that instead of a typical value of 20cm, the mean seeing is equal to 64cm, with peaks reaching 2m. The mean seeing level is not a serious problem, since it is just a matter of scaling between segment size and a turbulence screen. However, as we will see, the strong variability of the instant seeing appears to contribute to the difficulty of comparing observations and simulations. For the long exposure images (1 second), representing approximately a one third of a screen rotation, the mean seeing was estimated to 61 cm with a standard deviation of 11cm (Figure 8, dashed line). A qualitative comparison indicates very good correspondence between the two, but a more quantitative analysis (Figure 9) gives a more complex picture. Compared with the measurements without seeing, results for the small piston values have much larger variability and are generally below the expected values. A better fit is obtained for the two larger piston steps, but only at the cost of even larger variability.

In addition to the problems mentioned above for the case without turbulence, it seems that the problems encountered here may be due to the large variability of the instantaneous seeing condition. While the simulations are made using a sequence of 1000 independent phase screens each created using identical turbulence statistics, 1-second exposures with our turbulence simulator corresponds to some 120 independent phase screens with largely different statistics. As one can see from the simulated curves in Figure 10, the turbulence statistics has a great influence on the signal PTV, especially for large piston steps.

Another error source is related to the atmospheric tip-tilt error, causing time-variable misalignment between the pinhole and the seeing disk. Problematic in itself, this effect is aggravated by the fact that the three images used to construct the Mach-Zehnder signal are not taken simultaneously. Although the effect should be reduced by increasing the exposure time, it may be interesting to consider the use of a real-time tip tilt corrector in a practical implementation of this concept.
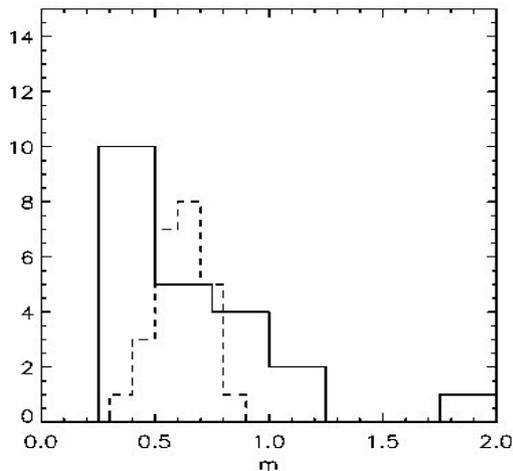

Figure 8. Seeing statistics for our atmospheric turbulence generator in the case of short exposures (solid line) and long exposures (dash line).
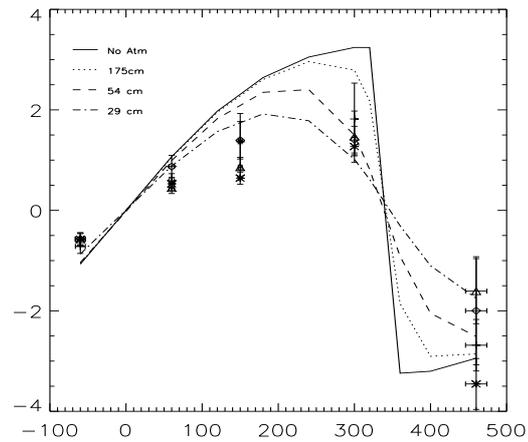
Figure 9. Comparison of the averaged experimental PTV signal amplitude (symbols) with simulated data (lines) for different atmospheric conditions.
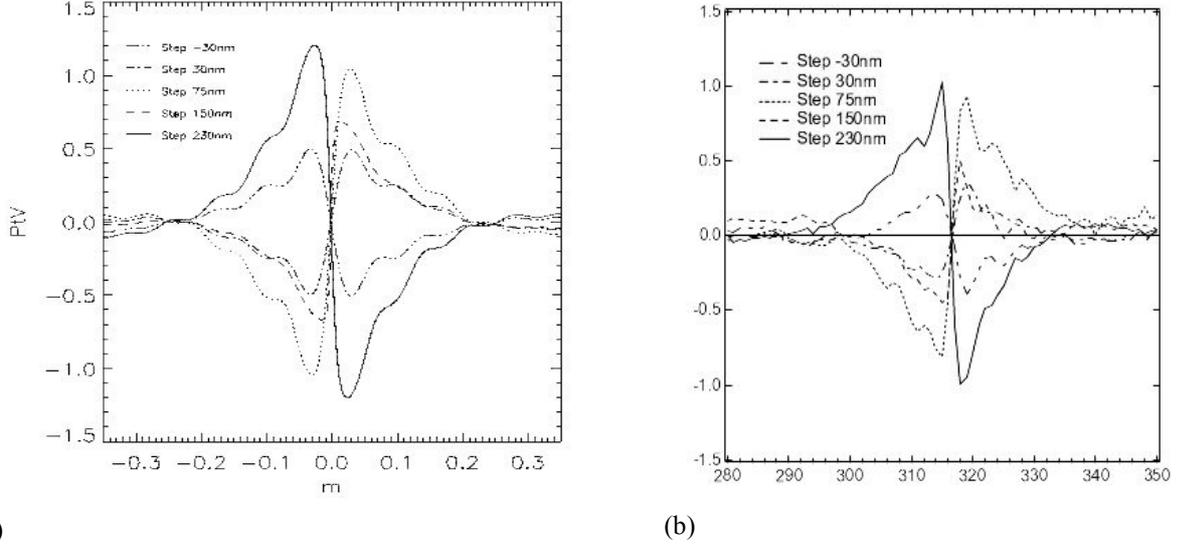
(a)   (b)

Figure 10. Simulated (a) and experimental (b) signal profiles for one border of each segment with atmosphere.

3. CLOSE LOOP SIMULATION

So far we considered the particular properties of the Mach – Zehnder interferometer. However, the signal retrieval algorithm for phasing close loop for the multi-segmented mirrors is general for all phasing techniques. It is based on the symmetric and anti –symmetric properties of the signal. In the following we describe this method together with the close loop results for the case of the Mach – Zehnder interferometer. In the cases of a curvature sensor and a pyramid sensor the functions J_1 and J_2, introduced below, will have different analytical expression keeping the same general properties.

3.1 Signal symmetric and anti-symmetric properties

One of the most important features uniting all phasing techniques is the localization of the   signal near the intersegment boundary. That means that on can retrieve the relative phase step between two adjacent segment edges by measuring the signal only near the given boundary. Of course to phase the whole segmented mirror one has to measure the relative phase step over all boundaries and then use the matrix algebra to calculate piston, tip and tilt for each segment. The close loop algorithm based on Singular Value Decomposition (*SVD*) is described later.

Let consider a given boundary and bound with it local Cartesian coordinate system: axis *y* coincides with the boundary and axis *x* goes through the segments' centres. Six independent values describe an arbitrary segment configuration in this coordinates. Phase piston on the left segment (in the half plane *x*<0) is φ_1, its physical bent about axis *x* is δ_{ly}, and about the axis orthogonal to *x* going through center of the left segment – δ_{lx}. The analogous three values for the right segment (in the half plane *x*>0) are marked with the index 2: φ_2, δ_{2y} and δ_{2x}. Although at this point we speak about the relative displacements of two segments and could set φ_1 equal zero, nevertheless it is more convenient to keep a zero phase offset with respect to the whole mirror as a shift of the central segment for example. For the following calculation it is convenient to express all values through the wavefront aberration component. The phase error in the segment center due to the corresponding segment bent is: $s_{1x} = 2\pi\delta_{1x}d/\lambda, \quad s_{2x} = ...$

The expression for Mach - Zehnder signal as function of piston, tip and tilt aberrations on each segment is [the paper in print]:

$$S(x, y) = \begin{cases} \sin[\Delta\varphi(x, y)]\operatorname{Re}J_2(x) + \operatorname{Im}J_1(x) - \cos[\Delta\varphi(x, y)]\operatorname{Im}J_2(x), & x < 0 \\ \sin[\Delta\varphi(x, y)]\operatorname{Re}J_1(x) + \operatorname{Im}J_2(x) - \cos[\Delta\varphi(x, y)]\operatorname{Im}J_1(x), & x >= 0 \end{cases} \quad (2)$$

where

$$\Delta\varphi(x,y) = \frac{2x}{d}(s_{2x} - s_{1x}) + \frac{2y}{d}(s_{2y} - s_{1y}) + (\varphi_2 - \varphi_1) - (s_{1x} + s_{2x}), \tag{3}$$

d is a segment flat to flat width, λ is a wavelength. For the Gaussian type of the pinhole function J_{12} is error function of a complex argument:

$$J_{12} = \text{sign}(x)\exp\left[-\frac{s_{12x}^2 + s_{12y}^2}{(db)^2}\right]\left[1 - \Phi\left(b|x| + i\frac{s_{12x}}{db}\right)\right]. \tag{4}$$

Parameter b is related to the pinhole full width half maximum a of the Gaussian pinhole as $b = 0.6\pi a/\lambda$. Real and imagery parts of J_{12} are shown in Figure 11. For the case of the round pinhole, as well as for two other types of the segment error sensors they are not anymore expressed through the error function, but have the similar general behavior.
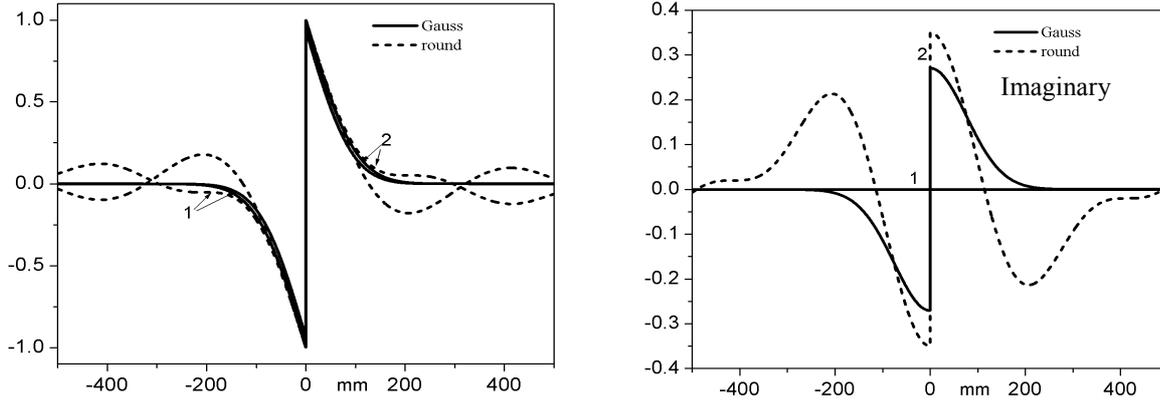

Figure 11. Real and imaginary parts of the function J. Curve 1: no tilts, curve 2: $s_x = 0.4db$, $s_x = 0$. For the zero tilts the imaginary part is zero.

In a case of the small errors the linear approximation for the signal is

$$S(x,y) \approx \Delta\varphi(x,y)\text{sign}(x)[1 - \Phi(b|x|)]. \tag{5}$$

From Eqs.3 and 5 it follows that the information about the difference $\varphi_2 - \varphi_1$ and the sum $s_{2x} + s_{1x}$ is contained in signal antisymmetric component with respect to the y axis, the difference $s_{2x} - s_{1x}$ is in the signal symmetric component with respect to the same axis, and the difference $s_{2y} - s_{1y}$ is in a signal antisymmetric component with respect to the x axis.

The area of signal localization we split into four identical zones as it shown in Figure 12 and integrate the signal $S(x, y)$ within each of this zone, calculating the integral values

$$I_n = \int_{\varepsilon_n} S(x,y)dxdy, \quad n=1...4. \tag{6}$$

Using this values we define the integral criteria: K_0 – symmetry coefficient with respect to y axis; K_1 – antisymmetry with respect to y axis and K_2 – antisymmetry with respect to y axis:

$$K_0 = (I_1 + I_2 + I_3 + I_4); \quad K_1 = (I_1 + I_4) - (I_2 + I_3); \quad K_2 = (I_1 + I_3) - (I_2 + I_4) \tag{7}$$

It can be seen that from Eq. 5 that each criterion is responsible for different aberrations:

$$K_0 \sim s_{2x} - s_{1x}, \quad K_1 \sim (\varphi_2 - \varphi_1) - (s_{2x} + s_{1x}), \quad K_2 \sim s_{2y} - s_{1y}. \tag{8}$$

With the increase of the segmentation errors the criteria K_n are not anymore the linear functions and their dependence on the different aberrations cannot be easily disentangled. Criteria K_n for the large rang of aberration values is shown in Figure 13. Criterion K_1 is a periodical sine function of the phase step, and the range of the measurable phase difference therefore is limited to $[-\pi/2, \pi/2]$. This problem, also called "π – ambiguity" appears in all co-phasing methods operating in a monochromatic regime. Within this capture range the phase can be reconstructed unambiguously. If the initial piston difference is beyond this limit, the segments may be phased not to the zero step, but to the integer number of wavelengths.
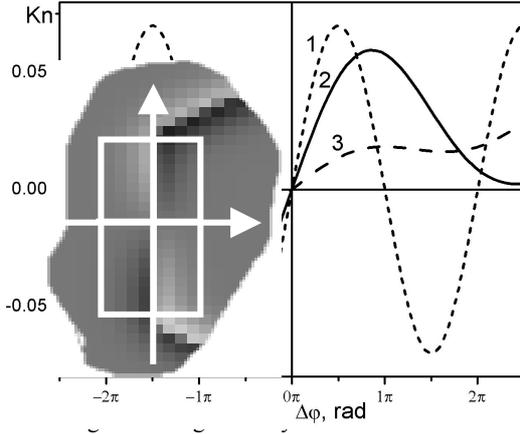
Figure 13. Behaviour of the criteria K_n. Curve 1: Criterion K_1 for the pistons only. Ordinate K_1; abscissa $\varphi_1 - \varphi_2$. Curve 2: Criterion K_2 for the difference of the y-tilts only. Ordinate K_2; abscissa $s_{2y} - s_{1y}$. Curve 3: Criterion K_0 for the sum of x-tilts only. Ordinate K_0; abscissa $s_{2x} + s_{1x}$.

3.2 Segmented mirror eigenmodes

In a sense of the reconstruction of the segmented mirror surface the criteria K_0, K_1, and K_2 are analogous to the measurements provided by the edge sensors. In the existing [Ref Keck] and the planned [Ref GTC] phasing systems two capacitive sensors, placed on each border of the segment, provide the information about the relative intersegment shifts. The sum of these two sensors reading is relevant to the piston between two segments and difference of two x-tilts. The difference between the readings contains the information about a relative y-tilt. That is completely analogous to the K_1 and K_2 criteria. Some edge sensors measure also the solid angle between segments or the sum of x –tilts, although with less sensitivity. This parameter is analogous to the criteria K_0, which is also much less sensitive to $s_{2x} + s_{1x}$ than K_1 to $\varphi_1 - \tilde{\varphi}_2$ or K_2 to $s_{2y} - s_{1y}$ (Fig. 4).

A vector $\mathbf{u} = \{K_{01}, K_{11}, K_{21}, \dots K_{0i}, K_{1i}, K_{2i}, \dots K_{0m}, K_{1m}, K_{2m}\}$, where m is the number of borders, forms a signal vector. An actuator vector consists of n triplets: three actuators v_{0i}, v_{1i}, v_{2i} for each segment, where n is a total number of segments: $\mathbf{v} = \{v_{01}, v_{11}, v_{21}, \dots v_{0i}, v_{1i}, v_{2i}, \dots v_{0n}, v_{1n}, v_{2n}\}$. The actuator vector $\mathbf{v}$ is related to the sensor vector $\mathbf{u}$ by the linear mapping represented as a two dimensional matrix $\mathbf{A}$ [ref. Chanan, Lothar]:

$$\mathbf{A}\mathbf{v} = \mathbf{u}. \tag{9}$$

An optimum modal correction requires the expansion of the signal u in an orthonormal set generated by SVD:

$$\mathbf{A} = \mathbf{U}\mathbf{\Sigma}\mathbf{V}^{\mathrm{T}}. \tag{10}$$

The $3n$ column vectors of $\mathbf{U}$ and $\mathbf{V}$ form orthonormal sets $\{\mathbf{u}_j\}$ and $\{\mathbf{v}_j\}$ correspondingly. Symbol $^{\mathrm{T}}$ denotes transpose. The matrix V defines an orthonormal basis for the system, i.e. segmented mirror modes. Any configuration of the segments can be expressed as a linear combination of those modes. The matrix $\mathbf{\Sigma}$ is diagonal and contains $3n$ singular values σ_j. Its value defines the sensitivity of the system to the mode with index j. So the modes which present the global mirror piston, global tip and tilt will have the singular value σ_j equal zero, because in these three aberrations there is no any relative segment shifts. Also the mode which corresponds to the global defocus will have σ_j very low, because it is formed only by the solid angle between segments and hence only criterion K_0 contributes in the measurement.

In modal control matrix $\mathbf{A}$ is found in calibration. The control matrix $\mathbf{B}$, which finds the actuator vector by a signal vector and is inverse to $\mathbf{A}$, is obtained as

$$\mathbf{B} = \mathbf{V}\mathbf{\Sigma}^{-1}\mathbf{U}^{\mathrm{T}}. \tag{11}$$

The diagonal matrix $\mathbf{\Sigma}^{-1}$ consists of the values σ_j^{-1}. To exclude the non-corrected modes with zero or very small singular values, the corresponding σ_j^{-1} in *SVD* are replaced by zero. The threshold depends on the value on noise in the system, because σ_j^{-1} defines the noise propagation from signals to actuator.

The difference between control provided by the edge sensors and the optical method is the signal vector **u** formed by criteria K_n. The mirror modes $\{u_j\}$ are the same as for the edge sensor as well as for the optical sensor if the mirror configuration is the same. So the performance of each of the methods can be analysed by a studying the singular values $\sigma_{j\cdot}$, which define the sensitivity to the modes and the noise propagation.

We simulated the segmented mirror consisted of 91 segments organized in 5 hexagonal rings. Pushing each segment by a given value for piston tip and tilt and calculating the criteria K_n, we constructed the calibration matrix. The area for signal analysis (Figure 11) was chosen to be square with the side $d/6$, where d is a segment flat to flat width. Applying a standard *SVD* algorithm on the calibration matrix, we obtained the eigenmodes and the singular values. The nine of the modes are shown in Figure 13, the singular values– in Figure 14. The low order modes are close to the classical optical aberrations – piston, tip-tilt, defocus, astigmatism, coma and etc. Piston, tip and tilt are not sensed by the system. The corresponding singular values are zeros. The defocus mode has a very low singular value $3 \cdot 10^{-3}$, compare to the mode with the highest singular value. Defocus is measured only by K_0, which is relatively weak
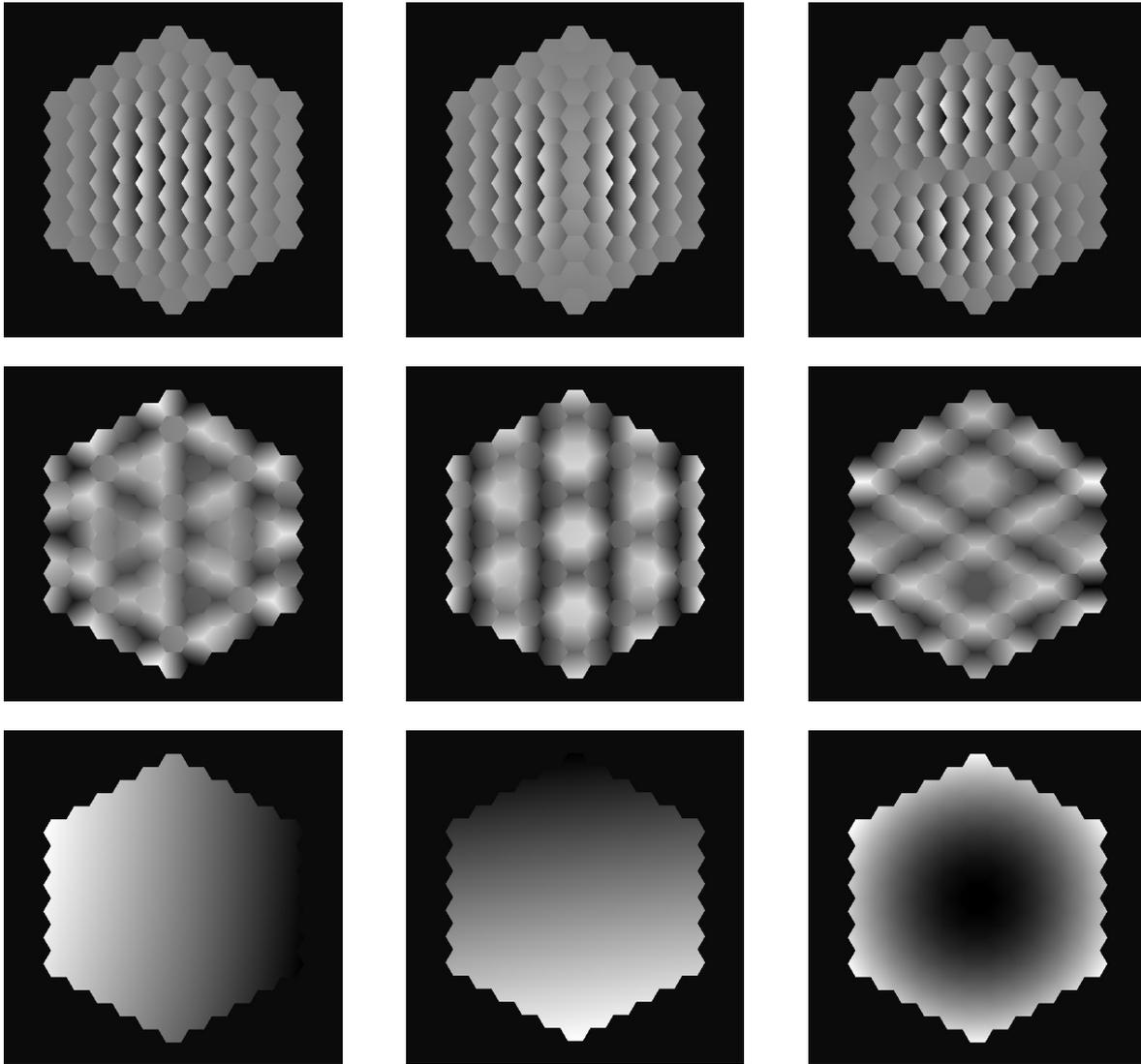

Figure 13. Nine out of 273 eigenmodes of the segmented mirror. The upper line is three highest modes with indexes 273, 272 and 271; in the middle – modes with the indexes 43, 42 and 41; and on the bottom: tip-tilt and defocus with the indexes 2, 3 and 4.
.
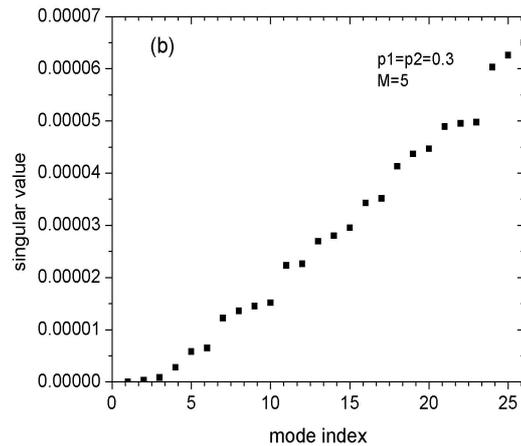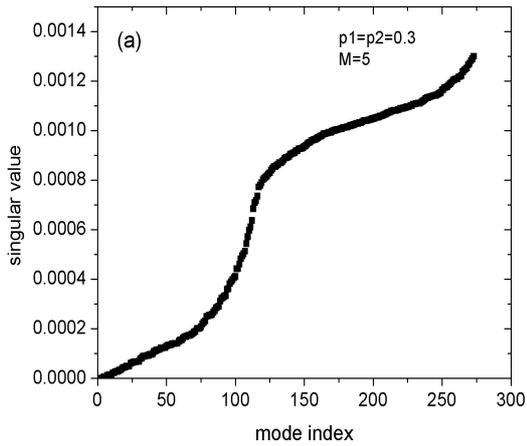
(a)   (b)

Figure 14. Singular values for the segmented mirror with 91 segments for all 273 eigenmodes (a) and for the last 26 modes with the lowest eigenvalues. Calculations include piston and tip-tilt for each segment.

Some telescopes use a separate method to correct tip-tilt if the segments, for example Schack – Hartmann sensor. Then the phasing camera is responsible only for the segment piston measurement. In this case only criterion K_1 is required. Among the mirror modes formed only by segment pistons one may recognize pseudo-defocus and pseudo-tip-tilt (Figure 7). Unlike the normal defocus and tip-tilt these ones are sensed by the system, because they are formed not by the solid angles between segment, but by the intersegment steps. The ratio between singular value corresponding to the pseudo defocus to the highest singular value is 0.2. For the pseudo tip and tilt it equals 0.15.

Figure 15.

Upper: Tip-Tilt and defocus formed by segment pistons

Left: Singular values for the segmented mirror with 91 segments. Calculations include only piston for each segment.

3.3 Close loop results

To close the loop we used the control matrix B given by Eq. 11. We did not introduce any additional noise into the system. The simulation was performed in the monochromatic regime using only one wavelength of 500nm. The result of phasing strictly depends on the initial 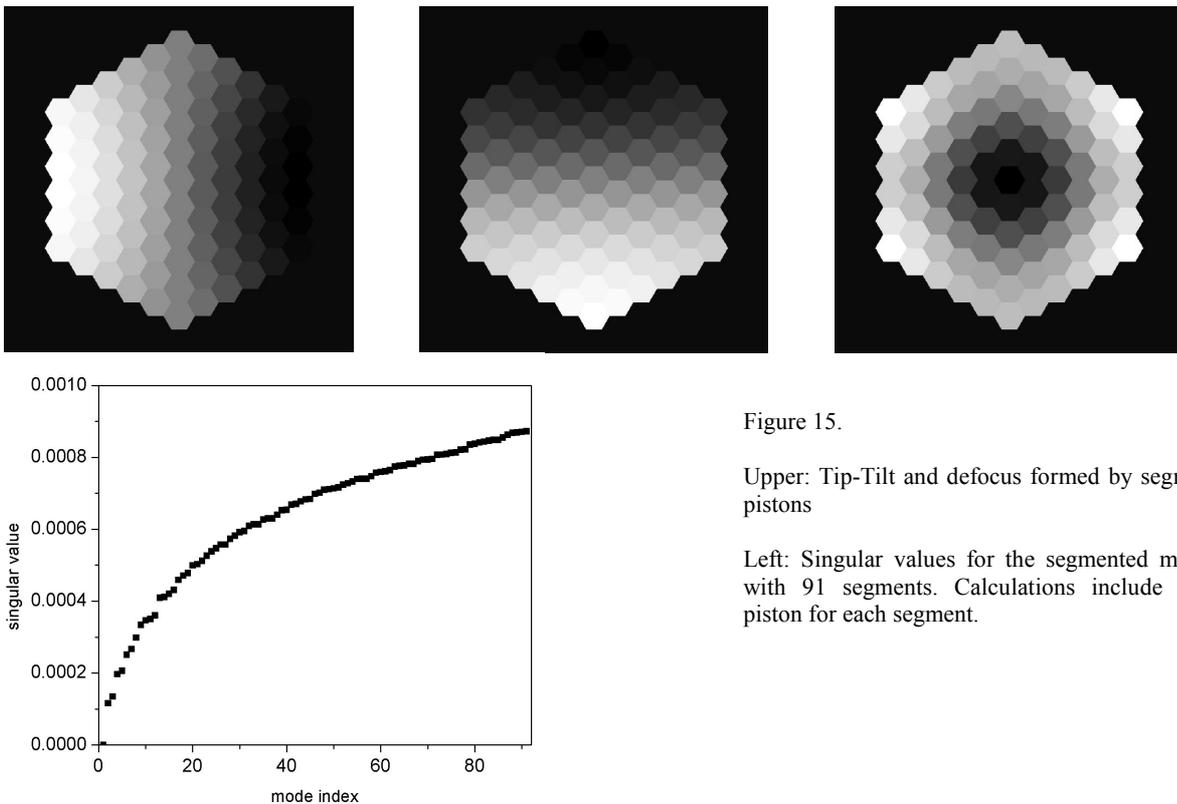rms. In Figure 16 we present a mirror *rms* evolving with phasing iteration for piston phasing only, as well as initial phase and the final phase for the large initial rms. For the small initial rms the residual wavefront is flat. If the initial *rms* is low all segment piston are within the capture range and in the result the zero error is achieved. With an increase of rms some segments are outside the capture range. They are "phased" to the nearest wavelength. As the result the initially randomly de-phased mirror contains some segments shifted by the integer number of the wavelength. To overcome this problem the multi -wavelength technique may be used.

In a case of piston and tip-tilt errors the situation is similar (Figure 17). Although in this case the capture range exists also for the tip – tilt value (curve 2 in Figure 12). We did not simulate the work of the active optics which would correct for the global tip- tilt and defocus. For the initially small rms the mirror is phased to the mode which is a linear combination of tip, tilt and defocus. For the large initial rms some other low order modes remain.

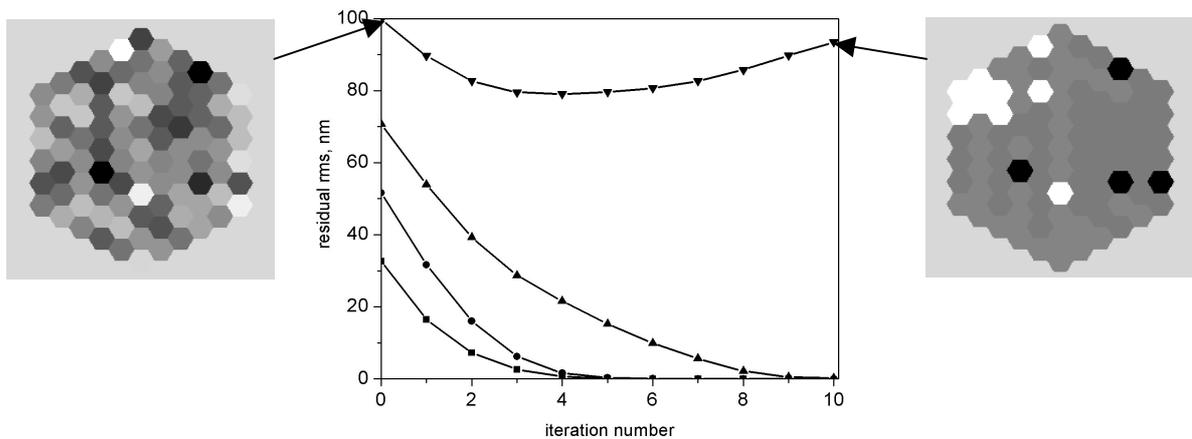Figure 16. Close loop on phasing for the piston error only for the different initial rms values. Initial and final segment errors distributions are shown for the case of a large initial rms.
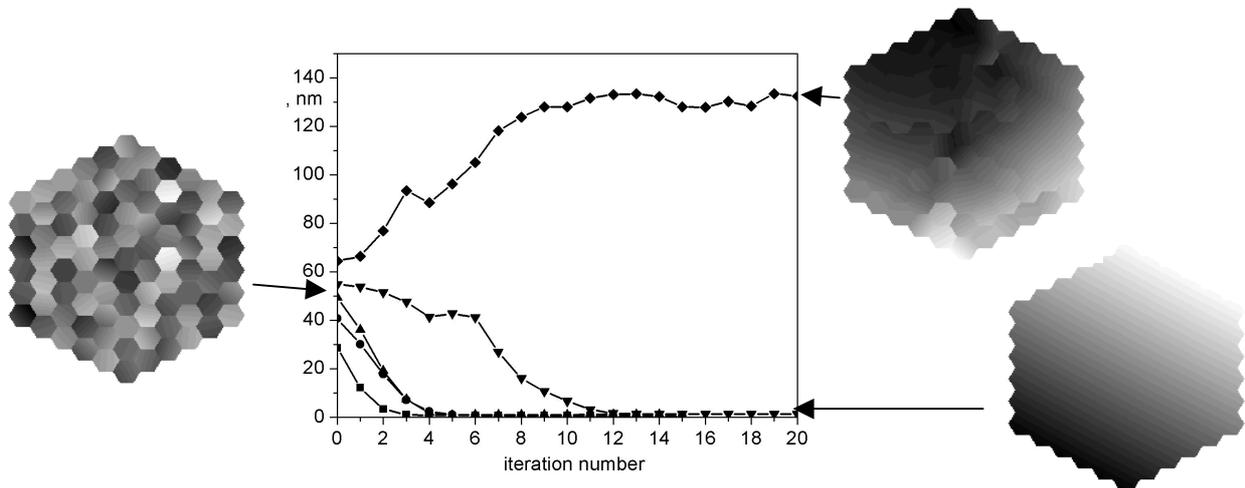

Figure 17. Close loop on phasing for the piston tip and tilt error for the different initial rms values. Initial and final segment errors distributions are shown for the case of a small and large initial rms.

4. CONCLUSION

Several optical methods for phasing of segmented mirrors were demonstrated experimentally and in the simulations. We presented the one based on the Mach – Zehnder interferometry. The signal predicted by the theory and in the computer simulations was observed experimentally in both conditions – with and without optical turbulence. The behavior of the signal on the intersegment step and the parameters of the system is in a good agreement with the theory and simulations.

The calculation of the symmetric and antisymmetric components of the signal makes an algorithm for the segment error retrieval analogous to the measurement with the use of the edge sensors. Both methods provide the same set of the mirror eigenmodes and show the same general behavior of the singular values. This fact makes the mirror control technique in both cases to be equivalent. The system is more sensitive to the high order segmented modes. They are corrected first. The low order modes are sensed less. These modes, which correspond to the classical optical aberrations, may remain uncorrected.

The main concern which is general for all optical approaches for segments phasing is the limited capture range. Even with the initial wavefront rms of $\lambda/5$ some segments of the mirror happen to be outside the capture range of $\pm \lambda/4$. In the used back loop control algorithm these segments are driven in a way to be at the wavelength difference with respect to their neighbors. In this respect it is required the more through study of the segmented mirror properties and of the behavior of the mirror eigenmodes together with the developing of the more accurate back loop control algorithm.

REFERENCES

1. E.T Brunetto, P. Dierickx, R. Gilmozzi, G.J. Monnet, "OWL phase A status report", 5489-23 at this conference.
2. G. Chanan and M. Troy, "Strehl ratio and modulation transfer function for segmented mirror telescope as function of segment phase error," Appl. Opt. 38, pp. 6642-6647 (1999).
3. N. Yaitskova, K. Dohlen, P. Dierickx, "Analytical study of diffraction effects in extremely large segmented telescopes" JOSA A/Vol. 20, No. 8, pp. 1563-1575 (2003).
4. J.N. Aubrun, K.R. Lorell, T.W. Havas, and W.C. Henninger (1988). "Performance analysis of the segmented alignment control system for the ten-meter telescope," Automatica, vol. 24, pp. 437-454.
5. S. Cuevas, V.G. Orlov, F. Garfias, V. Voitsekhovich and L. Sanchez, "Curvature equation for a segmented telescope," in *Optical Design, Materials, Fabrication, and Maintenanc*e, P. Dierickx, ed., Proc. SPIE **4003**, 291-302 (2000).
6. S. Esposito, E. Pinna, A. Tozzi, P. Stefenini, N. Devaney, "Co-phasing of segmented mirrors using pyramid sensor", in *Astronomical Adaptive Optics Systems and Applications*, R. K. Tyson, M. Lloyd - Hard, eds., Proc. SPIE **5169**, pp. 214-225 (2003).
7. A. Schumacher and N. Devaney, "DIPSS: cophasing segmented mirrors with minimal hardware requirement" (in preparation)
8. N. Yaitskova, "Performance analysis of Mach – Zehnder interferometer for detection of wavefront discontinuities", in *Astronomical Adaptive Optics Systems and Applications*, R. K. Tyson, M. Lloyd - Hard, eds., Proc. SPIE **5169**, pp. 62-71 (2003).
9. L. Montoya Martinez, N. Yaitskova, P. Dierickx, K. Dohlen "Mach-Zehnder wave front sensor for phasing of segmented telescopes", in *Future Giant Telescopes*, J. R. P. Angel and R. Gilmozzi, eds., Proc. SPIE **4840**, pp. 564-573 (2002).
10. K. Dohlen, A. Origné, D. Pouliquen, B. Swinyard, "Optical design of the SPIRE instrument for FIRST", in UV, optical, and IR space telescopes and instruments, J. B. Breckinridge, P. Jacobsen, Eds, Proc. SPIE **4013**, pp. 119-128 (2000).

APE: a breadboard to evaluate new phasing technologies for a future European Giant Optical Telescope

Frederic Gonte[a], Natalia Yaitskova[a], Philippe Dierickx[a],Robert Karban[a] Alain Courteville[b],
Achim Schumacher[c], Nicholas Devaney[c], Simone Esposito[d], Kjetil Dohlen[e], Marc Ferrari[e],
Luzma Montoya[e]

[a]European Southern Observatory,Karl-Schwarzschild-Str. 2, Garching, Germany;
[b]Fogale Nanotech,285 rue Gilles Roberval, Nimes, France;
[c]Instituto de Astrofisica de Canarias, Address,La Laguna, Tenerife,Espana;
[d]Arcetri Astrophysical Observatory,Largo E. Fermi, Florence, Italy;
[e]Laboratoire d'Astrophysique de Marseille,2 Place Leverrier, Marseille, France

ABSTRACT

The point spread function of a segmented aperture is seriously affected by the misalignment of the segments. Stringent requirements apply to position sensors and their calibration. The Active Phasing Experiment (APE) will be a technical instrument aimed at testing possible phasing techniques for a European Giant Optical Telescope (EGOT) in a representative environment. It will also integrate simultaneous control of segmented and monolithic, active surfaces. A mirror composed of 61 hexagonal segments is conjugated to the primary mirror of the VLT. Each segment can be moved in piston, tip and tilt and can be controlled in open or closed loop. Three new types of Phasing Wave Front Sensors dedicated to the measurement of segmentation errors will be tested, evaluated and compared: a modified Mach-Zehnder sensor developed by the LAM and ESO, a Pyramid Sensor developed by Arcetri, and a Curvature Sensor developed by IAC. A reference metrology developed by FOGALE will be added to measure directly the deformation of the segmented mirror and check the efficiency of the tested wavefront sensors. This metrology will be based on a synthetic wavelength instantaneous phase stepping method. This experiment will first run in the laboratory with point-like polychromatic sources and a turbulence generator. In a second step, it will be mounted at a Nasmyth focus of a VLT unit telescope. These activities are included in a proposal to the European Commission for funding within Framework Program 6.

Keywords: giant telescope, segmented mirror, phasing wavefront sensor, active optics

1. INTRODUCTION

The essential purpose of the APE experiment is to explore, integrate, and validate active, that is low temporal frequency, wavefront control schemes and technologies for an EGOT. This includes the evaluation and comparison of the performance of different types of wavefront sensors in the laboratory and on the sky on the one hand and the integration of the control of a segmented aperture control into an already existing active system (including field stabilization and active optics) and driving both the active system and the control of the segments from the output of the full system on the other hand.

To accomplish these taks APE will be designed as a technical prototype which will be installed and tested at a Nasmyth focus of a VLT unit telescope. The telescope provides all active functions (field stabilization, focusing, centering, active deformable mirrors) and the APE instrument emulates the optical effects of segmentation. The latter is done within APE by reimaging the telescope pupil onto a small Active Segmented Mirror (ASM) whose shape is measured by an internal metrology (IM). The ASM is composed of 61 hexagonal segments and has a diameter of approximately 15 cm. Each segments is controlled in piston, tip and tilt.

The final wavefront is measured by three new types of Phasing WaveFront Sensors (PWFSs), combined in the Phasing Metrology Module. The new types of PWFSs are a modified Mach-Zehnder interferometer, a curvature
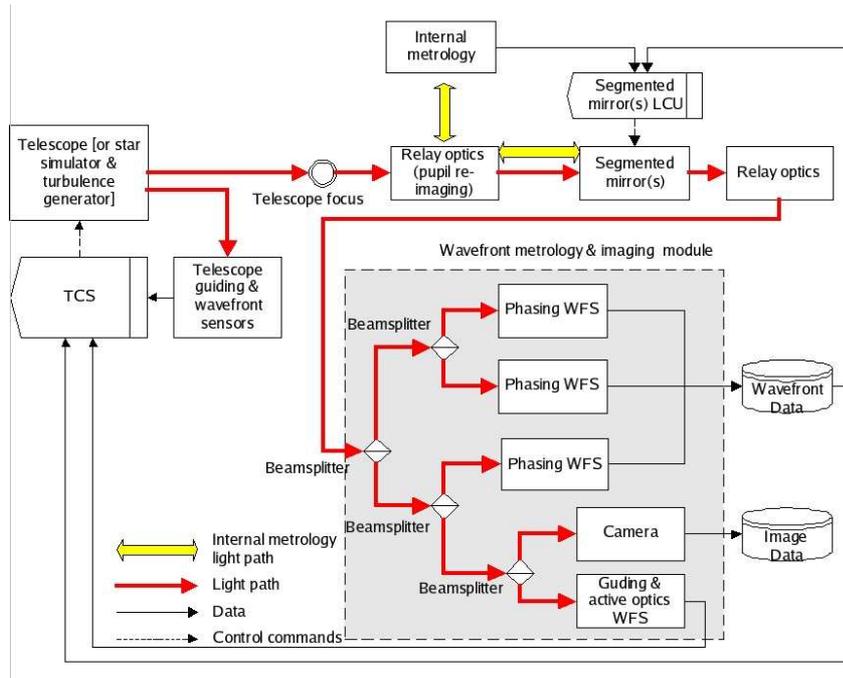

Figure 1. APE Schematic

sensor and a Pyramid sensor. For reference and comparison APE will also be equipped with a Shack-Hartmann sensor capable of measuring phase errors at segment edges.

APE is a four years project which starts in July 2004.

2. APE PRINCIPLE

Fig. 1 shows the principal components of APE. The light of the star collected by a VLT unit telescope or generated by a reference source and a turbulence generator is captured by the relay optics which re-images the primary mirror onto the ASM described in Ch. 3.4. The reflected light is then distributed to the different phasing sensors (see Ch. 4) and an imaging camera (see Ch. 3.3). An Internal Metrology (IM) described in Ch. 3.5 will measure the exact positions of the each of the 61 segments. It provides an independent check of the corrections applied to the segmented mirror. The ASM is controlled by the Telescope Control System (TCS). APE can work either be used to compare the measurements of the various phasing sensors with the measurements done by the internal metrology or work as a closed-loop control system correcting the telescope aberrations and the misalignments of the segmented mirror based on the measurements from one or more of the phasing sensors. Thereby it also serves as a testbed for the development of a control system for active optics of a telescope with segmented and flexible mirrors.

3. APE SUB-ELEMENTS

This chapter describes all components of APE except the Phasing sensors which are introduced in chapter 4). Fig. 2 shows the main components and elements of APE. In the hardware there is a clear distinction between the new PWFSs and the Shack-Hartman sensor (called Active Optics WFS), which is considered part of the Guiding & active optics group. It will be a reference against which the other sensors are tested. It will also supply information on the deformations of the meniscus mirrors in case this can not be delivered by the PWFS. In the Segmented mirrors group there is one in-pupil mirror, the ASM, and one out of the pupil mirror which will simulate a secondary segmented mirror on a giant telescope. The latter will either be a static segmented mirror or a transmissive phase plate.
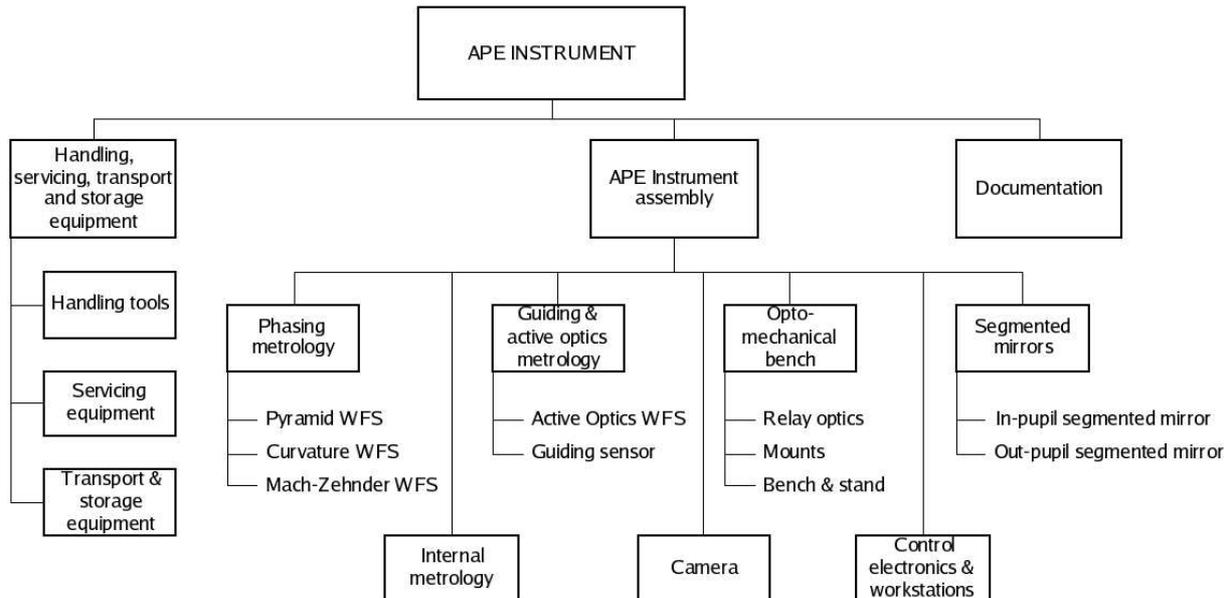
Figure 2. APE hardware Tree

3.1. Optical set up

Fig. 3 shows the optical design. The optical beam at the Nasmyth focus with a focal ratio of F/15, is collimated by a collimator, reflected by the segmented mirror, and then refocused by another collimator with the same focal ratio as the first collimator. The beam is then split into 5 different beams for the Phasing WFSs and the imaging camera. A system of two tip-tilt mirrors directs the light of a star or of the reference source to the WFSs. Each PWFS receive the same intensity. The static out of pupil mirror or piston plate is not represented in this design.

3.2. Mechanical set up

APE shall be mounted on an optical table with a size of 1.5 by 2.5 m. Since APE will be installed on the Nasmyth platform of a VLT unit telescope all the all components have to be compliant with the VLT standard. The derotator will directly be mounted on the interface of the VLT Nasmyth platform. The stability of the star on the phasing wavefront sensor shall be better than 0.1 arcsec. The calibration system is a copy of the MAD calibration system (see Marchetti & al.[1]).

3.3. Imaging camera

The imaging camera is composed of an ESO technical CCD having 1024*1024 pixels with a size of 13*13 microns. The CCD is Peltier cooled to less than -35 degrees Celsius and has a typical readout noise of less than below 50 e/pixel/sec. Its quantum efficiency is better than to 85%. The camera shall have a resolution better than 0.1 arcsec/pixel and a field of view of 1 arcmin. Because of the focal ratio of F/15 at the VLT Nasmyth focus, which is equivalent to 582 microns/arcsec, we need additional optics to obtain a magnification of 1/2.7.

3.4. Active segmented mirror

The segmented mirror is composed of 61 hexagonal segments as shown in Fig. 4. The size of the segments flat to flat is between 15 and 23mm. The gap between the segments is 0.15mm. The segments are aluminum coated to obtain a reflection of more than 85% from 450nm to 1400nm. The misfigure of the segments shall be less than 30 nm wavefront RMS. The segments are controlled in piston, tip and tilt, and the range of the position actuators shall be between ±5 and ±10 microns. The segmented mirror shall have has a closed loop bandwidth of 5 Hz.
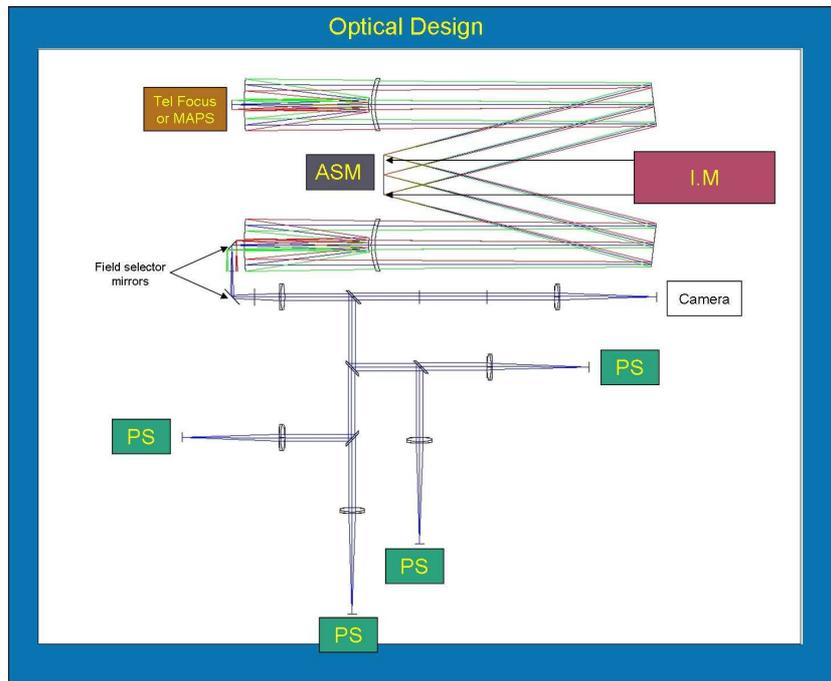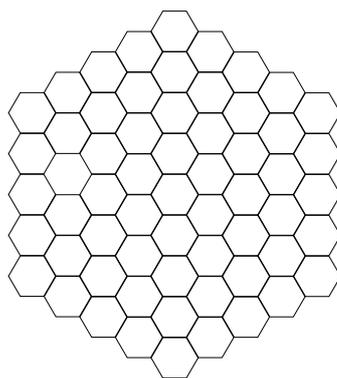
Figure 3. APE Optical Design
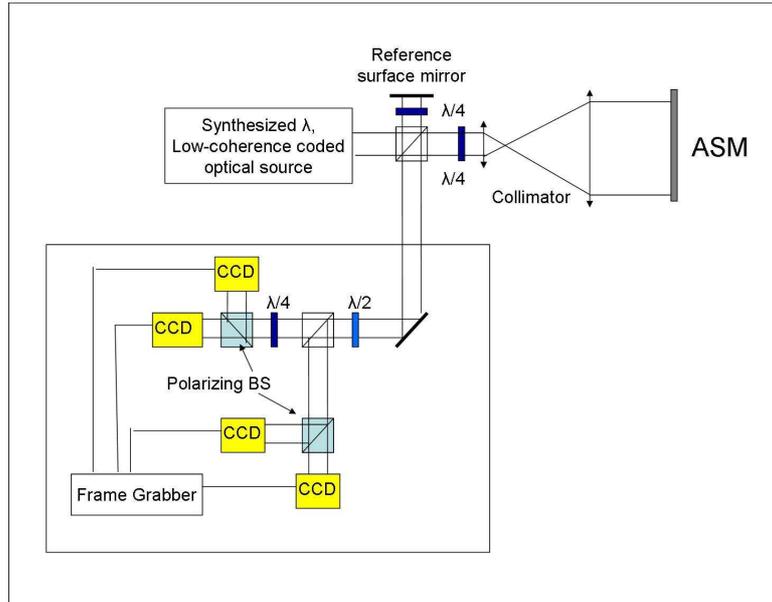

Figure 4. ASM design.

Figure 5. Internal Metrology design.

3.5. Internal metrology

The internal metrology is delivered by FOGALE nanotech. It is a synthetic wavelength interferometer. This is a polarization Twyman-Green interferometer illuminated by a synthesized wavelength low-coherence coded optical source. The synthetic wavelength is obtained from 2 wavelengths and can be adjusted by choosing the right separation between λ_1 and λ_2 and is given by

$$\Lambda = \frac{\lambda_1 \lambda_2}{\lambda_1 - \lambda_2}$$

The two wavelengths are 850 nm and 800 nm which gives a synthetic wavelength of 13.6 microns. The resolution of the piston measurement on the segments will be 1 nm RMS. Fig. 5 shows the proposed optical layout based on a Twyman-Green interferometer which measures the optical path difference between the reference mirror and the test surface (ASM).

3.6. Turbulence Generator

A combined star simulator and turbulence generator named MAPS has been developed, mounted and tested at ESO (See Kolb & al.[2]). It can simulate the effects of three turbulent layers in the atmospheres at different altitudes with a total seeing of up to 0.65 arc second using three transmissive phase screens which are conjugated to the three altitudes. It also simulates a field of 2 arcminutes containing up to 34 stars. This turbulence generator will first be used in the experiment MAD (see Marchetti & al.[1]) and then in APE.

4. PHASING WAVEFRONT SENSORS

One of the goals of APE is to compare simultaneously the performance of several PWFSs. They will therefore receive the same amount of light for simultaneous exposures and will use the same VLT technical CCDs with identical control systems. The four PWFSs to be compared are MAZES proposed by LAM, PYPS proposed by ARCETRI, DIPSS proposed by IAC/GTC, and a SHAPS which will be supplied by ESO.
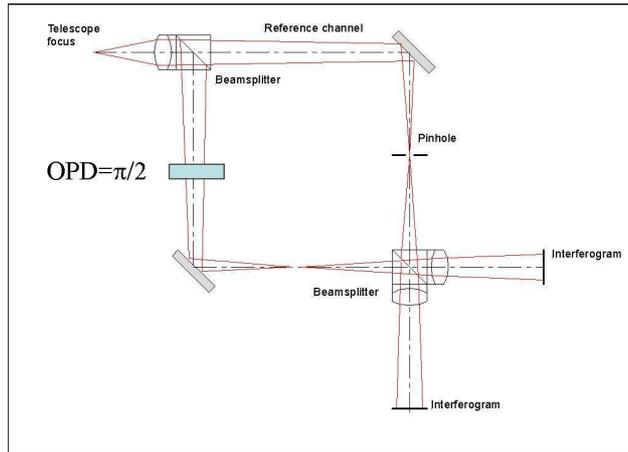
Figure 6. MAZES Principle.
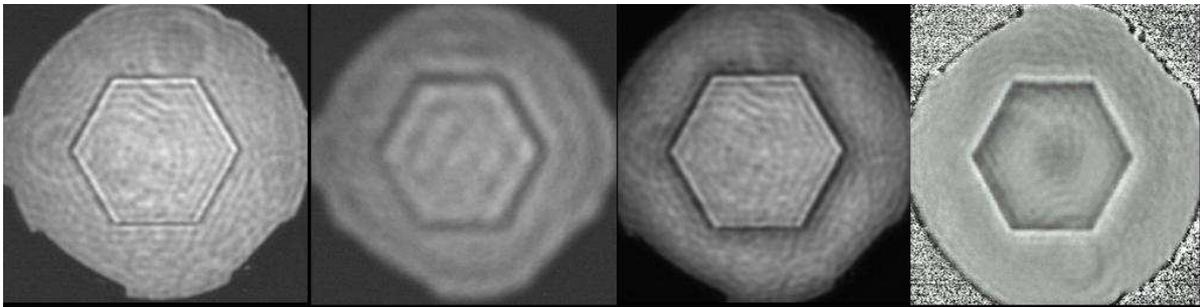
Figure 7. Measured intensity distribution of arm 1(a), arm 2(b), the interferogram(c) and of the normalized signal(d).

4.1. MAZES: Modified Mach-Zehnder Phasing Sensor

MAZES will be designed by LAM and ESO. A schematic view is given in Fig. 6. Its principle has been developed by Natalia Yaitskova, Kjetil Dohlen and Luzma Montoya (see Yaitskova & al.[3]). The telescope beam is focused inside the Mach-Zehnder interferometer. In one of the two arms at the point spread function at the location of the focus will be filtered spatially by a pin hole with a size of the same order as the size of the image, that is the diffraction pattern in the case without and the seeing pattern in the case with atmosheric disturbances. The segmented mirror is then reimaged after the interference via a lens onto the detectors. The optical phase difference between the two arms must be equal to $\pi/2$. This can be achieved by alignment or with a phase plate. The signal is obtained by taking the difference of intensities between the two arms. A prototype has been mounted at the Observatoire de Marseille and tested with a piston mirror. During the test a turbulence generator simulated seeing up to 0.45 arcsecond and $r_0 = 25.8$ cm at 680 nm. The recorded signals are shown in Fig. 7.

4.2. PYPS: Pyramid Phasing Sensor

The pyramid sensor has first been proposed by R. Ragazoni (see R. Ragazzoni[4]) for use in adaptive optics. PYPS will be developed by ARCETRI. A preliminary theoritical and experimental study has been made by S. Esposito (see Esposito & al.[5]) to adapt it to the phasing of mirror segments. According to this study with a star of visual magnitude 15 the resolution should be better than 40 nm RMS. The principle of PYPS is shown in Fig. 8.
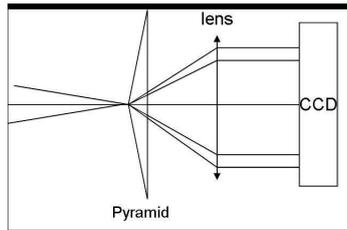
Figure 8. Principle of PYPS.
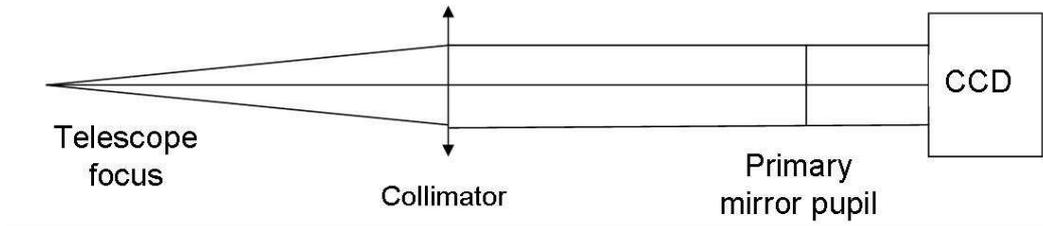
Figure 9. DIPSS Schematic.
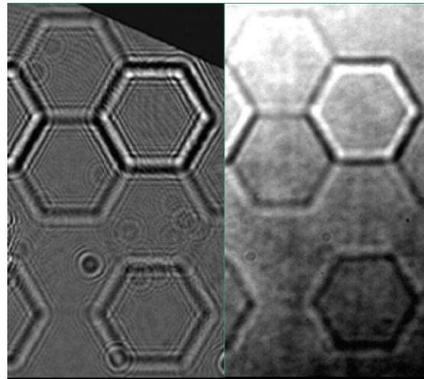
Figure 10. (a)DIPSS signal no turbulences (b) DIPSS signal with seeing = 0.65 arcsec.

4.3. DIPSS:Diffraction Image Phase Step Sensing

The principle of a curvature sensor has been first described by Roddier. The Institute of Astrophysics of the Canaries Island (IAC) proposes a modified curvature sensor called DIPPS. The principle has been developed by Achim Schumacher. (see Schumacher & al.[6]). A schematic view is shown in Fig. 9.

A preliminary experiment has been done in Garching using a turbulence generator and a piston plate, The piston plate was composed of 37 segments with 4 levels of piston steps and was placed on the pupil position of the primary mirror. The experiment has been done with and without turbulence equivalent to a seeing up to 0.6 arcsec. The first analysis of the result shows an error of less than 15 nm RMS without turbulences and better than 25 nm RMS with seeing of 0.6 arcsec. Further analysis will be done. Fig: 10 shows the signal without and with atmospheric turbulence.

4.4. SHAPS: Shack-Hartmann Phasing Sensor

The Shack-Hartmann sensor called SHAPS will be developed by ESO. It will be the reference for the other PWFSs and it will be used also as the guiding and active optics WFS. An ESO technical CCD will be used with
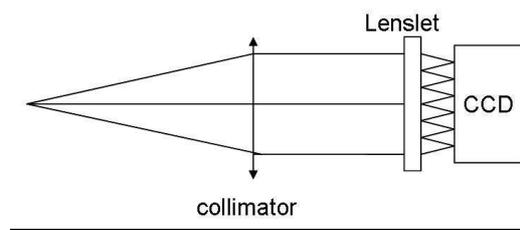
Figure 11. SHAPS.

a size of 1024*1024 pixels. The microlenses will be designed to specifically measure piston, tip and tilt of each segment. Its principle is shown in Fig. 11.

5. APE CONTROL SYSTEM

The Active Phasing Experiment Control Software (APECS) is required to carry out the APE project. The control software has to provide the means to interface, control and monitor the various devices needed for this project. The software will provide all the necessary functionality to evaluate the control system under laboratory conditions and under the conditions in the VLT environment.

The system must accomplish the coordination between the wavefront analyses done by several PWFSs, control of the segment mirror ASM and the VLT active optics and the coordination between the imaging camera used to select the star and the field selector composed of 2 scanning mirrors. It shall control all TCCDs (Technical CCD) (from the PWFSs and of the imaging camera), the field selector and its scanning mirrors, the ASM, the 3-axis table of the calibration unit, the derotator since APE will be on the Nasmyth platform, the Z-tables for the imaging camera and the PWFSs (focusing).

APECS shall deliver the control loops of the ASM in open and closed loop with the IM or with any of the PWFS at up to 5Hz.

The system shall provide extended test facilities, both for individual APE devices and for higher level operation. The system shall interface the IM with ASM control LCU (Local Control Unit), it also shall interface and control the VLT TCS-active optics of M1 and M2 with the data from the PWFS and active optics WFS.

The baseline of the control software will be the VLT Common Software (VLTSW).

6. APE MEASUREMENTS CAMPAIGNS

APE Technical runs shall last a year with a first period in laboratory and then a second period on the VLT. The first period shall last 6 months. the second is on the Paranal mountain and shall consist of 3 campaigns of the maximum duration of 2 weeks each. Between each campaign we shall reserve 2 to 3 months for the processing and analysis of the measurements and planning of the next campaign.

REFERENCES

1. E. Marchetti and al, "MAD status report," in *Advancements in Adaptive Optics*, *Proc. SPIE* **5490**, 2004.
2. J. Kolb and al, "MAPS: a turbulence simulator for mcao," in *Advancements in Adaptive Optics*, *Proc. SPIE* **5490**, 2004.
3. N. Yiatskova and al, "A Mach-Zehnder phasing sensor for extremely large segmented telescopes: Laboratory results and close loop algorithm," in *Ground-based Telescopes*, *Proc. SPIE* **5489**, 2004.
4. R. Ragazzoni, "Pupil plane wavefront sensing with an oscillating prism," *J. Mod. Opt.* **43**, pp. 289–293, 1996.
5. S. Esposito and al, "Co-phasing of segmented mirrors using pyramid sensor," in *Astronomical Adaptive Optics Systems and Applications*, R. Tyson, ed., *Proc. SPIE* **4839**, pp. 72–78, 2003.
6. A. Schumacher and N. Devaney, "DIPSS: cophasing segmented mirrors with minimal hardware requirements," *Applied Optics.* **To be published**, 2004.

MACH-ZEHNDER WAVEFRONT SENSOR
FOR PHASING OF SEGMENTED TELESCOPES

L. Montoya Martinez*[a], N. Yaitskova**[b], P. Dierickx**[b], K. Dohlen*[a]
[a]Laboratoire d'Astrophysique de Marseille
[b]European Southern Observatory

ABSTRACT

Segmented mirror technology has been successfully applied to 10m class telescopes (Keck, HET, GTC) and is widely recognized as mandatory for Extremely Large Telescopes. For optimal performance the wavefront error associated with segmentation should remain within conservative limits, typically $1/20^{th}$ of a wave. Several phasing techniques and associated metrologies are under development, with a view to extrapolate such methods to the 100-m OWL telescope. We investigate a novel technique based on Mach-Zehnder interferometry, whereby the wavefront in one of the interferometer arms is spatially filtered so as to provide a reference wave, prior to having the two arms recombined to produce suitable interferograms. We introduce a theoretical description of the interferometer, as well as results of simulations, showing that with proper settings of the interferometer's parameters, the technique can be made insensitive to atmospheric turbulence and, more generally, to almost any error source not associated with the segmentation. It also appears that, in a telescope that would include more than one segmented mirror, simple processing allows to disentangle the signal associated to each of them. Finally, we outline the development still required to complete a full qualification of this approach.

Keywords: phasing, segmented mirrors, OWL, Mach-Zehnder interferometry.

1. INTRODUCTION

Optical segmentation is widely recognized as prerequisite to extrapolating telescope sizes much beyond current figures. While the technology has been successfully demonstrated with the Keck 10-m telescopes, Extremely Large Telescopes (ELTs) will require a one to two orders of magnitude increase in the number of segments, hence in the number of degrees of freedom to be controlled reliably and accurately. The techniques generally promoted for ELTs are, in their principle, identical to that routinely implemented in the Keck. Position sensors conveniently located at the back or the edges of the segments provide, in real time, measurements of the inter-segments steps, down to a few nanometers accuracy. Whichever technology such sensors rely on, periodic calibration of their readings appears necessary. This calibration is ideally performed on-sky; Chanan et al[1] have successfully developed a wavefront sensing technique which allows re-calibration of the Keck sensors, within adequate accuracy and at an affordable cost in terms of operational overheads –typically a few hours on a monthly basis. The technique seems scalable to a very large number of segments, within existing technology [1]. In the case of OWL, which has segmented primary and secondary mirrors, the technique would most likely require two wavefront sensors, each fitted with proper pupil masks centered on the images of segment boundaries. Those would provide independent calibrations of each segmented mirror.

Even though the progress of sensor technologies should logically lead to better temporal stability than in the Keck, ELTs are required to routinely achieve diffraction-limited resolution, thus implying tighter phasing requirements and lower allowances for sensor drift. In addition, the Keck technique implies a tight centering of the pupil mask in the wavefront sensor and requires relatively bright stars. Even though improvements seem possible, as proposed by the Gran Telescopio de Canarias (GTC) team[2], there are strong incentives to develop alternative calibration techniques.

Within the framework of a European Community-funded Research and Training Network (RTN) on adaptive optics for Extremely Large Telescopes, the Laboratoire d'Astrophysique de Marseille and the European Southern Observatory are jointly evaluating a technique based on Mach-Zehnder interferometry. This is one of several alternatives explored by the Network, which is in the process of establishing a comprehensive review of possible phasing techniques. Different techniques are evaluated with respect to accuracy, capture range, reference source brightness, sensitivity to wavefront errors not directly related to segmentation, sensor complexity and tolerances, and operational overheads. In the following, and after detailing its theoretical properties, we will use simulations to show that a properly tuned Mach-Zehnder interferometer is relatively insensitive to atmospheric turbulence and any error source of lower spatial

frequency, thus allowing it to measure phasing errors on seeing-limited star images and, by implication, on strongly aberrated images. We will also provide results indicating that the signal could easily be processed to deliver the phasing information associated to multiple segmentation, as required in the 100-m OWL telescope. Although a complete characterization of the sensor still requires proper evaluation of tolerances and of practical implementation aspects, current results suggest that a sensor tailored to OWL properties could be built using readily available technology.

2. MACH-ZEHNDER COPHASING SENSOR CONCEPT

2.1 Concept overview

The purpose of the Mach-Zehnder wavefront sensor is to measure phase properties of the incoming wavefront by applying appropriate spatial filtering in one of the interferometer arms. In practice, this can be done by making sure the beam goes through a focus within the interferometer, as shown in Fig.1. The idea to use this kind of interferometer to measure atmospheric wavefront errors was first introduce by Angel [3]. A pinhole of size (as projected onto the sky) of the order of λ/D, where D is the telescope diameter, is placed in the focal plane of one of the arms, producing a spherical wavefront. When recombined with the wavefront coming from the other arm an interferogram is produced, from which atmospheric errors can be deduced. However, when atmospheric aberrations are large, this technique becomes very inefficient since the pinhole is much smaller than the seeing disk. Also, the number of fringes is large, making interferogram analysis very difficult.

We propose to use a modified version of this technique for measurement of segment phasing errors. Phase steps create wavefront errors of all spatial frequencies, and, as we will show, the step-induced errors becomes dominant over atmospheric errors for spatial frequencies higher than about λ/r_0. Increasing the pinhole size to about the size of the seeing disk allows to cancel out phase errors due to the atmosphere while retaining enough information about phase steps to generate a useful signal. Fig. 2 illustrates the selective blurring effect of increasing the pinhole size. In this simulation, we generated an arbitrary wavefront, and calculated the interferograms with increasing pinhole sizes.
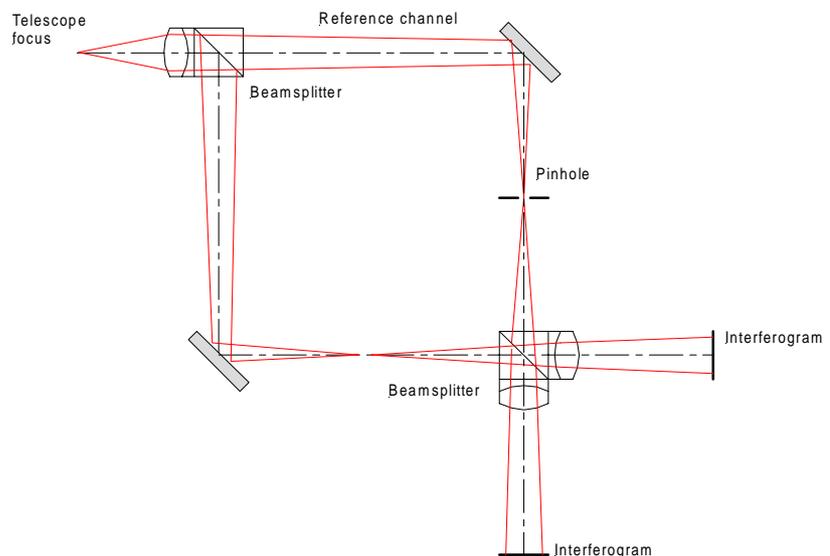

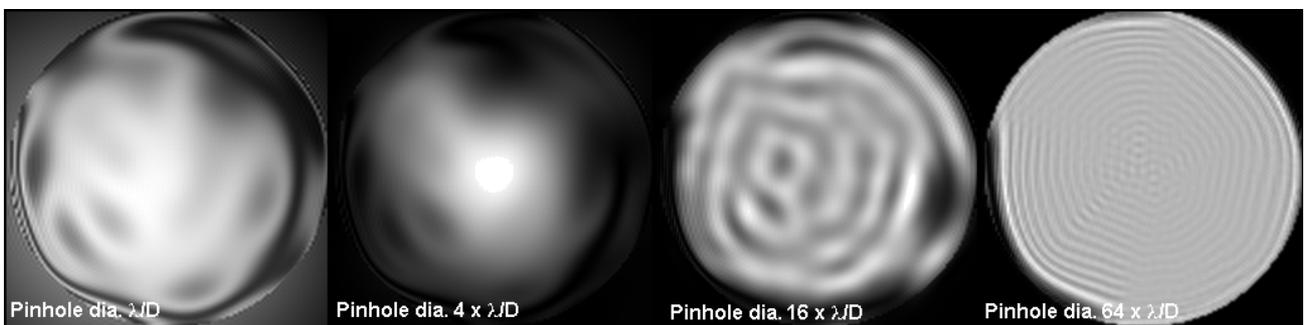Fig1:.Layout of a Mach-Zehnder interferometer.

Fig.2: Simulated Mach-Zehnder interferograms in the presence of atmospheric seeing for different size of pinhole.

2.2 Theoretical analysis

One advantage of the Mach-Zehnder sensor is that the wavefront errors are measured directly from the interference pattern registered on the detectors. The intensity in the two interferograms is proportional to the cosine of the phase difference between the two arms. By conservation of energy, these two patterns are complementary when the beam-splitter is non-absorbing: maxima in one correspond to minima in the other. If both interferograms can be detected, calculating their difference doubles the sensitivity as compared with a single interferogram and eliminates the common background.

The two complex amplitudes at the output pupil plane are:

$$\mathbf{A}_1 = \frac{1}{\sqrt{2}}\left(A'e^{i\varphi'} + A''e^{i\varphi}\right) \qquad\qquad \mathbf{A}_2 = \frac{1}{\sqrt{2}}\left(A'e^{i\varphi'} - A''e^{i\varphi}\right)$$

where A' and φ' are the amplitude and phase of the wavefront after the pinhole and A'' and φ are the amplitude and phase of the reference wavefront.

The intensities of the interferograms are calculated as $I = |AA^*|^2$

$$I_2 = \left(\frac{I'}{2} + \frac{I''}{2}\right)(1 - V\cos(\varphi - \varphi')) \qquad\qquad I_1 = \left(\frac{I'}{2} + \frac{I''}{2}\right)(1 + V\cos(\varphi - \varphi'))$$

where $I' = A'^2$ is the intensity after the pinhole in one of the arms, $I'' = A''^2$ is the intensity in the other arm before recombination, and V is the visibility of the fringes in the output pupil plane. As expected, the intensities of the interferograms are, apart from a constant, proportional to the cosine of the phase difference.

From these interferograms we can not retrieve the sign of the phase because of the symmetry of the *cosine* function, $cos(\varphi-\varphi')=cos(\varphi'-\varphi)$. This problem can be solved if a constant optical path difference (OPD) is introduced in one of the arm. If the OPD=$\lambda/4$, corresponding to a phase difference of $\pi/2$, the intensities are proportional to $cos(\varphi-\varphi'+\pi/2)=sin(\varphi-\varphi')$, and the anti symmetry of the *sine* function permits the sign distinction, $sin(\varphi-\varphi')=-sin(\varphi'-\varphi)$.

As discussed in section 2.1 the pinhole acts as a low pass spatial filter in one of the arms. When the two wavefront coming from two arms recombine the whole Mach-Zehnder acts as a high pass filter. In this sense this type of Mach-Zehnder sensor is equivalent to a Smartt interferometer or a stellar coronograph.
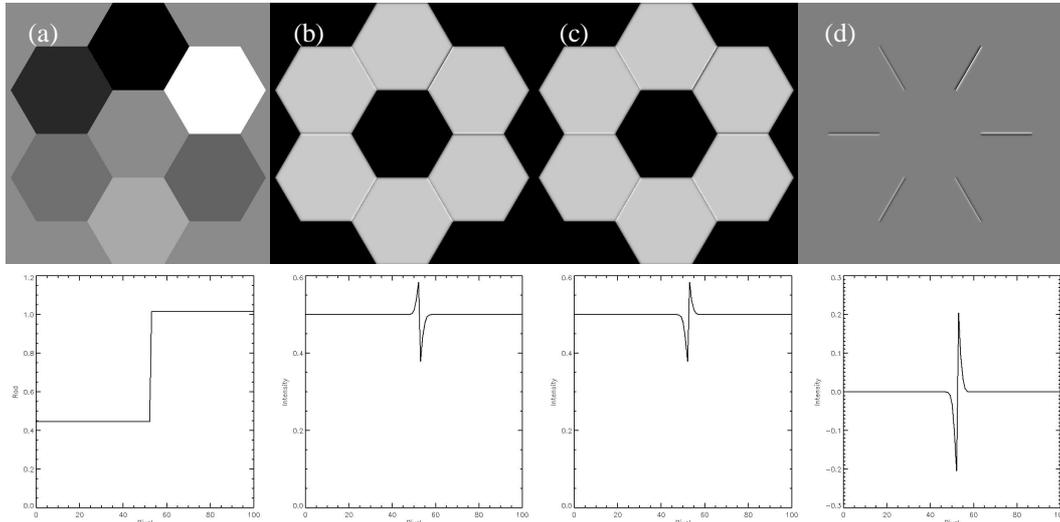

Fig3: Mach Zehnder simulation for segmented mirror with random rms piston error of $\lambda/8$ and pin hole size=2.3", (a)input wavefront,(b) Interferogram output 1,(c)Interferogram output 2,(d) difference between interferograms. The lower row represents a transversal cut along the segment edge.

3. PERFORMANCE OF A MACH-ZEHNDER PHASING INTERFEROMETER

In this section we explore the effect of some of the parameters of the Mach-Zehnder wavefront sensor. Those parameters are the shape and size of the pinhole, which are directly related to the pupil sampling, and the optical path difference (OPD) between two arms of the interferometer. The goal is to find an optimal configuration to extract the phase errors with the maximal accuracy.

For this purpose we have simulated a segmented pupil with seven 0.9m side hexagonal mirrors with random piston errors. In Fig.3 we show an example of this configuration, in the left we show the input wavefront for a segmented pupil with random piston error of $\lambda/8$ with $\lambda=0.656$ μm. In the middle we plot the two outputs interferograms, using a pinhole size 100 times the size of the airy disk ($100\lambda/D\approx2.3$''). On the right the difference between the two interferograms is plotted. We are interested in the profile of the interferogram along the segment edge, as plotted at the bottom of Fig.3.

3.1 Pinhole profile
To avoid diffraction artefacts associated to the pinhole sharp edge, the circular top hat mask may be replaced with an apodized mask with a Gaussian profile. The comparison of illumination profiles for the two mask types is shown in Fig.4. Segment piston in both cases is $\lambda/6$, wavefront. The FWHM of the Gaussian mask is equal to the diameter of the top hat mask in the first case. Diffraction artefacts are clearly eliminated with a pinhole having a gaussian profile.
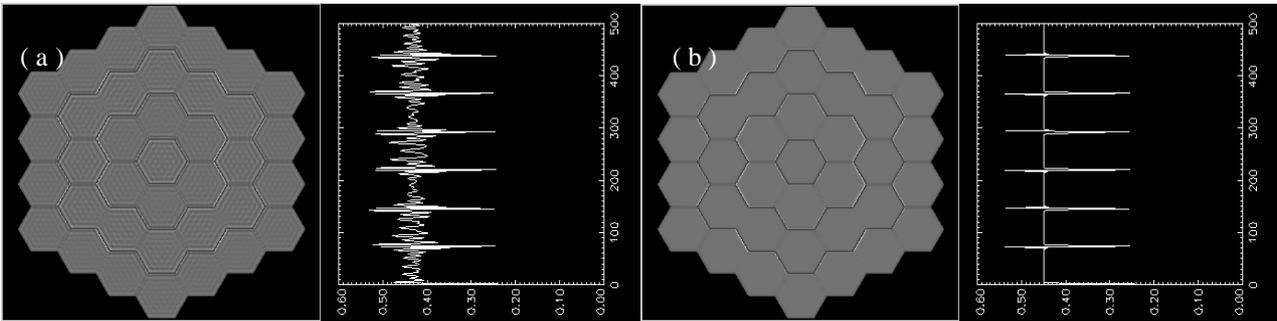
Fig.4: Comparison between the Mach Zenhder interferogram using a pinhole with circular shape (a) and pinhole with gaussian shape(b). A transversal cut along the main y-axis of the interferogram shows the elimination of bound effect.

3.2 Mask size, pupil sampling
The optimal pinhole size is defined by the number of pixels required to resolve the signal profile and by the range of frequencies to be spatially filtered. Pupil sampling and pinhole size are evidently correlated, as the pinhole acts as aperture for the pupil imaging system. The smaller the pinhole size, the larger the Point Spread Function (PSF)of this system is, hence the larger the width of the signal profile. This relation is illustrated by plotting the width of the signal fluctuation as a function of the inverse of the pinhole size, Fig.5.

We find a linear relation between the size of the pinhole and the width of the profile, shown in Fig.6. To resolve the profile signal at least 4 pixels are required. This means the diameter of the hole should be less than 0.8304 Nλ/D, where N is the number of pixels accross the interferogram, λ is the wavelength and D is the pupil diameter. For OWL, with a primary of D = 100m, and assuming λ = 500nm, the pinhole should be smaller than 1.65" for a 2Kx2K detector. For a 4Kx4K detector the maximal size is 3.3". If we want to blur the effect of atmospheric turbulence, the hole size will also depend on the size of λ/r_0 (we will come back later to this point).

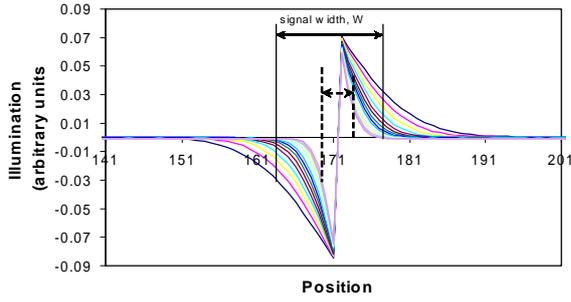Fig.5: Intersegment illumination for different size of pinhole from FWHM=2" to FWHM=0.5".
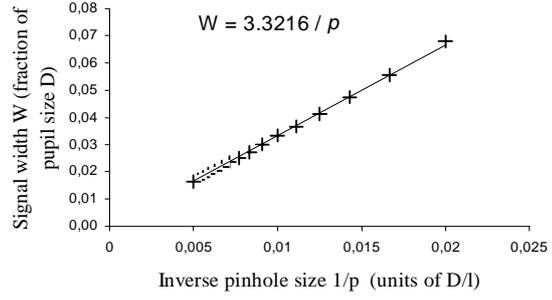
Fig.6: Linearity of width of interference profile with pinhole size.

3.3 Phase retrieval algorithm

In this section we introduce an OPD between the two arms of the interferometer and we describe a simple algorithm to retrieve the phase from the profile of the difference between the two outputs at the segment boundary.

In Fig.7 we show three sets of interferograms for different OPDs, conveniently introduced as a constant phase shift in the reference arm of the interferometer. From left to right, the figure shows the interferogram profiles for the two outputs and their difference (referred to as differential interferogram). At zero OPD (upper row) the phase information is contained within a distinct peak appearing at the segment boundary. The height of the peak is proportional to the square of the phase step; the sign of the phase value is therefore lost. At non-zero OPD, a signal oscillation appears at the segment edge. We refer to the amplitude of this oscillation as the peak-to-valley (PtV) value. In Fig.8 we show the PtV value as a function of OPD for $\lambda=0.656\mu m$. The phase shift $\lambda/4$ (or $3\lambda/4$, due to the symmetry) allows achieving the maximum PtV i.e., maximum contrast. As seen in the lower panel of Fig. 7, with this OPD the two interferograms have the same background level so that when we subtract them the background is eliminated.

For small intersegment steps, the PtV is proportional to the phase step between segments, representing a good estimate of residual phasing errors. In Fig.9, we plot the PtV for two wave lengths, $\lambda_1=0.656\mu m$ and $\lambda_2=0.5\mu m$. As expected these functions are of the form:

$$\nu(p,\lambda) = A \sin(2\pi \frac{OPD}{\lambda}) \sin(2\pi \frac{p}{\lambda}),$$

where ν is the PtV value of the differential interferogram, p is the local intersegment piston and A is a coefficient which deepens on external parameters, such as pinhole size, sampling, intensity of input wave, and absorption coefficients.
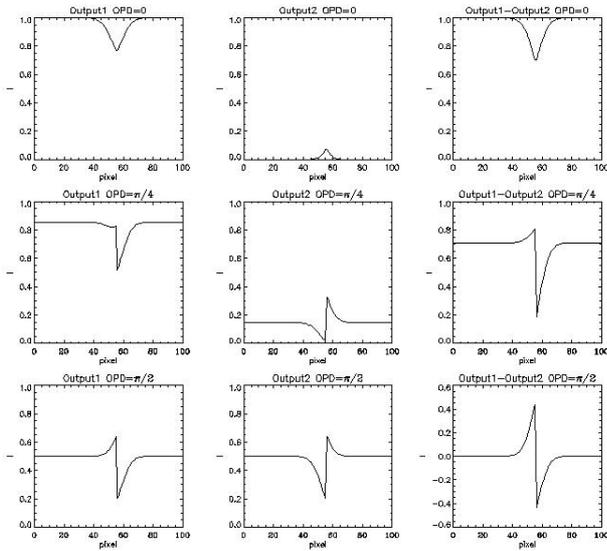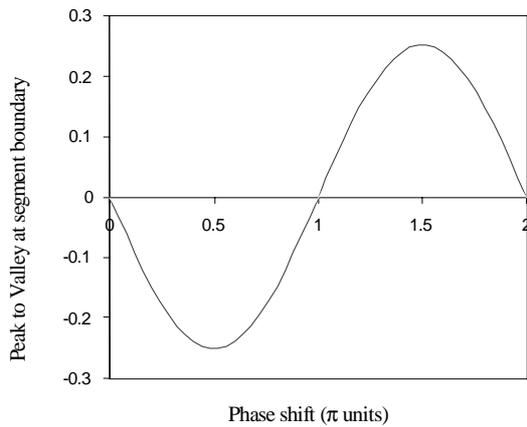

Fig.7: Profile of the two outputs interferograms (column 1 and 2) and difference of interferograms (column 3) at the segment edge for different OPDs.

Fig.8: Peak to valley at segment boundary (signal) as a function of the phase shift (OPD), λ=0.656μm, piston error is λ/4 wavefront , FWHM of the pinhole is 1".
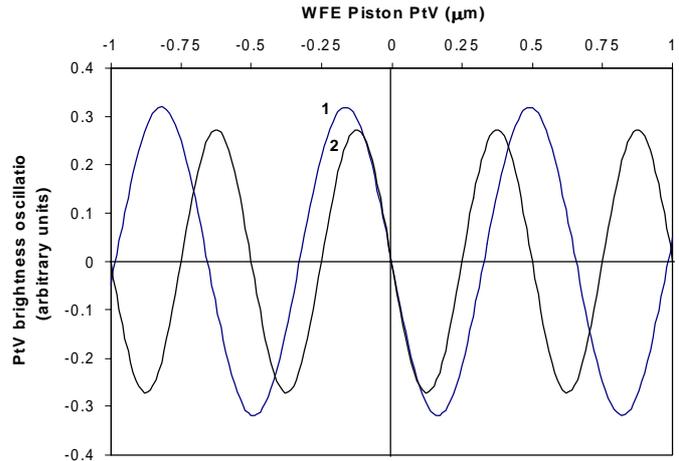
Fig.9: PtV of the oscillation across the intersegment boundary, as a function of piston for two wavelengths λ_1=0.656μm (curve 1) and λ_2=0.5μm (curve 2).

Due to the π ambiguity the monochromatic regime does not allow to unequivocally determine piston errors outside the range ± λ/4. That problem can be solved by the use of two or more wavelengths. Two outputs of the interferometer give an opportunity to measure signals in two different wavelengths simultaneously. The capture range is limited by the number of wavelengths used, the measurement error[2] and filter bandwidth. For cophasing a capture range of the order of 5 to 10μm is desirable. If we use two wavelengths (e.g., 650nm and 840nm), the measurement error should be less than 10nm to achieve such range without ambiguities. Assuming that the Mach Zehnder sensor has a precision of about 30 nm, this means that the maximal capture range we could get with two wavelengths is 3μm and it may not be enough. If we use three wavelenghts (e.g., 650nm, 795nm, 835nm), a precision of 30 nm will provide the desired range.

3.4 Pupil registration

Signal retrieval requires the precise knowledge about the location of intersegment boundary. The presence of intersegment gaps provides a convenient way to register the pupil. That can be achieved by removing the pinhole, filters and recording white light images of the pupil. These images will show the exact location of the segment boundaries and hence will indicate where the signal is to be measured. The signal being proportional to the segment gap size, its intensity is low and there are compelling reasons for enlarging the wave band as much as possible. In the case of OWL, assuming 4Kx4K detectors and ~6-mm gap size, pixels conjugated to intersegment gaps would reveal a ~25% drop in an otherwise uniform signal.

In the case of OWL, there are two segmented mirrors (primary and secondary) which need to be phased independently. In the whole interferogram the two segmentation structures appear together and need to be separated. Being projected onto the pupil plane these two structures have different spatial frequencies, corresponding to different projected distance between segments. Simple Fourier filtering allows to disentangle the patterns associated to each segmented surface.

Fig.10 shows the registration image, which contains the information about the two segmented mirrors. The results of a two spatial Fourier filtering are also shown, the filters being tailored to the geometry of each segemented surface. In each case the "undesired" structure has almost disappeared.
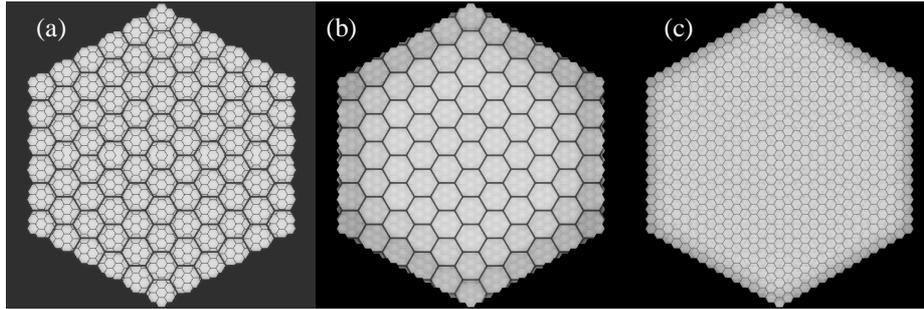
Fig.10: Interferogram of two mirrors before (a) and after Fourier filtering (b and c),
segment size 1.5m, gap=20mm,. Waveband=[328nm,875nm]

4. ATMOSPHERIC TURBULENCE

One of the main difficulty in any cophasing method is the influence of the turbulent atmosphere. One possible but generally inconvenient option is to perform the calibration on an adaptively compensated image. Another one is to try to "beat" the atmosphere, either by using very short exposures or by retrieving the relevant information from subapertures smaller than the atmospheric coherence length. A mach-Zehnder wavefront sensor would be quite efficient in that respect, since the effect of atmospheric turbulence can already be blurred out on short exposure.

In Fig.11 we show simulated interferograms obtained with increasing pinhole width. The input wavefront is shown in Fig.11.a. It contains the atmospheric turbulence component (0.65'' seeing, von Karman spectrum) and 109nm piston error (completely blurred out by the atmosphere).
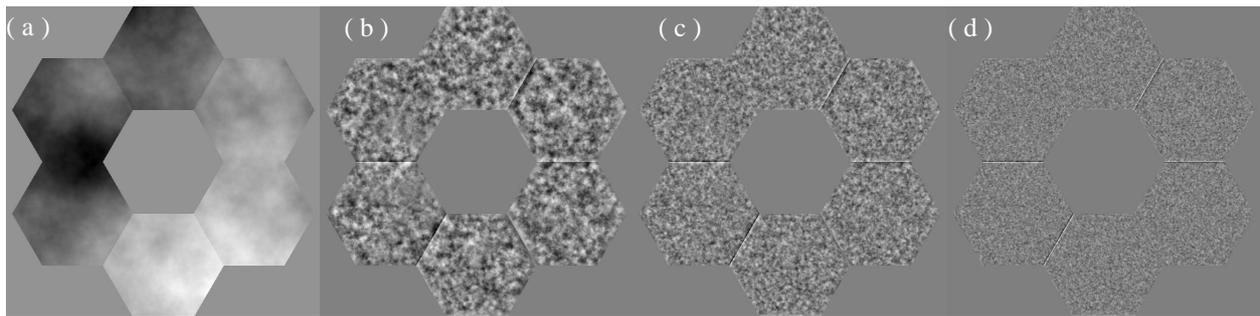
Fig.11: Wavefront containing piston error and atmospheric aberration (a). Short exposure interferogram for pinhole size 0.65" (b), 1.3"(c), 2.6" (d). Seeing 0.65", piston error 109nm, λ=0.656μm.

4.1 Optimal pinhole size for short exposure image

In terms of frequencies we have to optimise the size of the hole in such way to blur out all spatial frequencies up to that of the atmospheric turbulence. In Fig.12 we show the PSF corresponding to a wavefront in presence of turbulence with a seeing equal to 0.41"(solid) and the PSF corresponding to a wavefront with a step difference between segment of λ/4 (dotted). We observe that the effect of the atmosphere (solid line) dominates up to a radius of 0.4", while it is the effect of piston (dotted line) which dominates beyond that radius.
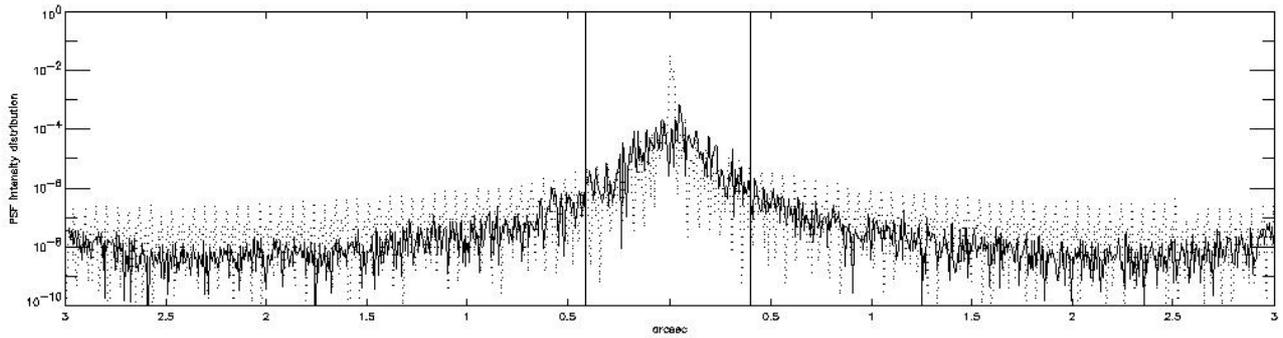
Fig.12: Intensity distribution of the PSF for an input wavefront with piston error (dotted) and atmospheric errors (solid)

In principle the size of the pinhole should be adjusted to the turbulence conditions. In Fig.13 we show the PtV value of the differential interferogram as a function of pinhole size for different atmospheric conditions. As expected the peak difference is bigger with better seeing. We also note that the optimum size of the hole increases as the turbulence becomes worse.
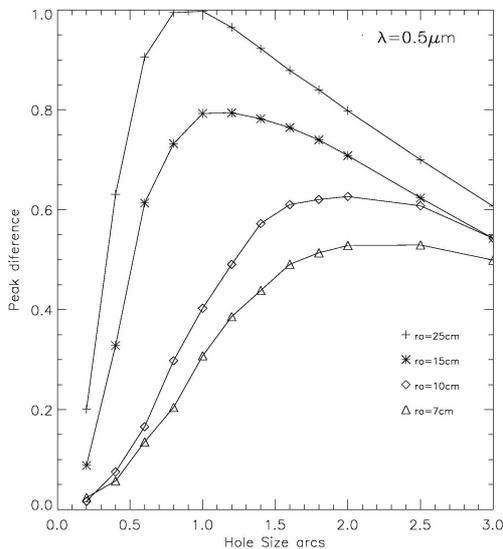
Fig.13: PtV value of the differential interferogram for different size of r_0.
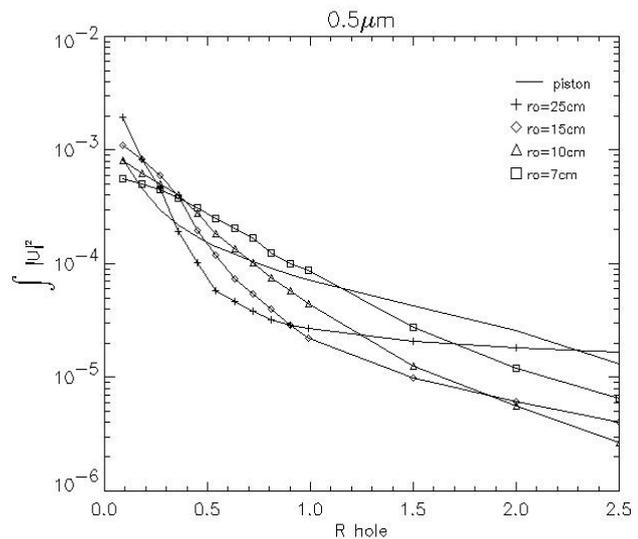
Fig.14: Total energy as a function of pinhole size.

We have calculated the total energy in the focal plane that comes through the hole for different turbulence conditions, changing the size of the hole. If the size of the pinhole is smaller than the size of the atmosphere(λ/r_o) the total energy due to the atmosphere is bigger than the total energy due to piston errors. For each atmospheric condition there is a hole size where this relation is reversed and the energy due to piston becomes higher than that associated to atmosphere. This is shown in Fig.14.
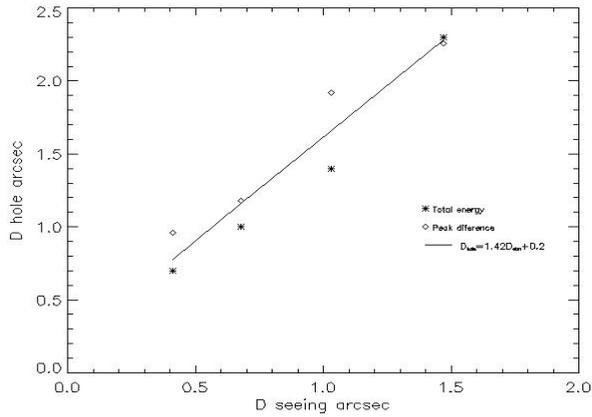
Fig.15: Linear relation between the size of the seeing disk and the optimal pinhole size.
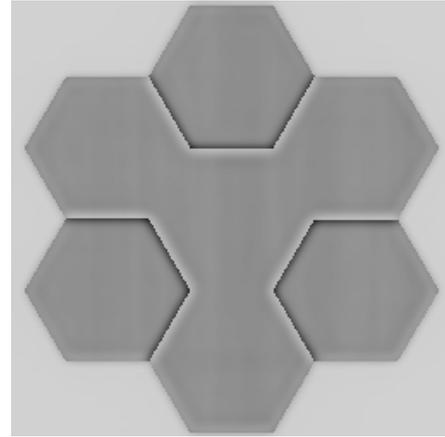
Fig.16: Long exposure signal with 0.65" seeing and 80nm piston

In Fig.15 we plot the optimal pinhole diameter for different values of seeing. We choose two different criteria, one is the maximal value of the PtV in the differential interferogram obtained from Fig 13, and the other is the point where the total energy coming through the hole is dominated by piston (Fig.14). A linear fitting gives the following relation between the optimal pinhole size and seeing disk,

$$D_{pinhole} = 1.42 \, D_{atm} + 0.2$$

where $D_{atm} = \lambda/r_0$ in arcsec and $D_{pinhole}$ is the diameter of pinhole.

4.2 Long exposure image

Long exposure imaging can provide better contrast for the signal and allows to use fainter reference sources. Fig.16 shows the illumination profile obtained after 5min exposure. The phase screen which presents the turbulence in this case was moving with the wind speed 5m/sec across the pupil. The background feature caused by an atmosphere, which we observed in the previous example, is in this case completely smoothed, leaving the constant background.

5. FUTURE WORK

Current results will have to be completed by a full characterization of a Mach-Zehnder wavefront sensor for the phasing of Extremely Large telescopes.

Most of this work will rely on simulations and will concentrate on expected accuracy limiting magnitude, implementation and alignment requirements, but also on the effect of segments edges misfigure. The latter is deemed as a serious weakness of this type of wavefront sensor –the reason being that such misfigure has a higher spatial frequency content than atmospheric turbulence, and may not be efficiently filtered out. Would this difficulty be eventually overcome, operational schemes will have to be explored as well.

A laboratory experiment is being assembled by the Laboratoire d'Astrophysique de Marseille. This experiment will eventually include a phase screen aimed at simulating the disturbing effect of the atmosphere. Would this experiment be concluded successfully, and under the provision that the effect of segments edge misfigure can be reasonably dealt with –i.e. by other means than unrealistically tight segments figuring tolerances, a prototype may eventually be integrate in the ESO Active Phasing Experiment (APE) and tested on the sky.

6. CONCLUSION

We have described the principle of a Mach-Zehnder wavefront sensor and shown by simulation that it may provide an efficient mean to measure inter- segments steps. The piston error is directly measured from interferograms at planes conjugated with the segmented aperture(s). By implication and taking into account the fact that the entire segmentation patterns is recorded by the cameras of the wavefront sensor, segments relative tilt may be measured as well by analysing the profile of the signal oscillation along the segments boundaries.

Introducing an OPD in one arm of the interferometer allows the contrast of the two output interferogram to be optimised and removes the sign ambiguity. Use of an amplitude mask instead of a pinhole allows to clean the interferograms from undesirable diffraction artefacts. A strong advantage of this type of wavefront sensor is its relative insensitivity to any error sources of spatial frequency lower than that to be detected, and in particular to atmospheric turbulence. Taking the latter into account, we find a minimum pinhole size or FWHM of the Gaussian filter ~1.42 λ/r_0 + 0.2. Using OWL aperture characteristics, we also find a practical upper size of ~1.65 to 3.3 arc seconds, depending on sampling, and compatible with the lower limit. The phase information can be retrieved from both short- and long-exposures, the latter delivering a better signal-to-noise ratio. Another advantage is its likely ease of implementation, no complex pupil mask being required as in the Keck[1].

ACKNOWLEDGMENT

REFERENCES

1.   G.Chanan, M.troy, C.Ohara, "Phasing the primary mirror segments of the Keck telescopes: a comparison of different techniques", *Proc.SPIE*, **4003**, 188-201,2000.
2.   A. Schumacher,N.Devaney, L.Montoya, "Phasing segmented mirrors: a modification of the Keck narrow-band technique and its application to extremely large telescopes", *Applied Optics*, **41**, 1297-1307, 2002.
3.   J.R.P.Angel, "Ground-based imaging of extrasolar planets using adaptive optics", *Nature*, **368,** 203-207,1994.
4.   P. Dierickx et al, "Eye of the beholder: designing the OWL", *Proc SPIE conf. on Future Giant Telescopes*,2002.

*montoya@oamp.fr; phone +34 0495044112; fax 0034 0491621190; www.oamp.fr; Laboratoire de'Astrophysique de Marseille,2 Place Leverrier,3248 Cedex 4,France;**nyaitsko@eso.org, phone +49 893200 60; fax +49 89 320 2362, www.eso.org, ESO, Karl-Schwarzschild-Str. 2 D-85748 Garching bei München.

Phasing segmented mirrors: a modification of the Keck narrow-band technique and its application to extremely large telescopes

Achim Schumacher, Nicholas Devaney, and Luzma Montoya

Future telescopes with diameters greater than 10 m, usually referred to as extremely large telescopes (ELTs), will employ segmented mirrors made up of hundreds or even thousands of segments, with tight constraints on the piston errors between individual segments. The 10-m Keck telescopes are routinely phased with the narrow-band phasing technique. This is a variation of the Shack–Hartmann wave-front sensor in which the signal is the correlation between individual subimages and simulated images. We have investigated the applicability of this technique to ELTs, and in the process we have developed what to our knowledge is a new algorithm in which each subimage provides on its own a piston-dependent value. We also discuss an alternative algorithm to resolve the λ ambiguity that allows detection of problematic cases, and a modification of the singular-value-decomposition procedure used to phase the whole mirror, using weightings on individual measurement errors. By means of simulations we show that the modified technique shows improved performance and that it can work with sufficient precision on telescopes as large as 100 m. © 2002 Optical Society of America

OCIS codes: 120.5050, 010.7350, 110.6770, 040.1240, 220.1140.

1. Introduction

In addition to the usual optical errors associated with monolithic telescopes, segmented mirror telescopes present other errors resulting from segment misalignment. In general, the segments have six degrees of freedom: translation along two axes in the plane of the segment, rotation about a vertical axis, rotation about two horizontal axes (tip and tilt), and translation along the vertical axis (piston). Undesired motion in any of these degrees of freedom will give rise to departure from the ideal mirror shape and hence affect the wave-front quality. Movement in piston or tip–tilt generally produces wave-front discontinuities. Movement in the first three degrees of freedom is restricted by attachment to the primary mirror cell and will not be considered further here. The segments usually have three actuators each, al-

lowing the segment to be positioned in tip, tilt, and piston. The effect of these errors on long-exposure image quality has been examined elsewhere,[1] and the effect on diffraction-limited images has also been presented.[2] Because it is anticipated that practically all extremely large telescope (ELT) observations will employ adaptive optics (AO), we are particularly concerned with the effect of these errors on diffraction-limited images.

We will consider piston and tip–tilt separately. The effect of random segment piston errors on Strehl ratio depends on the statistics of the piston errors. However, in the limit of small piston errors, the average Strehl ratio is given by[3]

$$\langle S \rangle \approx 1 - \sigma^2 \left(1 - \frac{1}{N} \right), \qquad (1)$$

where N is the number of segments and σ^2 is the variance of the segment piston errors. The effect is larger as the number of segments increases, and for ELTs the Strehl ratio can be approximated by $1 - \sigma^2$. In the near infrared this expression may be taken to imply quite relaxed values of piston. However, since piston will be only one term in a long list of wave-front error sources, it will in fact be necessary to control it precisely. For example, a Strehl requirement of 0.95 at a wavelength of 1.25 μm implies an

A. Schumacher (achims@ll.iac.es) and N. Devaney are with the Instituto de Astrofisica de Canarias, GTC Project, 38200 La Laguna, Tenerife, Spain. L. Montoya is with the Laboratoire d'Astrophysique de Marseille, 2 Place Le Verrier, 13248 Marseille Cedex 4, France.

accuracy of 44 nm in the segment piston control (note that in this paper piston values are referred to the wave front, and values at the mirror are a factor of 2 smaller). Of course, if it is hoped to carry out adaptive optics at visible wavelengths, then the piston errors will have to be small. For example, a Strehl ratio larger than 0.9 at a wavelength of 0.55 μm implies piston errors of less than 25 nm (12.6 nm at the mirror).

In the case of small tip–tilt errors, the Strehl ratio is given by[4]

$$\langle S \rangle \approx 1 - \sigma_\theta^2 \gamma , \qquad (2)$$

where σ_θ^2 is the variance of the tip–tilt angle and $\gamma = 5/36$ in the case of hexagonal segments. For example, for a segment dimension of 2 m, a Strehl ratio greater than 0.95 at a wavelength of 1.25 μm corresponds to rms tip–tilt errors of less than 54 nrad (0.011 arcsec). We can measure tip–tilt errors with high precision using, for example, a Shack–Hartmann wave-front sensor.

This discussion assumes that the AO system will not correct any of the wave-front error introduced by segment misalignment. In fact, AO will always provide partial correction, even if the AO system is not specifically designed to do so.[5] This is especially true in the case of high-order AO. For low-order AO where there are not many subapertures per segment it would be advantageous to choose the geometry of the AO wave-front sensor so that there are subapertures that cross segment edges in a regular way,[6] although this may be complicated by pupil rotation. In general, it is necessary to carry out numerical simulations for accurately determining the performance of a given AO system in the presence of segment misalignments. However, in the absence of simulations, expressions (1) and (2) may be taken as pessimistic estimators of the effect of piston and tip–tilt on the Strehl ratio.

There are several possible approaches to segment alignment. The strategy employed at the Keck telescope is to carry out relative piston and relative tip–tilt measurements with two capacitive edge sensors on the segment edges. These measurements are not sensitive to modes that do not give rise to edge discontinuities, e.g., global tilt, global piston, or global focus mode, in which the segments move in piston and tilt to give rise to a primary mirror defocus. These modes—apart from global piston, which does not need to be measured—can be determined by low-order wave-front sensing. The edge sensors need to be calibrated optically from time to time, with, e.g., the narrow-band technique described in this paper. Applying the Keck approach on ELTs implies some extra requirements because of the large number of segments. It may be the case that propagation of errors will lead to degraded performance on large telescopes. Furthermore, the periodicity of edge sensor calibrations may have to be increased. At the Keck, monthly calibrations result in a moderate loss of operation time. At ELTs, the time needed for cal-
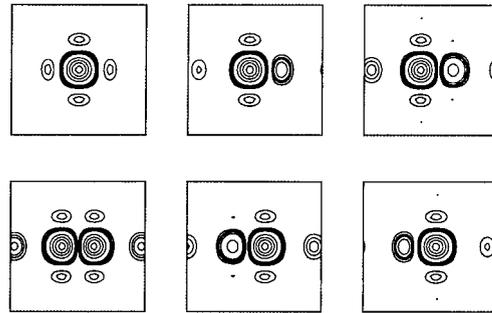
Fig. 1. Simulated diffraction patterns for a split squared subaperture with wave-front step δ between the two halves given by $k\delta = 0, 2\pi/6, 4\pi/6, \dots, 10\pi/6$.

ibration runs will become a concern. In this paper we deal with these requirements and investigate the precision that can be expected from this technique under various conditions.

2. Keck Narrow-Band Algorithm

This technique is based on a Shack–Hartmann-type wave-front sensor, in which the lenslet array is preceded by a mask that defines small subapertures at the center of each of the intersegment edges. In the case of the Keck telescopes, these subapertures are circular; in this paper we refer to square subapertures as will be used at the 10-m Gran Telescopio Canarias (GTC).[7] The size of the subapertures is chosen to be smaller than the average Fried parameter, r_0, of approximately 20 cm at a wavelength of 500 nm. At the Keck and at the GTC this size is 12 cm with respect to the primary mirror.

A. Description of the Algorithm to Extract the Phase

We first concentrate on the algorithm applied to extract phase information from a single intersegment edge step (or piston step). The original Keck narrow-band technique[8] is described and compared with a modified algorithm. Both techniques exploit the diffraction pattern produced by a small intersegment subaperture and monochromatic light from a bright stellar source. The resulting simulated diffraction patterns for various piston steps are shown in Fig. 1, and their projection on the x axis is shown in Fig. 2. The two algorithms under comparison differ in how they use these images.

Fig. 2. x projection of images of Fig. 1.

Fig. 3. Peak ratio calibration curve (λ = 650 nm). WF, wave front.

Fig. 4. Measurement precision of the Keck (diamonds) and the peak ratio (triangles) technique under perfect conditions.

In the Keck approach,[8,9] an image taken from a subaperture with unknown piston step is compared with a set of 11 simulated images like those of Fig. 1. The real piston step is somewhere between the piston steps of the two mo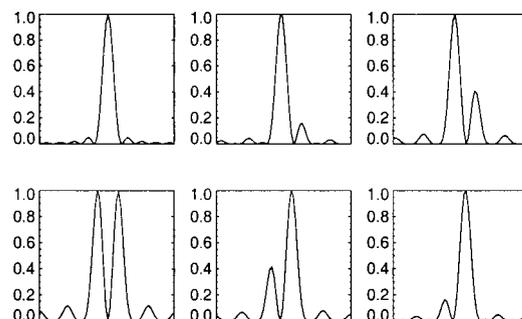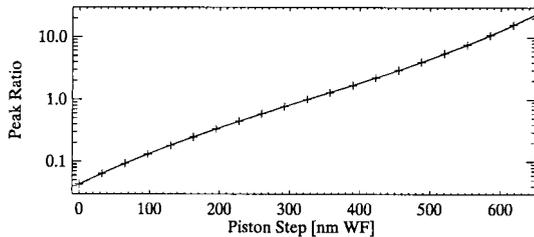st similar images. The degree of similarity is determined by calculation of a correlation coefficient; a finer resolution than the piston-step difference between two templates ($\lambda/11$ at the wave front) is achieved by quadratic interpolation of the correlation coefficients.

We propose a new approach that is based on extracting a single characteristic value from each simulated image related to the piston step and then calculating a calibration curve. One possible characteristic value, which will be applied here, is the ratio between the two main peaks in the diffraction pattern (see Fig. 2). We refer to this technique as the peak ratio technique.[6] Defining the peak ratio as PR = Max(right peak)/Max(left peak), we obtain the calibration curve shown in Fig. 3. In this figure the calibration points obtained from the simulation are plotted together with a fitted polynomial of third degree to (the logarithm of) these points; this represents the data with sufficient accuracy. The coefficients of this polynomial are used as calibration data. For a given subaperture image, the peak ratio is calculated and processed with the calibration data in order to obtain the required piston step.

Our comparison of both techniques is based on simulated subaperture images. This has the advantage that the effect of distinct error sources on the precision of the techniques can be investigated without interfering effects. We will present the results of separate simulation runs with a range of possible systematic as well as statistic errors. Furthermore, in simulations one can exactly define the precision, because the exact piston step to be measured is known, whereas in experiments the precision can be described only in terms of reproducibility and cross checks with other techniques. Systematic errors common to all applied techniques will hardly be recognized in an experiment, and those errors detected may not be easily interpreted. However, some systematic errors may arise in practice that have not been taken into consideration in simulations. The point is that for an overall determination of the precision of a particular technique, a combination of experiment and simulation is desirable. T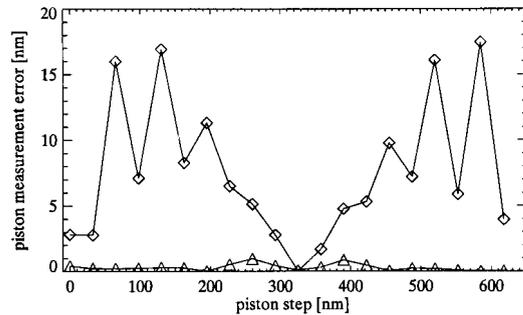o make a first comparison of techniques, we believe that simulations are advantageous. We will be able to perform additional experimental tests once the GTC telescope is completed. We would also like to stress that for an implementation of the peak ratio technique at the Keck no change in hardware would be necessary; it is merely an alternative analysis method on the same data.

We will first compare the intrinsic error of both techniques, resulting from the analysis principle itself. The results of simulations without taking into account any kind of error one has to deal with in practical measurements—referred to as perfect conditions—are plotted in Fig. 4. The precision of the peak ratio technique is limited only by the validity of the polynomial fit to the calibration data and by calculation round-off errors, whereas the original Keck technique shows an intrinsic error of up to 18 nm. Note that if in an experiment a measurement were made repeatedly at a piston step yielding 18-nm error in Fig. 4 (e.g., at 130 nm) without stepping the segments substantially, the reproducibility of this measurements would be given by other effects and thus in principle could be in the subnanometer range. Here we deal with a systematic error that could be detected in practice only if (i) in subsequent measurements the piston step were changed by a known amount and thereby change the amount of the systematic error, or (ii) if measurements at two different wavelengths were performed, which should result in different systematic errors. Possible sources for the intrinsic error of the original Keck technique are the following: (i) To calculate the correlation coefficients, all images first have to be reregistered, so that the centroids coincide exactly with the array center and not just to within the nearest pixel. (ii) The correlation coefficients do not exactly show a quadratic dependence. Chanan *et al.*[8] report a deviation of up to 0.7% between the coefficient and its quadratic approximation. (iii) The process of calculating the correlation coefficient itself could be an error source. Note that we used our own analysis code, based on the principles used at Keck, so it is possible that the original code used at Keck is further optimized and shows less-intrinsic errors. However, published results[9] indicate a rms error of 17 nm in practice, which is approximately what we would expect from our simulations under imperfect conditions. (The authors
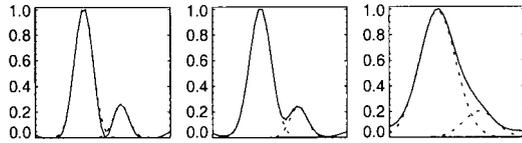
Fig. 5. One-dimensional diffraction patterns at various seeing conditions r_0 (500 nm) = ∞, 16 cm, 6 cm.

Fig. 7. One-dimensional diffraction patterns at various photon noise levels N_γ = 2000, 500, 200.

state 12-nm mirror surface rms differences between measurements performed at different wavelengths, presuming that measurements at both wavelengths result in the same rms error and the errors adding quadratically, one gets $12 \times 2/\sqrt{2}$nm = 17-nm rms wave-front error for a single measurement.)

The peak ratio technique would be potentially problematic in practice, if one defined Max(peak) simply as the highest value of all pixels involved in the peak. This is shown in Fig. 5, where the resulting point-spread function for various seeing conditions and a fixed piston step of $\lambda/4$ are plotted (straight line). As the seeing gets worse, the binary structure gets less distinct. But even when there is barely any binary structure it is still possible to extract the maximum heights of the two peaks involved. Fitting the sum of two Gaussians to the point-spread function will yield the results shown in Fig. 5 (dotted curves). It was claimed that the original Keck technique is more robust and numerically efficient than surface fitting.[9] In fact, getting stable fit results is not a straightforward task. One has to use fit procedures in which the fit parameters can be limited to certain ranges. Applying the restrictions that (i) both peaks have approximately the same width, (ii) the peak width is always within a certain limit, and (iii) the distance between the two peaks is constant for all piston steps, one can achieve a robust fit procedure that outperforms the numerical efficiency of the original Keck technique. With this method it is possible to obtain a result for Fried parameters as small as $r_0 \approx 6$ cm at 650 nm. As is shown in Fig. 6, the calibration curves obtained for different seeing conditions differ slightly, leading to measurement errors as discussed in Subsection 2.D. This Gaussian fit method is also suitable for the case of having photon noise as shown in Fig. 7 and discussed in Subsection 2.E. An important advantage of the Gaussian fit method is that it provides not only the values of the
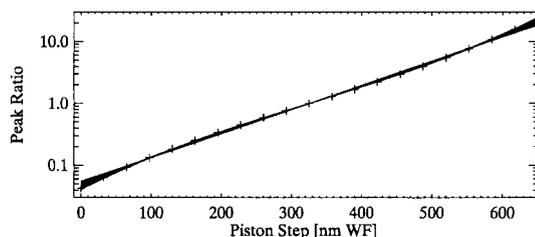

Fig. 6. Peak ratio calibration curves at various seeing conditions down to r_0 (500 nm) = 8 cm (λ = 650 nm).
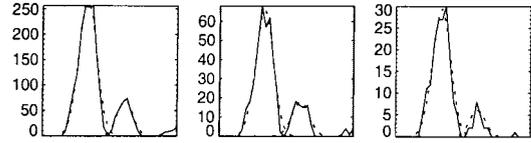
two peak heights but also an estimation of their uncertainties. Knowing the precision of each piston-step measurement allows us to perform a weighting when calculating the segment piston values from all measured subaperture piston-step values, as described in Subsection 2.F.

B. Measurement Range

Both the Keck and the peak ratio technique have a useful range that depends on the wavelength used. The maximum unambiguous piston step is $\pm(\lambda/2)$ at the wave front. The maximum deviation from the mean value of the segment pistons is then $\pm(\lambda/8)$ at the mirror. In the case of λ = 650 nm this means that the segments have to be already aligned to better than 162 nm. It is therefore convenient to take another measurement at a different wavelength in order to avoid the ambiguities. If λ_1 = 650 nm and λ_2 = 850 nm, then the range is more than 10 times greater. The procedure we use to achieve this is basically identical to that described in detail by Löfdahl and Eriksson.[10] In the following we give a short description of the procedure and show that the peak ratio technique offers substantial enhancements.

When we take two measurements at different wavelengths λ_1 and λ_2, the peak ratio method gives two different results $x_1 \in [0, \lambda_1]$ and $x_2 \in [0, \lambda_2]$. If no measurement errors are considered, then the following equation is valid for the piston step PS:

$$\text{PS} = x_1 + k\lambda_1 = x_2 + j\lambda_2, \qquad k, j \in I. \qquad (3)$$

To ensure an unambiguous result we have to set the following restrictions on k and j:

$$|x_1 + k\lambda_1| < \lambda_{\text{Max}},$$
$$|x_2 + j\lambda_2| < \lambda_{\text{Max}}, \qquad (4)$$

where the maximum unambiguous piston step λ_{Max} is the smallest value which satisfies the relation $2\lambda_{\text{Max}} = |k|\lambda_1 = |j|\lambda_2$. The factor of 2 reflects the fact that end results can be negative. In the case of λ_1 = 650 nm, λ_2 = 850 nm, we get λ_{Max} = 5525 nm, thus gaining a factor of 17 in measurement range with respect to a single-wavelength measurement at λ_1.

Of course, the measurements x_1 and x_2 are prone to errors, and usually no solution will be found to fulfill

Eq. (3). Taking measurement errors into account, relations (3) and (4) will become

$$PS = x_1 \pm \sigma(x_1) + k\lambda_1$$
$$= x_2 \pm \sigma(x_2) + j\lambda_2,$$
$$|x_1 + k\lambda_1| + \sigma(x_1) < \lambda_{\text{Max}},$$
$$|x_2 + j\lambda_2| + \sigma(x_2) < \lambda_{\text{Max}}. \quad (5)$$

The analysis code will now search for all possible PS that fulfill the conditions of Eq. (5). This differs from the algorithm described by Löfdahl and Eriksson,[10] in which a fixed maximum error is used in order to calculate the capture range. This is useful when one tries to find the pair of wavelengths that results in the best capture range. In practice, no such maximum error can be given that is guaranteed to be met by actual measurements. Because of statistics, single measurements might exceed the defined maximum error and yield a wrong result. We take a fixed pair of wavelengths and employ the fact that the peak ratio technique provides reliable error estimates for every piston-step measured. For the pair of wavelengths that we have chosen, all possible combinations of k and j result in a difference between the left- and the right-hand sides of Eq. (3) of at least 50 nm (0 nm for the right solution). As a result, for a sum of the estimated measurement errors $\sigma(x_1)$ and $\sigma(x_2)$ exceeding 50 nm, there may be two or more solutions found for Eq. (5). However, if the errors are underestimated, it is possible that no solution will be found. If one has to use Eq. (5) with fixed $\sigma(x_1) = \sigma(x_2)$ for the whole mirror, then one has to choose σ as a compromise between having too many measurements with no solution and too many measurements with ambiguous solutions. This restriction is valid if on some piston-step measurements the sum of the errors exceeds 50 nm. In our simulations of ELTs with hundreds of piston steps measured, this was frequently the case, when seeing and photon noise were included. This is confirmed by Keck results, in which a run of 624 piston-step measurements with two wavelengths resulted in three measurements with the combined error exceeding 101 nm.[9] Knowledge of the individual measurement errors thus allows minimization of the number of cases that have no solution or ambiguous solutions. In simulations we found $\lambda_{\text{Max}} \approx 4500$ nm as a practical limit to ensure stable results at all times.

There will still be some cases with no or with ambiguous solutions. If the percentage of these cases on the whole mirror is low, then this will not necessarily affect the overall performance, because (up to) six piston-step measurements are performed on each segment. It is still possible to extract the piston values of all mirror segments, even if only one unambiguous piston step could be measured on some segments. The key is to detect the problematic cases and to exclude them from the piston calculation, as explained in Subsection 2.F. If these measurements were included in the singular-value-decomposition (SVD) procedure, the resulting rms piston error could

be worsened to tens or hundreds of nanometers, as shown in our simulations as well as in experimental results.[8]

Note that λ_{Max} is a limiting value to be used in the analysis code. Single piston steps are still allowed to exceed this value without affecting the piston measurement, if for all segments at least one piston step is smaller than λ_{Max}. This is because these measurements will be detected as ambiguous and automatically excluded from SVD.

The approach used at the Keck Telescope[9] is to use Eq. (3) in conjunction with a χ^2-minimization technique that in all cases will find exactly one result. This result is guaranteed to be correct if (for the Keck wavelengths $\lambda_1 = 651$ nm and $\lambda_2 = 852$ nm) the piston step lies within a range of 1278 nm and the combined error is below 101 nm. (The higher allowed combined error is achieved by the reduction of capture range.) If this condition is violated, Chanan et al. find that "failures are common enough that the algorithm is essentially useless" (Ref. 9, p. 4711). Since Chanan et al.[9] lack information on individual measurement errors, they are forced to apply an additional procedure that allows one to find sufficient piston-step measurements that still are guaranteed to be correct. These cases will be found when the segments are already prephased to within the capture range of a single-wavelength measurement. In fact, the above-stated results were obtained when the mirror was already prephased to within ± 325 nm by means of an additional phasing technique, the broadband technique. In this way, the two-wavelength algorithm is not used to enhance the measurement range (broadband is used for this) but to enhance the accuracy of the broadband technique. Applying Eq. (5) in conjunction with the peak ratio technique allows us to detect the problematic cases without additional measurements (see Fig. 18, below), thus preserving the advantages of the narrow-band over the broadband technique.[9] Making use of the knowledge of the piston-step measurement errors thus extends the range of the two-wavelength method from $\lambda_{\text{Max}} \approx 325$ nm to $\lambda_{\text{Max}} \approx 4500$ nm, the first value resulting from considerations of the principle, the latter resulting from simulations assuming realistic conditions.

C. Figure Errors and the Use of a Phase Plate

The investigations described in this paper are based on perfectly shaped segments without figure errors. Low-spatial-frequency aberrations can yield edge steps between adjacent segments even when the mean piston step between the segments is zero. However, these aberrations can be measured by a slow wave-front sensor and the data used to correct the piston measurements. We are currently working on a simulation of this.

High-spatial-frequency aberrations, such as polishing errors, cannot be measured easily. They may alter the shape of the point-spread function and thereby change the peak ratio at a given piston step. As can be seen in Fig. 8 where the measurement
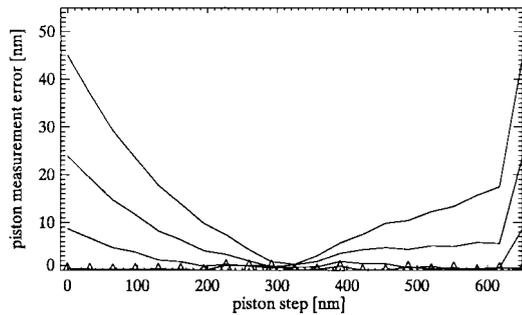
Fig. 8. Measurement precision of the peak ratio technique with high spatial-frequency wave-front aberrations resulting from segment polishing with an amplitude of 10, 20, and 30 nm (wave front). Note that one example aberration structure is used; each segment will have its own characteristic aberration. Triangles indicate data without segment figure errors, higher polishing errors produce higher measurement errors.

errors of the peak ratio technique in the presence of polishing errors are plotted against the piston step, these errors are high at piston steps near zero and tend toward zero at piston steps near $\lambda/2$. This is a characteristic behavior for the peak ratio technique for all kinds of errors investigated except photon noise (see also Fig. 12, below) and applies also to the original Keck technique. It is possible to change this behavior to have the highest precision at piston steps near zero by addition of a phase plate to one half of the subaperture, covering only one of the two segments. The phase plate has to apply a phase shift of $\lambda/2$ and should be optimized for the shortest wavelength used in piston measurements, since this plate will be an integral part of the lenslet and cannot be altered between measurements.

The performance gain of the phase plate is highest when the mirror segments are already aligned with good precision. Figure 9 shows as an example the results of phasing a segmented mirror with normally distributed piston values with rms = 20 nm. Imperfect conditions were assumed, yielding relatively high
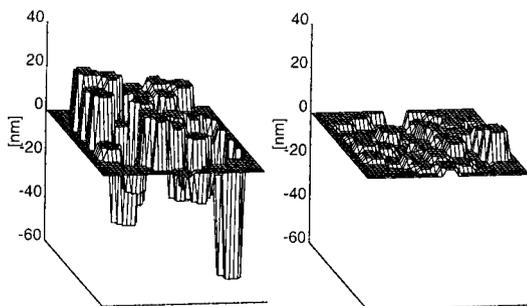

Fig. 9. Performance of the peak ratio method on a whole mirror. The original piston values are normally distributed with a rms of 20 nm (not shown). In this simulation a seeing of 20 cm and 5000 photons per subaperture were assumed. The peak ratio method without phase plate (left) resulted in a rms piston error of 19.5 nm and a rms piston-step measurement error of 15.4 nm. Using a phase plate (right) resulted in a rms piston error of 4.5 nm and a rms piston-step measurement error of 4.9 nm.
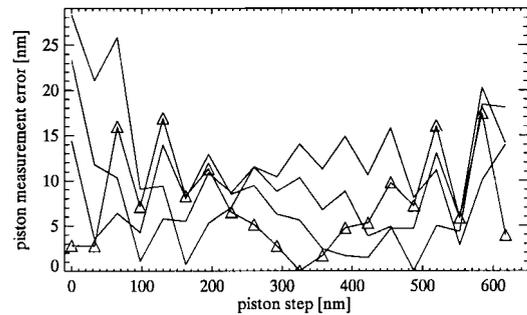

Fig. 10. Measurement precision of the Keck technique under the same polishing conditions as in Fig. 8. Triangles represent data without segment figure errors; higher polishing errors produce higher measurement errors.

piston-step measurement errors. Without application of a phase plate (left plot), the resulting rms piston error shows the original rms error of 20 nm. Applying the phase plate (right plot) results in a rms piston error of 4.5 nm.

In the case of polishing errors, using the phase plate and repeating the piston measurements in an iterative way should minimize measurement errors rapidly, when the peak ratio technique is used. With the Keck technique the same polishing errors as in Fig. 8 affect the measurements in a different way, as can be seen in Fig. 10. The largest measurement error is smaller than that of the peak ratio technique, but there is no point of near-zero error over the whole range of piston steps. Iterative measurements will not minimize measurement errors caused by high-spatial-frequency segment figure errors when the Keck technique is applied. It is however possible that high-spatial-frequency errors could be retrieved from the segment polisher's data. Taking into account that such errors are stable in time, it would, in principle, be possible to calibrate their effect, and so iterative measurements will not be needed. Even if this turns out not to be possible, making an iterative measurement with the peak ratio technique would be needed only once in a segment's lifetime, stepping through the measurement range to obtain a calibration curve including the high-spatial-frequency effects of each particular subaperture.

D. Performance as a Function of Seeing

As described in Subsection 2.A and shown in Fig. 5, the shape of the diffraction pattern changes with the seeing conditions. The way this affects the measurement precision depends on the method chosen to extract phase information. At the Keck telescopes, 11 images at perfect seeing conditions are simulated and compared with the real image under investigation. Surprisingly, the original Keck technique works better when seeing gets worse, as is shown in Fig. 11. In the peak ratio technique worse seeing conditions will produce a greater peak ratio error because of a systematic error in the Gaussian fit. The resulting measurement errors for various seeing conditions are shown in Fig. 12. The precision is
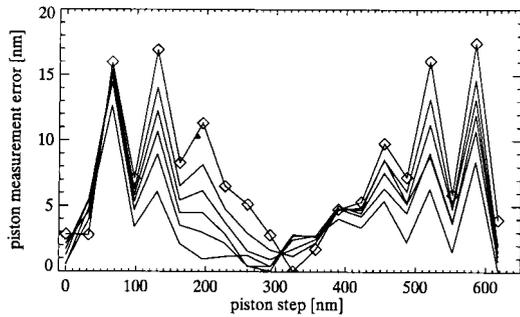
Fig. 11. Measurement precision of the Keck technique under various seeing conditions. Diamonds, data with perfect seeing conditions.

greatly affected by the seeing condition. However, since the error of the Gaussian fit is systematic, one can correct for it. Calculated calibration curves for various seeing conditions are shown in Fig. 6. The real seeing condition can be estimated from the width of the fitted peaks, and one can apply the corresponding calibration curve. The resulting piston-step measurement error is then almost reduced to its value at perfect conditions, as can be seen in Fig. 13.

E. Performance as a Function of Magnitude

In this section we calculate the stellar magnitude needed to phase the mirror using the narrow-band
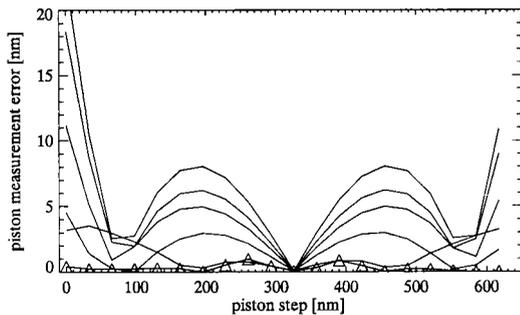

Fig. 12. Measurement precision of the peak ratio technique under various seeing conditions, with calibration data obtained for best seeing conditions. Triangles, data with perfect seeing conditions.
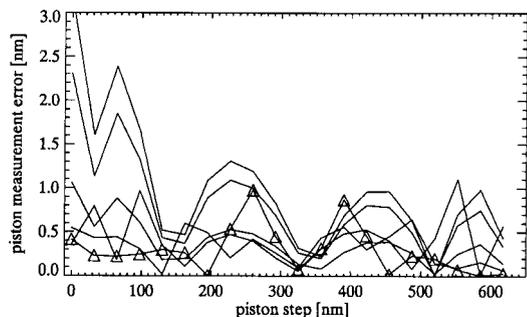

Fig. 13. Measurement precision of the peak ratio technique under various seeing conditions, with the calibration data corresponding to the actual seeing condition. Data with perfect seeing conditions are marked.
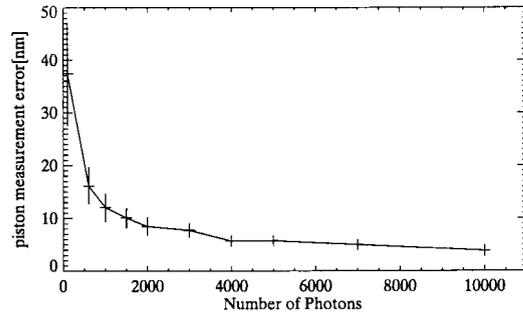

Fig. 14. Rms measurement precision of the peak ratio technique under various photon noise conditions ($\lambda = 650$ nm).

technique with the peak-ratio algorithm. The limiting stellar magnitude will depend on the number of photons required for measuring the piston errors with the specified accuracy. The magnitude of a star is related to the number of photons arriving at the detector as follows:

$$n - \eta t A \epsilon 10^{-0.4M} \Delta\lambda , \qquad (6)$$

where ϵ is the system efficiency, t is the exposure time, A is the collecting area, η is the number of photons per centimeter squared per nanometer from a zero-magnitude star, $\Delta\lambda$ is the bandwidth, and M is the magnitude of the star.

Figure 14 shows the error in the piston measurement for different photon levels. The given error is the standard deviation of 360 random simulations at different piston steps—it turned out that in the case of photon noise the Gaussian fit error does not depend on the piston-step value. To keep the standard deviation that is due to photon noise in the piston-step measurement below 5 nm, approximately 10,000 photons per subaperture are required. Although 5 nm seems to be small when compared with the 50-nm limit for the sum of the errors of two measurements at different wavelengths (see Subsection 2.B), one should bear in mind that this is a standard deviation and that single measurements may be affected by higher errors. From simulations of whole mirrors we found that 10,000 photons per subaperture will give stable results at all times.

Table 1 shows the limiting stellar magnitude and the corresponding required accessible field to find such a star with a probability of 90% for different photon levels at the North and the South Galactic

Table 1. Limiting Stellar Magnitude and the Corresponding Required Accessible Field (FOV) to Find such a Star with a Probability of 90% for the Peak Ratio Method at Different Photon Levels at the North and the South Galactic Poles[a]

N_γ	Precision (nm)	Magnitude	FOV$_{NGP}$ (arcmin)	FOV$_{SGP}$ (arcmin)
10000	5	11.8	10.1	8.0
2000	10	13.7	5.4	4.7

[a]The given precision is the standard deviation of a piston step measurement at otherwise perfect conditions.

Poles. Here we assumed the following values: $\epsilon = 0.8$, which is the product of the transmission from the top of the atmosphere to the detector, and the detector quantum efficiency, $t = 60$ s, which is typical of active optics time scales, $A = 144$ cm^2, corresponding to square subapertures with a side length of 12 cm, $\Delta\lambda = 10$ nm, and $\eta(650\text{ nm}) = 8730$ cm^{-2} nm^{-1}. The required field of view (FOV) can be obtained from the probability P of finding at least one star within a given radius, r, on the sky. Since the distribution of stars on the sky follows Poisson statistics, P is given by

$$P = 1 - \exp(-r^2 \nu \pi / 3600^2), \qquad (7)$$

where ν is the density of stars brighter than magnitude M per degree squared in the considered region. This star density can be obtained from models of the galaxy or from measurements by use, for example, of the Guide Star Catalog,[11] which has been employed here. From the results shown in Table 1, it can be seen that a minimum accessible FOV of 10-arcmin diameter is necessary to ensure accurate piston measurements at all times. This is comparable with the FOV of OWL (OverWhelmingly Large Telescope), a 100-m telescope project.

F. Performance as a Function of Telescope Size or Number of Segments

So far we have restricted our discussion to the determination of a single intersegment piston step. For the whole mirror made up of N_{segments} hexagonal segments with one subaperture on each side there will be $N_{\text{subapertures}} < 3N_{\text{segments}}$. The exact value of $N_{\text{subapertures}}$ depends on mirror design aspects such as the outer shape and the central obscuration, since segments on the outer or the inner borders have less than six neighbors. Each segment piston is determined by (up to) six piston-step measurements and affects the segment piston measurements of all of its neighbors and hence of the whole mirror. This can be expressed mathematically as a system of linear equations of the form

$$\text{Piston1}_i - \text{Piston2}_i = \text{PS}_i\,,$$
$$i = 1, \ldots, N_{\text{subapertures}}, \qquad (8)$$

where Piston1$_i$ and Piston2$_i$ are the piston values of the two segments corresponding to subaperture i and PS$_i$ is the measured piston step. Since the absolute average phase of the mirror is not of interest, it makes sense to keep it constant, with addition of a further constraint

$$\sum_{j=1}^{N_{\text{segments}}} \text{Piston} = 0\,. \qquad (9)$$

Equations (8) and (9) constitute a simple linear system of $N_{\text{subapertures}} + 1$ equations with N_{segments} unknowns (PS$_i$). At the Keck telescopes the technique of SVD is used to solve this system.[8] We used this method on simulations of mirrors with up to 1000 segments and found it powerful and robust even on

Fig. 15. Segmented mirror of the Keck/GTC type (36 segments) before (left) and after (right) one phasing iteration. In this simulation perfect conditions were assumed. The original piston values are uniformly distributed with a range of 6530 nm and a rms of 1990 nm. Two measurements at different wavelengths were performed (λ = 650, 850 nm). The resulting rms piston error is 0.27 nm, and the rms piston-step measurement error is 0.31 nm.

the scale of ELTs. Figures 15–18. show the results of some example simulations of mirrors of different sizes.

In the SVD method one essentially provides a matrix, **A**, defined by the left-hand sides of Eqs. (8) and (9), and a vector defined by the right-hand side. The SVD procedure returns a vector of piston values. In the process, a pseudoinverse of **A** (of $N_{\text{subapertures}}$ columns and N_{segments} rows) is constructed that defines the linear system. Since we deal with an overdetermined system, that has more equations than unknowns, and furthermore the measured (here, simulated) values are not perfect, SVD provides a best fit (in the sense of least squares) to the set of data.

Fig. 16. Segmented ELT mirror (1002 segments) before (top) and after (bottom) one phasing iteration. In this simulation perfect conditions were assumed. The original piston values are uniformly distributed with a range of 3900 nm and a rms of 1180 nm. Two measurements at different wavelengths were performed (λ = 650, 850 nm). The resulting rms piston error is 0.46 nm, and the rms piston-step measurement error is 0.33 nm.
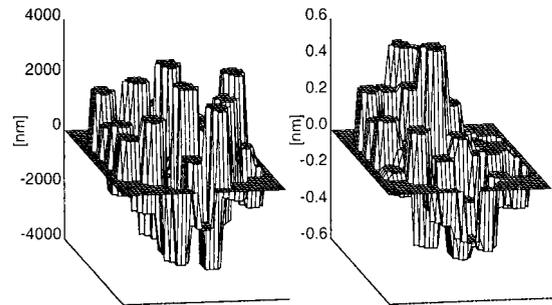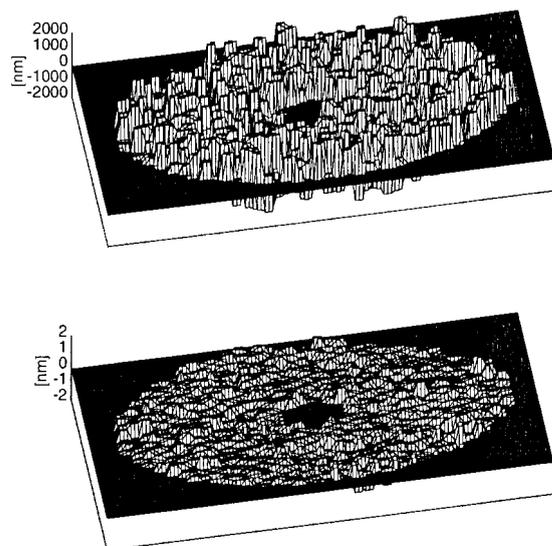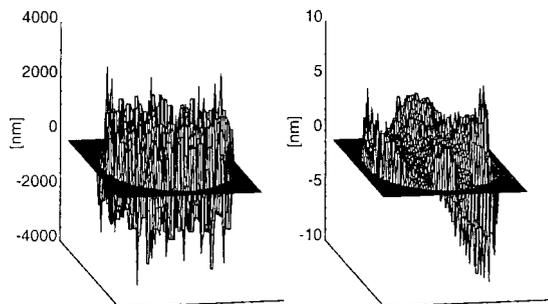
Fig. 17. Segmented ELT mirror (846 segments) before (left) and after (right) one phasing iteration. In this simulation perfect conditions were assumed. The original piston values are uniformly distributed with a range of 4000 nm and a rms of 1125 nm. Two measurements at different wavelengths were performed ($\lambda = 650$, 850 nm). The resulting rms piston error is 2.0 nm, and the rms piston-step measurement error is 0.4 nm. The smooth residual is an example of the propagation of errors for which the sensitivity of the technique is low.

It makes sense then to perform a weighting on the measured data to ensure that the piston-step measurements with higher precision will have more influence than those with less precision. We found that to achieve this no modification of the well-known SVD code[12] is necessary. All that needs to be done is to modify the matrix **A** by simply dividing Eqs. (8) by the absolute error of the piston-step measurement $\sigma(\text{PS}_i)$:

$$\frac{\text{Piston1}_i - \text{Piston2}_i}{\sigma(\text{PS}_i)} = \frac{\text{PS}_i}{\sigma(\text{PS}_i)},$$

$$i = i, \ldots, N_{\text{subapertures}}. \quad (10)$$

Mathematically, Eqs. (8) and (10) are identical, but in the actual SVD algorithm only the left-hand side (the
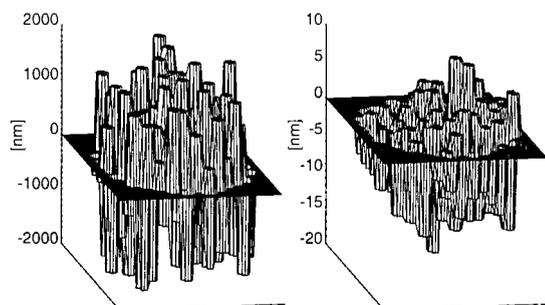

Fig. 18. Segmented mirror (120 segments) before (left) and after (right) one phasing iteration. In this simulation a seeing of $r_0 = 24$ cm and an exposure time yielding 20,000 photons per subaperture were assumed. The original piston values are uniformly distributed with a range of 3800 nm and a rms of 1153 nm. Two measurements at different wavelengths were performed ($\lambda = 650$, 850 nm). The resulting rms piston error is 4.5 nm, even though the rms piston-step measurement error is 231 nm. This is because in two measurements the λ-ambiguity algorithm yielded a wrong result. This did not affect the overall measurement, because the ambiguity was detected and a higher error was automatically assigned. The rms piston-step measurement error excluding these two cases is 3.7 nm.
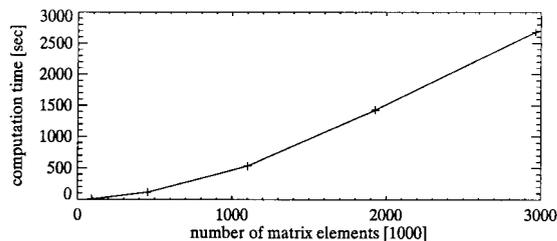

Fig. 19. Computation time needed for the SVD algorithm as a function of matrix size for our current, unoptimized code. Crosses represent data for mirrors with 180, 396, 612, 810, and 1002 segments.

matrix **A**) is used, and in a later stage the right-hand side is used to obtain the resulting piston values. Thus using Eq. (10) provides additional information to the SVD algorithm that is used to perform the required weighting. To understand this, consider the extreme case of $\sigma(\text{PS}_i) \to \infty$. Row (i) of matrix **A** will be made up of zeros, and PS_i will not be considered in the SVD calculation.

In practice, one should furthermore exclude the piston-step measurements for which the Gaussian fit procedure apparently did not find a valid solution and those in two-wavelength measurements that yield ambiguous solutions. Alternatively, the more probable solution can be chosen and the corresponding error set to a high value to reflect the ambiguity. Applying these corrections to the straightforward implementation of SVD will give better results and furthermore will substantially enhance the robustness of the method. If weighting is not applied, then a single erroneous or high-error piston-step measurement cannot only lead to a wrong piston estimation for the two corresponding segments but can also affect a large number of their neighbors. In the worst case it will not be possible to phase any of the segments. In our simulations we found that for ELTs in the presence of seeing and photon noise, SVD without weightings often failed to find a solution or resulted in parts of the mirror not being properly phased. Applying the weightings on the same data sets solved these problems in almost all cases.

There are further possibilities to enhance the performance of the SVD procedure that should be used when applied to ELTs. First, a large number of subapertures leads to accumulating round-off errors. The overall precision of the phasing procedure could be enhanced by iterative improvements of the solution to the linear equations. Second, a large number of subapertures means a large matrix **A** in the SVD calculations. One can save computation time and memory space by using the fact that we deal with a sparse linear system—**A** is mainly made up of zeros that should not be processed and occupy memory. These enhancements are not yet implemented in our analysis. The computation time of the SVD method as a function of the number of segments for our actual unoptimized analysis code on a Sun Ultra-4 with 4 CPUs, each of 400 MHz, and a total of 4096-MByte

memory is plotted in Fig. 19. To get the complete computation time for a phase measurement, one has to add the time needed for the Gaussian fits. At least $N_{\text{subapertures}}$ fits have to be calculated, each taking ~ 70 ms. With high photon noise the fit sometimes has to be repeated with different parameters until a valid result is achieved, leading to a higher computation time when the exposure time is reduced. Using optimized analysis code will reduce the computation time by a large factor. At optimum, the SVD matrix would not count $N_{\text{segments}} \times N_{\text{subapertures}}$, but only $2 \times N_{\text{subapertures}}$ elements. For a 1000-segment mirror this is a factor of 500 for matrix size and approximate computation time, making the time needed for the SVD algorithm negligible when compared with the Gaussian fits. This indicates a computation time of the order of seconds when implemented on ELTs, if faster CPUs and parallel processing are employed. For further discussion of SVD as well as the code, see Press *et al.*[12]

G. Practical Aspects

It is clear that for this technique, the number of subapertures increases with the number of segments. If we consider a regular grid of hexagonal lenslets mapped onto an image of the segmented mirror, then in order to measure the piston step at each segment edge we need to map at least $2N + 1$ lenslets onto N segments. There is an extra lenslet centered on each segment, which can be used to measure tip–tilt. In the case of the OWL telescope, there are 64 segments on its longest axis, and the corresponding number of subapertures is 129. If the hexagonal edge length of the lenslets is 0.3 mm, then the length of the lenslet array would be 67 mm, and the corresponding pupil demagnification would be approximately 1700. The lenslets used for phasing would be masked, leaving a 70-μm subaperture at the center. The lenslet array has to be precisely aligned to the image of the primary mirror for the Keck narrow-band technique to work. The alignment should at least be better than the size of the gaps between the segments. An alignment accuracy of 1 mm referenced to the primary mirror would imply aligning the lenslet array to better than 0.6 μm. These specifications can be met with currently available technology. The alignment accuracy can be relaxed by including cross hairs in the lenslet masking, with the cross hairs aligned to the segment edges. These cross hairs can also relax the requirements on distortion in the pupil imaging; pupil distortion may be difficult to reduce when a large pupil demagnification is required. The drawback is a reduction in the light-gathering area of the subaperture. This can be compensated to some extent by means of elongating the subaperture in the direction perpendicular to the segment edges. This idea is implemented in the GTC where rectangular apertures are used for the phasing.[7]

Another point to consider is the detector size. To avoid overlap, the FOV of the images given by the rectangular subapertures must be at least 5σ, where σ is the rms motion due to seeing, given by

$$\sigma^2 = 0.348(\lambda/d)^{1/3}(\lambda/r_0)^{5/3}, \qquad (11)$$

where λ is the wavelength, r_0 is the Fried parameter, and d is the subaperture size. We will have $N + 1$ images across the detector. Assuming a wavelength of 650 nm, the size of the rectangular subapertures as 12 cm, the number of images on the detector in one dimension as 65, and assuming a scale of 0.2 arcsec/pixel, then a detector of 1024×1024 pixels will be enough if the seeing is not worse than 0.9 arcsec ($r_0 = 14.5$ cm). In this case every image is within a square window of side 3.2 arcsec (16 pixels). If the seeing is worse, then a 2048×2048 pixel detector will be necessary. Again, this technology is currently available. See also Ref. 13 for a discussion of the application of Shack–Hartmann phasing to ELTs.

3. Conclusions

In our process of evaluating several possible methods to phase the segments of ELTs, so far we have investigated in detail the Keck narrow-band technique. We showed that a modified version of it can work with sufficient precision and is feasible on telescopes as large as 100 m. The modification consists first of a new analysis method, the peak ratio technique, that in our simulations yielded more precisely determined segment-to-segment steps than the original Keck technique. The second modification is to use weightings on individual measurement errors when the piston values of all segments are calculated by SVD. Applying these weightings and excluding erroneous measurements is made possible with the peak ratio technique. This enhances the robustness of the algorithm as well as the resulting precision and allows a substantially higher measurement range.

References

1. C. D. Bello, N. Devaney, and J. Castro, "The effect of piston errors on the image quality of ground-based segmented mirror telescopes," Rev. Mex. Astron. Astrofis. **36,** 57–66 (2000).
2. G. W. Zeiders and E. E. Montgomery, "Diffraction effects with segmented apertures," in *Space Telescopes and Instruments V*, P. Y. Bely and J. B. Breckinridge, eds., Proc. SPIE **3356,** 799–809 (1998).
3. N. Yaitskova and K. Dohlen, "Simulation of imaging performance for extremely large segmented telescopes," in *Optical Design, Materials, Fabrication, and Maintenance*, P. Dierickx, ed., Proc. SPIE **4003,** 279–290 (2000).
4. N. Yaitskova and K. Dohlen (both of Observatoire de Marseille, 2 Place Le Verrier, 13248 Marseille cedex 4, France) are preparing a manuscript to be called "Theoretical and computational study of the image quality in extremely large segmented telescopes."

5. D. Gavel, "The effect of the Keck telescope's segmented primary on the performance of the Keck adaptive optics system," in *Adaptive Optics and Applications*, R. K. Tyson and R. Q. Fugate, eds., Proc. SPIE **3126,** 144–150 (1997).

6. C. D. Bello Figueroa, "Improving the image quality of large segmented mirror telescopes," Ph.D. dissertation (Instituto de Astrofísica de Canarias, La Laguna, Tenerife, Spain, 2000).

7. N. Devaney, L. Cavaller, L. Jochum, C. D. Bello, and J. Castro, "Guacamole: the GTC guiding, acquisition and calibration module," in *Optical Design, Materials, Fabrication, and Maintenance*, P. Dierickx, ed., Proc. SPIE **4003,** 146–153 (2000).

8. G. Chanan, M. Troy, F. Dekens, S. Michaels, J. Mast, and D. Kirkman, "Phasing the mirror segments of the Keck telescopes: the broadband phasing algorithm," Appl. Opt. **37,** 140–155 (1998).

9. G. Chanan, C. Ohara, and M. Troy, "Phasing the mirror segments of the Keck telescopes II: the narrow-band phasing algorithm," Appl. Opt. **39,** 4706–4714 (2000).

10. M. Löfdahl and H. Eriksson, "An algorithm for resolving 2π ambiguities in interferometric measurements by use of multiple wavelengths," Opt. Eng. **40,** 2019–2058 (2001).

11. B. Lasker, C. Sturch, B. McLean, J. Russel, H. Jenker, and M. Shara, "The Guide Star Catalog. I. Astronomical foundations and image processing," Astron. J. **99,** 2019–2058 (1990).

12. W. H. Press, B. P. Flannery, S. A. Teukolsky, and W. T. Vetterling, *Numerical Recipes in C: the Art of Scientific Computing* (Cambridge University, New York, 1992), Chap. 2.

13. G. Chanan, M. Troy, and C. Ohara, "Phasing the primary mirror segments of the Keck telescopes: a comparison of different techniques," in *Optical Design, Materials, Fabrication, and Maintenance*, P. Dierickx, ed., Proc. SPIE **4003,** 188–201 (2000).

Phasing ELTs for Adaptive Optics: Preliminary results of a Comparison of techniques
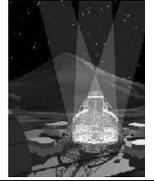
Achim Schumacher[a], Luzma Montoya[b], Nicholas Devaney[a], Kjetil Dohlen[b] and Philipe Dierickx[c]

[a]Instituto de Astrofisica de Canarias, GTC Project, 38200 La Laguna, Tenerife, Spain,

[b]Laboratoire d'Astrophysique de Marseille, 2 Place Leverrier, 13248 Marseille Cedex 4, France,

[c]European Southern Observatory, Karl Schwarzschildstr. 2, D-85748 Garching bei München, Germany

ABSTRACT

There is no doubt that the future telescopes of diameter more than 10m, dubbed 'ELTs', will employ segmented mirrors. The performance of these telescopes may be severely limited by discontinuities in the wavefront, caused by segmentation errors such as segment piston, tip-tilt, figure errors and edge effects. These will particularly affect AO performance, and it is therefore of interest to know what techniques are available to reduce these errors, and what performance can be expected of them. In the framework of a Research and Training Network on Adaptive Optics for ELTs, funded by the European Commission, we are in the process of evaluating the performance of various piston measurement techniques which are either in use on current segmented telescopes, or which have been proposed. In this article we present an overview of these phasing techniques and the performance criteria we will use to compare them. We give detailed results on our study of one particular technique, the Chanan narrow-band phasing technique, which is employed on the 10m Keck telescopes and will also be employed in a modified form on the 10m Gran Telescopio Canarias (GTC). We have developed a new algorithm for extracting the phase information and show that this leads to improved performance. We show that the technique can work with sufficient precision on telescopes as large as 100m.

1. INTRODUCTION

In addition to the usual optical errors associated with monolithic telescopes, segmented mirror telescopes present other errors due to segment misalignment. In general, the segments have six degrees of freedom; translation along two axes in the plane of the segment, rotation about a vertical axis, rotation about two horizontal axes (tip and tilt), and translation along the vertical axis (piston). Undesired motion in any of these degrees of freedom will give rise to departure from the ideal mirror shape and hence affect the wavefront quality. Movement in piston or tip-tilt generally produces wavefront discontinuities. Movement in the first three degrees of freedom is restricted by attachment to the primary mirror cell and will not be considered further here. The segments usually have three actuators each, allowing the segment to be positioned in tip, tilt and piston. The effect of these errors on long-exposure image quality has been examined elsewhere (Bello et al., 2000) and the effect on diffraction-limited images has also been presented (Zeiders, 1998). As it is planned that practically all ELT observations will employ adaptive optics, we are particularly concerned with the effect of these errors on diffraction-limited images.

We will consider piston and tip-tilt separately. The effect of random segment piston errors on Strehl ratio depends on the statistics of the piston errors. However, in the limit of small piston errors, the average Strehl ratio is given by (Yaitskova, 2000)

$$< S > \approx 1 - \sigma^2 \left(1 - \frac{1}{N} \right),$$

(1)

where N is the number of segments and σ^2 is the variance of the segment piston errors. The effect is larger as the number of segments increase, and for ELTs the Strehl ratio can be approximated by $1 - \sigma^2$. In the near infrared, this expression may be taken to imply quite relaxed values of piston. However, since piston will be only one term in a long list of wavefront error sources, it will in fact be necessary to control it precisely.

For example, a Strehl requirement of 0.95 at a wavelength of 1.25 microns implies an accuracy of 44nm in the segment piston control (note that in this article piston values are referred to the wavefront, values at the mirror are a factor of two smaller). Of course, if it is hoped to carry out Adptive Optics at visible wavelengths, then the piston errors will have to be small. For example, a Strehl ratio larger than 0.9 at a wavelength of 0.55 microns implies piston errors less than 25nm (12.6nm at the mirror).

In the case of small tip-tilt errors, the Strehl ratio is given by (Yaitskova, in prep.)

$$<S> \approx 1 - \sigma_\theta^2 \cdot \gamma, \tag{2}$$

where σ_θ^2 is the variance of the tip-tilt angle and $\gamma = 5/36$ in the case of hexagonal segments. For example, for a segment dimension of 2m, a Strehl ratio greater than 0.95 at a wavelength of 1.25 microns corresponds to rms tip-tilt errors of less than 54 nrad (0.011 arcsec). Tip-tilt errors can be measured with high precision using, for example, a Shack-Hartmann wavefront sensor.

This discussion assumes that the AO system will not correct any of the wavefront error introduced by segment misalignment. In fact, AO will always provide partial correction, even if the AO system is not specifically designed to do so (Gavel, 1997). This is especially true in the case of high-order AO. For low-order AO where there are not many subapertures per segment, it would be advantageous to choose the geometry of the AO wavefront sensor so that there are subapertures which cross segment edges in a regular way (Bello, 2000). In general, it is necessary to carry out numerical simulations in order to accurately determine the performance of a given AO system in the presence of segment misalignments. However, in the absence of simulations, expressions (1) and (2) may be taken as pessimistic estimators of the effect of piston and tip-tilt on the Strehl ratio.

A now classical method for phasing segmented mirrors is that implemented in the Keck telescope. Individual segment tilt and piston are adjusted in closed loop using position actuators, the error signal being provided by capacitive sensors measuring inter-segment steps. Periodic calibration of these sensors is required, and a number of convenient techniques have been developed by Chanan et al. (2000), and will be further discussed in Sect. 3. The loss of operational time implied by periodic calibration is moderate; at the Keck, the reported duration of a calibration run is less than an hour and the periodicity is counted in weeks. Accuracy is deemed sufficient for seeing-limited performance. In view of the technological progress made since the design of the Keck telescopes, substantial improvements in sensor characteristics should allow a further reduction of the operational load implied by this methodology, and Chanan indicated that the technique could readily be extrapolated to a large number of segments (Chanan, 2000).

In the case of Extremely Large Telescopes, for which near-diffraction limited performance is mandatory, it remains to be established whether this technique can meet the requirements. In addition, in view of the large number of segments – up to several thousands – reliability considerations may imply that the frequency of calibration or cross-checks has to be increased. It is in this context that this article is presented.

Quite a number of alternative calibration techniques have been proposed over the last few years. Our long-term purpose is to assess the potential performance of each method, devise and perform laboratory and on-sky experiments for the most promising ones, and eventually establish a phasing methodology for an adaptive, Extremely Large Telescope such as the 100-m OWL. This article covers a brief overview of existing or proposed on-sky calibration methods, and provides preliminary simulation results.

2. OVERVIEW OF TECHNIQUES

There are several considerations to be taken into account when comparing segment alignment techniques. The precision of the technique should of course be better than the alignment specification, while the range should cover the expected errors due to thermal and gravitational deformations, sensor drift etc. It would also be desirable for the technique to have sufficient range to align segments after they have been installed. The measurement should be fast so as not to take up useful observing time. Even if it can be carried out in parallel with observation, the time taken should be short compared with typical active optics timescales (minutes). The technique should not require interaction with the telescope (e.g. stepping the segments). Finally, the comparison should evidently include cost and operational complexity.

Several approaches to segment alignment can be found in the literature. In order to correctly position a segment, it is necessary to determine the three dimensional position of three non-colinear points on the segment surface. The approaches to determining segment position can be grouped as follows (Glecker, 1991): (i) absolute position (ii) relative piston and absolute tip-tilt and (iii) relative piston and relative tip-tilt.

The absolute position of the segment in three dimensions can be obtained using techniques such as absolute distance interferometry. The practical implementation would be complex and the accuracy in measuring (for example) the distance from the segments to a point on the secondary mirror would be several microns at best.

The absolute tip-tilt of the segments can be found using a Shack-Hartmann wavefront sensor with a single subaperture per segment. If an AO system is operating, the segment tip-tilt could be determined by low-pass filtering applied to subapertures falling within segments. It would be necessary to know the orientation of the subaperture array with respect to the segmentation pattern at all times. In principle, the absolute tip-tilt can also be determined by other techniques which would not require part of the light to be diverted to a wavefront sensor e.g. using a laser scanner and small reflectors or holographic optical elements on the segments. However, it would appear more practical to employ wavefront sensor information from the AO system or from a dedicated sensor which can be deployed in the field of view. Relative piston can be sensed either optically or using capacitive or inductive edge sensors. The Keck telescope employs capacitive edge sensors (Minor, 1990), while inductive edge sensors have been proposed for the CELT telescope (Nelson, 1999). In either case, optical calibration of these sensors will be required on a regular basis.

Finally, relative piston and relative tip-tilt measurement can be carried out using two edge sensors on the segment edges. This is the strategy employed at the Keck telescope. It is not sensitive to modes which do not give rise to edge discontinuities e.g global tilt, piston or focus mode, in which the segments move in piston and tilt to give rise to a primary mirror defocus. These modes can be determined by low-order wavefront sensing. Again, the edge sensors need to be calibrated optically from time to time.

The optical techniques which are either employed or proposed to measure relative piston will be outlined in the remainder of this section (see also Owner-Petersen et al. (1999)).

2.1. Wave-Optics Shack-Hartmann Sensing

This technique was developed to optically phase the Keck telescopes. It is based on a wave-optics generalization of Shack-Hartmann wavefront sensing. It will be considered in detail in this article (Section 3).

2.2. Curvature Sensing

Curvature sensing is based on measuring the difference in intensity between images obtained equal distances before and after the telescope focus, and is employed in several adaptive optics systems (Roddier, 1991). It has been proposed that curvature sensing can be used to detect piston errors (Rodriguez-Ramos,1996). Cuevas (2000) has shown that the curvature signal does indeed contain information on relative pistons. When the extra-focal distance is large, the relative piston between two segments gives rise to a 'double-delta' function in the curvature signal along the segment boundary. The amplitude of the delta functions is proportional to the relative piston. In the approach of Rodriguez-Ramos & Jimenez (Rodriguez-Ramos, 1996), the extra-focal distance is small and the signal dependence on relative piston is non-linear. An iterative algorithm is therefore used to extract the piston information. Chanan (Chanan, 2000) has used a curvature-type sensor to measure piston errors at the Keck telescope. In his experiments, he obtained de-focused images on an infrared camera operating at a wavelength of 3.3 microns. He determined the piston error on a segment-by-segment basis by comparing the curvature signal with numerical simulations of the curvature signal corresponding to different piston errors in a single segment. He reports an accuracy of $\approx$40nm.

2.3. Interferometry

Relative piston errors can be measured using different interferometric techniques, such as Mach-Zehnder (Angel, Jacobsen, 1994) or shearing interferometry (Horton, 1990). In general, white-light interferometry is necessary in order to identify zero piston error, while narrow-band interferometry is required to increase precision. In the Mach-Zehnder scheme, light from a star is divided between the two arms of the interferometer; the light is passed through a pinhole on one arm and then re-combined with the light in the other arm. If used with adaptive optics, the pinhole size can be diffraction-limited. The technique can measure piston errors for all segments simultaneously. In the radial shearing approach proposed by Horton (1990), the image of one segment is magnified and made to interfere with light from surrounding segments. In the absence of adaptive correction, the interference fringes will be randomly (and rapidly) distorted by atmospheric turbulence, and this represents a fundamental limitation of these techniques. Dohlen (1998) proposed making interferometric measurements simultaneously at two wavelengths in order to remove the 2π ambiguities in the piston measurements. It has also been proposed to mount a Michelson interferometer on a robotic arm which positions the interferometer in front of the segment edges (Arasa, 2000). This technique has the advantage of being able to operate in the
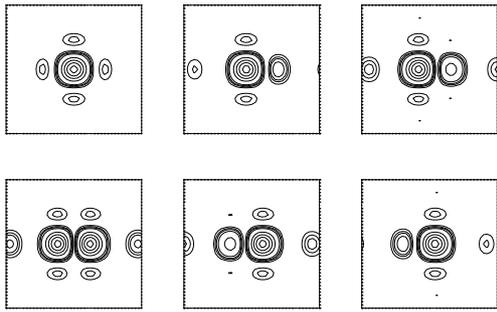
Figure 1. Simulated diffraction patterns for a split squared subaperture with wavefront step δ between the two halves given by $k\delta = 0, 2\pi/6, 4\pi/6, ..., 10\pi/6$.
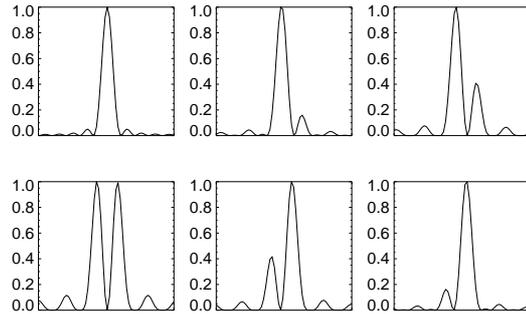

Figure 2. x-projection of images of Fig. 2

daytime, and therefore does not use any useful observing time. The interferometer needs to include active fringe stabilization in order to cancel the effect of mechanical vibrations.

2.4. Pyramid Wavefront Sensing

It has recently been suggested that pyramid sensing could be used for piston sensing. This idea has been examined using simulations and the results are presented elsewhere in these proceedings (Esposito & Devaney).

2.5. Phase Diversity

In phase-diverse wavefront sensing, pairs of in-focus and out-of-focus images are recorded. The amount of defocus is small and precisely known. An iterative technique is used to find the pupil aberrations which best match the measured data. This is similar to phase retrieval, but the de-focused image provides extra constraints on the solution. It was predicted that it should be possible to use this technique to determine piston errors (Paxman, 1988). An experiment was carried out at the Keck telescope, but the results were inconclusive. This may be due to the fact that the seeing was poor and the stellar reference source, which was supposed to be point-like, was in fact resolved by the telescope (Lofdahl, 1998). They propose to repeat the experiment in parallel with operation of the Keck adaptive optics system.

3. THE CHANAN NARROW-BAND ALGORITHM APPLIED TO ELTS

This technique is the first we have investigated in detail. It is based on a Shack-Hartmann-type wavefront sensor, where the lenslet array is preceded by a mask at the position of the exit pupil that defines small subapertures at the center of each of the intersegment edges. In the case of the Keck telescopes, these subapertures are circular; in this paper we refer to square subapertures as will be used at the GTC (Devaney, 2000). The size of the subapertures is chosen to be smaller than the average Fried parameter, r_0, of approximately 20cm at a wavelength of 500nm. At the Keck and at the GTC this size is 12cm with respect to the primary mirror.

3.1. Description of the Algorithm to Extract the Phase

In this section we will concentrate on the algorithm applied to extract phase information from a single inter-segment edge step (or piston step). The original Chanan narrow-band technique (Chanan, 1998) is described and compared to a modified algorithm. Both techniques exploit the diffraction pattern produced by a small intersegment subaperture and monochromatic light from a bright stellar source. The resulting simulated diffraction patterns for various piston steps are shown in Fig. 1, and their projection on the x-axis in Fig. 2. The two algorithms under comparison differ in the way they make use of these images.

In the Chanan approach, an image taken from a subaperture with unknown piston step is compared to a set of 11 simulated images like those of Fig. 1. The real piston step is somewhere between the piston steps of the two most similar images. The degree of similarity is determined by calculation of a correlation coefficient; a finer resolution than the piston step difference between two templates ($\lambda/11$ at the wavefront (WF)) is achieved by quadratic interpolation of the correlation coefficients. For improved accuracy the primary mirror segments are stepped though 11 piston values spanning $\lambda/11$ (WF) using the segment actuators.
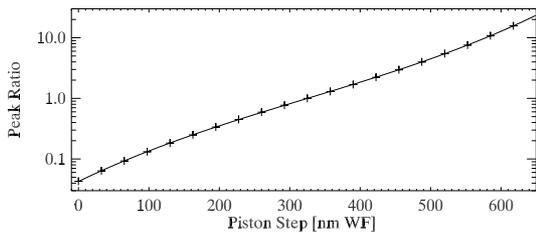
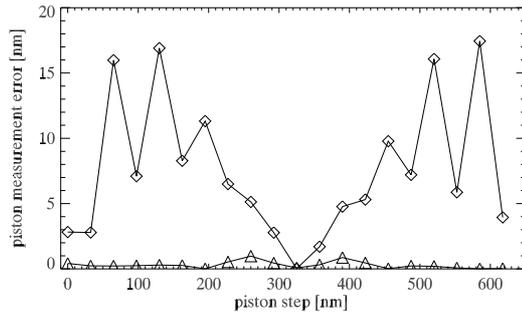**Figure 3.** Peak ratio calibration curve (λ = 650nm).

Figure 4. Measurement precision of the Chanan (diamonds) and the peak ratio (triangles) technique under perfect conditions.

We propose a new approach which is based on extracting a single characteristic value from each simulated image related to the piston step, and then calculating a calibration curve. One possible characteristic value, which will be applied here, is the ratio between the two main peaks in the diffraction pattern (see Fig. 2). We will refer to this technique as the peak ratio technique (See also (Bello, 2000)). Defining the peak ratio as $PR = Max(right\ peak)/Max(left\ peak)$ we obtain the calibration curve shown in Fig. 3. In this figure the calibration points obtained from the simulation are plotted together with a fitted polynomial of third degree to (the logarithm of) these points; it represents the data with sufficient accuracy. The coefficients of this polynomial are used as calibration data. For a given subaperture image, the peak ratio is calculated and processed with the calibration data in order to obtain the required piston step.

The resulting precision under perfect conditions of the Chanan technique (without stepping the segments) and of the peak ratio technique are plotted in Fig. 4. The precision of the peak ratio technique is only limited by the validity of the polynomial fit to the calibration data and by calculation roundoff errors, whereas the original Chanan technique shows an intrinsic error of up to 18nm. The performance under non-perfect conditions is discussed in the following sections. Possible sources for the intrinsic error of the original Chanan technique are the following: (i) To calculate the correlation coefficients, all images first have to be re-registered, so that the centroids coincide exactly with the array center, and not just to within the nearest pixel. (ii) The correlation coefficients do not exactly show a quadratic dependence. In (Chanan, 1998) a deviation of up to 0.7% between the coefficient and its quadratic approximation is stated. (iii) The process of calculating the correlation coefficient itself could be an error source. Since we used our own analysis code, it is possible that the code used at Keck is further optimized and shows less intrinsic errors.

It is possible to extract the maximum values of the peaks even in bad seeing conditions or with relatively high photon noise. In Fig. 5 the resulting PSF for various seeing conditions and a fixed piston step of $\lambda/4$ are plotted (straight line). As the seeing gets worse, the binary structure gets less distinct. But even in the case of barely having a binary structure it is still possible to extract the maximum heights of the two peaks involved. Fitting the sum of two gaussians to the PSF will yield the results shown in Fig. 5 (dotted lines). With this method it is possible to obtain a result for Fried parameters as small as $r_0 \approx$ 6cm at 650nm. As is shown in Fig. 6, the calibration curves obtained for different seeing conditions differ slightly, leading to measurement errors as discussed in Sect. 3.2. This Gaussian fit method is also suitable for the case of having photon noise as discussed in Sect. 3.3. An important advantage of the Gaussian fit method is the fact that it provides not only the values of the two peak heights, but also an estimation of their uncertainties. Knowing the precision of each piston step measurement allows us to perform a weighting when calculating the segment piston values from all measured subaperture piston step values, as described in Sect. 3.4.

Both the Chanan and the peak ratio technique result in a useful range which depends on the wavelength used. The maximum unambiguous piston step is $\pm\frac{\lambda}{2}$ at the wavefront. The maximum deviation from the mean value of the segment pistons is then $\pm\frac{\lambda}{8}$ at the mirror. In the case of $\lambda = 650$nm this means that the segments have to be already aligned to better than 162nm. It is therefore convenient to take another measurement at a different wavelength in order to avoid the ambiguities. If $\lambda_1 = 650$nm and $\lambda_2 = 850$nm then the range is about 10 times greater.

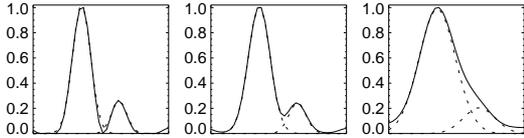**Figure 5.** 1d-diffraction patterns at various seeing conditions $r_0(500nm)=\infty$, 16cm, 6cm.

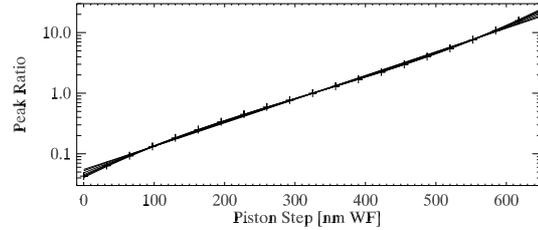**Figure 6.** Peak ratio calibration curves at various seeing conditions down to $r_0(500nm)=8cm$ ($\lambda=650nm$).
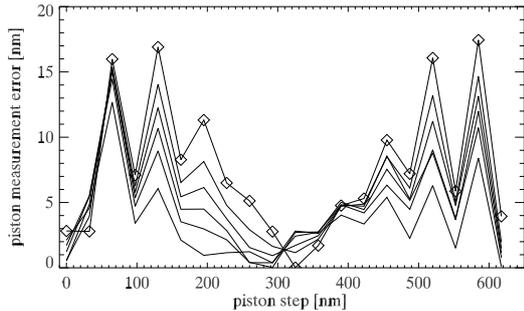

Figure 7. Measurement precision of the Chanan technique under various seeing conditions. Diamonds represent data with perfect seeing conditions.
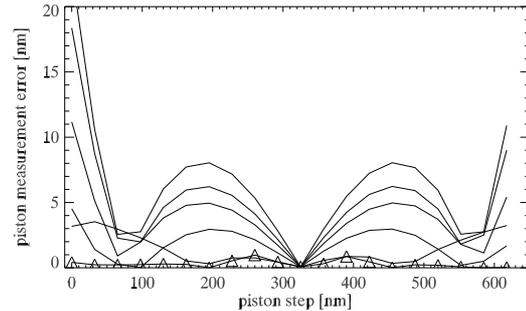

Figure 8. Measurement precision of the peak ratio technique under various seeing conditions, using calibration data obtained for best seeing conditions. Triangles represent data with perfect seeing conditions.

3.2. Performance as Function of Seeing

As described in Sect. 3.1 and shown in Fig. 5 the shape of the diffraction pattern changes with the seeing conditions. The way this affects the measurement precision depends on the method chosen to extract phase information. At the Keck telescopes, only 11 images at perfect seeing conditions are simulated and compared to the real image under investigation. Surprisingly, the original Chanan technique works better when seeing gets worse, as can be seen in Fig. 7. In the peak ratio technique worse seeing conditions will produce a greater peak ratio error due to a systematic error in the gaussian fit. The resulting measurement errors for various seeing conditions are shown in Fig. 8. The precision is greatly affected by the seeing condition. However, since the error of the gaussian fit is systematic, one can correct for it. Calculated calibration curves for various seeing conditions are shown in Fig. 6. The real seeing condition can be estimated from the width of the fitted peaks and one can apply the corresponding calibration curve. The resulting piston step measurement error is then almost reduced to its value at perfect conditions, as can be seen in Fig. 9.

3.3. Performance as Function of Magnitude

In this section we will calculate the stellar magnitude required to phase the mirror using the narrow-band technique with the peak-ratio algorithm. The limiting stellar magnitude will depend on the number of photons required to measure the piston errors with the specified accuracy. The magnitude of a star is related to the number of photons arriving at the detector as follows:

$$n = \eta t A \epsilon 10^{-0.4M} \Delta\lambda \tag{3}$$

where ϵ is the system efficiency, t is the exposure time, A is the collecting area, η is the number of photons per cm^2 per nm from a zero magnitude star, $\Delta\lambda$ is the bandwidth, and M is the magnitude of the star.

Figure 10 shows the error in the piston measurement for different photon levels. The given error is the standard deviation of 360 random simulations at different piston steps – it turned out that in the case of photon noise the gaussian fit error does not depend on the piston step value. In order to keep the standard deviation
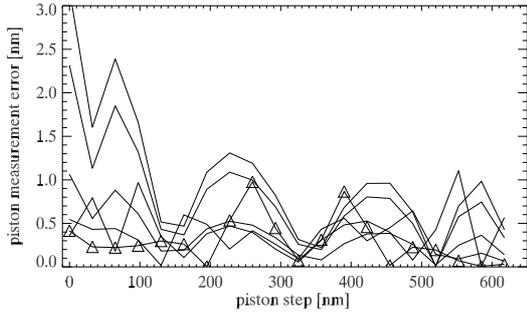
Figure 9. Measurement precision of the peak ratio technique under various seeing conditions, using the calibration data corresponding to the actual seeing condition. Data with perfect seeing conditions are marked.
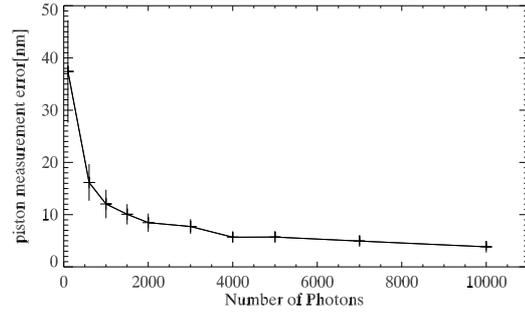
Figure 10. Rms measurement precision of the peak ratio technique under various photon noise conditions (λ=650nm).

due to photon noise in the piston step measurement below 5nm, approximately 10000 photons per subaperture are required. Although 5nm seems to be small, one should bear in mind that this is a standard deviation and single measurements may be affected by higher errors. From simulations of whole mirrors we found that 10000 photons per subaperture will give stable results at all times.

Table 1 shows the limiting stellar magnitude and the corresponding required accessible field to find such a star with a probability of 90% for different photon levels at the North and South Galactic Poles. Here we assumed the following values: ϵ=0.8, which is the product of the transmission from the top of the atmosphere to the detector, and the detector quantum efficiency, t=60 seconds, which is typical of active optics timescales, A=144 cm^2, corresponding to square subapertures with a side length of 12cm, $\Delta\lambda$=10 nm, and η(650nm)=8730 cm^{-2}nm^{-1}. The required field of view (FOV) can be obtained from the probability P of finding at least one star within a given radius, r, on the sky. Since the distribution of stars on the sky follows Poisson statistics, P is given by:

$$P = 1 - e^{-r^2 \nu \pi / 3600^2} \tag{4}$$

where ν is the density of stars brighter than magnitude M per deg^2 in the considered region. This star density can be obtained from models of the galaxy or from measurements using for example the Guide Star Catalog, which has been employed here. From the results shown in Tabl. 1, it can be seen that a minimum accessible field of view of 10 arcminutes diameter is required to ensure accurate piston measurements at all times. This is comparable to the FOV of OWL.

3.4. Performance as Function of Telescope Size/Number of Segments

So far we have restricted our discussion on the determination of a single intersegment piston step. For the whole mirror made up of $N_{segments}$ hexagonal segments with one subaperture on each side there will be $N_{subapertures} < 3N_{segments}$. The exact value of $N_{subapertures}$ depends on mirror design aspects such as the outer shape and the central obscuration, since segments on the outer or inner borders have less than 6 neighbors. Each segment piston is determined by (up to) 6 piston step measurements and affects the segment piston measurements of all of its neighbors and hence of the whole mirror. This can be expressed mathematically as a system of linear equations of the form

Table 1. Limiting stellar magnitude and the corresponding required accessible field (FOV) to find such a star with a probability of 90% for the peak ratio method at different photon levels at the North and South Galactic Poles. The given precision is the standard deviation of a piston step measurement at otherwise perfect conditions.

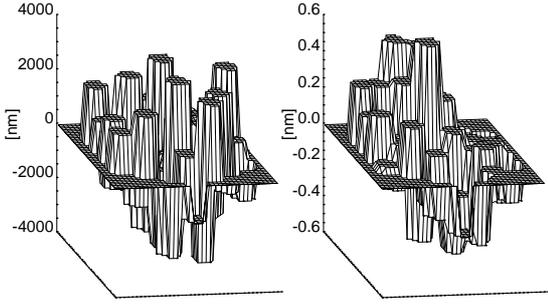| N_γ	Precision	Magnitude	FOV_{NGP} [arcmin]	FOV_{SGP} [arcmin]
10000	5 nm	11.8	10.1	8.0
2000	10 nm	13.7	5.4	4.7

Figure 11. Segmented mirror of the Keck/GTC type (36 segments) before (left) and after (right) one phasing iteration. In this simulation perfect conditions were assumed. The original piston values are uniformly distributed with a range of 6530nm and a rms of 1990nm. Two measurements at different wavelengths have been performed ($\lambda = 650$nm, 850nm). The resulting rms piston error is 0.27nm, the rms piston step measurement error is 0.31nm.
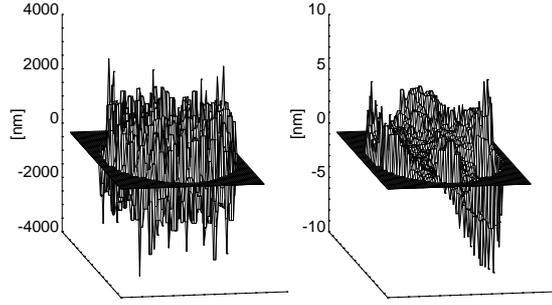

Figure 12. Segmented ELT mirror (846 segments) before (left) and after (right) one phasing iteration. In this simulation perfect conditions were assumed. The original piston values are uniformly distributed with a range of 4000nm and a rms of 1125nm. Two measurements at different wavelengths have been performed ($\lambda = 650$nm, 850nm). The resulting rms piston error is 2.0nm, the rms piston step measurement error is 0.4nm. The smooth residual is an example of the propagation of errors for which the sensitivity of the technique is low.

$$\text{Piston1}_i - \text{Piston2}_i = \text{PS}_i, \tag{5}$$

$$i = 1, ..., N_{subapertures},$$

where Piston1_i and Piston2_i are the Piston values of the two segments corresponding to subaperture i and PS_i is the measured piston step. Since the absolute average phase of the mirror is not of interest, it makes sense to keep it constant, adding a further constraint:

$$\sum_{j=1}^{N_{segments}} \text{Piston} = 0. \tag{6}$$

Eqs. (5) and (6) constitute a simple linear system of $N_{subapertures} + 1$ equations with $N_{segments}$ unknowns (PS_i). At the Keck telescopes the technique of singular value decomposition (SVD) is used to solve this system (Chanan, 1998). We used this method on simulations of mirrors having up to 1000 segments and found it powerful and robust even on the scale of ELTs. Figures 11 and 12 show the results of some example simulations of mirrors of different sizes.

In the SVD method, one essentially provides a matrix, A, defined by the left hand side of Eqs. (5) and (6), and a vector defined by the right hand side, and SVD returns a vector of piston values. In the process, a pseudo-inverse of A (of $N_{subapertures}$ rows and $N_{segments}$ columns) is constructed that defines the linear system. Since we deal with an over-determined system, having more equations than unknowns, and furthermore our measured values are not perfect, SVD provides a best fit (in the sense of least-squares) to the set of data.

The measured data can be weighted to ensure that the piston step measurements with high precision will have more influence than those with less precision. This is done by simply dividing all equations i by the absolute error of the piston step measurement $\sigma(\text{PS}_i)$. Furthermore, piston step measurements for which the gaussian fit procedure appearantly did not find a valid solution can be excluded by making the corresponding line of the SVD matrix equal to zero. The same procedure should be applied if in a two-wavelength measurement a certain piston step measurement yields an ambiguous solution. Alternatively, the more probable solution can be chosen, and the corresponding error set to a high value to reflect the ambiguity. Applying these corrections to the straight forward implementation of SVD will give better results and furthermore will substantially enhance the robustness of the method. If weighting is not applied then a single erroneous or high-error piston step measurement can not only lead to a wrong piston estimation for the two corresponding segments, but can also

8

affect a large number of their neighbors. In the worst case, it will not be possible to phase any of the segments. In the case of ELTs with hundreds or thousands of segments there is a high probability that there will be some faulty piston step measurements. Applying these weightings will provide stable results even in the presence of seeing and photon noise.

There are further possibilities to enhance the performance of the SVD procedure that should be used when applying on ELTs. First, a large number of subapertures leads to accumulating roundoff errors. The overall precision of the phasing procedure could be enhanced by iterative improvements of the solution to the linear equations. Second, a large number of subapertures means a large matrix A in the SVD calculations. One can save computation time and memory space by using the fact that we deal with a sparse linear system – A is mainly made up of zeroes that should not be processed and occupy memory. The computation times we find with the current, unoptimized code, indicate a computation time of the order of seconds when implemented on ELTs, if faster CPUs and parallel processing are employed. For further discussion of SVD as well as the code, see (Press, 1992).

3.5. Practical Aspects

It is clear that for this technique, the number of subapertures increases with the number of segments. If we consider a regular grid of hexagonal lenslets mapped onto an image of the segmented mirror, then in order to measure the piston step at each segment edge we need to map at least 2N+1 lenslets onto N segments. There is an extra lenslet centered on each segment, which can be used to measure tip-tilt. In the case of the OWL telescope, there are 64 segments on its longest axis and the corresponding number of subapertures is 129. If the hexagonal edge length of the lenslets is 0.3mm then the length of the lenslet array would be 67mm, and the corresponding pupil demagnification would be approximately 1700. The lenslets used for phasing would be masked, leaving a 70 micron subaperture at the center. The lenslet array has to be precisely aligned to the image of the primary mirror for the Chanan technique to work. The alignment should at least be better than the size of the gaps between the segments. An alignment accuracy of 1mm referenced to the primary mirror would imply aligning the lenslet array to better than 0.6 microns. These specifications can be met with currently available technology. The alignment accuracy can be relaxed by including 'cross-hairs' in the lenslet masking, with the cross-hairs aligned to the segment edges. These cross-hairs can also relax the requirements on distortion in the pupil imaging; pupil distortion may be difficult to reduce when a large pupil demagnification is required. The drawback is a reduction in the light-gathering area of the subaperture. This can be compensated to some extent by elongating the subaperture in the direction perpendicular to the segment edges. This idea is implemented in the GTC where rectangular apertures are used for the phasing.

Another point to consider is the detector size. In order to avoid overlap, the field of view of the images given by the rectangular subapertures must be at least 5σ, where σ is the rms motion due to seeing.

$$\sigma^2 = 0.348(\lambda/d)^{1/3}(\lambda/r_0)^{5/3} \tag{7}$$

where λ is the wavelength, r_0 is the Fried parameter and d is the subaperture size. We will have N+1 images on the detector. Supposing a wavelength of 650nm, the size of the rectangular subapertures as 12cm, the number of images on the detector in one dimension as 65, and supposing a scale of 0.2"/pixel, then a detector of 1024x1024 pixels will be enough if the seeing is not bigger than 0.9" (r_0=14.5cm). In this case every image is within a square window of side 3.2" (16 pixels). If the seeing is worse then a 2048x2048 pixels detector will be necessary. Again, this technology is currently available.

4. CONCLUSIONS AND PLANS

The phasing techniques addressed in this article have been tentatively reviewed for their potential accuracy. We so far investigated in detail the Chanan narrow-band technique. We showed that a modified version of it can work with sufficient precision and is feasible on telescopes as large as 100m. A comparison of the original Chanan technique and the alternatively developed peak ratio technique showed substantial performance improvements of the latter.

Much work still lies ahead before completing an extensive assessment, which will have to take into account a complete and representative set of error sources. So far we have assumed that phasing is dealt with the same way as it is done in the Keck telescopes i.e., closed-loop phasing with position sensors, the techniques described in this article being used for calibration of the sensors. An alternative could be on-sky, closed loop phasing i.e. a scheme that would make phasing an integral part of wavefront control as it is done in active

telescopes, thereby providing higher reliability and full transparency. Whether such approach is feasible at all is yet unknown; the key issues to be addressed will not only deal with accuracy, but also with the limiting magnitude of the reference source(s) and the implied sky coverage, the affordable integration time in relation to the stability of segments phase errors, and the interface with adaptive optics. In particular, any technique that would require prior adaptive correction of atmospheric turbulence will necessarily reduce the field available for suitable phasing references. On the other hand, piston and tilt detection prior to adaptive correction will most likely require short exposure or rely on sub-aperture measurements (the size of the sub-apertures being comparable to atmospheric coherence length), thereby implying brighter sources and limited sky coverage.

ACKNOWLEDGMENTS

REFERENCES

J. Arasa, F. Laguarta, C. Pizarro, N. Tomas, A. Pinto, *Design of an interferometric system for piston measurements in segmented primary mirrors*, Proc. SPIE, 4093, 397-406, 2000

C. D. Bello Figueroa, *Improving the image quality of large segmented mirror telescopes* PhD thesis, Instituto de Astrofísica de Canarias, La Laguna, Tenerife, 2000

C. D. Bello, N. Devaney, J. Castro, *The effect of piston errors on the image quality of ground-based segmented mirror telescopes*, Rev. Mex. Astron. Astrofis., 36,57-66, 2000

G. Chanan, M. Troy, F. Dekens, S. Michaels, J. Mast, D. Kirkman, *Phasing the mirror segments of the Keck telescopes: the broadband phasing algorithm*, App.Opt., Vol. 37 (1), 140-155, 1998

G. Chanan, M. Troy, C. Ohara, *Phasing the Primary Mirror Segments of the Keck Telescopes: A comparison of Different Techniques*, Proc. SPIE 4003, 188-201, 2000

S. Cuevas, V.G. Orlov, F. Garfias, V.V. Voitsekhovich, L. Sanchez, *Curvature equation for a segmented telescope*, Proc. SPIE, 4003,291-302, 2000

N. Devaney, L. Cavaller, L. Jochum, C.D. Bello, J. Castro, *Guacamole: The GTC Guiding, Acquisition and Calibration Module*, Proc. SPIE, 4003, 146-153, 2000

K. Dohlen, F. Decertiat, F. Fresneau, P. Lanzoni, *A dual wavelength random phaseshift interferometer for phasing large segmented primaries*, Proc. SPIE, 3352, 551, 1998

D. Gavel, *The effect of the Keck Telescope's Segmented Primary on the Performance of the Keck Adaptive Optics System*, Proc. SPIE, 3126, 144-150, 1997

A.D. Glecker, K.P. Pflibsen, B.L. Ulich, D.D. Smith, *Surface control techniques for the segmented primary mirror in the Large Lunar Telescope*, Proc. SPIE, 1494, 454-471, 1991

R. Horton, E. Huber, L. Bernotas, L. Yee, A. Roberts, J. Norton, E. Corbett, R. Humphries, *Absolute piston phasing of segmented-mirror optical systems using depth-modulated white-light interferometry*, Proc. SPIE, 1236, P974, 1990

B. Jacobsen and R. Angel, *High accuracy wavefront stellar wavefront sensing using a Zernike interferometer*, Bull. American Astron. Soc., 26, p1373, 1994

M.G. Lofdahl, R.L. Kendrick, A. Harwit, K.E. Mitvhell, A.L. Duncan, J.H. Seldin, R.G. Paxman, D.S. Acton, *A Phase Diversity Experiment to Measure Piston Misalignment on the Segmented Primary Mirror of the Keck II Telescope*, Proc. SPIE, 3356, 1190-1201, 1998

R.H. Minor et al., *Displacement sensors for the primary mirror of the W.M. Keck telescope*, Proc. SPIE, 1236, 1990

J. Nelson and T. Mast, *Giant Optical Devices*, Proc. Backaskog Workshop on Extremely Large Telescopes, 1-11, 1999

M. Owner-Petersen and T. Andersen, *Overview of Optical Metrology for Segment Phasing*, Proc. Backaskog Workshop on Extremely Large Telescopes, 152-161, 1999

R.G. Paxman and J.R. Fienup, *Optical misalignment sensing and image reconstruction using phase diversity*, J.Opt.Soc.Am. A, 5, 914-922,1988

W.H. Press, B.P. Flannery, S.A. Teukolsky, W.T. Vetterling, *Numerical Recipes in C: the art of scientific computing*, Cambridge U. Press, New York, 32-70, 1992

F. Roddier, M. Northcott, J.E. Graves, *A simple low-order Adaptive Optics system for Near-Infrared applications*, PASP, 103, 131-149, 1991

J.M Rodriguez-Ramos and J.J Fuensalida, *Piston Detection of a Segmented Mirror Telescope using a Curvature Sensor. Preliminary Results with Numerical Simulations*, Proc. SPIE 2871, 613-616, 1996

N. Yaitskova & K. Dohlen, *Simulation of imaging performance for extremely large segmented telescopes*, Proc. SPIE, 4003, 279-290

N. Yaitskova & K. Dohlen, *Theoretical and computational study of the image quality in extremely large segmented telescopes*, in preparation

G.W. Zeiders, E.E. Montgomery, *Diffraction Effects with Segmented Apertures*, Proc. SPIE, 3356, 799-809, 1998